DEPOSITION OF SODIUM CARBONATE AND SODIUM SULFATE IN SUPERCRITICAL WATER OXIDATION SYSTEMS AND ITS MITIGATION

by

MOHAMMAD SULTAN KHAN

B.Sc., University of Engineering and Technology Lahore, 1990
M.Sc., King Fahd University of Petroleum and Minerals, 1996

A THESIS SUBMITTED IN PARTIAL FULFILMENT OF
THE REQUIREMENTS FOR THE DEGREE OF

DOCTOR OF PHILOSOPHY

in

THE FACULTY OF GRADUATE STUDIES
(MECHANICAL ENGINEERING)

THE UNIVERSITY OF BRITISH COLUMBIA

March 2005

©Mohammad Sultan Khan, 2005

Abstract

Supercritical water oxidation (SCWO) is a technique to destroy wet organic waste. The oxidation reaction takes place at high temperature (T > 374°C) and pressure (P > 22 MPa). Organics are miscible with water at these conditions but inorganic salts, such as Na_2SO_4 and Na_2CO_3, are not soluble and crystallize on the reactor surface leading to the problem of heat exchanger fouling. Solubility and deposition of these salts on a tubular heat exchanger (reactor) surface have been studied in this work. Experiments were performed to determine solubility of these salts in binary phase and in ternary phase systems, for a wide range of temperatures. A rapid decrease in the salt solubility was observed just above the pseudo-critical temperature. For supercritical conditions, the solubility of each salt in the form of a mixture was quite close to the solubility of pure salt.

In order to reduce the net salt deposition, particulate instead of crystalline deposition was encouraged. In the presence of particulate fouling, the deposit buildup was not steady. The flowing fluid partially removed the deposited layer, once it reached a certain thickness, and then the deposition process continued over a number of cycles. Compared to pure crystalline fouling, combined particulate-crystalline fouling resulted in a three times longer operating period, before the system had to be shut down for removing salt deposits. Salt solution leaving the reactor was four times higher than the saturation limit. The structure of the deposits, both pure crystalline and combined particulate-crystalline, were analyzed using Scanning Electron Microscope (SEM) and Energy Dispersive X-ray (EDX). The crystalline scale structure was found to be dense and tenacious, whereas the combined particulate-crystalline deposit was relatively less dense and easy to remove. A computer program has been developed, in MATLAB, to simulate heat and salt mass transfer in order to determine the salt deposition at various reactor locations. The model predicts the clean tube surface temperature quite accurately. The surface temperature change after the salt deposition is also in good agreement with the actual experimental measurements. The calculated location of the peak surface temperature change, due to fouling resistance, was found to be quite close to the experimental data.

Acknowledgements

All praise to the merciful God, who bestowed me the strength and patience to accomplish my goals.

I consider myself fortunate to work under the supervision of Dr. Rogak and would like to thank him for his guidance and cooperation. It is due to his competence and expertise that my research work progressed smoothly. I am indebted to his expert suggestions and advice. I also wish to thank Dr. Branion for his enthusiastic and thoughtful comments and discussions during our group meetings. Thanks are due to Dr. Watkinson for his expert and valuable advice. I am grateful for the time he spared for my research from his busy schedule. I am thankful to Dr. Bushe for his guidance and discussions we had regarding my research work and other heat transfer issues.

I have had the pleasure of meeting many bright and interesting people during my studies at UBC. It has been wonderful knowing my colleagues Davood Faraji, Ivette Vera-Perez, Bülent Güzel, Timothy Wang, Heather Jones, Eduard Asselin, Conner Reynolds and Greg Brown. I am grateful to Davood Faraji for not only helping me in virtually all my experiments but also for his positive and encouraging attitude. I appreciate his assistance during experiments on weekends & late nights and his eagerness to run the experiments.

I certainly owe my success to my wife Mariam, who always gave priority to my academic goals. I am grateful for her encouragement and support during tough times. I appreciate her patience and understanding. Thanks are due to my parents for their prayers that enabled me to see this work to its completion.

Finally, financial support provided by NSERC and NORAM is acknowledged.

Contents

List of Tables

List of Figures

Nomenclature

A_c	cell cross-sectional area	m^2
b_k	Boltzmann constant	J/K
C	dissolved salt concentration	kg/m^3
C_p	specific heat at constant pressure	J/kgK
C_T	total salt concentration	kg/m^3
C_o	salt concentration in the effluent	kg/m^3
d	tube diameter	m
dl	mixing step length	m
d_p	salt particle diameter	m
$\mathcal{D}_m$	molecule diffusion coefficient	m^2/sec
$\mathcal{D}_T$	turbulent diffusivity	m^2/sec
dx	integration step length	m
f	friction factor	
H	fluid enthalpy	J/kg
h	convective heat transfer coefficient	W/m^2K
h_m	mass transfer coefficient	m/sec
J	salt particle nucleation rate per unit volume	
J_m	salt molecule condensation rate	
k_d	thermal conductivity of the deposit layer	W/mK
k_t	thermal conductivity of the tube	W/mK
K_{12}	salt particle coagulation coefficient	m^3/sec
L	length	m
Le	Lewis number	
m	number of cells in pure water	
$\dot{m}$	fluid mass flow rate	kg/sec
$\dot{m}_m$	molecule deposition rate	kg/sec
m_{p^*}	mass of nucleated salt particle	kg
m_{p^1}	mass of grown salt particle	kg
m_{p^o}	mass of average sized salt particle	kg
n	number of cells in salt solution	

N_m	molecule concentration	
N_p	particle concentration	
Nu	Nusselt number	
P	system pressure	MPa
Pr	Prandtl number	
Q	heat supplied	W
q	heat flux	W/m^2
r	tube radius	m
$r*$	salt particle critical radius	m
R	average number of fluid parcels in a cell	
Re	Reynolds number	
R'	actual number of fluid parcels in a cell	
r_f	final particle radius	m
r_p	particle radius	m
S	degree of salt saturation	
Sc	Schmidt number	
Sh	Sherwood number	
$SLSI$	salt layer solution interface	
t	time	sec, hr
T	temperature	^oC
u'	velocity fluctuation	m/sec
V	fluid mean velocity	m/sec
V_d	salt particle deposition velocity	m/sec
V_m	volume of salt molecule	m^3

Greek symbols

Δd	cell height	m
Δz	distance moved by the fluid parcels	m
ϵ	kinetic energy dissipation rate	m^2/sec^3
$\acute{\epsilon}$	tube surface roughness	m
γ	surface tension	N/m
μ	fluid dynamic viscosity	$N.s/m^3$
ν_T	turbulent viscosity	m^2/sec
ρ	density	kg/m^3
τ_D	characteristic time for turbulent diffusion	
τ_p	particle relaxation time	
τ_w	wall shear stress	N/m^2

Subscripts

A	salt solution
B	pure water
b	bulk fluid conditions
e	conditions in cell at the edge of SLSI
ep	particle concentration in the cell at the edge of SLSI
f	fluid
i	inner surface
m	molecule
o	outer surface
p	particle
pc	pseudo-critical
s	salt layer solution interface
sat	saturated condition
sp	particle concentration at SLSI
w	at tube wall condition

Chapter 1

Introduction

1.1 Supercritical water oxidation (SCWO)

Supercritical Water Oxidation is a process for the destruction of aqueous organics (waste), which is made possible due to special properties of supercritical water. For pure water, the critical point corresponds to 22.09 MPa and 374.14°C [1]. When exceeding its critical point, the values of density, dielectric constant, and ionic product of water decrease, so supercritical water acts as a non-polar solvent of high diffusivity and excellent transport properties (see Fig 1.1 [2]). At supercritical conditions, the reactants consist of a homogeneous single-phase mixture facilitating complete reaction i.e., organics and oxygen are completely miscible which allows oxidation of organics without any interphase mass transfer resistance. As a medium of chemical reactions, depending on its density, supercritical water has both gas-like and liquid-like properties. The gas-like low viscosity promotes mass transfer. The liquid-like density promotes solvation. The low dielectric constant promotes dissolution of non polar organic materials and the high temperature increases the thermal reaction rates [3].

SCWO is a non-polluting alternative to other waste-disposal techniques such as incineration and biological treatment when the others are inefficient or potentially hazardous to the environment. Furthermore, SCWO is a compact, energy-efficient process, which can be integrated into a closed cycle chemical plant since its effluent components can be separated. The process is totally enclosed up to the point of final discharge to the environment. This feature is very useful when treating highly toxic or radioactive wastes. The operating temperatures are much lower than incineration, so nitrogen oxides are not formed. The SCWO process involves pressurizing aqueous waste and oxidant to the working pressure. This is followed by mixing the pressurized streams; preheating to the temperature at which reaction is initiated; oxidation reaction with subsequent cooling. Finally, the system is depressurized and the gaseous, liquid and solid products separated. In a typical SCWO waste treatment system, dilute aqueous organic waste is combined with an oxidizer at elevated pressure and temperature in a reactor for res-

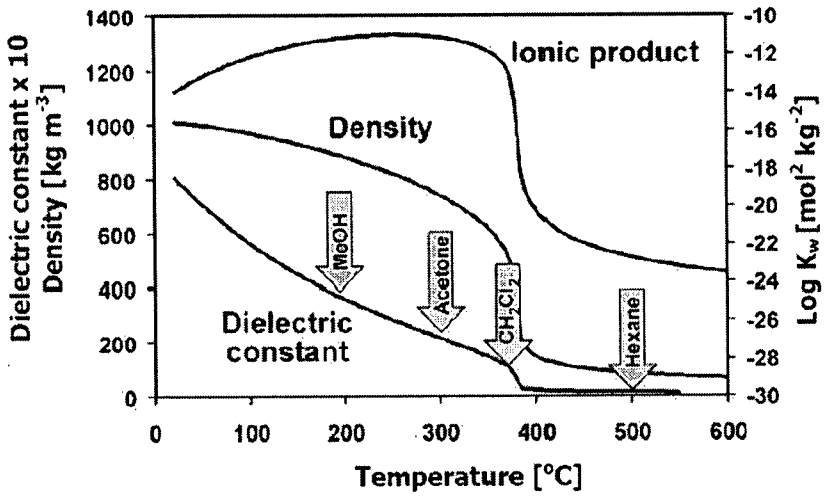

Figure 1.1: Physical properties of water at a pressure of 24 MPa versus temperature. Dielectric constants of typical organic solvents at room temperature are indicated [2]

idence times on the order of 30 to 90 seconds which strongly depends on the reaction temperature. Typically SCWO is carried out at reaction temperatures of 500-700°C and pressures of 24-50 MPa. The products of the reaction are CO_2, H_2O and for some wastes inorganic salts also. The salt may be present in the waste itself or could be a product of the oxidation reaction. Water at room temperature is an excellent solvent for most salts, with solubility at typically 100 g/l. However, whereas the organics are totally miscible at SCWO conditions, the inorganic compounds are not soluble. In low-density supercritical water, the solubility of most salts is low, typically 1-100 ppm [4–7]. This results in the precipitation of salts when a sub-critical salt containing solution is heated to supercritical temperature. Common examples of such compounds are Na_2SO_4, Na_2CO_3 and $CaSO_4$.

1.2 Problems associated with SCWO

The reason why SCWO has not yet become a current waste treatment technology can be seen in three reasons [2]:

- Severe reactor corrosion caused by acids, which are formed during the waste treatment process.
- Serious plugging of the reactors caused by precipitating salts at supercritical temperatures and low densities.
- Due to lack of experimental data, cost evaluations, especially for the scale-up of SCWO plants to an industrial scale, are unreliable.

The problems hindering the commercialization of SCWO are corrosion, due to acids produced during the reaction and salt deposition due to the undissolved salts. Solid salts tend to agglomerate and coat internal surfaces thereby inhibiting heat transfer to/from exterior surfaces. When scale buildup is not controlled, plugging of transport lines and/or the reactor can occur. It then becomes necessary to remove the plugs by flushing them out with cold water, by mechanical means or by chemical means (acid wash) [8]. Often, this results in substantial and costly downtime in the SCWO process. During the heat-up in the absence of oxidant, polymerization of certain organics may also lead to scale buildup in the form of char or tar [8].

Plugging of reactors caused by precipitating salts at supercritical temperature and low densities is one of the major reasons for SCWO not being a current waste treatment technology so far. It is not yet clear if SCWO will really become competitive process to classical incineration because technical problems related to corrosion and plugging need to be solved [9].

1.3 Current status of SCWO technology

In 1966 Connolly [10] published data on hydrocarbon solubilities in water at high temperature and pressure. It was reported that, in some regions of the phase diagram, hydrocarbons and water are miscible in all proportions. Rapid development of experimental techniques made this work possible and speculations began about the consequences of the observations [3]. For example, in 1970 Schneider [11] suggested the extension of wet air oxidation to higher temperatures for disposal of organic wastes. After the experiments done by Modell and Amin [12] to convert carbohydrates in supercritical water in the mid 1970s, the potential of the supercritical water oxidation process was recognized. Active chemical and engineering R&D began in the 1980s at national laboratories and universities in the USA [13].

A simplified flow sheet of the process is shown in Fig. 1.2. There are at least three broad categories of feeds or wastes for SCWO treatments applications [14]:

1. Military wastes - chemical agents, munitions, energetics, smokes and dyes which typically contain high concentrations of salt and corrosive species.

2. Sludges with "inert" solids such as oxides and lower salt content than halogenated waste streams.

3. Specific chemical wastes and sludges from variety of industrial sources.

Military wastes are extremely challenging with respect to corrosion and salt plugging. Commercial industrial wastes, including waste water sludge, are relatively benign with respect to corrosion and salt plugging. The more challenging feeds require

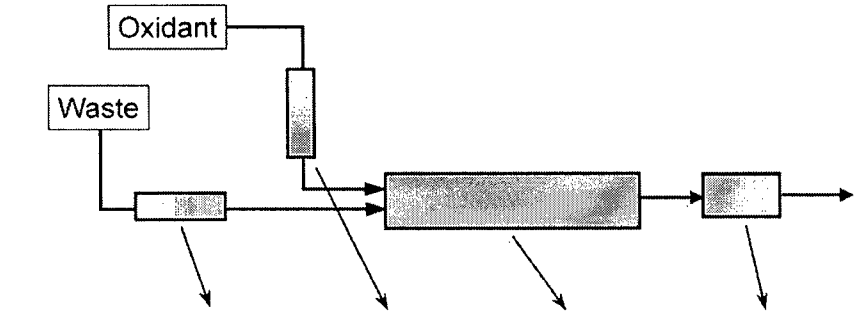

	Waste Preheater	Oxidant Preheater	Reactor	Heat exchanger
T (°C)	25 → 380		600	600 → 25
Reactions	Pyrolysis may occur		Oxidation	Formed acids dissociate
Agressive species	Salts, (HCl) no O_2	O_2	HCl; O_2	H^+; Cl^-; O_2
Main Problem	Slight corrosion	No problem	Salt precipitation	Severe corrosion

Figure 1.2: Conventional SCWO process and reaction leading to problems in the particular parts of the plant [2]

more elaborate SCWO designs or operating techniques to manage the associated corrosion and salt plugging problem [15]. Some examples of companies pursuing the former include General Atomics (USA) and Foster Wheeler Development Corporation (USA), while examples of companies pursuing the latter are Chematur Engineering Group (Sweden), HydroProcessing (USA) and NORAM Engineers and Constructors (Canada). While military applications are most challenging and currently driving the development of SCWO, the wider and long term market for SCWO is in the private sector handling the less challenging feeds.

Table 1.1 contains a list of full-scale facilities of the SCWO processes developed by several companies, along with recent feed materials that have been processed [16]. State of SCWO technology is now summarized by regions.

United States and Canada

A commercial plant for civic waste treatment has been in operation in Texas since 1994 by the Huntsman Corporation [3,17]. The plant was designed and constructed by ECO Waste Technology (EWT) supported by the comprehensive development work done at the University of Texas [18]. The tubular reactor made of a non-specified alloy is 200 m long and is usually operated at 25-28 MPa and between 540-600°C. The normal throughput amounts to 1100 kg/hr. Typical organic concentration is about 10 wt.%. The plant is not suitable for processing waste with high chlorine content and

Table 1.1: Commercially designed SCWO facilities currently in existence [16]

Company	Large scale plants	Applications
MODAR	Organo, Japan	Semiconductor manufacture waste
MODEC	None	Pharmaceutical wastes,pulp and paper mill waste, sewage sludge
General Atomics	US Army Newport, IN	Bulk VX nerve agent hydrolysate, explosives, shipboard waste, rocket propellant
Foster-Wheeler	US Army Pine Bluff, AR	Smokes and dyes, shipboard wastes
EcoWaste Technology	Huntsman Chemical, Austin, TX	Oxygenated and nitrogen-containing hydrocarbons
Chematur	Japan	Municipal sludge
Hydro-Processing	Harlingen Wastewater Treatment, Harlingen, TX	Mixed municipal and industrial wastewater sludge

salt containing waste. However, EWT operates a pilot plant, where such material has been successfully treated [12].

Currently, the main activities in the USA are directed toward hazardous wastes from the defense sector. Such wastes include propellants, explosives, dyes, poisons, and nuclear waste. The programs are executed in a close collaboration between the institutions of the US Forces and national laboratories, universities and industry [3]. General Atomics has three pilot (or demonstration) systems now operable. At Los Alamos National Laboratory, research is being carried out to treat radioactive and explosive wastes. General Atomics, ECO Waste Technologies and University of Texas are partners of the Air Force waste treatment program. At Sandia National Laboratories, a consortium led by Foster Wheeler Corporation has treated US Army smoke and dye wastes (polyaromatics, salts) in the transpiring wall reactor. US Navy as a part of their "environmentally sound ships" program, has commissioned SCWO reactors for disposal of sewage, paint, solvents, fuel and oil, etc. Two units are in test: a down-flow tubular design by General Atomics and a transpiring wall by Foster Wheeler/Aerojet [3]. MODAR developed a reactor to treat wastes from the pharmaceutical plant in 1986 and had a successful demonstration operating 50-500 gal/day. A change in environmental regulations removed the need for this plant and it is not in operation [3]. In 1995, MODAR was acquired by General Atomics.

In Canada, University of British Columbia (UBC) in collaboration with NORAM Engineers and Constructors have built a SCWO pilot plant at UBC. Among other hazardous wastes, "red water" and 2,4 Di-nitrophenol destruction has been successfully carried out. Research is focused on heat and mass transfer in SCW, salt solubility, salt

deposition & mitigation, and corrosion of the reactor tubes [7, 19–24].

Europe

Most of the European development work in SCWO is done in Germany at Forschungszentrum Karlsruhe (FZK) [12]. A film-cooled two-zone reactor (porous inner pipe rinsed with cold water to avoid salt deposits) is in testing since 1998 [25]. The Fraunhofer Institute developed a tubular reactor for the treatment of electronic scrap in collaboration with Daimler Chrysler and built a mobile plant (20 l/hr) to treat hazardous waste at the source of generation [26]. The Swedish company Chematur started experimental work with an industrial scaled plant ("Aqua Critox") licensed from Eco Waste Technologies (EWT), USA, in 1997 [27]. The plant consists of a tubular nickel-base alloy 625 reactor and has a capacity of 250 kg aqueous organic waste per hour [24]. A variety of waste-streams have been successfully treated. Among these were wastes from the amine production, de-inking sludge from paper recycling, and cutting liquid. However, none of these waste streams contains the acid-forming hetero-atoms chlorine, sulfur, or phosphorus which are usually present in the organic wastes, and corrosion has not been a critical item for that plant so far. Building of a larger plant to treat electronic scrap is under consideration [12].

Japan

Organo Corporation in Tokyo has acquired licenses of MODAR (acquired by General Atomics in 1995) and MODEC built the first plant in Japan. Japanese companies Hitachi and NGK are also licensees of MODEC. The Shinko Pantec Company in Kobe has signed a cooperative agreement with EWT to develop the technology for the Japanese market. The companies Komatsu and Kurita have an agreement concerning technical support by General Atomics [12].

The present status of salt deposition and mitigation research with emphasis on SCWO related conditions is reviewed in the next chapter. The objective of this study is also discussed in Chapter 2.

Chapter 2

Literature Review on Salt Deposition and Fouling Mitigation

2.1 Salt deposition studies

The problem of salt precipitation is multivariant, dependent on at least the following parameters [14]:

1. Temperature - affects density and solid salt behavior.
2. Pressure - affects density.
3. Density - affects water properties and interaction of water and salts.
4. Composition - different salts have dramatically different behaviors, e.g. NaCl vs Na_2SO_4, Na_2CO_3, or $CaSO_4$.
5. Time - salt morphology can be affected by time both in the initial precipitation as well as in the aging of salt deposits. Salt deposition is frequently localized to a region where a rapid drop in salt solubility occurs.
6. Geometry - reactor geometry, diameter expansions and contractions, and condition of surfaces can play a significant role in the accumulation of salt deposit.
7. Fluid dynamics - velocity and flow patterns play a significant role in the accumulation of salt deposits. For example, rapid changes in velocity in sudden expansions or contractions can be important in increasing susceptibility to both scaling and erosion.

In general, the deposition of unwanted solids on the heat transfer surface is defined as fouling. The deposition may be crystalline, biological material, products of chemical reactions or particulate matter [28]. In the initiation of the fouling process, the interaction is between the heat transfer surface and the foulant. Subsequently, the interaction

is between the foulant material clinging to the surface and the fresh foulant arriving at the fluid/solid interface. Long range attraction forces serve to bring the foulant to the surface and to provide the basis of contact. The forces involved may include van der Waals forces and electrostatic forces [28]. Due to fouling, the thermal-hydraulic performance of the heat transfer equipment is affected. Considering the consequence of fouling, much concern has developed among scientists and engineers regarding the importance of fouling related research. It is necessary to understand its nature, to formulate methods for its elimination, (or at least control). Three basic processes may be visualized in relation to deposition of solids on surfaces from a moving fluid. They are [28]:

- The diffusional transport of the foulant across the boundary layers adjacent to the solid surface within the flowing fluid. The transport of the foulant could be in the form of both ions and salt particles nucleated in the bulk.
- The adhesion of the deposit to the surface itself.
- The transport of the material away from the surface.

Salt deposition kinetics depends on whether or not particles of salt form in the bulk fluid. If the salt solution in a heated tube is rapidly taken above the critical temperature, a super-saturated solution may result. Either nucleation of salt particles, or diffusion of salt ions to the walls, with subsequent nucleation, may reduce the super-saturation. Particulate salt, depending on the particle size and flow Reynolds number may be transferred to the wall at a greater or lesser rate than individual salt ions, which result in crystalline fouling. According to homogeneous nucleation theory, whether or not particles form depends on the super-saturation of the solution, the particle surface tension and diffusional parameters. Armellini [29] studied some aspects of Na_2SO_4 nucleation in supercritical and near-critical water. Armellini and Tester [5] have presented results of an experimental study of the solubility of sodium chloride and sulfate in supercritical and near-critical water. The objective of the study was to obtain solubilities of the two common salts, sodium chloride and sodium sulfate, at conditions prevalent in the supercritical water oxidation process.

LaJeunesse et al. [30] conducted experiments on Sandia's SCW flow reactor with alloy-625 tubing of 0.47 cm ID. A 0.5 wt.% solution of Na_2SO_4, at 2-5 kg/hr, was heated to approximately 400°C to quantify the deposition rate of Na_2SO_4 over a range of pressures, flow rates and heating rates. Pressure transducers were placed at different locations of the reactor to monitor the pressure during the tests such that the development of a constriction or plug could be detected. As the plug was formed a pressure differential occurred. The test was then terminated and reactor cooled down. The plug was re-dissolved by passing pure water and all effluent was collected. Evaluation of effluent by ion specific electrode yields a deposition rate. The results

suggested that at lower flow rates, the rate the plug formed is proportional to the rate that salt is injected into the reactor. It took longer for the tubes to be plugged at higher flow rates. The pressure range studied was about 25-26 MPa and it was reported that the higher-pressure conditions produced the plugging slightly faster than the lower pressure.

Chan et al. [31], at Sandia National Laboratories (USA), conducted experiments to study salt solubility and deposition kinetics in the Na_2SO_4-H_2O system at conditions relevant to SCWO. A 50-cm long, alloy-625 tube served as a tubular reactor. The OD and ID of the reactor were 14.3 and 4.7 mm respectively. The reactor had a maximum operating temperature of 650°C and pressure of 51 MPa. In the deposition experiments a 0.5 wt.% salt solution was pumped through the reactor and the fluid temperature at the exit of the reactor was near 400°C. Rapid precipitation was reported due to an extreme drop in salt solubility concentration that occurred as the feed stream became supercritical. Flow rate at ambient condition feed (25°C) could be varied from 0.2 to 1.5 ml/s (1.1 to 8.4 cm/sec). The reactor section was heated with six 375 W cable heaters used to maintain isothermal conditions along the reactor. Pressure transducers were placed at three locations and their readings were recorded continuously such that the development of plug could be detected as pressure differential from one transducer to the next. The reactor got plugged in about 30 minutes in the majority of the test runs. The concentration of the Na_2SO_4 salt in the solution was obtained experimentally by varying the fluid temperature and measuring salt effluent concentration. At a given pressure, the salt concentration is a function of fluid temperature. It was assumed that the undissolved salt precipitates as a solid and the deposition occurs at the place of precipitation. A model was thus developed from the principle of mass conservation. The concentration gradient was obtained by determining the solubility as a function of temperature and combining the solubility information with the temperature profile of the fluid as a function of axial position within the reactor.

Hodes et al. [32] presented the results of their study of salt deposition rates from a near supercritical aqueous sodium sulfate solution to a heated cylinder. The purpose of the study was to develop an understanding of salt deposition kinetics and nucleation phenomenon in SCWO reactors. Experimental deposition rate data have been provided for sodium sulfate containing SCW and a predictive model based on the data was developed.

Teshima [33] carried out an experimental study on UBC-NORAM SCWO pilot plant to study the deposition of Na_2SO_4. The deposition experiments were done with a maximum salt concentration of about 1 wt.% and the 6.2 mm ID reactor was plugged within 20 minutes of operation. Since the tube walls were heated and hence at a higher temperature compared to the bulk fluid, salt molecules were crystallizing at

the wall. The outer surface temperature of the fouled-heated tube was examined for inferring Na_2SO_4 thickness profiles. Models were developed for predicting deposition of Na_2SO_4 and compared molecular deposition to particulate fouling. The fouling rates predicted by the model were fairly close to the actual experimental values but the axial location of the deposit, with maximum thickness (peak of the scale deposit) could not be predicted accurately. Experiments were also conducted to determine the solubility of Na_2SO_4 in water at 25 MPa and for a temperature range of 370-500°C. It was reported that the solubility decreases rapidly at the pseudo-critical temperature (385°C and 25 MPa) and then less rapidly once the critical temperature is exceeded. (The pseudo-critical temperature is defined as that corresponding to maximum isobaric heat capacity). Furthermore, it was observed that the salt deposition profiles were influenced by mass transfer limitations and wall temperature in addition to the solubility. It was also reported that the fouling rates are most affected by how quickly the solubility limit is decreasing. The solubility limit is a strong function of temperature and it was recommended to have small temperature gradients especially near the critical region where the solubility limit is decreasing quite rapidly. It was also observed that the monitoring of outer tube temperature appears to give a good indication of extent of fouling and in conjunction with the differential pressure measurement would be useful to predict the location of the deposition peak. Rogak and Teshima [7] presented the results of a heat and mass transfer model for the tubular reactor, developed and tested experimentally for Na_2SO_4 deposition at 25 MPa. It was observed that the salt deposition profiles were influenced by mass transfer limitation in addition to the solubility. The model uses empirical heat transfer relations to estimate mass transfer rates. The diffusion coefficient of the salt is calculated from the Stokes-Einstein relation using a hydrodynamic diameter of 2-6 Å. The solubility was found to reduce by a factor of 1000 as the temperature increases from 380-400°C. The bulk solution never became supersaturated, therefore salt particle nucleation was not modeled.

Filipovic [34] investigated NaCl deposition in the UBC-NORAM SCWO pilot plant. Solubility measurements were made for various pressure and temperature ranges. It was reported that the solubility of NaCl decreased with temperature and increased with pressure. NaCl-water solution in the bulk was passed through the two-phase vapor-liquid region before the transition to vapor-solid region. During the experimental study two distinct regions of depositions were observed: the vapor-liquid region, and the vapor-solid region. It was reported that the deposition rates did not change with time. It was observed that the heat transfer coefficient increased by 20-75% when salt solution was introduced into the system. The salt thickness profiles were inferred from the tube outer surface temperature. Models were developed for heat and mass transfer.

2.2 Fouling mitigation techniques

A broad range of solids deposition control methods have been tested in SCWO reactors [14]:

- Control precipitation/reaction zone, e.g., keep precipitation away from the wall.
- Utilize inert solids as nucleation sites to avoid wall deposition.
- Utilize inert solids to scour wall deposits.
- Take advantage of favorable regions of phase equilibrium, e.g., use high pressure or relatively low temperature to keep salt in the solution.
- Carry out continuous (e.g. transpiring wall) or intermittent flushing.
- Control feed chemistry to yield transportable solids.
- Use high velocity to reduce deposition.
- Use acid washing for occasional descaling.
- Use quenching to redissolve salts at the reactor exit or brine zone.
- Control temperature profile to have higher salt solubility at reactor wall.
- Filter hot solids mechanically.
- Use mechanical devices for periodic or continuous removal of scale buildup.

Investigation of anti-fouling methods has received much attention in the past and a variety of chemical and mechanical methods have been suggested to reduce the formation of deposits on heat transfer surfaces. One way of overcoming, or at least reducing the problem, is in some way to interfere with the fouling process by the addition of chemicals to the flowing fluid. The use of such an additive technique for reducing or eliminating the deposition of the foulant on heat exchanger surface during the operation of the heat exchanger may be regarded in broad terms, as on-line cleaning. Other on-line techniques are used that depend on physical and mechanical mechanisms and do not involve the use of chemicals. However, these techniques involve additional equipment needed at the design stage. An alternative to on-line cleaning is to stop the operations and clean the heat exchanger either chemically or mechanically.

2.2.1 On-line cleaning

Brush and cage systems

The principle of the brush and cage system is that a brush, fabricated from suitable wires, is passed through the tubes by the liquid flow. At either end of the tube there is a cage located so as to arrest the brush projectile. Cleaning takes place by running a wire brush through the system while it is operating. The brush is pulled or pushed through the reactor by a pigging mechanism. However, such a system cannot be used for any thing other than straight tubes.

In the oil industry, pipelines are frequently cleaned by "pigs" transported with the bulk flow, with the object of scraping away deposits on the pipe wall. Conco [35] developed an air gun that fires small "pigs" through the fluid in tubes to clean them in regular intervals. This technique could be a good tool for scale removal in the SCWO systems. However, there are some problems associated with the pigging system. The tubes to be cleaned should be of uniform diameter without any weld protrusions in the inner side of the tube. The brushes attached to the pig would produce some drag and thus the pig must develop a sufficient pressure drop so as to provide enough thrust to not only move itself through the tubes but also to push (or pull) the cleaning brush itself. Online removal of the scale in SCWO systems using this technique has also been suggested in [36] & [19].

Magnetic devices

The use of magnetic fields to reduce or eliminate scale formation in pipes has been attempted for many years [28]. It could be supposed that slightly soluble compounds such as $CaCO_3$ existing in solution as charged ions, would be affected by the application of an electric field, and this could form the basis of the technique to alleviate fouling. Duffy [37] reported that magnetic devices had not been used extensively for industrial applications due to the strong criticism, which they have received from engineers. He described work that demonstrated no influence of magnetic fields on the precipitation of $CaCO_3$. The skepticism is still apparent in the industry, despite the fact that successful applications have been reported. Donaldson [38] for instance, reports a successful use of a magnetic device. The use of the magnetic device resulted in the removal of calcium phosphate scale that had formed on a plate heat exchanger.

The other examples of scale reduction are reported by Nordell [39], Donaldson & Grimes [40] and Donaldson & Grimes [41]. The evidence of these examples cannot be ignored. Donaldson [38] reports carefully controlled laboratory tests where a pipe badly scaled with calcite gradually became clean over prolonged exposure to a magnetic field under flowing water conditions. Donaldson [38] attributes the beneficial effects of magnetic devices to a number of closely related changes brought about by the application of

magnetic fields.

- Crystal size is increased with less opportunity for the incorporation in a scale structure.
- Evidence from research with zinc phosphate solutions suggests an increase in solubility in the presence of a magnetic field.

It would appear that the technique shows promise but more work need to be done on the use of magnetic devices for the reduction of the scaling problems before the technology can be used with confidence. Furthermore the possibility of inducing electric currents in metallic structures, that could result in enhanced corrosion, must be considered.

Use of inserts

Inserts have been used for many years to improve heat transfer, particularly from viscous liquids. The principle involved is to disturb the viscous sub-layer near to the heat transfer surface thereby reducing the resistance to heat flow. Since the problem of fouling is very concerned with the transport of foulants across the viscous sub-layer it is expected that any attempt to reduce the resistance to heat flow will also effect the propensity toward fouling. Hewitt et al. [42] have given some backgrounds to the use of heat transfer enhancement techniques. The inserts are usually twisted tapes or wire matrices. It has been reported that inserts can reduce fouling problems where reactions are involved [43] and where wax and other organic precipitates arise [44, 45]. Some inserts are primarily designed to reduce fouling e.g. wire spring-like configurations that are free to oscillate and move under the influence of the flow conditions. The movement of the insert against the wall knocks or rub off, any deposit as it is formed. A more robust design is when the insert is held tightly within the tube by a "push fit" or anchored at the end of the tube.

Gough and Rogers [43] report the use of matrix tubulators inside the tubes of a shell and tube heat exchanger for heating tar oil. Without the inserts, a reduction of 50% in the heat transfer coefficient was encountered over a period of four months. The heat transfer coefficient fell about 4% only over the same period when inserts were installed. Crittenden et al. [46] conclude that the disturbance of the hydrodynamics by the tubulators is largely responsible for the beneficial effects on fouling. It is not clear if these devices would be effective in reducing the salt deposition in SCWO systems, where the flow conditions are already highly turbulent.

Surface treatments

From the point of view of surface science, the formation of deposits on a metal surface may be considered as an interaction between the deposits and the heat transfer surface. Forster et al. [47] carried out an experimental study for fouling mitigation by using

different reactor materials in order to increase the induction period. The approach was to change the interface crystal/heat transfer surface so that an increase in removal rate may be achieved by decreasing the adhesive strength due to modification of inter-facial characteristics. Various surface materials were deployed in the fouling test runs with an aqueous $CaSO_4$ solution. The solution was passed through the heat transfer surface with initial wall temperature at 75°C, heat flux of 31.8 kW/m^2, velocity of 0.2 m/s and salt concentration of 2.5 g/l. A new surface, known as diamond like carbon DLC, proved to be a good choice to increase the duration of the induction period significantly. The performance of DLC material was found much better then copper, aluminum, steel and brass.

Low energy surfaces are likely to reduce the tendency of particles to attach. Changes in the surface characteristics therefore, have the potential to reduce the incidence of fouling. In addition to reducing fouling the surface also prevent corrosion. Muller-Steinhagen and Zhao [48] investigated low fouling surface alloys made by ion implantation technology. Fouling experiments during pool boiling of $CaSO_4$ solutions demonstrate that fouling is significantly reduced for all investigated conditions of heat flux and $CaSO_4$ concentration. It may be concluded that the pre-requisite condition for a surface to posses low fouling behavior is that the surface has a low surface energy [48].

Ion implantation is the introduction of atoms into the surface layer of a solid with ions in the keV to MeV energy range [49]. The environment of particles on the surface of a solid differs from that in the interior. In the interior, a particle is evenly acted on by forces exerted by the particles around it. On the surface, where the coordination number is reduced, an unsaturated force field exists. There is a tendency for the particle to be pulled into the main body in order to reduce the surface area to a minimum; hence surface tension is produced. Surface free energy is a function of internal energy, temperature and surface entropy (surface energy = U-TS). Entropy increases when foreign particles are implanted in the surface. Therefore, the surface energy would decrease with an increase of entropy. Low fouling surface alloys produced by ion implantation will have unique advantages:

- Alloy elements implanted exist in a solid state so there is no interface and the alloy layer is not easily removed.
- Additional heat transfer resistance is negligible.
- Alloy surface is weldable.

The majority of the techniques to mitigate fouling can only increase the duration of induction period. Thus changing the material, implanting ions on the tube surface etc., are all temporary measures, which may be adopted to prolong the induction period. Thus the above mentioned techniques would only increase the interval between the

actual cleaning process. A regular cleaning procedure is thus required after a certain period of plant operation.

2.2.2 Other fouling mitigation techniques reported in SCWO systems

In the early 1980s, SCWO was claimed to be the technology to solve every waste treatment problem. The boundless optimism of the inventors covering up the serious problems, which might never be solved for all kinds of wastes, hindered (and still hinders) an industrial application and thus a broader distribution of the technology. It must be pointed out that SCWO can only become an alternative to incineration in special - limited cases [2]. Salt-free waste streams can easily be oxidized in tube reactors. For wastes containing only C, H, O, and N, no special reactor design is necessary. For wastes containing salts, the precipitating salts lead to plugging of reactor tubes and to overcome this problem various techniques have been suggested recently.

Many of the companies that have attempted to commercialize the SCWO technology over the past two decades have developed innovative approaches to dealing with the salt deposition problems. Table 2.1 summarizes the commercially designed approaches that have been developed for precipitation control, mostly within the last decade. They are arbitrarily divided into two categories: those that involve unique system or component designs and those that employ specific operating techniques [16].

Some studies [2] suggest increasing the system pressure and thus increase solubility of some salts. However, at higher pressure corrosion problems are also enhanced. Other studies present special reactor designs to prevent settling-down at wall surface. Such concepts include simple tank reactors in which the salts sink down to the zones of low subcritical temperature where they are dissolved again [2] & [50]. However, in such designs, the low settling speed and high vertical turbulence present a problem. Alternatively, salts precipitating in the reactor zone have to be dissolved before the deposition at the wall. Crooker et al. [51] implemented a transpiring wall reactor to address the technical problems of corrosion and salt plugging in SCWO systems. The reactor pressure boundary was exposed to controlled-temperature deionized water, resulting in a safer design. The transpiring platelet liner flows supercritical water that forms a film barrier from undissolved salt. The salts formed during the oxidation were carried out of the reactor. The plant has been designed to destroy US Navy excess hazardous materials. Salt-producing solutions have been processed at feed rates of 45 and 95 kg/hr. Tests were conducted at a pressure of 24.1 MPa and reactor temperatures between 594 and 816°C. Post-test inspections have not revealed any obvious reactor liner corrosion or salt deposition. However, it should be evaluated, if a salt separation as a first step (e.g. by filtration) followed by SCWO in a tube reactor

Table 2.1: Commercially developed approaches to SCWO salt precipitation control [16]

Approach	Method	Companies using the method
Reactor designs	Reverse flow, tank reactor	MODAR
	Transpiring wall reactor	Foster Wheeler
	Adsorption/reaction on solid phase	SRI International
	Reversible flow, tubular reactor	Abitibi-Price
Specific techniques	High velocity flow	MODEC, Chematur, Organo
	Mechanical brushing	MODEC
	Rotating scraper	MODAR, General atomics
	Reactor flushing	General atomics, Abiti-Price, Chematur
	Additives	EcoWaste Technologies, General Atomics
	Low turbulence, homogeneous precipitation	HydroProcessing
	Crossflow filtration	University of Texas, Austin
	Density separation	Oxidyne, General Atomics, Hydroprocessing
	Extreme pressure operations	Los Alamos National Laboratory, EcoWaste Technologies

may be a cheaper way of treatment. A fundamental problem of this kind of treatment might be a simultaneous separation of the organics leading to another contaminated waste. Essentially three reactor concepts (see Fig. 2.1 [50, 52]) have been developed and studied: tubular reactor, tank reactor with the reaction zone in the upper part and a cool zone in the lower part of the tank to dissolve the salts [50], and the "transpiring wall reactor" with an inner porous pipe which is rinsed with water to prevent salt deposits at the wall [52]. Tubular reactors are the most common.

A technique, using the control of operating conditions, such that salts precipitate only in the bulk fluid has been patented by HydroProcessing in their SCWO process [53]. It is claimed that salts which have nucleated in the bulk fluid tend not to adhere to surfaces. One way to minimize salt buildup in a solid wall SCWO reactor is to ensure that the particles are well suspended in a high speed flow. The particles must remain suspended until they redissolve once the effluent is cooled, or until they can be otherwise removed [16]. This approach has been utilized by Modell et al. [54], and is primarily applicable to feeds with a relatively high proportion of nonsticky to sticky salts. The downside to this approach is that the reactor length must be

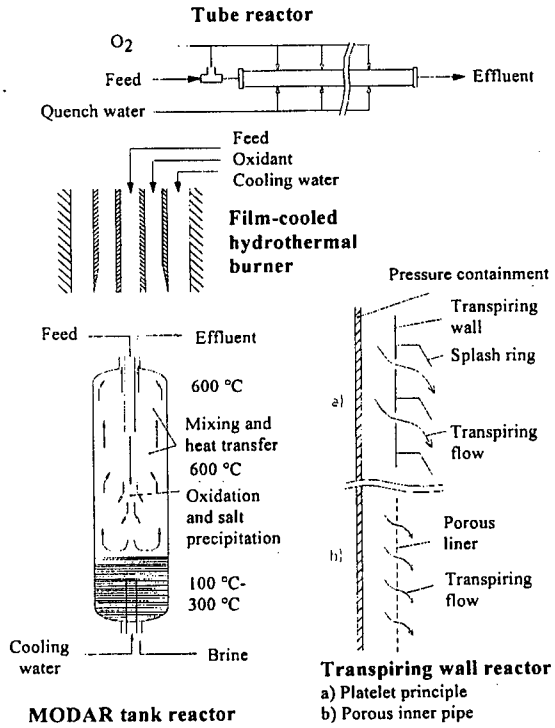

Figure 2.1: Reactor concepts for SCWO [50,52]

correspondingly increased in order to maintain the residence time.

Aymonier et al. [55] developed a hydrothermal-sonochemical reactor to degrade acetic acid. In order to avoid plugging of the heat exchanger, a new reactor concept, has been introduced based on the use of ultrasonics under cavitation conditions. The ultrasound activation increased the yield of acetic acid oxidation reaction by 40%. The influence of the horn vibration amplitude on acetic acid conversion was studied. Furthermore, tests with an industrial waste containing salts and halogens showed the performance of the titanium liner of the reactor for overcoming salt precipitation and corrosion. Tests, to study the salt precipitation, were carried out for pressures of 2.8 MPa and at a temperature of 220°C. It was reported that the ultrasound considerably improved the salt recovery at the reactor outlet. Long time tests to prove the suitability of these reactor concepts for an industrial application have not yet been performed with any of these new designs. In a review study, Kritzer and Dinjus [2] concluded, that the new reactor concepts seem to be too susceptible to fail in long term application.

Corrosion is a serious problem for treating chlorinated wastes by SCWO because of the formation of hydrochloric acid. Muthukumaran and Gupta [56] proposed addition of sodium carbonate to reduce the corrosion related to SCWO treatment of chlorinated

wastes because of the formation of hydrochloric acid. Data were provided to show the enhancement of oxidation, by addition of sodium carbonate. It was reported that the improvement of oxidation might be due to a combination of the catalytic effects of Na_2CO_3 and removal of HCl by Na_2CO_3. Addition of Na_2CO_3 was said to play a key role on reducing corrosion on reactor walls by neutralizing the acid. However, it was reported that Na_2CO_3 is insoluble under supercritical conditions because of low dielectric constant of supercritical water and thus presented a problem. No plugging of reactor tube was reported for their conditions of experiment (30 MPa and 400°C). It was mentioned that the concentration of Na_2CO_3 was kept low enough to avoid plugging and about 1 mm or smaller size Na_2CO_3 particles were expected during the SCWO process. After the product mixture was cooled down later, Na_2CO_3 re-dissolved into the fluid and thus avoided any plugging problems in the back-pressure regulator.

The reactor flushing technique involves rinsing of the SCWO reactor periodically during operation with a fluid that will dissolve accumulated salts scale. The most common flushing fluid is cool (subcritical temperature) pressurized water. Ravich [57] presents some data for the solubility of Na_2CO_3 at various pressure and temperature levels. The solubility reported at 24.8 MPa and fluid temperature of 400°C is almost zero. But at lower temperature i.e., at 300°C, the solubility increases to about 15 % (weight). Therefore rinsing technique can be employed in order to remove plugging of the tube. During the test, when plugging of tubes occurs, the heaters can be turned off to decrease the fluid temperature. The plug may thus be removed due to higher salt solubility. This technique has been tried by Chan et al. [31] for $CaSO_4$ deposit removal. By reducing the fluid temperature to 320°C at 25 MPa (corresponding to 20 wt.% of $CaSO_4$ solubility), the accumulated salt re-dissolved in the bulk fluid. Thus by reducing the temperature of effected portion of the reactor by 100°C, the salt can be re-dissolved and removed as a brine stream. They suggested that if the location and time profile of the deposit is known, the affected portion can be isolated by valves and pure water feed can be substituted and the reagent feed is diverted to a parallel tube for continuous processing. This technique seems to be useful for laboratory experiments to remove the plug. But using a similar technique on a commercial plant would require a complicated system of valves and monitoring devices for automatic switching to remove the plugging and processing the influent in parallel.

Fouling can be a major problem in evaporators used to concentrate pulping liquor in alkaline pulping mills. Two types of scales predominate. They are $CaCO_3$ and water soluble Na_2SO_4-Na_2CO_3 scales. The term soluble scale refers to water-soluble inorganics which deposits on black liquor evaporators. They form by crystallizing from a saturated solution when their concentrations exceed the solubility limit. For salts whose solubility decreases with temperature, supersaturation may be due to the temperature gradient existing at the hot surface as well as concentration changes. Kraft pulp is obtained from wood and treated with aqueous solutions of NaOH and

Na_2S. Kraft spent pulping liquor solids may contain up to 12 wt.% of Na_2CO_3 and 10 wt.% of Na_2CO_3 [58]. Soluble scales are easily removed from heat transfer surfaces by water washing. There are two approaches to control soluble scales. The first is to avoid exceeding the saturation limit of the inorganics, which deposit as scales. The second approach is to recirculate product liquor back to the evaporator. Liquor recirculation is beneficial because the recycled liquor contains precipitated solids, which act as nucleation sites to relieve supersaturation. It has been shown that increasing the velocity of the recirculation liquor reduces the fouling rate [58].

2.3 Objectives of this work

The problems associated with SCWO have hindered an industrial scale-up of the process so far. Salt plugging seems to be most severe of them and all attempts to solve it in a satisfactory way, lead either to new problems, make a long-time solution doubtful or increase the cost. These techniques are yet to be tested in an actual SCWO plant. The plugging of the reactors cannot be avoided by variation of the process parameters without simultaneously triggering a new problem [2]. The current possible ways of reducing the problem have not been totally effective and seem to be susceptible to failure in long term application. Thus none of these approaches has achieved any commercial success and scaling of inorganic salts remains a major obstacle in long term SCWO operation treating organic waste with inorganic compounds. It is to be noted that the techniques discussed above have been used to delay the problem of fouling. This would only prolong the time intervals between the shut down of the equipment, for actual scale removal, and can not totally eliminate the problem of scaling [2]. For an industrial application, it is of minor interest if a destruction rate of a certain organic compound is 99.99 or 99.999% (which seems to be the objective of most of the studies carried out so far). On the other hand, it is absolutely necessary to prove the long time applicability of an industrial process. Waste streams that contain salts in too high concentration will sooner or later lead to plugging of every kind of reactor. Furthermore, SCWO is not and most probably will never become a "general" technology for all kinds of waste-streams. Consequently, the wastes suitable for SCWO have to be found and selected carefully [2].

Benzene, toluene and several other hydrocarbons are nitrated on a large scale by industry mostly as an initial stage in the manufacture of polymers, dye and insecticides etc. Nitration generally occurs in a mixed acid media containing mostly sulfuric acid (acts as catalyst) and nitric acid (reacts with organics). The nitrated products contain inorganic acid (H_2SO_4) and nitrated byproducts, which have to be removed. The byproducts typically are nitrophenols that have water-soluble salts that can be removed by alkaline wash. Treatment of chemical wastes (e.g. phenol) using NaOH,

as a base, leads to production of salts (Na_2SO_4 and/or Na_2CO_3) which precipitate at high temperatures and elevated pressure conditions. Schmieder and Abeln [12] in a review suggested that for better understanding of the salt deposition problem, more salt-water phase diagrams are required. Besides the many salt-water binary phase diagrams determined until now, ternary (salt1-salt2-water) systems have to be determined. The determination of the phase diagrams has to be completed with data of the kind of the precipitate, e.g., morphology, stickiness etc.

NORAM Engineers and Constructors is a leading Mononitrobenzene (MNB) plant manufacturing engineering firm and is collaborating with University of British Columbia in SCWO research projects. Use of SCWO in MNB plants in the next few years is most likely and requires technical know-how for better understanding of fouling related problems in this field. Na_2CO_3 and Na_2SO_4 are thus good candidates for determining solubility, studying deposition and fouling mitigation. From the literature reviewed, it has been noticed that only a few Na_2SO_4 deposition studies have been reported and not much information is available for Na_2CO_3 solubility at SCWO conditions. In the literature, no detailed fouling research has been found for Na_2CO_3 salt deposits in SCWO systems. So far there have been no results published for Na_2CO_3 deposition in supercritical water on a heated tube and the fundamental data needed to model the nucleation are not known. The analysis of the actual deposits on the reactor surface, under turbulent flow conditions, has never been reported. This analysis is important in order to study the structure of the scale and to determine deposit layer properties such as thermal conductivity. The objective of the present study is to determine the solubility of these salts in supercritical water and thus develop a relation between the solubility and fluid density for estimation purpose. The solubility of Na_2CO_3 and Na_2SO_4 in pure form and in the presence of each other is to be determined, for the temperature range relevant to SCWO. The next step is to study the deposition behavior of Na_2CO_3 and develop a mitigation technique to prolong the operating period of the system before the reactor gets plugged due to salt deposition. The salt particles are to be nucleated in the bulk fluid for fouling mitigation purposes. This would result in combined particulate and crystalline fouling instead of the usual pure crystalline scale which occurs due to salt molecule deposition. The hypothesis of the fouling mitigation technique is that the structure of the combined particulate and crystalline deposit would be weaker than the pure crystalline deposit. Thus removal of deposited salt layer may occur due to the drag force of the flowing fluid. SEM and EDX analysis of both types of deposits, crystalline and particulate, will be carried out to study the deposit structure. Heat and mass transfer models will then be developed, for the two types of fouling phenomena, in order to simulate the deposition process.

The experimental setup, which includes various components of the UBC-NORAM SCWO pilot plant, is discussed in Chapter 3. Heterogeneous-nucleation experiments have been performed to determine the solubility of these salts and salt molecules crys-

tallized on the reactor surface. Chapter 4 covers the procedure adapted for determining the solubility of the salts and results of the solubility experiments. A computer code, to simulate these experiments is also discussed in this chapter. Chapter 5 discusses the fouling mitigation technique adapted to prolong the operation of the SCWO system prior to the plugging of the reactor due to salt deposition. The modified experimental setup, to apply this technique, is also discussed in this chapter. Results of the fouling mitigation runs are compared with the tests carried out following the usual procedure. The scale structure and elemental composition analysis are presented in Chapter 6. A heat and mass transfer model developed to simulate the fouling mitigation experiments is discussed in Chapter 7. The experimental results are compared with the simulation model estimations. Finally Chapter 8 summarizes the conclusions of the study and recommendations for future research in this field.

Chapter 3

Experimental Facility Description

3.1 Process equipment

The UBC-NORAM SCWO facility was constructed for research and development purposes using a tubular type reactor, for the destruction of wet organic wastes. A wide range of pressures, heat fluxes, temperatures and mass flows can be achieved. Figure 3.1 shows a schematic of the experimental setup. Two 550-liter cylindrical storage tanks supply the system with water and waste. Water is pressurized with a triplex plunger pump (GIANT P57) while gas is pressurized using an air pressure operated booster compressor. A pulsation damper (Hydrodynamics Flowguard DS-10-NBR-A) is used with the plunger pump to suppress the flow variations. The speed of the pump and hence the flow rate is controlled by a variable frequency drive (Reliance Electric ISU21002). The pump can be operated between flow rates of 0.6 to 2.2 kg/min at a maximum outlet pressure of 45 MPa. For a given tube diameter and fluid mass flow rate, the Reynolds number is a function of the fluid dynamic viscosity only ($Re \propto \mu^{-1}$), which decreases with temperature. Under typical SCWO conditions, the flow is thus highly turbulent (see Fig. 3.2). The liquid flow is measured with a graduated cylinder and stopwatch at the system outlet, when it is cold.

The main heat transfer elements of the SCWO system are the recuperative heat exchanger, two pre-heaters, the test section, the reactor and the process cooler. The heat exchanger is a counter flow double pipe type, with 1.27 cm diameter Schedule 80 pipe (SS 347) on the shell side. The fluid coming from the influent tank passes through the tube side of the heat exchanger. The recuperative heat exchanger is designed to recover approximately 30 kW of power from the reactor outlet. The process cooler is 6.2 m long stainless steel tube. All other tubing is made of nickel base alloy-625 high pressure tubing (6.2 mm ID and 9.52 mm OD). In the heated tube sections, electrical current is passed through the tube wall. The electrical resistance of the wall causes it to heat up as the current passes through the wall. The power is supplied from silicon controlled rectifiers (SCR) panel directed through two step-down transformers (240/24

VAC, Hammond Manufacturing) for each heated section as shown in Fig. 3.3. Each pair of transformers is wired in series in input and parallel in output and is capable of delivering 24 V at 45 amps. The transformers are attached to the heated sections by 2.5 cm thick copper cables that lead to barrel connectors which are attached to stainless steel rods. The steel rods are silver-soldered onto the tube. The high (max. 24 VAC) voltage connections are made at the middle of the heated section and the ground wires are attached to the ends, eliminating the possibility of any ground loops in the system. The wiring arrangement also provides a balanced load to each half of the heated section. Each pre-heater is 4.7 m long. The power to pre-heater 1 is adjusted manually on the SCR panel. The power to pre-heater 2 can be adjusted with a feedback temperature controller that has a manual and automatic mode. The heating for the test section is achieved in the same way as for the pre-heaters. Power control of the test section is manual. The test section is made from four tube sections. Two shorter sections (0.3 m), placed at the inlet and the outlet of the test section are not heated. The other two (1.52 m each) are electrically heated as shown in Fig. 3.4. Test section is the part of the system where most of the measurements are done. After passing through the test section the fluid enters a 140 m long reactor section with 17 U-shaped bends, which can be heated in the same manner as discussed above. Then the fluid enters the recuperative heat exchanger where it heats up the incoming feed from the influent tank. Finally, the fluid is cooled down further in a process cooler. A back-pressure regulator is used to control the system pressure. A gas dome back-pressure regulator is used in the system.

3.2 Pressure measurement and calibration

Pressure transducers, located at the inlet and outlet of the test section, are used to measure the gauge pressure. The pressure transducers have been calibrated with a digital calibrator (Cole Parmer 68036 series). The uncertainty of the pressure measurement, considering the errors in the data acquisition system and variation along the test section is approximately 0.1%. Pressure can also be measured at three other locations in the system as shown in Fig. 3.1 but is not logged during the experiment.

3.3 Temperature measurement and calibration

In the test section, K-type Chromel-Alumel thermocouples are used to measure the outer tube surface temperature. A total of 29 thermocouples are spot welded to the test section to measure outer surface temperature as shown in Fig. 3.5. In the test section, the thermocouples are spot welded to the test section tube as shown in Fig. 3.6. The surface between the two wires acts as a junction for the thermocouple. This is the intrinsic type of thermocouple arrangement and the temperature measured is

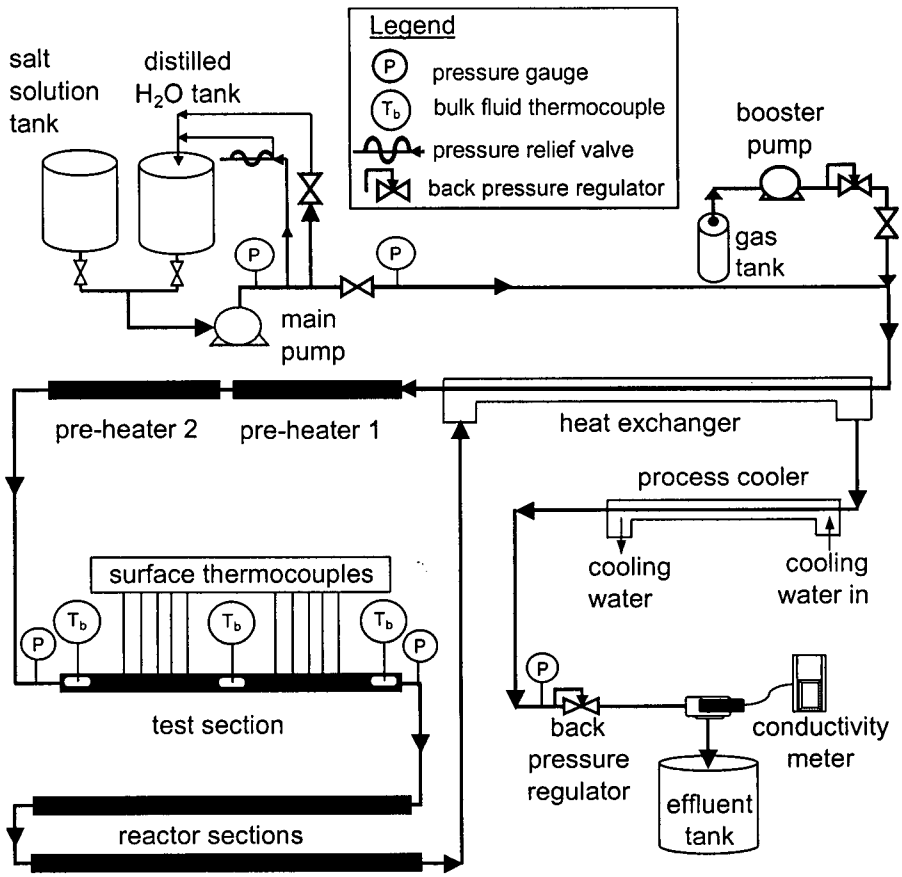

Figure 3.1: UBC-NORAM SCWO pilot plant

actually the average of the temperatures at the two spots. The peripheral temperature variation across the short distance between the two spot welds is infinitely small. Even along the axial direction, where the temperature variations are important, the distance between the spot welds is too small for a noticeable change in temperature. Insulating ceramic is used to prevent contact between the unshielded thermocouple wire and the tube surface. Twisted shielded wires are used to extend the thermocouple from the junction to the data acquisition system. Surface temperatures are also measured at other sections of the system and some of them are attached to the alarm system. There are three thermocouples in the test section, which are used to measure the bulk fluid temperature. These are located at the inlet, middle and outlet of the test section at the unheated unions, as shown in Fig. 3.5. These thermocouples have been inserted in the union fittings and their junction extend to the center of the tube to measure bulk fluid temperature. Since these union fittings are unheated, the fluid passing through them is at uniform temperature.

As mentioned earlier, stainless steel rods were soldered to the test section tube

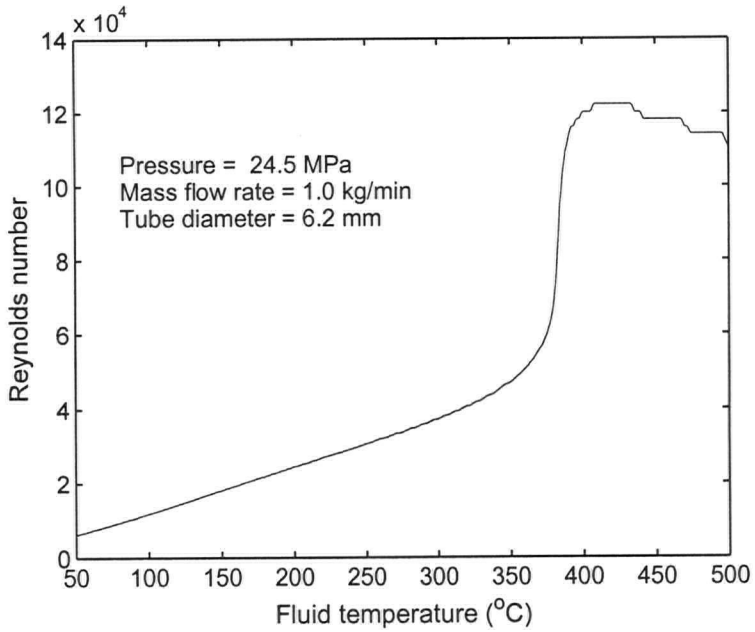

Figure 3.2: Reynolds number versus fluid temperature

for electric power cable connections. On the test section, the distances of all the thermocouples are measured from the downstream edge of the steel connector just after union 2 shown in Fig. 3.3 and is mentioned in Table 3.1.

The thermocouples have been calibrated by measuring the saturation temperatures of pure water at known pressures and the calibration procedure is as follows. The fluid temperature and pressure was set above the critical values and then the pressure was decreased below the critical value, without adjusting the heat input to the system. The fluid in the test section would thus be in the saturated state during the calibration procedure. The measured temperatures were then compared with the saturation temperature values from the steam tables. For the surface thermocouples, a similar

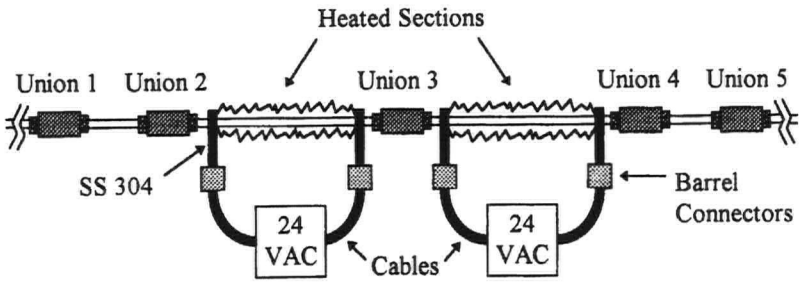

Figure 3.3: Schematic of electric heating for pre-heaters and test section

Table 3.1: Distance of thermocouples (measured from the electric power connection)

Thermocouples at the top surface	Thermocouples at the bottom surface	Distance from electric connector (cm)
	S10	6.1
SB9		15
	S9	25
SB8		34.2
	S8	44.3
SB7		52
	S7	61.3
SB6		67.6
	S6	75.1
SB5		80.7
	S5	83.7
SB4		90.2
	S4	96.8
SB3		103.1
	S3	111.4
SB2		117.7
	S2	125.5
SB1		132.8
	S1	140
SB11		157.7
SB12		173.8
SB13		192.2
SB14		209.7
SB15		221.6
SB16		230
SB17		243.7
SB18		257.2
SB19		271.7
SB20		287.4

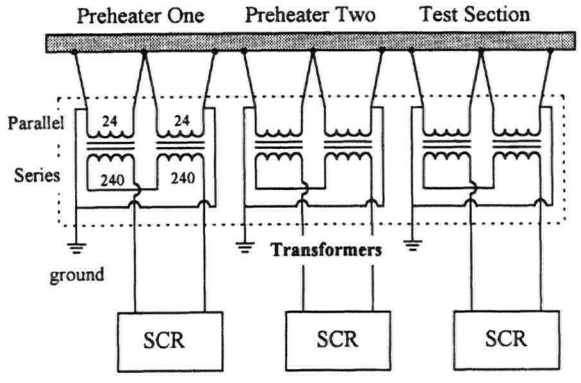

Figure 3.4: Electric heating schematic of the heated tube sections

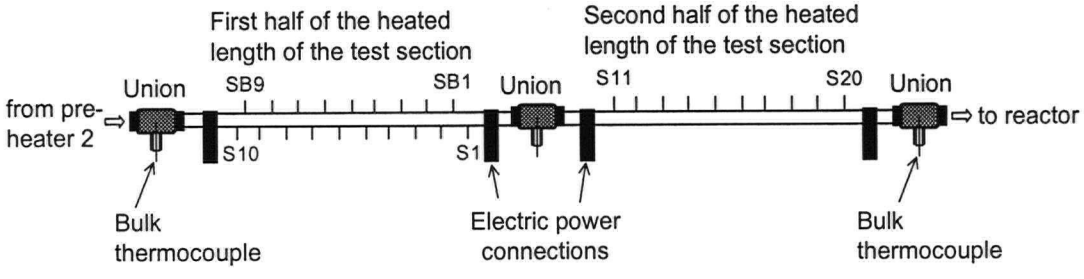

Figure 3.5: Location of thermocouples in the test section

procedure was followed assuming the test section to be adiabatic and the condensing heat transfer coefficient to be very high. The error in the temperature is less than 1 K.

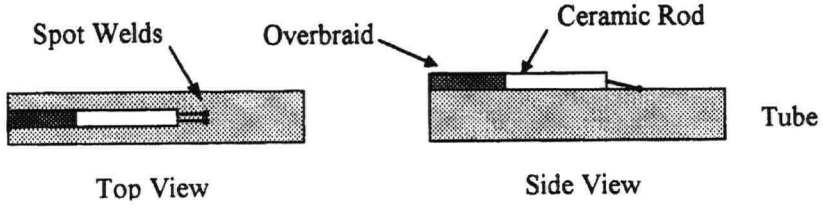

Figure 3.6: Thermocouple spot welded to the test section surface

3.4 Heat flux measurement

The heat gained by the fluid in a section can be determined by the heater power input. However, not all electric power generated is transferred to the fluid due to thermal losses. The heat lost is a function of tube surface temperature. A simple energy balance

is done instead, to determine the gain in fluid enthalpy across the test section. The increase in bulk fluid temperature across the heated test section permits the calculation of the heat flux. The heat flux q (W/m^2) can be determined as:

$$q = \frac{\dot{m}(H_2 - H_1)}{\pi dL} \tag{3.1}$$

where $\dot{m}$ is the mass flow rate of the fluid and H_2 & H_1 are the fluid enthalpies at the outlet and inlet of the test section of inside diameter d and length L.

3.5 Salt concentration measurement

Salt concentration was inferred from the effluent conductivity measurement. The conductivity meter was first calibrated for various concentrations of salt solutions, prior to the actual solubility experiments. The conductivity of the salt solution is a function of the salt concentration. Several solutions were prepared of various salt concentrations ranging from 10^{-5} to 1 wt.% of salt and conductivity of each solution was measured. Several conductivity measurements were taken at each concentration and then averaged.

Figure 3.7 shows the calibration graph plotted for conductivity versus Na_2CO_3 concentration for the range of our experimental study. A trend line, was then fit to the experimental data giving a R^2 value (coefficient of determination) of 0.9969. This figure shows salt concentration versus conductivity for 15 measurements. In terms of salt concentration (wt.%), about 70% of the data points lie within ±7% of the fitted equation. A similar calibration was made for Na_2SO_4 in order to determine the concentration of salt in the effluent interpreted from the measured conductivity and is shown in Fig. 3.8. A fitted curve predicted within ±10% of the measured conductivity with an R^2 value of 0.9989.

3.6 Data acquisition

The temperature, pressure and conductivity measurements are sent to a high speed data acquisition system (Omega MultiScan 1200) which has a channel to channel isolation. The MultiScan board can sample data from each channel once every 520 μsec. There are 24 channels on the acquisition system which is connected to a computer for data logging. TempView version 4.14 was used as the data acquisition program and was configured to a scan-time of about 5 sec for the 24 channels.

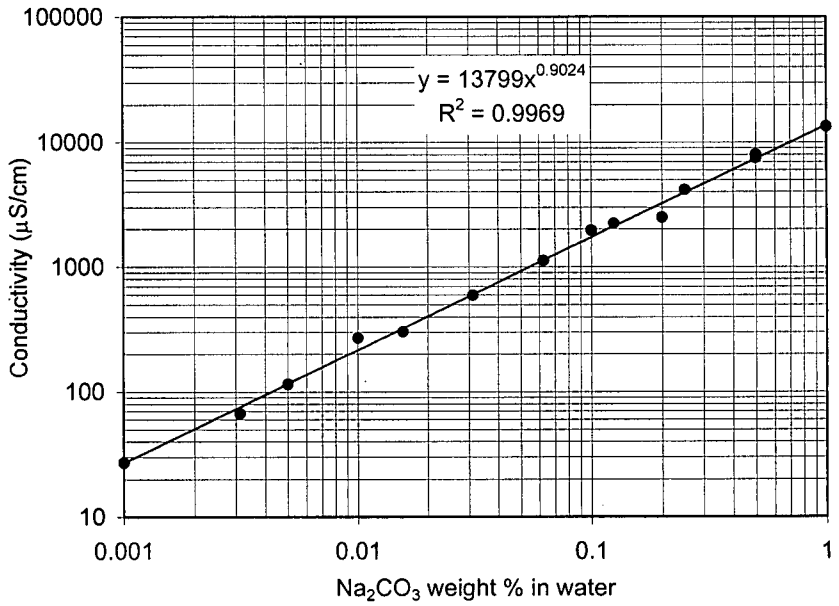

Figure 3.7: Conductivity meter calibration for Na_2CO_3

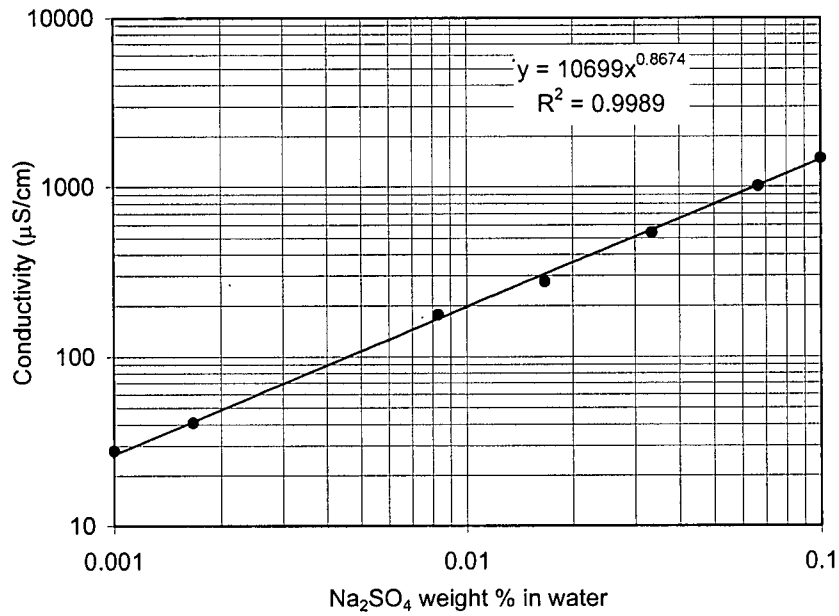

Figure 3.8: Conductivity meter calibration for Na_2SO_4

Chapter 4

Solubility of Na_2SO_4, Na_2CO_3 and Na_2SO_4-Na_2CO_3 mixture in Supercritical Water

4.1 Introduction

The solubility of inorganic salts in water at high temperature and high pressure is important in natural hydrothermal systems and some technological systems such as Supercritical Water Oxidation (SCWO) and Wet Air Oxidation (WAO). Supercritical water (i.e., water above 22.1 MPa and 374.14°C) has the ability to dissolve organic chemicals but the inorganic compounds are much less soluble at these conditions. These salts precipitate out of the supercritical water, agglomerate and usually stick to the reactor wall. In a tubular reactor a flow restriction is thus produced, in addition to a heat transfer resistance across the reactor wall, thus reducing the thermal-hydraulic performance of the reactor. In order to model the salt deposition, the salt solubility information is needed as a function of fluid temperature (or fluid density).

There are, in general, two types of salt phase behavior depending on whether the solubility curve intersects the critical curve (Type I) or not (Type II) [59]. Type I systems are often soluble in water at ambient conditions: NaCl-H_2O is a typical example. Type II salts - Na_2SO_4, K_2SO_4, Na_2CO_3, $CaSO_4$ - are generally less soluble; the solubility of Na_2SO_4 in SCW is about 1ppm at 250 bar and 450 °C and is about 3 orders of magnitude less than that of NaCl. The solubility of $CaSO_4$ is only about 1 ppb [4]. Not much information could be found about the phase behavior of Na_2CO_3 salt at conditions prevalent to SCWO systems.

Dell'Orco et al. [60] reported that sodium sulfate, chloride and bicarbonate appeared to be sticky salts. They were removed primarily by heterogeneous precipitation or impingement. The reported solubility of Na_2CO_3 in supercritical water is 26 ppm at

24.1 MPa and 450°C and that of $NaHCO_3$ is 86 ppm at 29.8 MPa and 509°C [61].

Measurements of isochoric heat capacity of sodium sulfate and sodium carbonate were made in a spherical high-temperature, high-pressure adiabatic calorimeter. Valyashko et al. [62] presented data regarding densities of liquid and vapor solutions in three-phase equilibrium for the sodium carbonate and water system data near the critical end point. Densities were reported for fluid mixtures, at around the critical temperature of pure water, for liquid and vapor solutions of sodium carbonate. It was reported that for an aqueous sodium carbonate solution the critical temperature is 649±0.2 K as compared to 647.1±0.1 K for pure water. Sodium carbonate and sodium sulfate are reported to exhibit Type-2 solid-fluid phase behavior (the solubility of salt starts declining before the critical temperature of the solvent is reached) [62].

The solubility of the salts being studied, Na_2CO_3 in particular, was available in the literature only for a few temperatures at elevated pressures. Several solubility measurements have been reported for sodium sulfate [4, 5, 7, 59]. Shvedov and Tremaine [63] developed a correlation for the solubility of sodium sulfate. For sodium carbonate, at supercritical conditions, Li and Gloyna [64] reported its solubility for two temperatures. Valyashko [65] presented solubility behavior of sodium carbonate at subcritical and near critical temperature. No information was available for these salts in the presence of each other.

4.2 Salt concentration measurement

As mentioned in the previous chapter the conductivity meter was calibrated for different concentrations of $[Na_2CO_3]$ and $[Na_2SO_4]$. For the experiments with sulfate and carbonate mixture, effluent samples were collected and analyzed for $[Na^+]$, $[CO_3^{2-}]$, $[HCO_3]$ and $[SO_4^{2-}]$ to determine the $[Na_2CO_3]$ and $[Na_2SO_4]$. $[Na^+]$ was measured using atomic absorption and titration was used for $[CO_3^{2-}]$ and $[HCO_3]$ measurement. For $[SO_4^{2-}]$ measurement, the turbidimetric method was used. The turbidimetric method, to determine the sulfate concentration, is based on the fact that light is scattered by particulate matter in aqueous solution. $BaCl_2$ is added to the sample to form milky-white precipitate and light absorption is then measured using a photometer. Standard procedures were followed to determine the concentrations of the ions and are discussed in Ref. [66]. Only the above ions were found in the effluent samples and no corrosion products were present, although atomic absorption was used to look for chromium and nickel.

4.3 Experimental procedure

For the solubility experiments, the salt solution was prepared by dissolving a certain mass of salt in a known volume (mass) of distilled water. An electric mixer was used to ensure a well-mixed salt solution. A series of experiments were performed around 24-25 MPa and at various temperatures. Initially distilled water was passed through the system to achieve a steady state condition. It usually took one hour to achieve steady state such that no change in temperature was observed with respect to time. The test section surface temperature was kept at the highest temperature in the system. Once steady state was reached, the salt solution was introduced into the system. It was assumed that the salt above the solubility limit at test section temperature would precipitate and stick to the tube wall. The fluid thus leaving the test section would be at the solubility limit at the test section temperature. This concept is shown in Fig. 4.1. The measured conductivity would then be used to determine the solubility. After running with salt solution for 10-15 minutes, distilled water was switched back on again. The distilled water would dissolve enough salt, deposited on the wall, to become saturated by the time it exits the *"salt bed"*. The effluent would thus again be at the solubility limit. The conductivity remained the same during the deposition and dissolution processes until there was no salt left on the tube wall. Therefore, the solubility measurements are not greatly affected by the deposition kinetics and integration resistance of the tube surface is negligible.

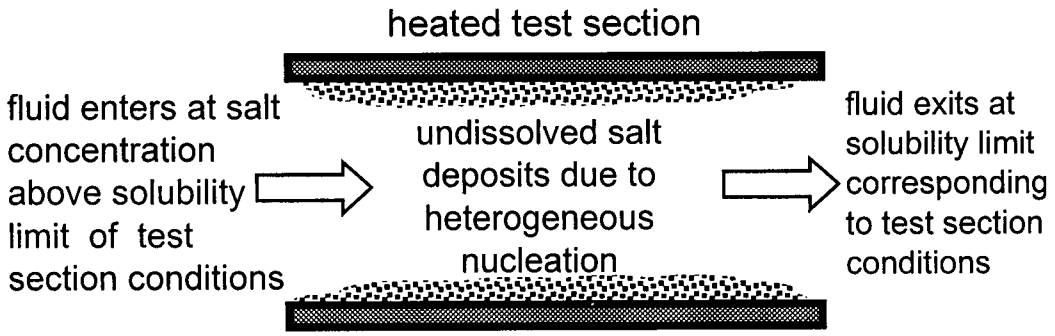

Figure 4.1: Concept of salt solubility experiments

Figure 4.2 shows the conductivity measurement for some sample experimental runs corrected for residence time. In all the experimental runs the conductivity increased from that of pure water to initially the conductivity of the salt solution in the influent tank. Although an initiation period is often exhibited in fouling systems, based on the literature reviewed, this is the first time it has been observed for the supercritical salt-water system. Unfortunately, the initiation period is very short compared to any reasonable SCWO operation period. After the initiation of the deposition, the conductivity decreased to a uniform value corresponding to the solubility limit. In the experimental

run shown in Fig. 4.2(a), the salt solution was introduced for about 10 minutes. The conductivity of the salt solution in the influent tank was about 1400 μS/cm. The solubility corresponding to the temperature for that run in terms of conductivity was 1330 μS/cm. When pure water was introduced at the end of the deposition part of the experiment, all the salt deposited on the tubes dissolved into the water and the dissolution period (*salt bed*) was quite short. For such cases only the deposition part was considered. However, it can be observed that the conductivity of the effluent did not change much during the deposition and dissolution parts of the experimental run until all the salt was removed from the tube. Figure 4.2(b) shows a similar run but with a longer dissolution duration. For some cases when the salt concentration in the influent tank was well above the solubility limit, as shown in Fig. 4.2(c), more salt deposited on the tubes. For such cases the dissolution period was much longer as it took a while for all the deposited salt to dissolve in the pure water.

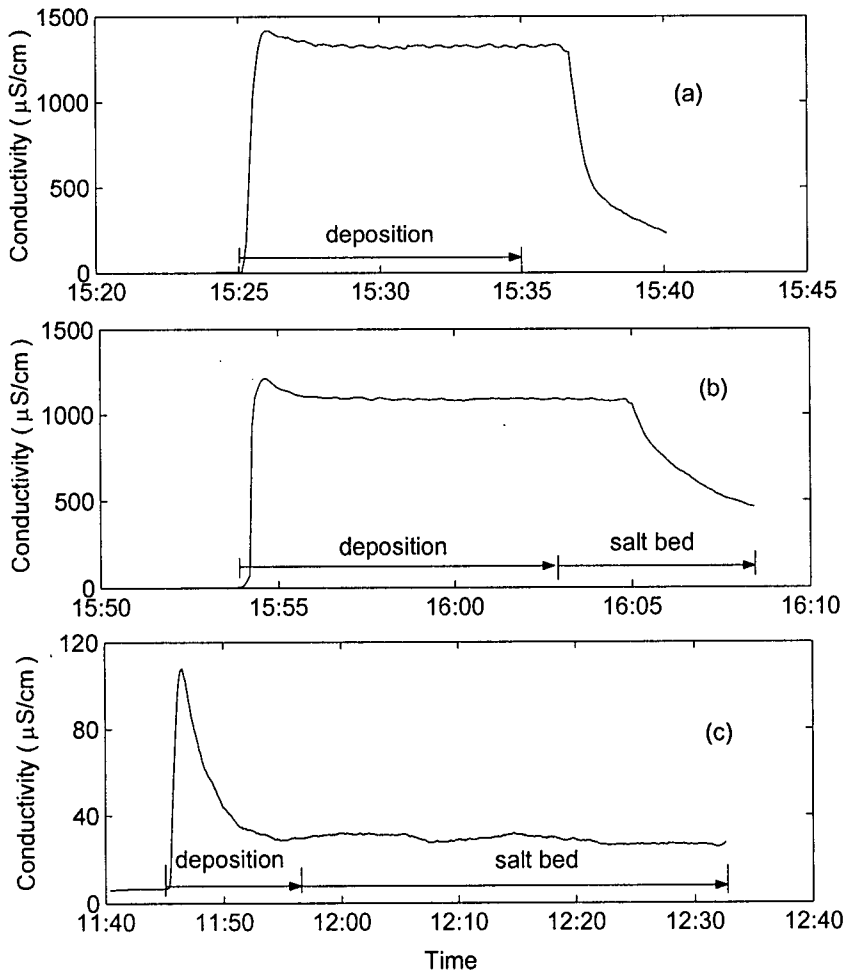

Figure 4.2: Effluent conductivity vs. time (a) run "S1", (b) run "S2" and (c) run "S3"

It was noticed that when the salt solution was introduced into the system the test section surface temperature decreased 1 or 2°C from the initial clean tube temperature. This decrease could be due to the higher heat transfer coefficient of salt solution as compared to water and initial negative resistance at the onset of fouling. The salt solution was used only for a short period so that the surface temperature rise was not more than about 3°C from the clean conditions. The heat input to the test section was kept low enough to ensure a small rise in the bulk fluid temperature across the test section. The bulk fluid inlet and outlet temperatures were also monitored and it was observed that the difference between the bulk inlet and outlet temperature remained almost constant during the experiment. This may indicate that the solid/solution interface temperature was close to the initial clean tube surface temperature.

In order to determine the solubility of the salt mixtures, the procedure adopted was the same as in pure salt experiments except that instead of a pure salt solution, a mixture of Na_2CO_3 and Na_2SO_4 was used.

4.4 Solubility reporting temperature

The tube inner surface temperature was calculated from the measured outer surface temperature and known heat input to the test section. The solubility was reported at a temperature taken to be clean tube average inner surface temperature of the second segment of the test section when the salt solution was introduced. This choice of reporting temperature is justified in Section 4.5.

The error range for the reporting temperature was determined in the following manner. The upper limit was taken to be the maximum surface temperature. Based on experience, 0.2°C was added to the measured temperature in order to include the effect of noise in the experimental data. For the lower limit, the minimum of; average inner surface temperature, fluid bulk outlet temperature and the temperature determined from the model (Section 4.5) was considered. Again, to include the effect of noise, 0.2°C was subtracted from this value.

4.5 Modeling the effect of heat and mass transfer on measurements

Salt deposition in the heated test section was modeled in order to understand the relation between an "underlying" solubility-temperature curve and the experimentally accessible parameters (outlet concentration and temperature). A one dimension model was developed by Teshima [33] for salt deposition on a heated tube. This model is reviewed below and extended by considering alternate heat transfer correlations.

Furthermore a more sophisticated method has been developed to estimate the temperature corresponding the salt solubility.

Once the solubility is exceeded in the salt solution, the salt can deposit on the tube surface due to homogeneous or heterogeneous nucleation. In this model it is assumed that the salt nucleating on the tube surface sticks to the wall. Precipitation of salt due to homogeneous nucleation, i.e., salt particles nucleated in the bulk fluid, has not been considered in the model.

For the heterogeneous mechanism, i.e., crystalline scaling, heat and mass transfer relations were programmed in the MATLAB environment (The MathWorks, Inc., Massachusetts, USA). As a simplification, pure water thermodynamic and transport properties were used to model the salt solution. The heat transfer coefficient must be known to determine the wall temperature. In order to calculate the heat transfer coefficient, an empirical correlation can be used. Two Nusselt number correlations, developed by Swenson et al. [67] and Yamagata et al. [68] have been considered. There are other empirical relations that can be used to calculate the heat transfer coefficient [69], however, the estimated values lie between the heat transfer coefficient values determined by the two considered correlations. The details of these correlations are discussed below.

The Swenson correlation: [67]

$$Nu = 0.00459\,(Re_s)^{0.923}\left[\left(\frac{H_s - H_b}{T_s - T_b}\right)\frac{\mu_s}{k_s}\right]^{0.613}\left(\frac{\rho_s}{\rho_b}\right)^{0.231} \tag{4.1}$$

where Re is the Reynolds number, H is the fluid enthalpy, μ is the fluid dynamic viscosity, k is the fluid thermal conductivity and ρ is the fluid density. The subscripts b and s correspond to conditions in the bulk and at the fluid/salt deposit surface respectively.

The Yamagata correlation: [68]

$$Nu = 0.0153 Re_b^{0.85} Pr_b^{0.8} F_c \tag{4.2}$$

Pr_b is the Prandtl number of the bulk fluid and

$$Fc = \begin{cases} 1 & (E > 1) \\ \left[\frac{(H_b - H_s)/(T_b - T_s)}{Cp_b}\right]^{n_2} & (E < 0), \quad n_2 = 1.44\left(1 + \frac{1}{Pr_{pc}}\right) - 0.53 \\ 0.67 Pr_{pc}^{-0.05}\left[\frac{(H_b - H_s)/(T_b - T_s)}{Cp_b}\right]^{n_1} & (otherwise), \quad n_1 = 0.77\left(1 + \frac{1}{Pr_{pc}}\right) + 1.49 \end{cases} \tag{4.3}$$

in which $E = \frac{T_{pc} - T_b}{T_s - T_b}$, Cp_b is the specific heat at bulk conditions and pc is for the pseudo-critical conditions. The heat transfer coefficient can then be calculated using

the Nusselt number:

$$h = \frac{Nuk_b}{d} \tag{4.4}$$

For the heterogeneous nucleation, the similarities for the heat and mass transfer were used to determine the deposition rate. The deposition rate would depend on the mass transfer coefficient, h_m and the dissolved salt concentration difference between the bulk and wall conditions:

$$\dot{m}_m = h_m \pi d L (C_b - C_w) \tag{4.5}$$

where C_b is the dissolved salt mass concentration in the bulk fluid, C_w is the dissolved salt mass concentration at the fluid/deposit surface or at the tube wall, d is the diameter of the tube, L is the length of the tube, $\dot{m}_m$ is the molecular deposition rate (kg/sec).

The mass transfer coefficient was determined as follows. When forced convection dominates transport and mass transfer does not significantly affect the flow field, given a correlation for the heat transfer coefficient, a mass transfer coefficient may be obtained and vice versa. This is accomplished by replacing the Nusselt number with Sherwood number ($Sh = h_m d/\mathcal{D}_m$) and the Prandtl number with the Schmidt number ($Sc = \nu/\mathcal{D}_m$). $\mathcal{D}_m$ is the molecular diffusion coefficient and can be determined from the Stokes-Einstein relation [70] using the molecule diameter d_m:

$$\mathcal{D}_m = \frac{b_k T}{3\pi\mu d_m} \tag{4.6}$$

where b_k is Boltzmann constant, μ is the dynamic fluid viscosity. The molecular diameter was varied from 3-9 Å and negligible change in T_{model} was noticed. For the results presented here, it is taken to be 5.1 and 5.3 Å for Na_2CO_3 and Na_2SO_4 respectively calculated using the Avagrados number, salt density and molar mass. Rogak and Teshima [7] used a similar approach to determine the molecular diameter of sodium sulfate and the calculated diffusion coefficient value appeared acceptable based on the experimental values reported by Hodes et al. [32]

This equivalence of correlations is subsequently referred to as the analogy between heat and mass transfer. Rogak and Teshima [7] presented the results of a heat and mass transfer model for the tubular reactor, developed and tested experimentally for Na_2SO_4 deposition at 25 MPa. The model uses empirical heat transfer relations by Swenson et al. [67] to estimate mass transfer rates. When natural convection is important, the analogy between heat and mass transfer applies only if the Lewis number $(\alpha/\mathcal{D}_m)$ of the fluids equals 1 i.e., similar temperature and concentration profiles [8].

The heat transfer coefficient is a function of Reynolds number and Prandtl number:

$$\frac{hd}{k} = f(Re, Pr) \tag{4.7}$$

and from the Sherwood number, the mass transfer coefficient, h_m, is a function of Reynolds number and Schmidt number:

$$\frac{h_m d}{\mathcal{D}_m} = f(Re, Sc) \tag{4.8}$$

Therefore using the Nusselt number correlation and an analogous equation for Sherwood number, the following relation for the mass transfer coefficient can be derived:

$$h_m = \frac{h}{\rho C_p L e^a} \tag{4.9}$$

where $a = 0.387$ and 0.2 for Nusselt number correlations developed by Swenson et al. [67] and Yamagata et al. [68] respectively.

Using Eq. 4.5, for a guessed value of saturated salt concentration in the bulk, the deposition rate was calculated. The experimental solubility curve was then used to determine the saturated salt concentration at the wall. The actual concentration of salt in the bulk can thus be calculated using Eq. 4.5. The test section was then discretized into 0.5-cm segments. A segment length of 0.5 cm was found to be appropriate for numerical analysis. The bulk fluid and wall temperatures were then calculated from the energy balance and heat transfer coefficient. The saturated salt concentration was estimated from the measured solubility and the salt concentration in the bulk fluid was calculated as:

$$\frac{\mathrm{d}C_b}{\mathrm{d}L} = -h_m \pi d \left(C_b - C_w\right) \tag{4.10}$$

The concentration of salt calculated from the model for a sample experimental run is shown in Fig. 4.3. The bulk fluid temperature increases from 388.7°C to 396.6°C in the test section. The salt concentration in the bulk fluid, C_b, calculated from the program is compared to the saturation concentration in the bulk, $C_{b(sat)}$, and saturation concentration at wall conditions, $C_{w(sat)}$.

The use of this heat and mass transfer model to interpret measurements is discussed below. The test section is not perfectly isothermal, so it is not obvious which temperature should be used as the "reporting temperature" for the measured concentration in the effluent. Provided that the fluid leaving the test section is not supersaturated or laden with particles, the reporting temperature should be greater than the bulk exit temperature. Considering that there is some mass-transfer limitation, the reporting temperature should be less than the maximum surface temperature. A simple approach is to take the average surface temperature as the reporting temperature. Normally this average is close to the bulk temperature anyway. Near the critical temperature, density and solubility vary dramatically with temperature, so a 2°C error in reporting temperature has a significant effect. For this reason, a more sophisticated model of the

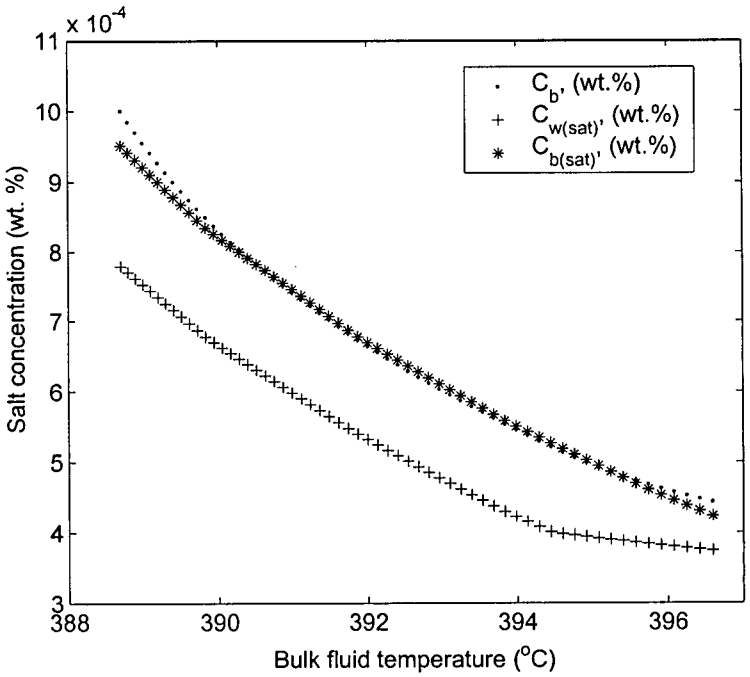

Figure 4.3: Modeled salt concentration along test section for run "S6"

experimental apparatus has been developed. The actual "reporting" temperature from model, T_{model} should be some weighted average of surface and bulk temperatures:

$$T_{model} = T_{b,exit} + x\left(\bar{T}_s - \bar{T}_b\right) \tag{4.11}$$

where x is a weighting factor. Average wall and bulk temperatures are used in the second term to minimize experimental noise.

The weighting factor x should mainly be a function of the mass transfer characteristics of the flow, and secondarily, the variation of solubility with temperature. The heat and mass transfer model was used to estimate x for each experimental run. In the model, it has been assumed that there is some underlying solubility function $C_{sat}(T)$ which is to be estimated from the bulk outlet concentration C_b, by choosing a temperature $\acute{T}$ such that $\acute{C}_b$=C$_{sat}(\acute{T})$. The model uses the actual measured bulk temperatures to determine the heat flux and wall surface temperatures. The modeled wall temperatures $\acute{T}_s$ are not exactly the same as the actual wall temperatures T_s, due to errors in the heat transfer model, but the modeled temperatures are not used directly. Instead, the model is used only to estimate x from:

$$x = \frac{\acute{T} - T_{b,exit}}{\bar{\acute{T}}_s - \bar{T}_b} \tag{4.12}$$

Table 4.1: Details of Na_2CO_3 solubility experiments

Experiment reference no. & Data File	Code	Influent salt concentration (wt.%)	Gauge pressure (MPa)	Mass flow rate (kg/min)	Bulk fluid temperature (°C)		Average surface temperature (°C)	Error range for temperature corresponding to the solubility (°C)		Temperature calculated from the Swenson model (°C)	Temperature calculated from the Yamagata model (°C)	Solubility (wt.%)[a]	Run type
					inlet	outlet		min	max				
May 10, 2002 MAY10,2002.xls	C1	0.19	24.5	0.66	398.3	408.2	409.5	407.2	411.6	407.3	407.2	0.0120	deposition & salt bed
May 06, 2002-03 MAY06,2002.xls	C2	0.56	24.5	0.68	382.2	383.1	384.2	382.9	386.1	383.5	383.1	0.1010	deposition & salt bed
May 06, 2002-02 MAY06,2002.xls	C3	0.56	24.4	0.68	378.1	380.7	380.1	379.9	381.0	380.5	380.6	0.3900	deposition & salt bed
May 06, 2002-01 MAY06,2002.xls	C4	0.56	24.2	0.68	373.4	378.6	378.3	378.0	379.5	378.0	378.1	0.5280	deposition & salt bed
May 03, 2002-01 MAY03,2002.xls	C5	0.56	24.3	0.70	385.4	390.0	390.2	389.8	391.3	390.6	390.4	0.0270	deposition & salt bed
May 03, 2002-02 MAY03,2002.xls	C6	0.1	24.3	0.70	380.8	384.9	384.7	384.5	385.7	385.6	385.6	0.0730	deposition & salt bed
Mar 12'02-NL MAR12'02NL.xls	C7	0.1	24.9	0.18	388.2	390.6	391.8	390.4	393.2	391.2	390.6	0.0220	deposition only
Mar 12, 2002-02 MAR12'02N.xls	C8	0.1	25.0	0.70	391.9	397.9	398.3	397.5	401.1	397.5	397.5	0.0160	deposition only
Mar 12, 2002-03 MAR12'02N.xls	C9	0.1	25.0	0.70	395.2	403.2	403.5	401.9	407.1	401.9	402.8	0.0120	deposition only
Mar 12, 2002-04 MAR12'02N.xls	C10	0.1	25.0	0.70	399.9	410.0	410.3	409.1	414.3	409.1	409.6	0.0090	deposition only
Mar 12, 2002-05 MAR12'02N.xls	C11	0.1	25.0	0.70	403.0	416.0	415.7	415.5	420.0	416.3	416.7	0.0079	deposition only
Mar 12, 2002-06 MAR12'02N.xls	C12	0.1	25.0	0.70	407.0	423.3	422.0	421.3	427.2	421.3	421.4	0.0057	deposition only
Mar 12, 2002-07 MAR12'02N.xls	C13	0.1	25.0	0.70	412.5	431.3	429.3	426.2	435.3	426.2	426.5	0.0043	deposition only
Mar 12, 2002-08 MAR12'02N.xls	C14	0.1	25.0	0.70	420.6	440.0	437.7	434.9	441.1	434.9	438.0	0.0038	deposition only

[a] 1 wt.% is about 10,000 mg/L

The T_{model} was then calculated for each experimental run. Tables 4.1 & 4.2 compare this temperature with various temperatures measured in the test section for Na_2CO_3 and Na_2SO_4 experiments. For the Na_2CO_3 runs, the difference between T_{model} and average test section temperature was less than 1°C for majority of cases. The run "C13" has the maximum difference i.e., 3.1°C. For the Na_2SO_4 runs, this difference was less than 1.4°C for all cases. It was therefore concluded, as a simple approach, that the average surface temperature of the test section should be the appropriate reporting temperature. However, as mentioned earlier in Section 4.4, this T_{model} was considered in determining the error range for the reporting temperatures.

Table 4.2: Details of Na_2SO_4 solubility experiments

Experiment reference no. (Data file: May24,2002.xls)	Code	Influent salt concentration (wt.%)	Gauge pressure (MPa)	Mass flow rate (kg/min)	Bulk fluid temperature (°C)		Average surface temperature (°C)	Error range for temperature corresponding to the solubility (°C)		Temperature calculated from the Swenson model (°C)	Temperature calculated from the Yamagata model (°C)	Solubility (wt.%)[a]	Run type
					inlet	outlet		min	max				
May 24, 2002-01	S1	0.1	24.4	0.66	379.6	383.1	382.2	382.0	383.4	383.2	383.2	0.0850	deposition only
May 24, 2002-02	S2	0.1	24.4	0.66	379.7	382.4	382.3	382.1	383.2	382.4	382.4	0.0670	deposition & salt bed
May 24, 2002-03	S3	0.1	24.5	0.66	382.3	383.6	383.6	383.4	384.4	383.7	383.7	0.0400	deposition & salt bed
May 24, 2002-04	S4	0.1	24.6	0.66	383.7	384.9	384.5	384.3	385.4	384.9	384.9	0.0220	deposition & salt bed
May 24, 2002-05	S5	0.1	24.4	0.66	385.4	388.4	388.7	388.2	389.6	388.4	388.4	0.0010	deposition & salt bed
May 24, 2002-06	S6	0.1	24.3	0.66	388.7	396.6	397.0	395.6	398.4	395.6	395.8	0.0004	deposition & salt bed

[a] 1 wt.% is about 10,000 mg/L

4.6 Results and discussion

4.6.1 Na_2CO_3 solubility

Figure 4.4 shows the solubility data for Na_2CO_3 for the temperature range of interest. A similar behavior of solubility versus water density is shown in Fig. 4.5. A third order polynomial has been fit to the experimental data. The empirical relation to predict the Na_2CO_3 solubility concentration (wt.%), as a function of fluid density, ρ (kg/m^3) is as follows:

$$\log\left[C_{Na_2CO_3}\right] = 6.24 \times 10^{-8}\rho^3 - 8.48 \times 10^{-5}\rho^2 + 0.046\rho - 9.74 \qquad (4.13)$$

Information available from the literature is also shown. The subcritical data were reported by Valyashko [65]. At supercritical conditions the solubility data were found at two temperatures [64] and are also shown in Figs. 4.4 & 4.5.

In order to test the assumption that the test section was long enough such that the undissolved salt deposits on the test section wall, run"C7" was done at 24.5 MPa and at a lower flow rate of 0.18 kg/min. If the assumption were false then a higher salt concentration should have been observed in the effluent for the higher flow rate, as compared to the lower flow rate run. The experimental results seem to be in good agreement with the existing information in the literature. As mentioned earlier, the average surface temperatures are considered to be the actual temperatures corresponding to the solubility limit. These temperatures are found to be quite close to the reporting temperatures calculated from the model program. The details of the operating parameters for the Na_2CO_3 experiments are shown in Table 4.1.

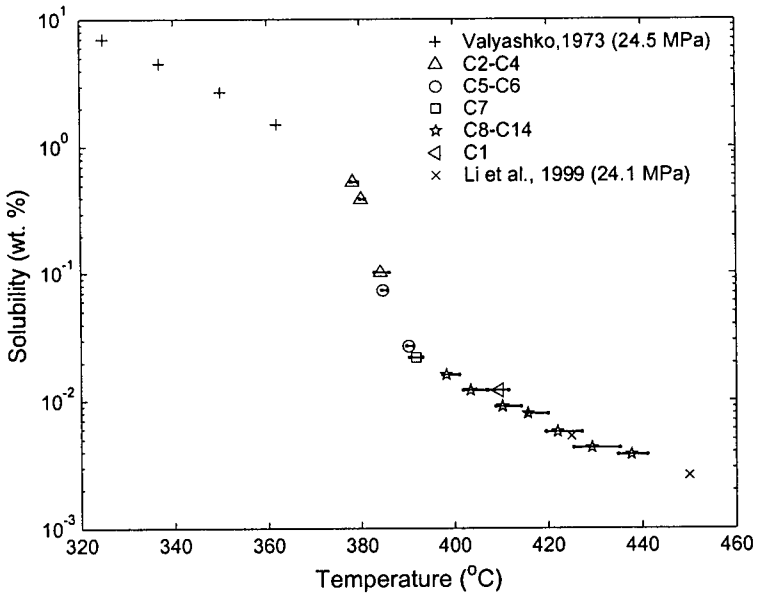

Figure 4.4: Na_2CO_3 solubility vs. temperature

4.6.2 Na_2SO_4 solubility

The solubility behavior for Na_2SO_4 versus temperature and density is shown in Figs. 4.6 & 4.7 respectively. A second order polynomial was fitted to calculate the Na_2SO_4 solubility concentration (wt.%), as a function of fluid density, ρ (kg/m^3). The relation is as follows:

$$\log\left[C_{Na_2SO_4}\right] = -2.16 \times 10^{-5}\rho^2 + 0.037\rho - 13.11 \tag{4.14}$$

Figures 4.6 & 4.7 also show the solubility measurements reported by Armellini & Tester [5] and Rogak & Teshima [7]. The thermocouples used to measure temperatures reported by Rogak & Teshima [7] were later found to have an offset of 2°C. The data shown here have been corrected for the offset. Furthermore, it is worth mentioning that the solubility data reported by Rogak & Teshima [7] correspond to the fluid temperature at the test section outlet. However, for this study, a more sophisticated procedure has been followed to determine the solubility reporting temperature. A correlation developed for Na_2SO_4 solubility by Shvedov & Tremaine [63] is also shown in Figs. 4.6 & 4.7. The correlation gives a good indication of the solubility up to a fluid density of 200 kg/m^3 and after that it underestimates the solubility. For example at 100 kg/m^3 the correlation underestimates the solubility by almost a factor of 3, compared to other measurements. The operating parameters and other details for Na_2SO_4 experiments are shown in Table 4.2. The average surface temperatures were found to be quite close to the reporting temperatures calculated, using the model. For the range of flow rates and heat input to the test section considered in this study, it was observed that the bulk fluid temperature at the outlet of the test section is a

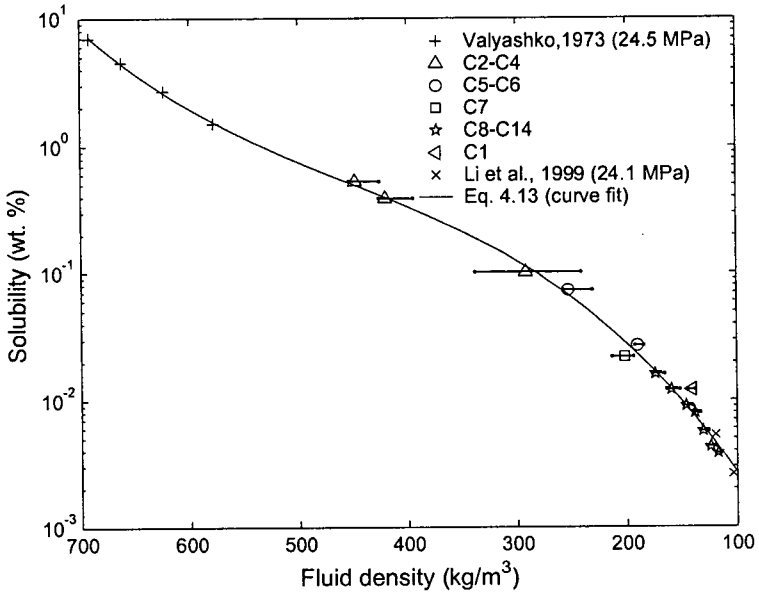

Figure 4.5: Na_2CO_3 solubility vs. density

good estimate for the actual temperature corresponding to the solubility limit. But for higher heat input or flow rate the wall-bulk temperature difference will be higher and for those cases the bulk fluid outlet temperature may not be a correct temperature corresponding to the solubility limit.

4.6.3 Solubility of Na_2CO_3-Na_2SO_4 mixture

For the solubility experiments in which a mixture of salts was used, chemical analysis of samples was done to determine the salt concentration. It was noticed from the chemical analysis that the $[Na^+]$ content was not always the exact amount of what was required to make Na_2CO_3 and Na_2SO_4 from measured $[CO_3^{2-}]$, $[HCO_3]$ and $[SO_4^{2-}]$. Therefore Na_2CO_3 and Na_2SO_4 concentrations in the solution were determined using two methods. $[Na^+]$ required to make Na_2CO_3 and Na_2SO_4 from the measured $[CO_3^{2-}]$, $[HCO_3]$ and $[SO_4^{2-}]$ was calculated and then the concentrations of Na_2CO_3 and Na_2SO_4 were calculated. Thus, in this method, the $[CO_3^{2-}]$ and $[SO_4^{2-}]$ measurements were assumed to be accurate. In the other procedure, the concentrations of these salts were calculated based on measured $[Na^+]$ and $[SO_4^{2-}]$. Thirteen experiments were performed with a mixture of salts. For these experiments, the percentage difference in $[Na^+]$ calculated, based on $[CO_3^{2-}]$, $[HCO_3]$ & $[SO_4^{2-}]$ and $[Na^+]$ detected ranged from -8.3% to 12.5%, with 70% of the data having less than $\pm 5\%$ difference. It was decided to report the results based on the former procedure, i.e., salt concentration calculated based on $[CO_3^{2-}]$, $[HCO_3]$ and $[SO_4^{2-}]$ measurements. The solubility behavior

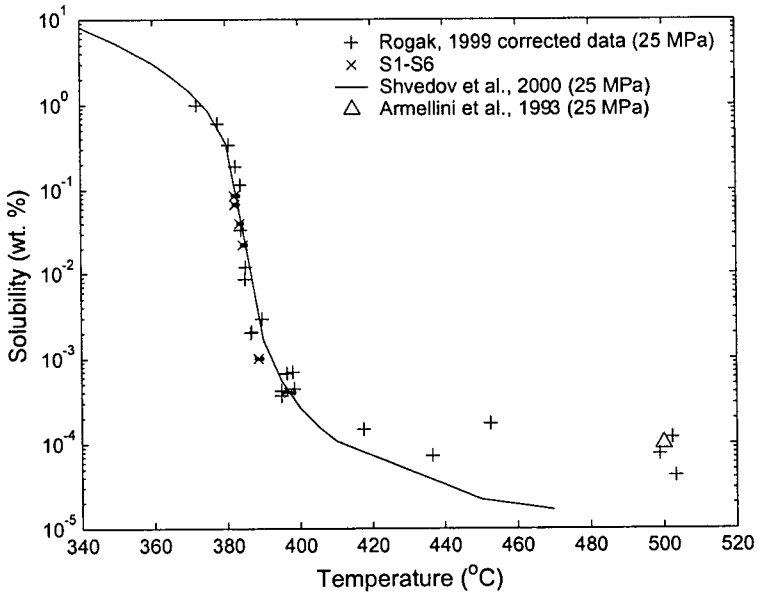

Figure 4.6: Na_2SO_4 solubility vs. temperature

of Na_2CO_3 and Na_2SO_4 in a mixture is shown in Fig. 4.8. It is interesting to note that at low fluid density, the solubility of each salt when present in a mixture is almost same as that of individual binary salt-water system. However, at a density of about 470 kg/m^3, Na_2SO_4 was found to be less soluble in the presence of Na_2CO_3. This could be due to the common-ion effect i.e., the shift in an equilibrium position caused by the presence of an ion involved in the equilibrium reaction. Thus the solubility of less soluble Na_2SO_4 can decrease due to the presence of Na^+, i.e., the common ion. The details of parameters for salt-mixture experiments are shown in Table 4.3.

4.7 Conclusion

Salt solubility information is needed to predict the deposition of these salts on the heat transfer surface. The pressure and temperature conditions focused were those which are usually encountered in SCWO systems. The solubility data reported cover a wide range of temperatures and fill the gap in the information available in the literature. Very few previous measurements in the critical region were found for Na_2CO_3. Furthermore, solubility of these salts, when present in the solution in the form of a mixture, has also been determined for the first time at SCWO conditions. It was noticed that the solubility of the salts studied in the form of a mixture, above supercritical conditions, was quite close to the solubility of the pure salt. However, at near critical conditions, the presence of Na_2CO_3 reduced the solubility of Na_2SO_4,

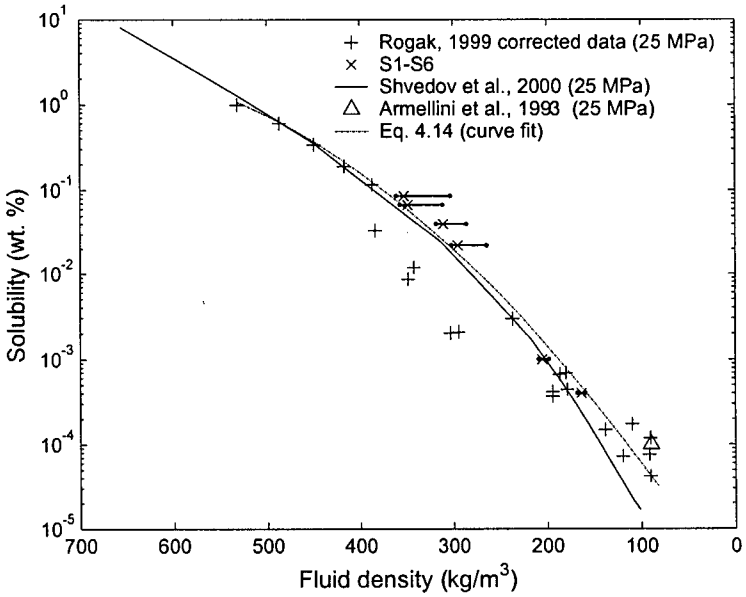

Figure 4.7: Na_2SO_4 solubility vs. density

presumably due to the common-ion effect.

For both salts considered in this study, there was a rapid decrease in solubility just above the pseudo-critical temperature. Furthermore the results show that a lower order polynomial in log of solubility limit versus density can be used to interpolate data. The reported temperatures were confirmed by developing a heat and mass transfer model to determine the temperature corresponding to the solubility limit. The experimental procedure adapted to measure the solubility seems to be quite reasonable given the fact that the measured values agreed well with the data existing in the literature.

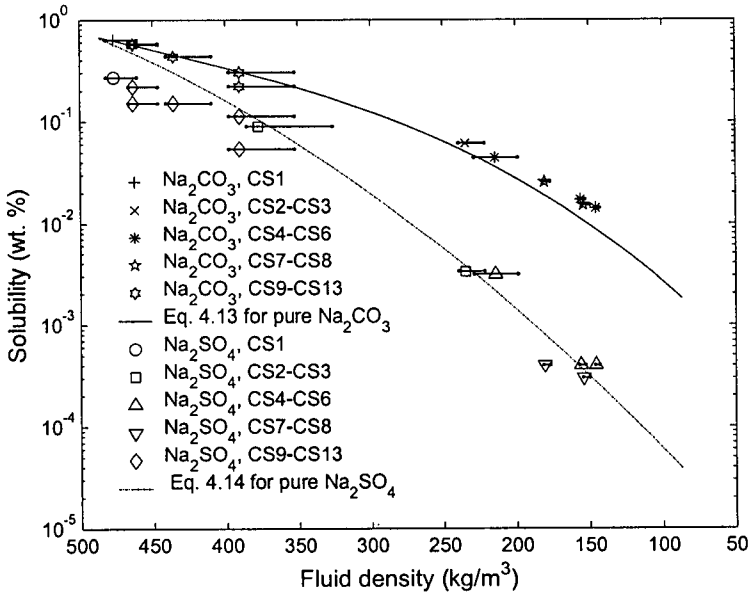

Figure 4.8: Solubility of mixture of Na_2CO_3 and Na_2SO_4

Table 4.3: Details of Na_2CO_3 - Na_2SO_4 mixture solubility experiments

Experiment reference no. & data file	Code	Influent salt concentration (wt. %)		Gauge pressure (MPa)	Mass flow rate (kg/ min)	Bulk fluid temperature (°C)		Average surface temper-ture. (°C)	Error range for temperature corresponding to the solubility (°C)		Solubility (wt.%)[a]		Run type
		Na_2CO_3	Na_2SO_4			inlet	outlet		min	max	Na_2CO_3	Na_2SO_4	
Aug 07, 2002-01 AUG07, 2002.xls	CS1	1.053	1.077	24.6	0.66	373.6	377.0	377.3	376.8	378.5	0.6320	0.2707	deposition & salt bed
Aug 08, 2002-01 AUG08, 2002.xls	CS2	0.140	0.131	24.5	0.66	380.7	382.4	381.9	381.7	383.2	0.1253	0.0899	deposition & salt bed
Aug 08, 2002-02 AUG08, 2002.xls	CS3	0.140	0.131	24.3	0.66	384.2	385.9	385.5	385.3	386.5	0.0611	0.0033	deposition & salt bed
Aug 14, 2002-01 AUG14, 2002.xls	CS4	0.051	0.006	24.7	0.66	385.4	388.0	389.3	387.8	391.2	0.0442	0.0031	deposition & salt bed
Aug 14, 2002-03 AUG14, 2002.xls	CS5	0.051	0.006	24.5	0.66	401.5	407.0	406.6	406.4	408.1	0.0142	0.0004	deposition & salt bed
Aug 14, 2002-04 AUG14, 2002.xls	CS6	0.051	0.006	24.4	0.66	396.3	400.3	400.6	400.1	402.1	0.0172	0.0004	deposition & salt bed
Aug 16, 2002-01 AUG14, 2002.xls	CS7	0.051	0.006	24.6	0.66	391.1	394.8	394.0	393.8	395.0	0.0255	0.0004	deposition only
Aug 16, 2002-02 AUG14, 2002.xls	CS8	0.051	0.006	24.6	0.66	398.2	403.2	403.0	402.8	405.1	0.0152	0.0003	salt bed only
Dec 11,2002-01 DEC11, 2002.xls	CS9	0.829	0.427	24.6	0.66	375.4	378.7	378.29	378.1	379.5	0.5661	0.1509	deposition & salt bed
Dec 11,2002-01 DEC11, 2002.xls	CS10	0.829	0.427	24.6	0.66	375.4	378.7	378.29	378.1	379.5	0.5815	0.2189	deposition & salt bed
Dec 11,2002-02 DEC11, 2002.xls	CS11	0.829	0.427	24.6	0.66	378.1	380.1	380.02	379.8	381.2	0.4332	0.1509	deposition only
Dec 11,2002-03 DEC11, 2002.xls	CS12	0.829	0.427	24.6	0.66	381.9	382.2	381.89	381.7	382.9	0.3033	0.0541	deposition & salt bed
Dec 11,2002-03 DEC11, 2002.xls	CS13	0.829	0.427	24.6	0.66	381.9	382.2	381.89	381.7	382.9	0.2212	0.1130	deposition & salt bed

[a] 1 wt.% is about 10,000 mg/L

Chapter 5

Salt Deposition and its Mitigation

5.1 Introduction

As discussed in the last chapter, it was observed that the solubility of inorganic salts decreases drastically around the pseudo-critical temperature. The heated reactor tube surface is at a higher temperature compared to the bulk fluid, hence salt molecules crystallize at the tube surface. This type of nucleation is known as *heterogeneous nucleation* and results in *crystalline scale* on the tube wall. On the other hand if the salt becomes supersaturated in the bulk fluid, salt particles nucleate in the fluid and this type of nucleation is known as *homogeneous nucleation.* Precipitation of salt particles lead to *particulate deposit.* Hodes [71] studied Na_2SO_4 deposition on a heated cylinder. Salt concentration and time in the deposition experiments were varied between 2 & 8 wt.% and 6 & 12 minutes. The salt solution was preheated to about 5°C below the solubility temperature corresponding to the concentration in the bulk solution surrounding a cylinder. The cylinder was heated beyond the solubility temperature to drive deposition. No homogeneous nucleation was observed through the visually accessible test cell during the experimental run. The purpose of the study was to develop an understanding of salt deposition kinetics and nucleation phenomenon in SCWO reactors. The results of the deposition study were presented by Hodes et al. [32]. Experimental deposition rate data have been provided for sodium sulfate and a predictive model based on the data was developed. Smith et al. [72] developed a model to predict whether or not homogeneous nucleation would occur in a natural convection boundary layer around a cylinder heated beyond the solubility temperature corresponding to the concentration of salt in the surrounding aqueous salt solution. Lewis number was found to be a critical property in this regard. The model was applied to the experiments run by Hodes [71] and yielded consistent results, i.e., homogeneous nucleation was absent.

This chapter discusses the deposition behavior of Na_2CO_3 due to heterogeneous nucleation. As a possible fouling mitigation technique, the salt was made to nucleate in the

bulk fluid just before the test section. The salt particles nucleating in the bulk fluid should agglomerate and are more likely to flow with the fluid, through the system, due to their larger size. The experimental procedure for this mitigation technique is discussed in this chapter. The deposition behaviors of both heterogeneous and combined homogeneous & heterogeneous type nucleations have also been compared.

5.2 Experimental procedures

5.2.1 Heterogeneous nucleation experiments

As mentioned in the last chapter, experiments were initially carried out to determine the salt solubility at SCWO conditions. The experimental method was to pass the salt solution through a near isothermal test section and the salt above the solubility limit was assumed to be depositing on the tube surface. The solution leaving the test section would thus be at its saturation limit. The test section was set to be the hottest section in the system such that the concentration of salt in the effluent should be the saturation limit corresponding to the test section temperature. The tube surface temperature was higher than the fluid temperature and thus the salt was nucleated on the tube surface and homogeneous nucleation was unlikely. The salt solution was passed for a short period of time (less than 20 minutes), in order to avoid plugging or excessive tube surface temperature rise. The flow was switched to pure water afterwards to dissolve the deposited salt. The fluid was heated in the pre-heaters to achieve temperatures above the pseudo-critical temperature. During the experiments it was noticed that the pre-heaters were most susceptible to plugging and/or overheating. Due to this reason, the system had to be shut down and thus these experiments could not be run for a longer period. These experiments are similar to those performed by Teshima [33] and later modeling work carried out by Rogak and Teshima [7] indicated only heterogeneous nucleation was occurring.

5.2.2 Combined heterogeneous and homogeneous nucleation experiments (heated test section)

In order to check the hypothesis that larger homogeneously nucleated particles are less likely to stick to the tube surface, the experiment set up was modified as shown in Fig. 5.1. Instead of the salt solution, only pure water was passed through the pre-heaters such that no salt deposition occurred before the test section. Salt solution was then injected into this stream of water, using a metering pump, at the test section inlet. A Bran+Luebbe metering pump (model N-K31), shown as pump # 2 in Fig. 5.1 was used for this purpose. The maximum discharge rate of the metering pump is about 0.2 kg/min and is adjusted by varying the stroke length of the plunger. The metering pump calibration was done at a system pressure of 24.7 MPa by measuring pump discharge

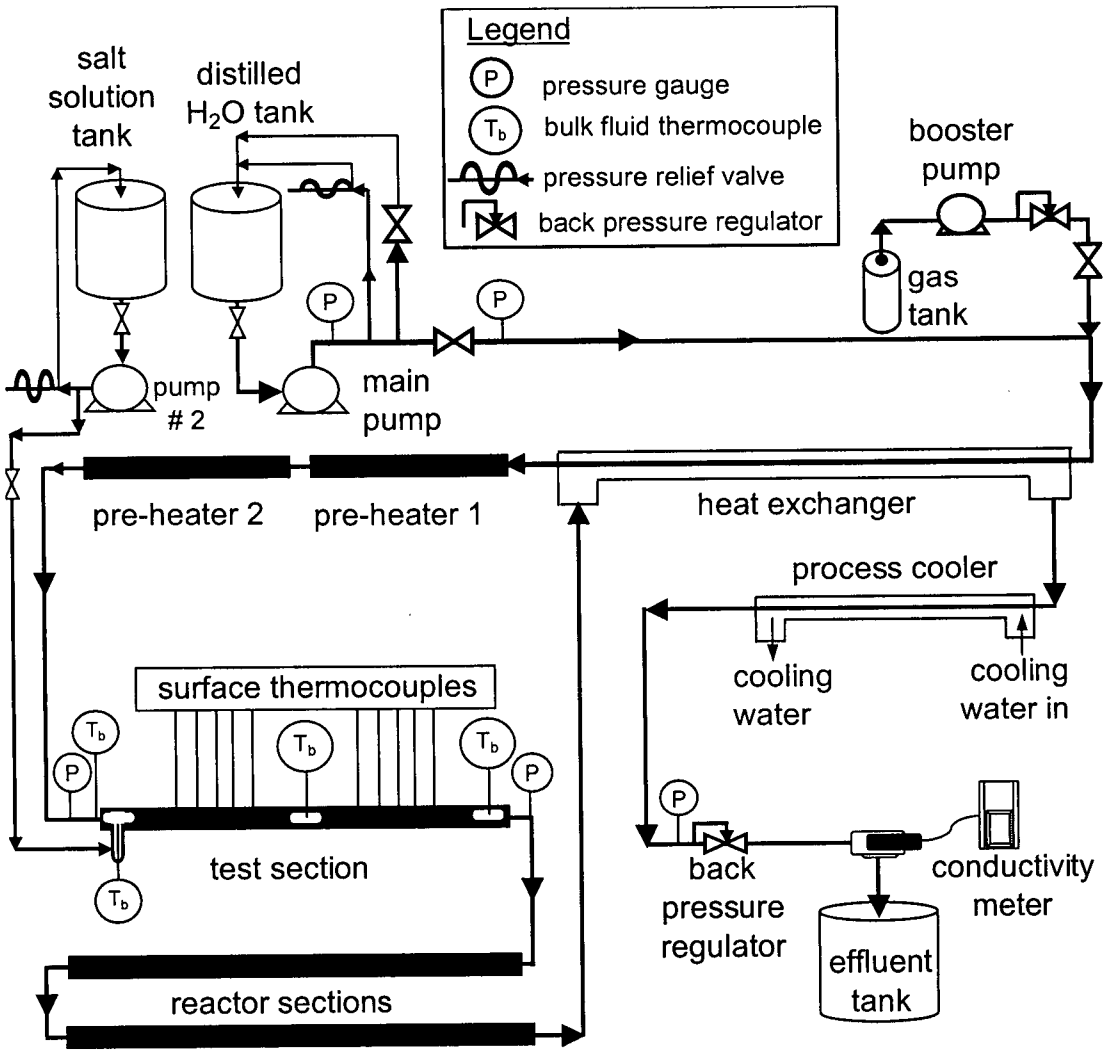

Figure 5.1: Modified process equipment for homogeneous salt nucleation

at various stroke length settings of the pump. The discharge and stroke length relation is shown in Fig. 5.2. A pulsation damper (Hydrodynamics Flowguard DS-10-NBR-A) was used to suppress the flow variations. The flow rate of the metering pump was set to 10% of the main pump's flow rate. The pure water stream was heated such that the temperature after mixing was beyond the solubility temperature corresponding to the salt concentration in the mixed streams. The temperatue of the salt solution was measured using a bulk temperature thermocouple just before it mixed into the main stream coming from pre-heater 2. Thus the salt particles were expected to nucleate in the bulk fluid. Since the test section was heated in these runs, therefore heterogeneous nucleation may also be expected. The heat input to the test section was kept low, usually about 1.25 kW, which corresponds to a nearly adiabatic condition. The experiment

was terminated when the test section was plugged due to the salt deposition and the pressure relief valve, just after the main pump, opened due to excessive pressure. Pure water was then pumped through the metering pump to dissolve the salt deposited on the tube walls. During the experiment, due to the salt deposition, a pressure increase at the inlet of the test section was noticed. The reactors were set to a temperature of about 5-10°C lower than the test section temperature. The pressure at the outlet of the test section remained constant thus indicating that nearly all the deposition was taking place in the test section.

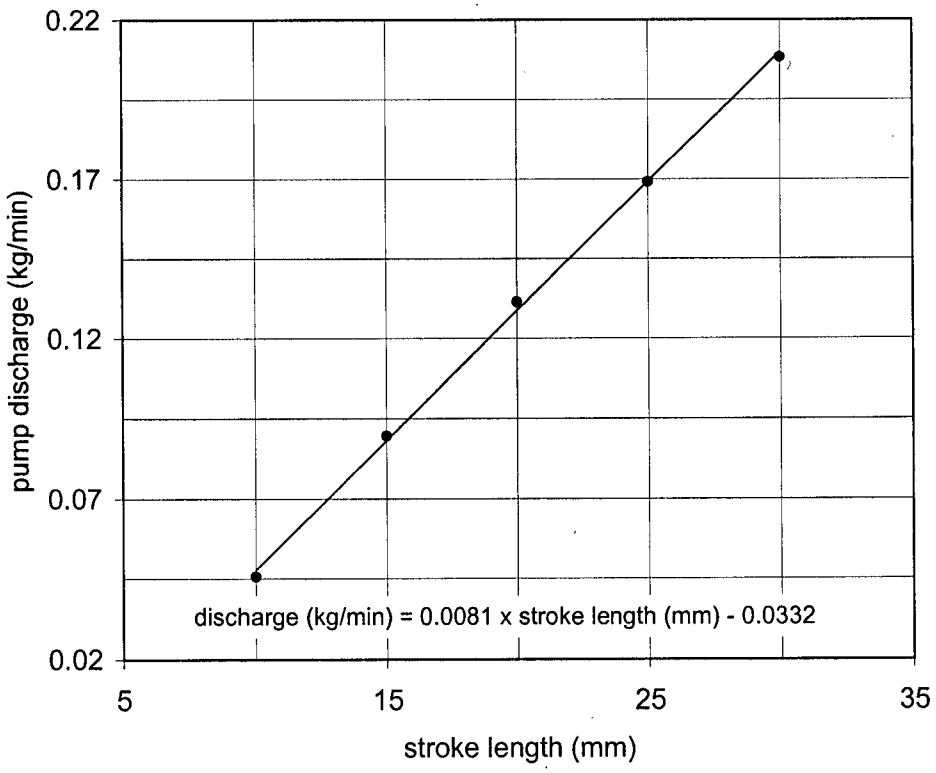

Figure 5.2: Metering pump calibration at 24.7 MPa

5.2.3 Combined heterogeneous and homogeneous nucleation experiments (unheated test section)

For this type of experiments, a similar procedure was followed as mentioned in the last section. However, in order to reduce heterogeneous nucleation, the test section was not heated in these experiments. This set of experiments was carried out to check if the net salt deposition could be further reduced by reducing heterogeneous nucleation. Some sample experiments from each of the above three types of experiments are discussed below.

5.3 Results and discussion

Results of salt deposition experiments performed are discussed below. The test section outer surface temperature was measured during the deposition process. The temperature measurement locations discussed in this chapter are of thermocouple locations mentioned in Table 3.1.

5.3.1 Heterogeneous nucleation

As mentioned earlier, such experiments could not be run for more than 30 minutes and the experiments had to be terminated due to excessive pre-heater surface temperature and/or pressure. The salt deposition rate, among other parameters, depended on the salt solution concentration and how fast the solubility was decreasing along the length of the tube. The surface temperature in the pre-heaters, which were at higher power input compared to the test section, increased quite rapidly due to the deposition of salt. However, there are not many thermocouples on the surface of pre-heaters and the temperatures over their entire length could not be measured. The test section surface temperature rise for a sample experiment (Experiment C1, see Table 4.1 for details) is shown in Fig. 5.3. The flow rate in this run was 0.66 kg/min with a Na_2CO_3 concentration of 0.19 wt.% in the influent tank. Thus the salt delivery rate at the system inlet was 1.25 g/min.

Based on the assumption that the salt solution leaving every section is at its saturation limit corresponding to the section temperature, the fluid entering the test section would be at the saturation limit corresponding to the pre-heater 2 temperature. The fluid salt concentration entering the test section was thus 0.018 wt.% and the actual salt delivery rate at the inlet of the test section would have been 0.12 g/min.

After operating for 15 minutes, a pressure increase of about 70 kPa was noticed at the inlet of the test section. However, it is to be noted that for this type of experiment, major deposition was taking place in the pre-heaters and the pressure at the inlet of the pre-heaters was not logged during the experiment. A monotonic increase in test section surface temperature was observed which indicated a steady buildup of salt on the tube surface. The concentration of salt leaving the system was also constant and thus all salt above the solubility limit was depositing on the heat transfer surface. Thus the ratio of salt concentration in the effluent to the saturation limit was 1.

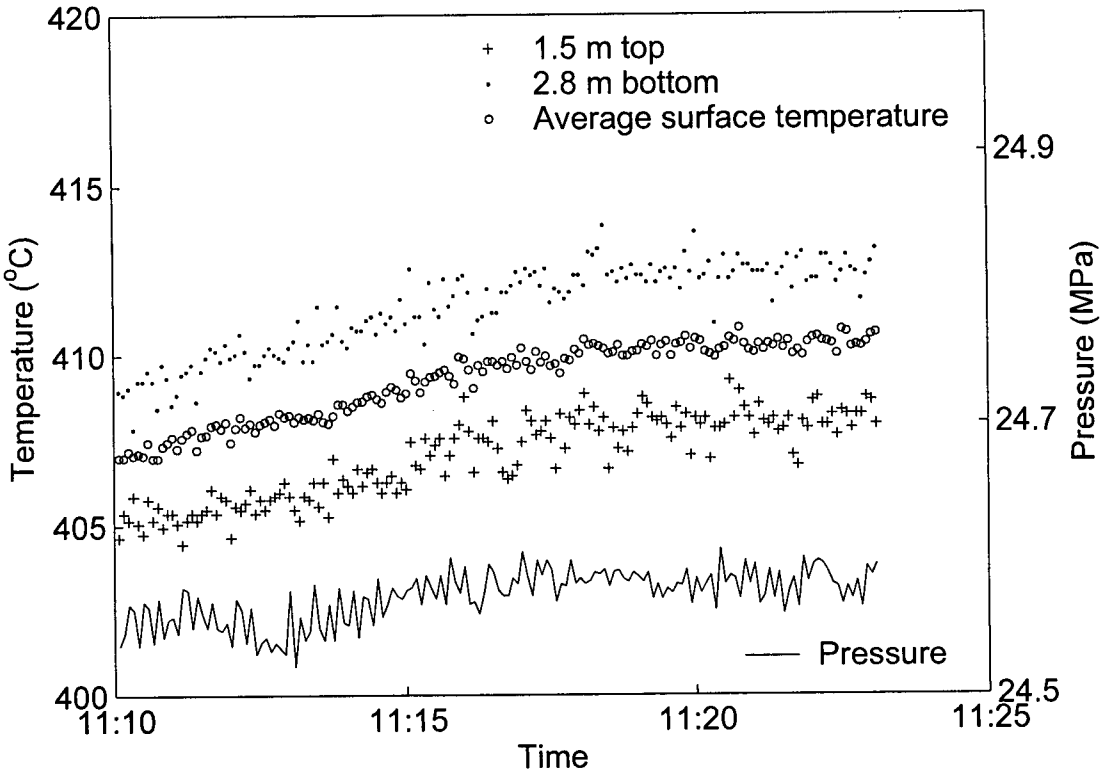

Figure 5.3: Temperature and pressure behavior for the heterogeneous nucleation run

5.3.2 Combined heterogeneous and homogeneous nucleation (heated test section)

These experiments were carried out to reduce the net salt deposition rate in order to increase the duration before the experiment had to be terminated due to either excessive surface temperature and/or pressure. In other words a higher ratio of salt concentration in the effluent to the saturation limit, compared to the experiments discussed in the last section, was desired. A sample experiment (Experiment 11, see Table A.1 for details) is shown in Fig. 5.4.

The flow rate of pure water from the main pump was 1.2 kg/min. The metering pump was set to 10% of this flow rate and was injecting salt solution in the pure water stream. Thus the total flow rate in the test section was 1.32 kg/min with a salt concentration of 0.1 wt.% at the test section inlet. The salt delivery rate at the inlet of the test section would thus be 1.32 g/min. The temperature of pure water at the outlet of pre-heater 2 was maintained at 415°C. The system was operated for about 90 minutes before the run was terminated, due to excessive pressure at the inlet of the test section. However, pressure at the outlet of the test section remained con-

stant through out the run, indicating all deposition was taking place in the test section.

It can be observed that the temperature rise (due to the salt deposition) was not continuous. The average clean test section inner-surface temperature was about 396°C. A temperature rise of about 12°C was noticed at the 0.15 m location in about fifteen minutes and then the surface temperature decreased suddenly. This indicated that the deposited salt layer was removed at the end of the cycle. This cycle was repeated nine or ten times during the 90-minute run. It seems that the salt was depositing and then at the end of the cycle the salt layer was removed due to excessive upstream pressure. During the period when pressure was increasing, the fluid temperature at the exit of pre-heater 2 also increased thus indicating a *plug*-like condition. During the run, the effluent conductivity fluctuated, indicating the salt deposition and removal were taking place in the system. At the 0.61 m location, three such cycles were observed but at the end of each cycle the temperature did not drop all the way to the clean surface condition, thus the salt layer was only partially removed. There was a steady temperature rise noticed at locations after 1.5 m and no sudden removal of deposit occurred. The thermocouple at the 1.5 m location showed a temperature increase of about 18°C over the 90 minutes of operation. Similarly at the 2.8 m location the temperature increased steadily by about 8°C. The system pressure relief valves were set to a pressure of about 29 MPa and the experiment was terminated when the pressure relief valve opened. The heaters were then turned off and the flow from the metering pump was then switched to pure water, to dissolve the salt deposit, in order to clean the system.

The deposition-removal cycles were studied by observing temperatures at different locations. In all of these cycles, the temperature at the 0.15 m location showed a different trend as compared to temperatures at downstream locations. When it was close to plugging the pressure and the pre-heater 2 temperature increased very quickly and only the thermocouple at 0.15 m behaved in the same manner. The temperatures at later locations either remained the same or reduced until the plug was removed and then a sudden increase in surface temperature was noticed. Thus the location of the plug was just after the 0.15 m location. Another observation was that after the salt was removed from the 0.15 m location, no sudden temperature increase was noticed at the downstream locations. Thus the removed salt layer was not sticking at downstream locations in the test section.

During the time when salt solution was being passed through the system, the effluent was collected in a tank. The salt concentration in the effluent tank was 0.075 wt.%. The saturation limit corresponding to the test section temperature was 0.018 wt.%. The ratio of effluent concentration and saturation limit is thus 4.2, which is four times higher as compared to the pure heterogeneous case. Thus due to homogeneous nucleation more salt was able to flow through the system and resulted in longer running time before

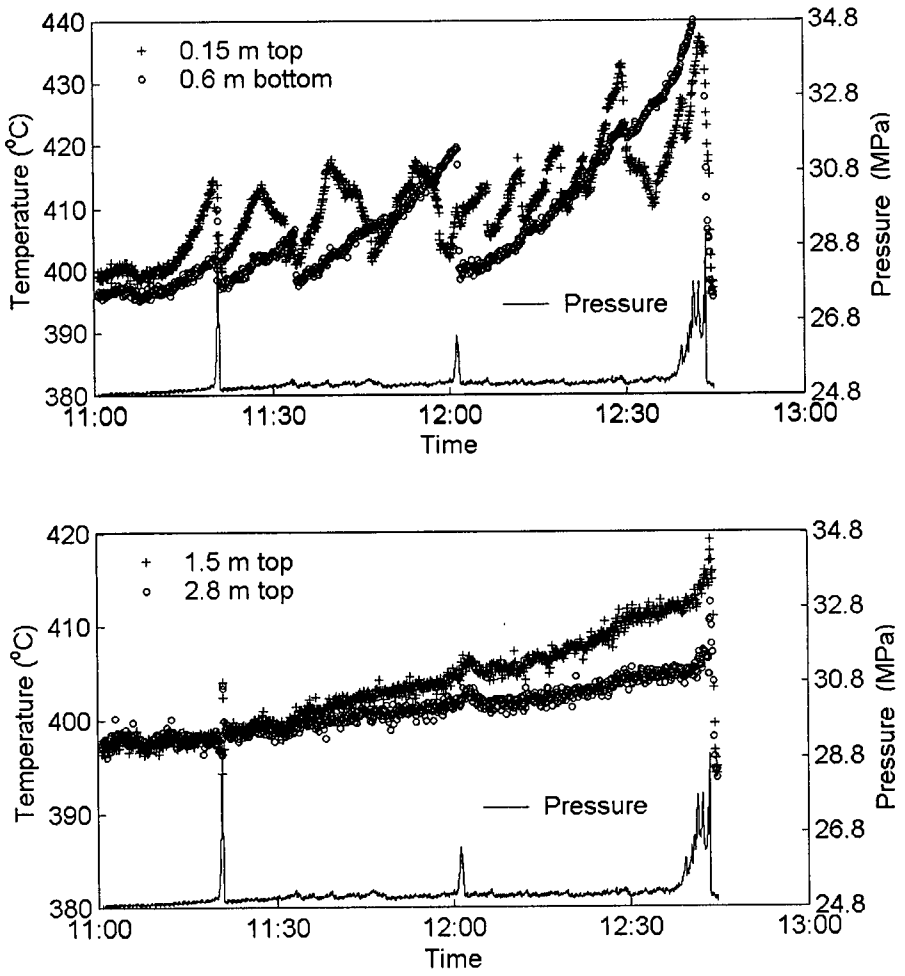

Figure 5.4: Temperature and pressure behavior for the combined homogeneous and heterogeneous nucleation run (heated test section)

the experiment had to be terminated.

5.3.3 Combined heterogeneous and homogeneous nucleation experiments (unheated test section)

These runs were made to further reduce the salt deposition such that more salt flowed through the system. The test section was not heated in these runs. Details of a sample experiment (Experiment 10, see Table A.1 for details) from this set of experiments are discussed below.

The total flow rate for this run was 1.32 kg/min. The salt delivery rate at the inlet of the test section would thus be 1.32 g/min. The average clean test section inner-surface

temperature was about 396°C and bulk fluid temperature leaving the test section was 394°C. The bulk fluid temperature at the end of the long reactor sections, which were also not heated, was 383°C. Thus a temperature drop of about 11°C was noticed due to heat losses. While the salt was being deposited, the surface temperature dropped due to the insulating salt layer. This is different compared to the other runs in which the surface temperature increased since the test section was being heated in those cases.

A number of deposition-removal cycles were noticed as shown in Fig. 5.5. At the 0.15 m location, there were about 10 of these cycles and at the 0.6 m location three such cycles occurred with temperature reducing back to clean surface conditions, thus indicating that all of the deposit was being removed. Furthermore, a small pressure increase was enough to remove the deposit, as observed from the pressure behavior in Fig. 5.5. One such cycle was observed at the 0.96 m location. During the 90 minute run the temperature at the 2.8 m location remained constant thus there was no deposition at that location. There was a pressure drop of only 138 kPa over the test section and pressure at the end of the test section remained constant. Due to this small pressure drop across the deposit, the bulk fluid temperature at pre-heater 2 outlet did not increase during the deposition process. It can therefore be concluded that no major plug was occurring in the test section. The run was terminated after running for 75 minutes.

The salt concentration at the inlet of the test section was 0.1 wt.%. During the time when salt solution was being passed through the system, the effluent was collected in a tank and the effluent salt concentration was 0.09 wt.%. The saturation limit corresponding to the average clean test section inner-surface temperature was 0.018 wt.%. For this type of experiments with unheated test secion, the surface temperature was calculated as the average surface temperatures at the first few locations in the test section. The ratio of concentration in tank and saturation limit for this run was 5, which is even higher than the last type of experiments. Thus more salt was able to flow through the system thereby increasing the time before the system plugged. Table 5.1 shows a comparison of these three types of Na_2CO_3 nucleation experiments.

5.4 Conclusion

Three types of Na_2CO_3 deposition, on the heat transfer surface at SCWO conditions, have been studied in this chapter. In the presence of pure crystalline fouling (due to heterogeneous nucleation) of salt on the tube surface, the fluid leaving the tube was at the saturation limit corresponding to the surface temperature and all the undissolved salt stuck to the tube wall. The system could not be run for more than 30 minutes for typical SCWO conditions and periodic removal of deposition needed to be done to operate the system. However if the salt was made to nucleate in the bulk fluid, the

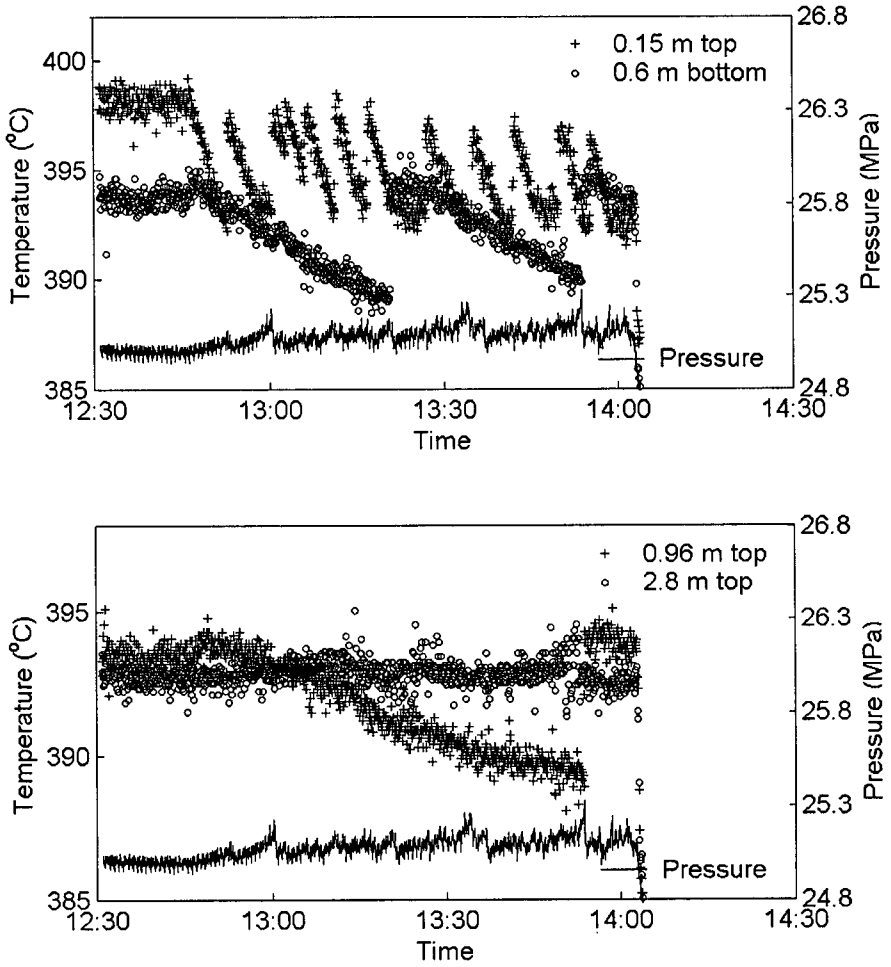

Figure 5.5: Temperature and pressure behavior for the combined heterogeneous and homogeneous nucleation run (unheated test section)

net deposition rate of the salt on the tube surface was reduced and the SCWO system could operate for a longer period of time. For a run in which both heterogeneous and homogeneous nucleation of salt was occurring the heated test section plugged after 90 minutes of operation. Salt concentration leaving the test section was four times higher than the saturation limit. The net deposition rate was further reduced when combined heterogeneous and homogeneous nucleation was occurring in unheated test section.

For an actual SCWO plant, this means that the waste treatment could be carried out for a longer period of time. The fouling of pre-heaters could be eliminated in this manner, since only water (and oxygen) would be flowing through them. Once the required fluid temperature was achieved at the end of the pre-heater sections, the waste could then be injected thereby encouraging homogeneous nucleation. The inor-

Table 5.1: Comparison of the three types of Na_2CO_3 nucleation experiments, C_o/C_{sat} is the ratio of effluent salt concentration to saturation concentration

Experiment type	Salt delivery rate (g/min)	C_o/C_{sat}	Comments
Heterogeneous nucleation only	1.25	1	Expected time to terminate experiment about 20-30 minutes.
Homogeneous and heterogeneous nucleation (heated test section)	1.32	4.2	Plugged after 90 minutes.
Homogeneous and heterogeneous nucleation (unheated test section)	1.32	5.0	No sign of plugging after 75 minutes.

ganics nucleated in this manner are thus more likely to flow through the tubular reactor.

The third type of experiment discussed in this chapter showed that the net deposition rate is further reduced if the section after mixing chamber was not heated. It is worth mentioning that the fouling mitigation method used is irrespective of the salt. It was noticed that almost all of the salt deposited within the test section with most of it immediately after the point of injection. Thus if the problem of plugging occurs during the process, the deposited salt has to be removed from only this short length of the reactor tube. This can be achieved online by mechanical means [19] & [36]. In this type of experiment a temperature drop of less than 15°C was noticed over the 140-m long unheated reactor. During the treatment of actual waste, which is an exothermic reaction, this temperature drop will be further reduced; thus the reaction should be self-sustaining. Otherwise, some fuel may be added, in the aqueous waste, which oxidizes and produces heat enabling the reaction to be self-sustainable. Since the reactor wall may not be heated in this case, therefore heterogeneous nucleation would be reduced.

Chapter 6

Collection and Analysis of Na_2CO_3 and Na_2SO_4 Deposits

6.1 Salt-deposit preservation procedure

Pure crystalline deposits and combined crystalline & particulate deposits have been collected for Scanning Electron Microscope (SEM) and Energy Dispersive X-ray (EDX) analysis. The sample collection of the deposits has been made possible using the nitrogen purging technique. The problem encountered in preserving a salt deposit on a tube surface is that the salt dissolves back into the fluid, when the heaters are shut off to cool down the system. This is due to the solubility characteristics of the salts. A nitrogen purge procedure, to preserve the sample for examination, was thus developed. As mentioned earlier, the inner diameter of the test section tube is 6.2 mm. A stainless steel tube of 6 mm outer diameter and 1 mm thickness was inserted into the first half of the test section. The tube-insert was used to collect salt deposits and was weighed before and after the salt deposition experiment. The schematic of the tube-insert is shown in Fig. 6.1. The inner radius of the tube-insert is r_c and the inner radius of the salt deposit is r_1.

The salt deposit collection procedure is discussed below. Homogeneous or heterogeneous nucleation experiments were performed following the procedures discussed in Section 5.2. The surface temperature of the test section was monitored while salt deposition was occurring on the inner surface of the tube-insert. The outer surface of the tube-insert was in contact with the inner surface of the test section tube. Once enough deposition had occurred, nitrogen gas at high pressure was inserted using the gas booster pump shown in Figs. 3.1 & 5.1. A back pressure regulator at the outlet of the booster pump was set to a pressure 1-3 MPa higher than the system pressure. The flow from the main pump into the system was reduced gradually using the by-pass mechanism while the gas flow rate was being increased. In case of the homogeneous nucleation type experiments, the metering pump was shut off. After a short time the fluid from the

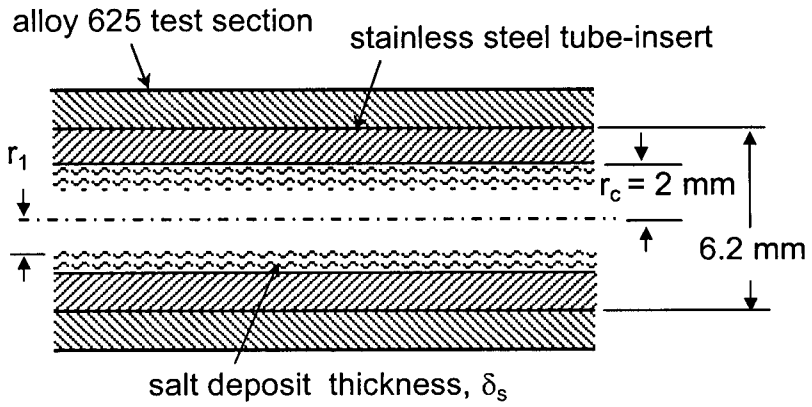

Figure 6.1: Schematic of the tube-insert

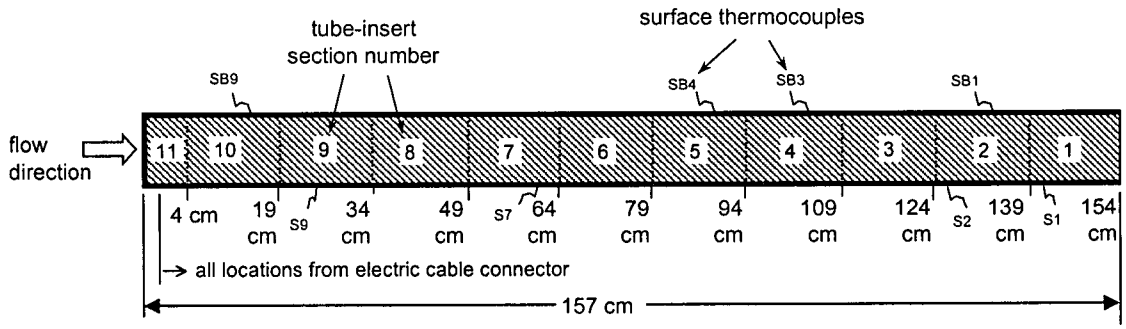

Figure 6.2: Location of tube-insert sections with respect to the thermocouples location

main pump was fully diverted back to the influent tank and only nitrogen gas flowed through the system. This procedure took about 20-30 sec to complete and after the liquid was completely purged from the system, the nitrogen flow rate was gradually reduced. The system was then de-pressurized and the test section dismantled to remove the tube-insert. The orientation of the insert in the test section was noted and it was again weighed to determine the weight of the salt deposit in the tube-insert. The insert was then cut into 15 cm long sections for SEM and EDX analysis of the deposits. Figure 6.2 shows the schematic of the sections of the tube-insert and details of their location with respect to the thermocouples are mentioned in Table 6.1. The section numbers of the tube-insert start from the end of the tube-insert and the first section is the most downstream. As mentioned earlier, stainless steel rods were soldered to the test section tube for electric power cable connections as shown in Fig. 3.3. The thermocouple and section number locations are shown in Fig. 6.2 and the distances shown are from the downstream edge of the steel connector. The edge of the tube insert extends about 3 cm further to the left (upstream) from this reference.

Table 6.1: Thermocouple and tube-insert-section locations

Thermocouple number	Thermocouple location (cm)	Tube insert section number	Tube insert section location (cm)
		11	4
SB9, top	15	10	19
S9, bottom	25	9	34
		8	49
S7, bottom	61	7	64
		6	79
SB4, top	90	5	94
SB3, top	103	4	109
S2, bottom	125	3	124
SB1, top	132	2	139
S1, bottom	140	1	154

6.2 SEM and EDX analysis of Na_2CO_3 and Na_2SO_4 deposits

Scanning electron microscope (Hitachi 2000N) was used to study the structure of the deposits and elemental composition analysis of the deposit was carried out using an EDX spectrometer system. The EDX is able to distinguish between different elements present in a sample by analyzing the energy of the X-rays given off. The technique is atomic weight sensitive. Samples of the tube-insert sections were mounted in the desired orientation and placed under vacuum in the SEM for analysis. It is worth mentioning that whereas EDX is quite reliable for qualitative analysis, the concentrations of the elements can not be measured with high accuracy. The error in measured concentration could be as high as 10 wt.% even for a well prepared sample. The EDX analysis of the deposit samples were basically carried out to determine the elements present in the deposits. The elemental analysis of standard Na_2CO_3 salt is shown in Fig. 6.3. Experiments have been performed to collect and analyze Na_2CO_3 and Na_2SO_4 deposits. Details of sample experiments are mentioned in Table 6.2. The details include the bulk fluid temperatures at the inlet and outlet of the test section. For the combined homogeneous & heterogeneous nucleation experiments the test section inlet temperature was the temperature of the pure water before the salt solution was injected into this stream. In order to determine the heat input, the fluid enthalpies at the test section inlet and outlet were used. For the combined heterogeneous & homogeneous nucleation experiments the fluid enthalpy at the inlet of the test section was determined from an experiment performed on May 26, 2003. The system was operated without fluid injected into the mixing-tee. The test section inlet temperature was set to the required

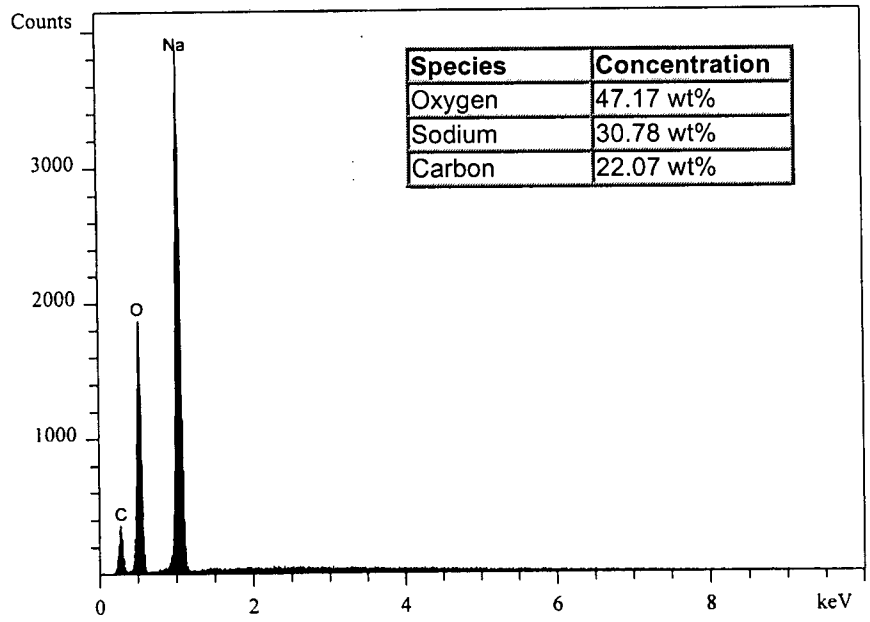

Figure 6.3: Elemental composition analysis of standard Na_2CO_3 salt

mixed stream temperature and flow rate. The fluid enthalpy at the end of test section was then determined for certain heat inputs to the test section. The SEM photographs and results of elemental analysis for the two different types of deposits are discussed below.

6.2.1 Pure crystalline fouling deposits of Na_2CO_3

The first salt-deposit collection run was performed without the tube-insert to confirm that deposits can be preserved on the tube surface using the nitrogen purging technique. In all the later salt-deposit collection experiments, a tube-insert was used. In this experiment the system pressure was 24.8 MPa and was the heterogeneous type nucleation experiment with Na_2CO_3. The flow rate was set to 0.74 kg/min and a 0.035 wt.% Na_2CO_3 solution was used. Fluid temperatures at the inlet and outlet of the test section were 393 and 438°C respectively and remained almost constant during the experiment. The maximum test section surface temperature was about 461°C. The test section was dismantled after the experiment and a small sample of deposit was scraped off the tube surface for analysis. The scraped sample was weighed. The remaining deposits on the first half of the test section were dissolved by passing distilled water through the tube and the salt concentration in the collected wash was measured to calculate the mass of salt deposited in the first half of the test section. Figure 6.4 shows the SEM image of Na_2CO_3 scraped from the test section after a heterogeneous nucleation experiment (Experiment SEM-1) and its elemental analysis is shown in Fig.

Table 6.2: Details of experiments performed to collect salt deposits

Experiment date	Experiment reference	Salt and type of nucleation	Bulk fluid temperatures (°C)		Salt concentration at test section inlet (wt.%)	Heat input to the first half of the test section (kW)	Salt collected in the first half of the test section (g)
			Test section inlet	Test section outlet			
March 11, 2003	SEM-1	Na_2CO_3, heterogeneous	393	438	0.021	0.3	4
March 31, 2003	SEM-3	Na_2CO_3, homogeneous & heterogeneous	415[a]	395	0.1	0.29	9.8
April 12, 2003	SEM-4	Na_2CO_3, heterogeneous	397	445	0.017	2.2	9.5
July 23, 2004	SEM-6	Na_2SO_4, homogeneous & heterogeneous	415[a]	395	0.1	0.29	8.6
August 06, 2004	SEM-7	Na_2SO_4, heterogeneous	388	412	0.001	2.3	3.5

[a] for the combined nucleation experiments, this is the temperature of pure water before mixing with the salt solution

6.5. The major elements found are sodium, carbon and oxygen. Long Na_2CO_3 crystals can be seen from the SEM photograph.

The scale analysis of another heterogeneous nucleation type experiment, SEM-4 is discussed now. This was performed with a tube-insert in the first half of test section on which the Na_2CO_3 scale was collected for analysis. The flow rate was set to 0.78 kg/min and 0.035 wt.% solution of Na_2CO_3 was passed through the system at a pressure of 24.5 MPa. The tube-insert was weighed after the experiment and the mass of deposit collected on the tube-insert was found to be 9.5 g. The tube-insert was cut into 15 cm long sections for scale analysis. Fig. 6.6 shows the photograph taken from insert-section 6 which was about 79 cm from the inlet of the tube-insert. A small portion of the tube can be seen on the top of the photograph and long crystals of Na_2CO_3 are also visible. These crystals seem to be nucleating from the tube surface (heterogeneous nucleation) and grew toward the center of the tube during the fouling process, resulting in a crystalline scale. A larger view of insert-section 2, showing almost the full cross section of the tube can be seen in Fig. 6.7. The location of this section was further downstream to the section shown in Fig. 6.6. The scale deposit can be seen on the inner surface of the tube and is of almost uniform thickness. Figure 6.8 shows a magnified view of the deposit. Again long salt crystals are observed, which nucleated from the tube surface and grew towards the center of the tube quite similar to the crystals seen

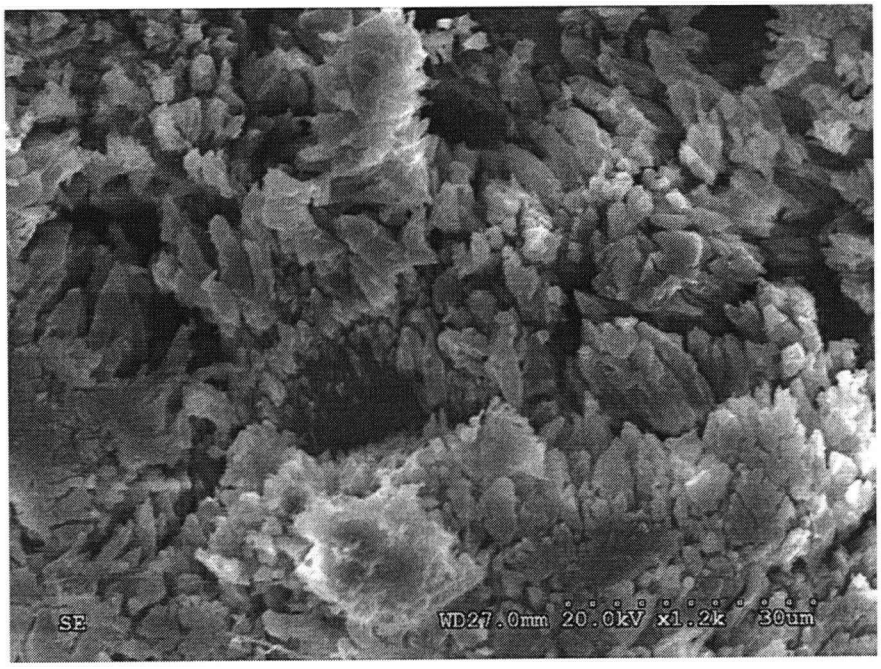

Figure 6.4: SEM photograph of the Na_2CO_3 deposition on test section wall due to heterogeneous nucleation (Experiment SEM-1)

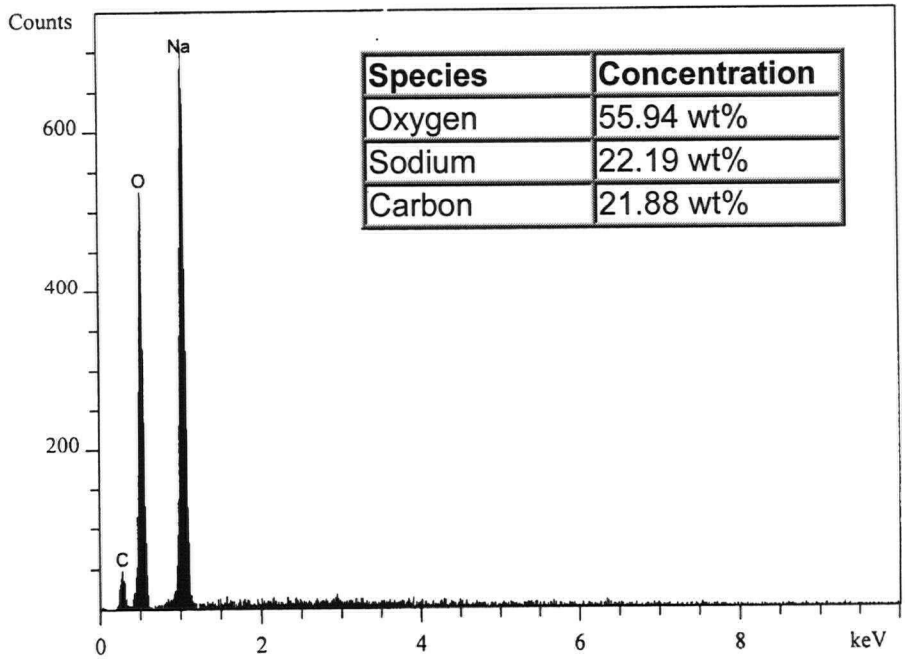

Figure 6.5: Elemental composition analysis of Na_2CO_3 deposit for the heterogeneous nucleation (Experiment SEM-1)

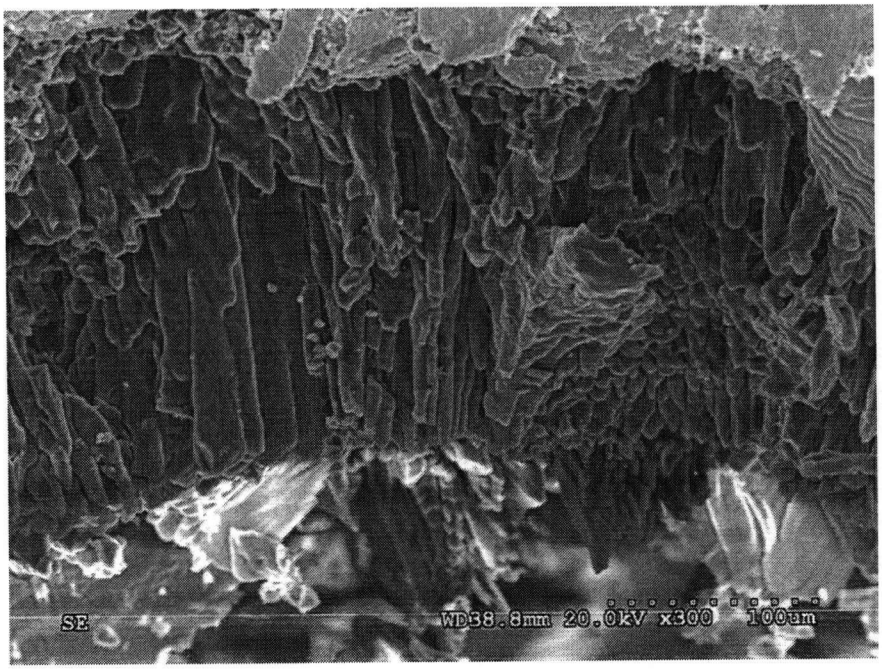

Figure 6.6: SEM photograph of the Na_2CO_3 deposition on test section wall due to heterogeneous nucleation at 79 cm location (Experiment SEM-4)

in the insert-section 6. Photographs of other sections showing deposits of Na_2CO_3 are shown in Appendix B.1.

6.2.2 Combined crystalline and particulate fouling deposits of Na_2CO_3

In this experiment (SEM-3), salt solution was injected into the supercritical water just before the beginning of the test section. The total flow rate was 1 kg/min with the main pump set to 0.9 kg/min. The system pressure was 24.6 MPa. About 9.8 g of deposits were collected after purging the system. Results of Na_2CO_3 deposit analysis of a combined homogeneous-heterogeneous type nucleation experiment performed on March 31, 2003 are discussed below. The elemental concentration analysis carried out with the EDX is shown in Fig. 6.9. Sodium, carbon and oxygen are the major constituents with concentration quite similar to that found in the deposits of experiments discussed in Section 6.2.1. Figure 6.10 shows the cross section of the insert-section 4 located at about 109 cm from the inlet of the tube-insert. Again the deposition is quite uniform all over the inner surface of the tube. However instead of long crystals, the deposit consisted of small particles. It seems that these salt particles nucleated in the bulk fluid (homogeneous nucleation) and deposited on the tube surface. The structure of this particulate fouling deposit was thus found to be different from that of crystalline

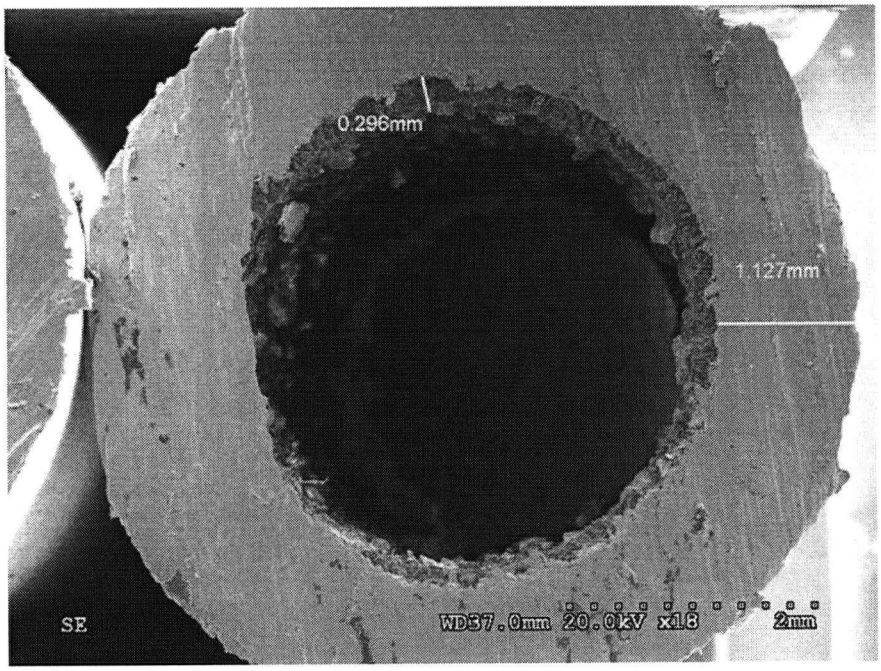

Figure 6.7: SEM photograph of the Na_2CO_3 deposition on test section wall due to heterogeneous nucleation at 139 cm location (Experiment SEM-4)

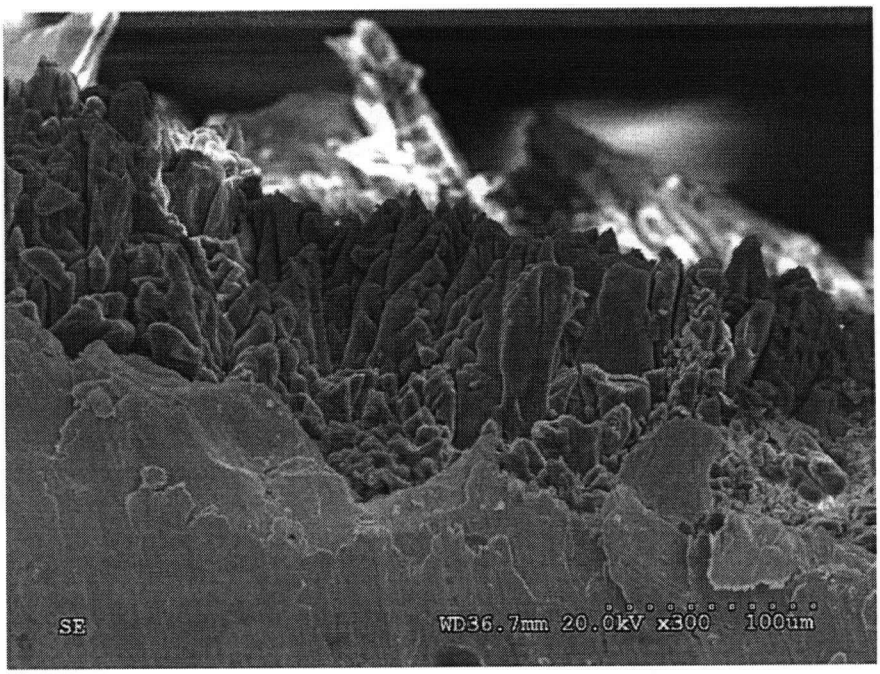

Figure 6.8: SEM photograph of the Na_2CO_3 deposition on test section wall due to heterogeneous nucleation at 139 cm location (Experiment SEM-4)

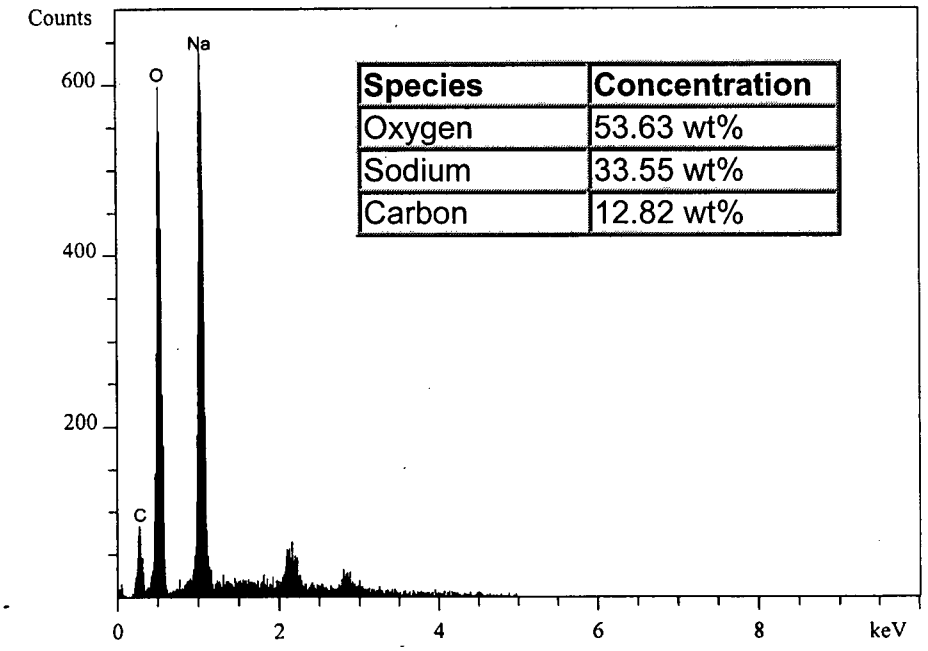

Figure 6.9: Elemental composition analysis of Na_2CO_3 deposit for the combined homogeneous & heterogeneous nucleation (Experiment SEM-3)

fouling deposits discussed in Section 6.2.1. It is worth mentioning that the magnification of this photograph is same as that of Figs. 6.6 & 6.8. Since the test section was heated, at some insert sections heterogeneous nucleation deposits were also observed with particle deposition. The photographs of the other sections are shown in Appendix B.1.

6.2.3 Pure crystalline fouling deposits of Na_2SO_4

Some of the SEM photographs of SEM-7 experiment, performed to study crystalline fouling structure are discussed below. The flow rate was 0.76 kg/min and 0.02 wt.% Na_2SO_4 salt solution was used. The system pressure was set at 24.6 MPa. About 3.5 g of salt deposits were collected on the tube insert. Figures 6.12-6.14 show the Na_2SO_4 crystals on the tube-insert surface. These crystal shapes are quite similar to those of the Na_2CO_3 crystals seen in Fig. 6.6. At some locations, these crystals formed a solid-fused layer as seen in Figs 6.13 & 6.14. At tube-insert section location of 154 cm some needle shaped crystals were observed grown out of the solid deposit as shown in Fig. 6.12. However, it can be observed that heterogeneous nucleation leads to crystal-deposition, which has a very dense structure and is quite different from the particulate fouling deposits of Na_2SO_4 particles as shown in Fig. 6.18.

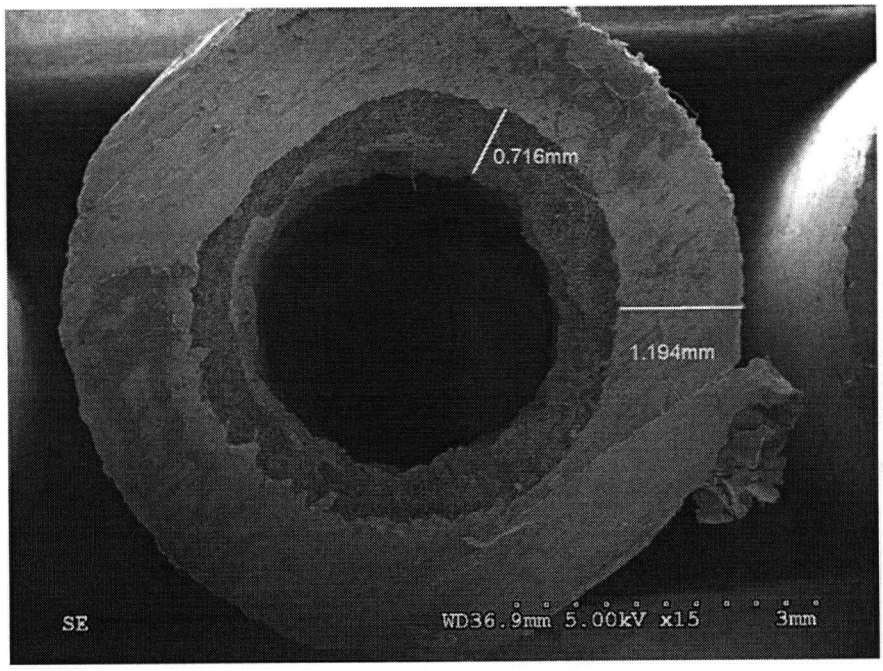

Figure 6.10: SEM photograph of the Na_2CO_3 deposit due to combined homogeneous-heterogeneous nucleation at 109 cm location (Experiment SEM-3)

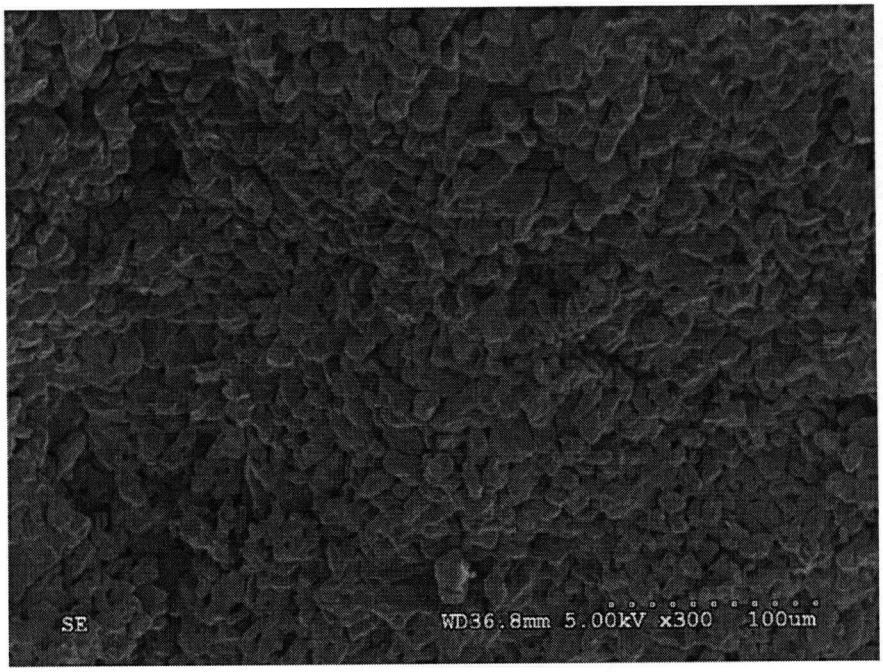

Figure 6.11: SEM photograph of the Na_2CO_3 deposit due to combined homogeneous-heterogeneous nucleation at 109 cm location (Experiment SEM-3)

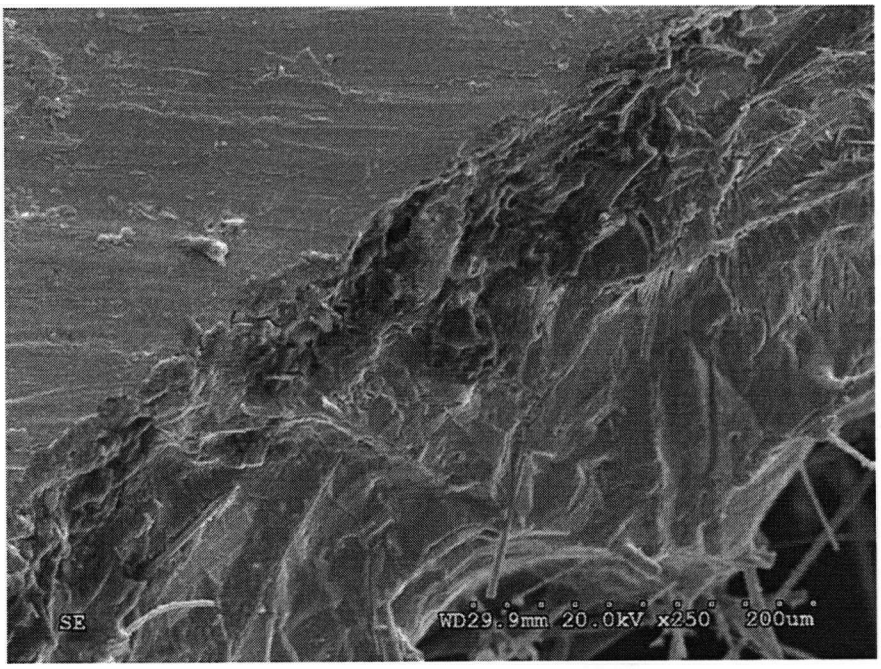

Figure 6.12: SEM photograph of the Na_2SO_4 deposit due to heterogeneous nucleation at 154 cm location (Experiment SEM-7)

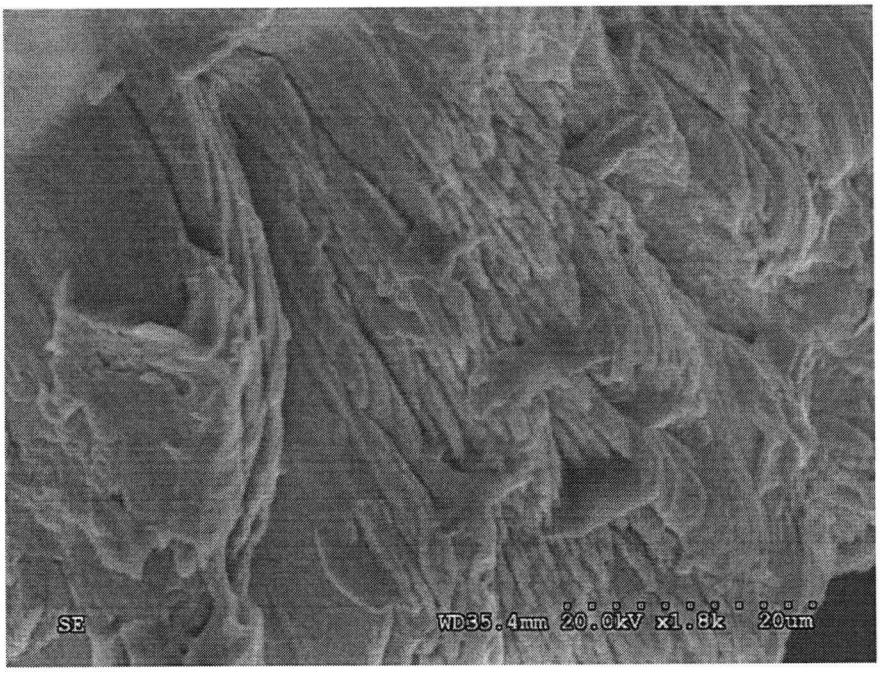

Figure 6.13: SEM photograph of the Na_2SO_4 deposit due to heterogeneous nucleation at 127 cm location (Experiment SEM-7)

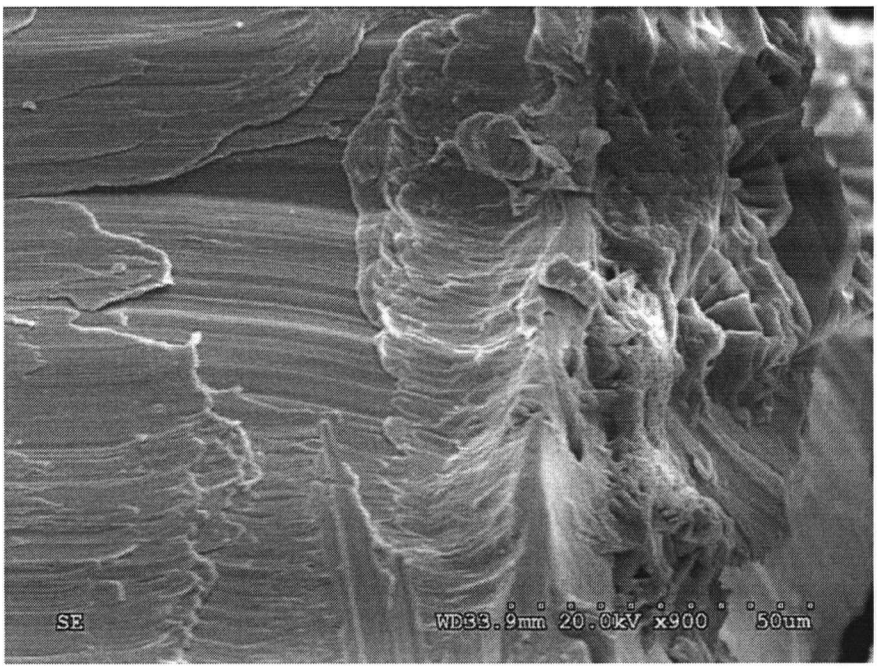

Figure 6.14: SEM photograph of the Na_2SO_4 deposit due to heterogeneous nucleation at 97 cm location (Experiment SEM-7)

6.2.4 Combined crystalline and particulate fouling deposits of Na_2SO_4

Results of a combined homogeneous & heterogeneous type nucleation experiment (SEM-6) are discussed in this section. The main pump flow rate was 0.85 kg/min and the total flow rate, including that of the metering pump, was 0.94 kg/min. The system pressure was set at 24.4 MPa. The weight of salt collected on the tube-insert was 8.9 g. The EDX analysis of the deposit sample is shown in Fig. 6.15. The major elements are sodium, sulfur and oxygen. Some of SEM photographs of experiments performed on July 23, 2003 are discussed in this section. The rest of SEM photographs of Na_2SO_4 deposits are included in Appendix B. This run (SEM-6) was performed following the procedure of the Na_2CO_3 homogeneous & heterogeneous type nucleation experiments. However, when the test section was dismantled, it was noticed that the Na_2SO_4 deposits were weaker than the Na_2CO_3 deposits. At some regions the salt-deposit was washed off making the tube inner surface visible. Some of the deposits did not cling on to the tube surface and fell off when the sections of the tube-insert were being cut. Thus some of the insert sections did not have a uniformly thick deposit layer. The test section in the experiment was heated and combined crystalline and particulate fouling deposits were expected and are observed in Figs. 6.16 & 6.17. These photographs are of the insert-section 1 which is the last section of the tube-insert. At the same location Na_2SO_4 particulate deposition was also observed and is shown in Fig. 6.18.

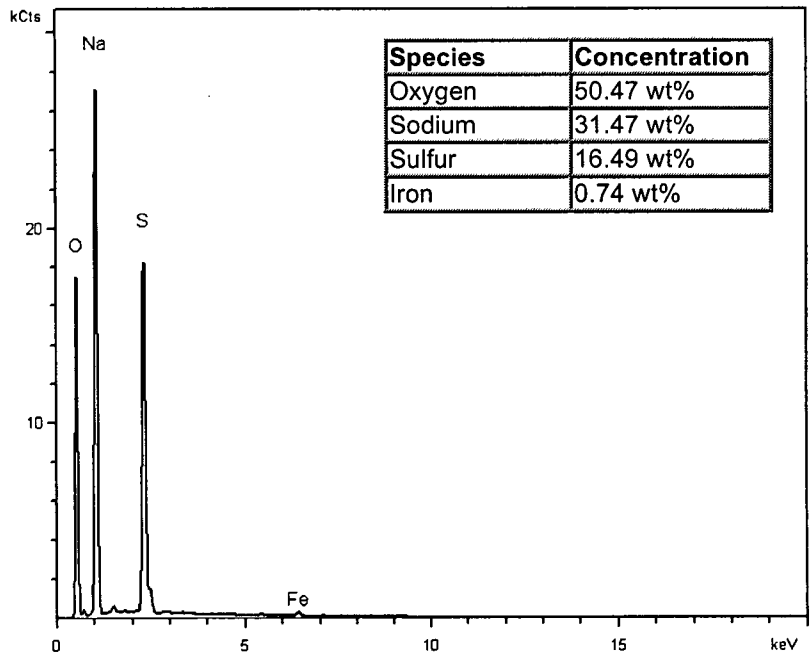

Figure 6.15: Elemental composition analysis of Na_2SO_4 deposit for the combined homogeneous-heterogeneous nucleation experiment (Experiment SEM-6)

Some of these deposited particles are hollow and their shape is quite different from the Na_2CO_3 particles deposits discussed above. Such particles, among other sections, were also noticed at the insert-section 7 and can be observed in Fig. 6.19.

6.3 Thermal conductivity of the Na_2CO_3 deposit

The thermal conductivity of the Na_2CO_3 deposit was determined using the known heat input, thickness of the salt deposit and the measured temperature difference across the deposit layer. The bulk fluid temperature at the outlet of the test section remained constant during the deposition process. Therefore, it can be assumed that the salt-deposit inner surface temperature was very close to the clean tube inner surface temperature. The increase in the surface temperature due to deposition is thus the temperature difference across the deposit layer, ΔT_s. The following relation was then used to determine the thermal conductivity of the salt-deposit, k_d (W/mK) [73].

$$k_d = \frac{Q \ln(r_c/r_1)}{2\pi L \, \Delta T_s} \tag{6.1}$$

The details of these salt-deposit analysis experiments are mentioned in Tables 6.2, 6.3 & 6.4. The deposit layer thickness was measured from the SEM photographs at each

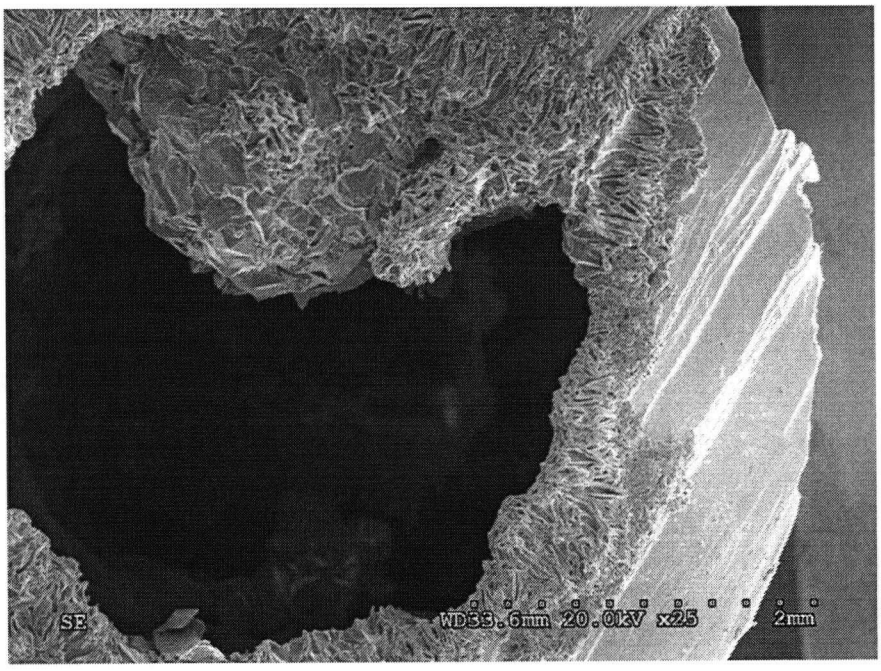

Figure 6.16: SEM photograph of the Na_2SO_4 deposit due to combined homogeneous-heterogeneous nucleation at 154 cm location (Experiment SEM-6)

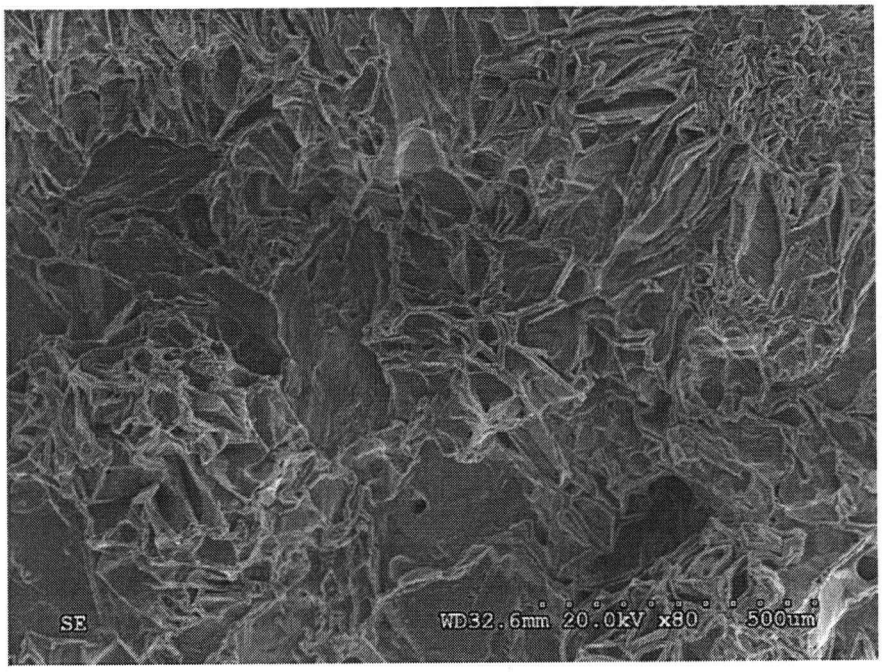

Figure 6.17: SEM photograph of the Na_2SO_4 deposit due to combined homogeneous-heterogeneous nucleation at 154 cm location, mostly crystalline (Experiment SEM-6)

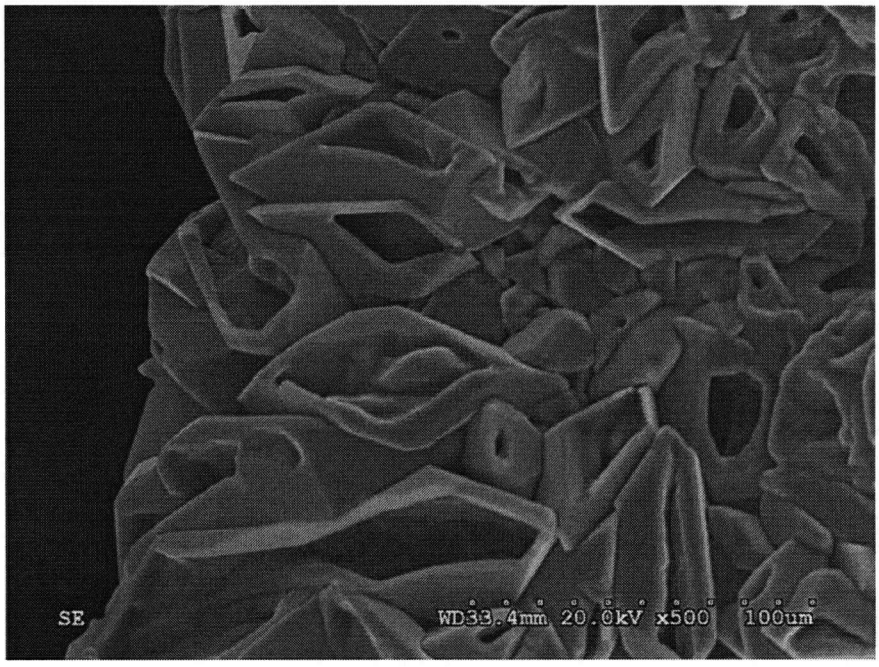

Figure 6.18: SEM photograph of the Na_2SO_4 deposit due to combined homogeneous-heterogeneous nucleation at 154 cm location, mostly particulate (Experiment SEM-6)

tube-insert section. However, the thermocouple locations did not coincide with the tube-insert section locations. The deposit layer thickness, at each thermocouple location, was thus interpolated using the layer thicknesses at section locations. Thus inner radius of deposit layer, r_1 at each thermocouple location could be inferred. Thermal conductivity of the Na_2CO_3 deposits, at various locations, was then calculated using Eq. 6.1 and is tabulated for different locations for both heterogeneous and combined heterogeneous & homogeneous type nucleation experiments. The deposition rate for the heterogeneous nucleation type experiment was found to be quite steady. However, for the combined heterogeneous & homogeneous type experiments, instead of a steady scale growth, deposition and removal of salt-deposit was noticed. Thus the thickness of deposit observed in the combined heterogeneous & homogeneous experiments might not necessarily correspond to the temperature rise before the liquid was purged from the system. Therefore, the thermal conductivity values of the heterogeneous nucleation type experiments should be relatively more accurate.

For Na_2SO_4, since the salt deposit was partially washed off the tube and some later fell off while cutting the sections, the actual deposit layer thickness could not be measured. Therefore, thermal conductivity of the Na_2SO_4 deposit was not calculated.

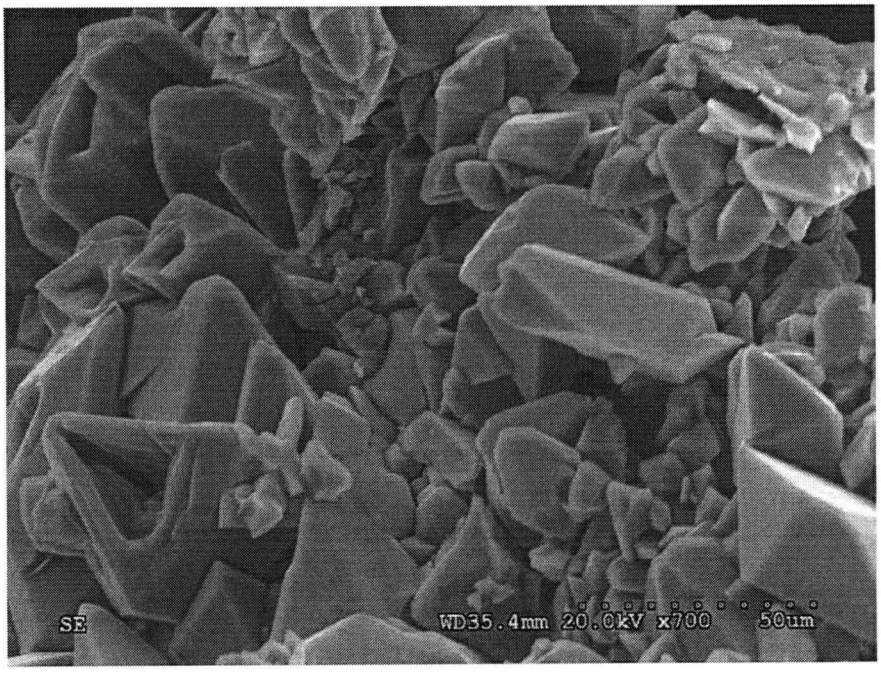

Figure 6.19: SEM photograph of the Na_2SO_4 deposit due to combined homogeneous-heterogeneous nucleation at 64 cm location, mostly particulate (Experiment SEM-6)

Table 6.3: Details of Na_2CO_3 scale thickness and surface temperature rise due to deposition for the heterogeneous nucleation experiment (Experiment SEM-4)

Section number	Section location	Measured salt deposit thickness	Thermo-couple location	Interpolated salt deposit thickness at thermocouple location	Test section clean outer surface temperature	Test section outer surface temperature with salt deposit	Surface temperature rise	Thermal conductivity of Na_2CO_3 deposit
	(cm)	(mm)	(cm)	(mm)	(°C)	(°C)	(°C)	(W/mK)
10	19	0	15	0	466	488.21	22.21	
8	49	0.364	25	0.182	469.4	510.2	40.8	0.44
7	64	0.406	61	0.406	488.05	549.05	61	0.69
6	79	0.361	90.2	0.333	490.39	546.89	56.5	0.60
4	109	0.305	103	0.305	475.7	550.64	74.94	0.41
2	139	0.296	132.8	0.296	509.76	550.46	40.7	0.73

Table 6.4: Details of Na_2CO_3 deposit thickness and surface temperature rise due to deposition for the combined homogeneous-heterogeneous nucleation experiment (Experiment SEM-3)

Section number	Section location	Measured salt deposit thickness	Thermo-couple location	Interpolated salt deposit thickness at thermocouple location	Test section clean outer surface temperature	Test section outer surface temperature with salt deposit	Surface temperature rise	Thermal conductivity of Na_2CO_3 deposit
	(cm)	(mm)	(cm)	(mm)	(°C)	(°C)	(°C)	(W/mK)
10	19	0	15	0	402.01	413.91	11.9	
8	49	0.1	25	0.05	402.9	412.6	9.7	0.07
6	79	0.218	61	0.159	405.45	420.65	15.2	0.14
4	109	0.716	90.2	0.467	410.19	434.69	24.5	0.28
2	139	0.59	103	0.716	403.52	435.62	32.1	0.36
1	154	0.66	132.8	0.59	407.96	438.46	30.5	0.30

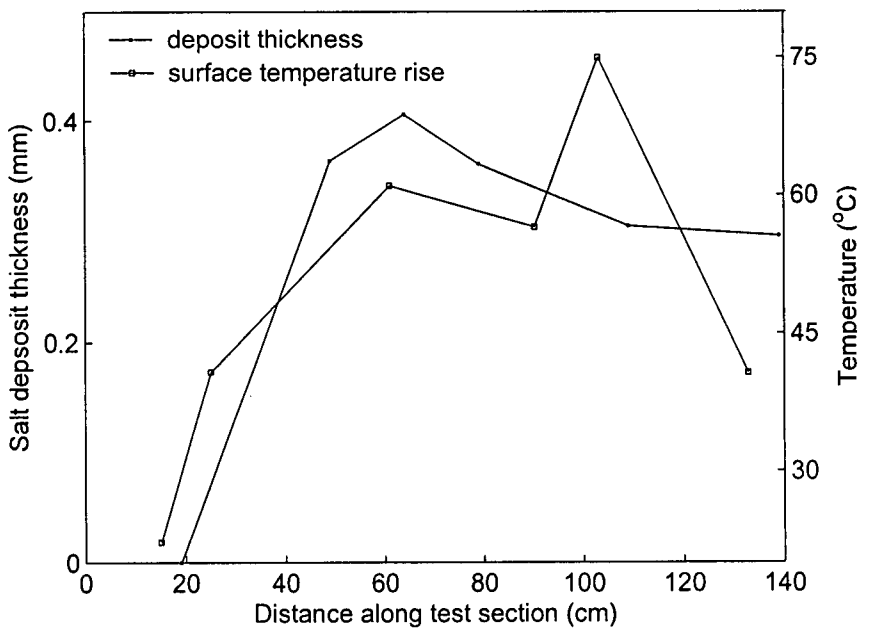

Figure 6.20: Na_2CO_3 deposit thickness and surface temperature rise along the test section for the heterogeneous nucleation (Experiment SEM-4)

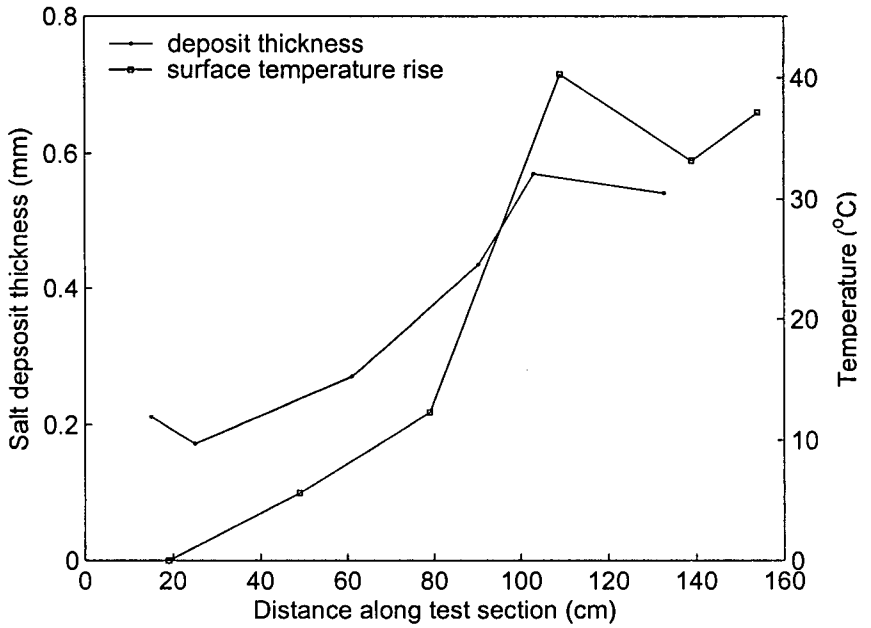

Figure 6.21: Na_2CO_3 deposit thickness and surface temperature rise along the test section for the combined homogeneous-heterogeneous nucleation (Experiment SEM-3)

6.4 Conclusion

A novel procedure has been developed to preserve salt deposits on the heat transfer surface for analysis. The Na_2CO_3 fouling deposits were harder to remove compared to the Na_2SO_4 deposits. It was noticed, at some locations of the tube insert, the cross section of the Na_2SO_4 deposits was not uniform. Furthermore, some of these deposits fell off the insert tube later, during sectioning of the tube insert.

For both Na_2CO_3 and Na_2SO_4, heterogeneous nucleation experiments led to pure crystalline scale. Long salt crystals were seen in the SEM photographs, which nucleated on the insert-tube surface and grew in the direction of the center of the tube. These deposits were found to be very dense and hard to remove. On the other hand, instead of long crystals, salt particles were seen in the combined crystalline-particulate fouling experiments. These particulate deposits were relatively less dense but at some locations deposits were quite similar to the pure crystalline scale. Since the pure crystalline deposits were found to be dense and strong, a steady increase in surface temperature was noticed in the heterogeneous type experiments. This was due to the steady growth of salt-scale layer on the tube surface. On the other hand, for the combined heterogeneous-homogeneous nucleation experiments the tube surface temperature, near the salt solution injection location, increased gradually and then

decreased suddenly. Thus both salt deposition and removal processes were occurring in the combined homogeneous type experiments. This was due to the less dense and easy to remove particulate-crystalline fouling deposits, which washed off when a certain deposit-layer thickness was achieved.

The deposit buildup of the combined crystalline-particulate fouling deposits was unsteady compared to a steady growth of pure crystalline scale. Therefore the thickness of salt deposit layer determined from the SEM photographs of pure crystalline scale is likely to be more accurate compared to the combined deposits. Thermal conductivity of the deposits has been inferred from the thickness of the deposit layer. Hence the thermal conductivity values calculated for the pure crystalline scale is more accurate compared to the other type of deposits. Elemental analysis of the scale was carried out using the EDX. Major elements found in Na_2CO_3 deposits were sodium, carbon and oxygen. Sodium, sulfur and oxygen were the major components of Na_2SO_4 deposits with less than 1 wt.% of iron.

Chapter 7

Modeling: Mixing, Heat and Mass Transfer

7.1 Introduction

In Chapter 5 experiments were discussed, in which a warm salt solution stream was mixed in a stream of supercritical water. When the salt solution is exposed to the hot supercritical water in the mixing-tee section, depending on the salt concentration and temperature, the solution may become supersaturated and homogeneous nucleation of salt particles may occur. The salt depositing on the tube surface would thus be due to the precipitation of the salt particles nucleated in the bulk fluid and salt molecules crystallizing on the tube surface. This chapter discusses the modeling of the mixing process, heat and mass transfer, to determine the salt deposition at various test section locations. Homogeneous nucleation of salt particles, their growth and coagulation, deposition of salt particles and salt molecules on the tube surface have been modeled. Pure water thermodynamic properties [74] were used. Similarly pure water transport properties were used to model the salt solution.

7.2 Salt particle nucleation

Formation of salt particles in the bulk fluid can be described as a homogeneous nucleation process. Salt enters the mixing-tee dissolved in a warm liquid stream and mixes with supercritical water. During the mixing process, rapid heating of the salt solution occurs and the salt solubility falls orders of magnitude leading to a high supersaturation values, causing rapid nucleation and growth of salt particles in the supercritical water. The number of salt particles nucleated can be determined by the classical theory of nucleation. There are other complicated theories which involve the direct generation of nuclei from ions [75]. However, they provide qualitatively similar results, and required information on the liquid-solid surface energy is still

unavailable [76]. Therefore, the desirability of selecting such sophisticated theories for modeling practical problems may be questioned, thus favoring the selection of classical theory.

In the classical theory of nucleation, the free energy required to form a cluster of molecules from the liquid (dissolved) phase is first determined. Both the energy from the phase change due to crystallization and energy required to form the surface of the cluster are considered. Once the energy for the formation of the surface is overcome, the nucleus will form, but it may redissolve. The free energy increases from zero to a maximum value at which the nucleus will not redissolve. So if the radii of a nucleus is less than r^*, it will have to either continue to grow toward a critical radius or to dissociate into its component molecules. This will continue until the size of the nucleus (or the number of molecules in the nucleus) reaches a critical value [77]. The nucleation rate per unit volume per unit time is then given by the following relation [78]:

$$J = A \exp\left[\frac{-16\pi\gamma^3 V_m^2}{3b_k^2 T^2 (\ln S)^2}\right] \tag{7.1}$$

in which A is the maximum number of particles that can nucleate and is usually taken to be $10^{30}\ \frac{particles}{cm^3 sec}$ [78], γ is the surface tension, V_m is the volume of the salt molecule, b_k is the Boltzmann's constant ($1.3805 \times 10^{-23} J/K$), T is the temperature and S is the degree of salt saturation. The fluid temperature, T and dissolved salt mass fraction, C are used to calculate the degree of saturation i.e., $S = \frac{C}{C_{sat}}$. The saturation limit, C_{sat} is determined from the correlations developed for Na_2CO_3 and Na_2SO_4 (Eqs. 4.13 & 4.14).

The effect of supersaturation on the nucleation rate is highly dependent on the interfacial energy or surface tension. The difficulty of obtaining a value of this energy by direct measurement is a major problem with the homogeneous theory of nucleation. For the majority of salts the value of surface tension reported is between 60×10^{-3} and 150×10^{-3} N/m [78]. If homogeneous nucleation occurs, many sub-micron particles are formed. Nucleation rate is highly dependent on temperature and supersaturation. The critical radius of nucleated particles can be determined as: [78] & [77].

$$r^* = \frac{2\gamma V_m}{b_k T \ln S} \tag{7.2}$$

If a warm salt solution stream, with salt mass fraction C_A at temperature T_A, is mixed with a pure hot water stream at temperature T_B then the mixture fraction Z may be defined as $Z = 0$, for pure water stream and $Z = 1$, for salt solution stream. For typical experimental conditions the salt particle nucleation rate can be determined as a function of mixture fraction Z and is shown in Fig. 7.1 for Na_2CO_3. The total salt mass fraction, C_T and salt mass fraction at saturated conditions, C_{sat} are also shown as a function of mixture fraction. For the conditions shown, the pseudo-critical temperature is about 384°C and for higher temperatures, there is a sudden drop in salt solubility.

The critical mixture fraction Z_{crit} i.e., corresponding to the pseudo-critical temperature is about 0.28. Salt particle nucleation occurs for supersaturated conditions and the rate of particles nucleated is maximum around mixture fraction value of about 0.14.

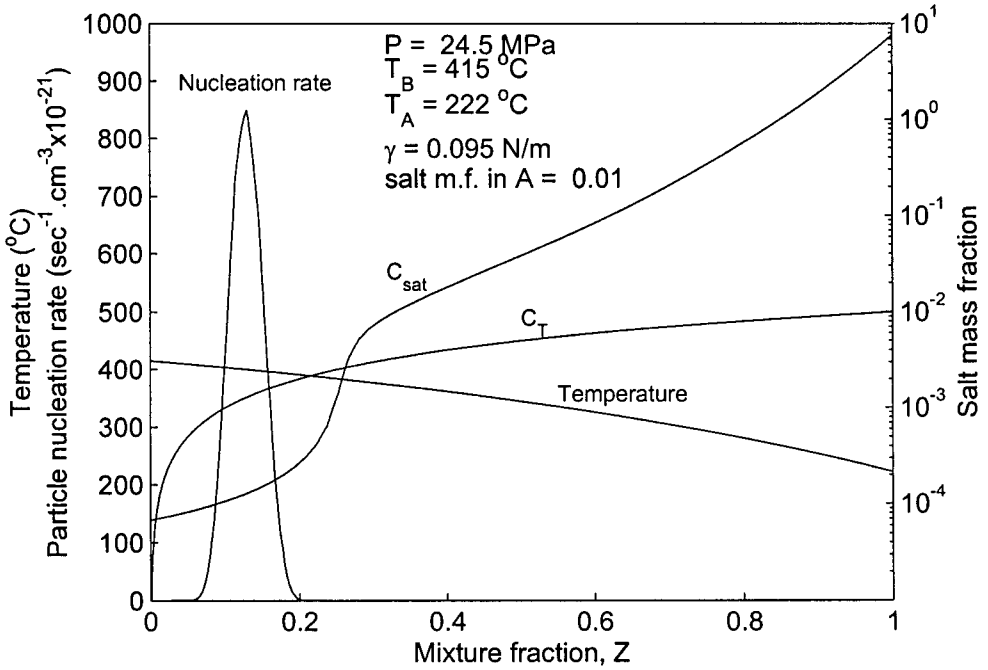

Figure 7.1: Salt particle nucleation rate, mass fraction and fluid temperature as a function of mixture fraction

7.2.1 Growth of nucleated particles

The nucleated particles grow by condensation of additional molecules from the fluid to solid phase, or by collision and coagulation with other particles. Diffusion limited growth is considered in this section. The rate at which the additional molecules diffuse towards the salt particle is given by the Maxwell equation [79]:

$$J_m = 2\pi \mathcal{D}_m d_p \left(N_m - N_m\left(sat\right)\right) \tag{7.3}$$

where N_m is the number of molecules per unit volume, $N_m\left(sat\right)$ is at saturation conditions and d_p is the diameter of the salt particle. $\mathcal{D}_m$ is the molecular diffusion coefficient and can be determined from the Stokes-Einstein relation [70] using the molecule diameter d_m.

$$\mathcal{D}_m = \frac{b_k T}{3\pi \mu d_m} \tag{7.4}$$

7.2.2 Coagulation of the particles

Brownian coagulation is considered in this study and turbulent induced coagulation has been neglected. The coagulation coefficient, K_{12} (m^3/sec) is calculated for two equal-sized particles and is given by: [79]

$$K_{12} = \frac{8b_k T}{3\mu} \tag{7.5}$$

From the discrete coagulation equation, the change in particles concentration with time is given by: [79]

$$\frac{\mathrm{d}N_p}{\mathrm{d}t} = -\frac{1}{2}K_{12}N_p^2(t) \tag{7.6}$$

If $N_p(0) = N_0$, then the solution of Eq. 7.6 is:

$$N_p(t) = \frac{N_0}{1 + t/\tau_c} \tag{7.7}$$

where $\tau_c = 2/K_{12}N_0$.

7.3 Modeling of the mixing process

The modeling of the mixing process of two streams along the test section is discussed in this section. A warm stream of salt solution, *stream A* was injected in the stream of pure supercritical water, *stream B*, in the mixing-tee. Flow rates of salt solution and pure water streams are $\dot{m}_A$ and $\dot{m}_B$ respectively. The exact location of the salt solution jet is not of interest here and transport of heat and mass to the wall is modeled using empirical transfer coefficients. Within the turbulent core of the pipe flow, some sort of closure model is needed to take into account the turbulent fluctuation correlations of concentrations and temperature. Due to this reason, commercially available CFD packages were not used for which it is hard to put a good closure model for turbulent fluctuations for temperature and salt concentration. To this end, a stochastic mixing process is developed that will approximate the length and timescale of turbulent flow. Recognizing that the initial trajectory of the salt solution is not to be modeled and the interest is only in closing the $\acute{C}$ and $\acute{T}$ fluctuations, the simulation treats the core flow as 1-D mixing process. Schematically, it can be shown as a flow between parallel plates, which is divided into slabs (cells). It is assumed that the salt solution is initially at the center of the tube surrounded by pure water. The salt solution has to move a distance equal to the tube radius, in the radial direction, to reach the tube surface. In order to determine the tube inner surface temperature and particle concentration at various test section locations, it is assumed that the fluid streams are flowing between

two parallel plates. The distance between the plates is equal to the test section inner diameter, d. Thus, if initially, the salt solution is in the center of the plates, it again has to move a distance equal to $d/2$, in the vertical direction, to reach the tube surface. The assumed flow in parallel plates is considered only to determine concentration of particles nucleated per unit time at each segment, the temperature and salt mass concentration in the cell at the edge of the salt deposition surface. The later modeling for that segment is carried out considering the actual circular tube geometry. The test section length, L is discretized into X number of segments such that each segment length $\Delta L = \frac{L}{X}$. The height of each segment is also discretized such that there are $m + n$ number of *cells*, each of height Δd and length ΔL. At the beginning of the mixing process, the salt solution is assumed to be sandwiched by the pure water cells as shown in Fig. 7.2. The number of cells in streams A and B are n and m respectively. The m:n ratio is determined from the desired $\dot{m}_B$:$\dot{m}_A$. The total number of cells in each segment are:

$$m + n = \frac{d}{\Delta d} \tag{7.8}$$

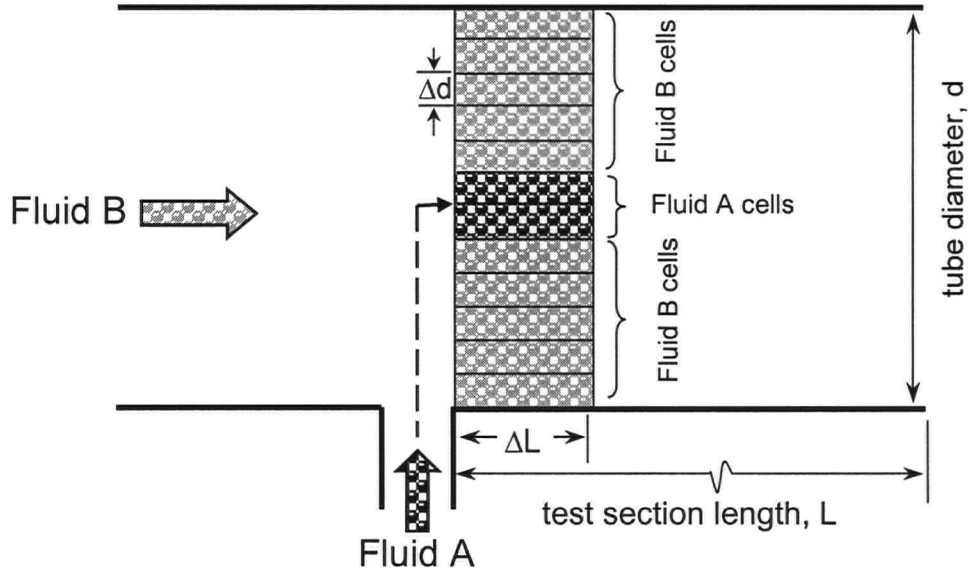

Figure 7.2: Schematic of the salt solution (*fluid A*) cells and pure water (*fluid B*) cells at the beginning of the mixing process

In each segment the fluid is assumed to comprise $R(m + n)$ number of fluid parcels such that there are R number of fluid parcels in each cell. The salt mass fraction and temperature of the fluid parcels are initialized with respect to their cell conditions. All fluid parcels move a vertical distance Δz in each ΔL. The cell height Δd is chosen such that while the fluid is moving through ΔL, each fluid parcel lands in another cell after moving a distance of Δz.

The radial distance Δz traveled by the fluid parcels is determined from the average dissipation rate of turbulent kinetic energy. For a circular tube geometry, the turbulent kinetic energy dissipation rate, $\epsilon = \frac{2fV^3}{d}$ [80] in which V is the mean fluid velocity and f is the friction factor, calculated from the following relation [81].

$$f = \left[1.8 \log\left(\frac{6.9}{Re_w} + \frac{\acute{\epsilon}}{3.7d}\right)^{1.11}\right]^{-2} \tag{7.9}$$

where Re_w is the Reynolds number corresponding to wall conditions and $\acute{\epsilon}$ is the tube surface roughness.

Using $L_o = d/2$ as the characteristic length, the velocity fluctuation can be calculated: $\acute{u} = (\epsilon L_o)^{1/3}$ [82]. The kinetic energy would thus be, $\mathbb{KE} = \frac{3}{2}\acute{u}^2$. The time taken by a fluid parcel to move a distance of L_o, in the radial direction, is the characteristic time. The characteristic time for turbulent diffusion is: [82]

$$\tau_D = \frac{L_o^2}{\mathcal{D}_T} \tag{7.10}$$

where $\mathcal{D}_T$ is the average turbulent diffusivity and is determined from the κ-ϵ model i.e., $\mathcal{D}_T = \frac{\nu_T}{Sc_T}$ [83]. Sc_T is the turbulent Schmidt number and is taken to be = 0.7 [80]. The turbulent viscosity, ν_T is calculated as $\nu_T = \frac{0.09\,\mathbb{KE}^2}{\epsilon}$ [82]. Thus the radial distance a fluid parcel moves in each segment ΔL is:

$$\Delta z = \sqrt{\mathcal{D}_T \frac{\Delta L}{V}} \tag{7.11}$$

The height of each cell, Δd is chosen such that the fluid parcel can land in a neighboring cell after moving a distance of Δz. Once Δd is computed, the total number of cells, $m+n$, can be determined from Eq. 7.8. In order to include the effects of fluctuations in cell temperature and salt concentration, due to turbulence, the fluid parcels move in a random direction, upward or downward. For each fluid parcel a randomly generated sign (+ or −) determines the direction in which the fluid parcel moves a distance of Δz. After each mixing step, the cell temperature, dissolved salt mass fraction and particulate salt mass deposition are updated using the mean salt mass fraction and temperature of the new parcels. The dissolved salt mass fraction and temperature at each cell can be used to determine the concentration of salt particles nucleated in each cell, as discussed in Section 7.2. The mass fractions of dissolved salt and particulate salt are required to determine the dissolved salt deposition rate (i.e., crystallization fouling) and salt particle deposition rate (i.e., particulate fouling) as discussed in Sections 7.5.1 and 7.5.2.

The characteristic time for turbulent diffusion is determined using Eq. 7.10. The axial length ΔL, is then calculated for this time and known flow velocity. Based on the

ratio of mass flow rates of streams A & B, minimum number of cells $(m+n)$ are determined. For a known tube inner diameter, the height of each cell Δd is calculated, which should be equal to the distance $\mathrm{d}z$, moved by the fluid parcels in each mixing time step. Thus for a given turbulent diffusivity, $\mathcal{D}_T$ the axial distance moved by the fluid $\mathrm{d}l$ is determined by the following relation:

$$\mathrm{d}l = \mathrm{d}z^2 \frac{V}{\mathcal{D}_T} \tag{7.12}$$

A mixing step occurs after every $\mathrm{d}l$ length along the test section.

7.4 Heat transfer calculation

As mentioned earlier two fluid streams are mixed in a mixing-tee at the test section inlet. The temperature of stream B, T_B is set such that supersaturation is achieved when stream A at temperature T_A and with salt concentration C_A is mixed in it. The enthalpy of the mixed stream and hence the mixed stream temperature can be determined for known mass flow rates of the streams.

The heat input to the test section is determined experimentally from the change in fluid enthalpy across the test section. A flow rate $\dot{m}$ is set with the injection port of the mixing-tee closed and test section fluid inlet temperature near the desired mixed stream temperature, T_1. The mass flow rate $\dot{m}$ is chosen such that:

$$\dot{m} = \dot{m}_A + \dot{m}_B \tag{7.13}$$

The heat supplied (W) to the test section would then be:

$$Q = \dot{m}(H_2 - H_1) \tag{7.14}$$

where H (J/kg) is the enthalpy of the fluid.

The schematic of the test section tube is shown in Fig. 7.3. Using Nusselt number correlations as discussed in Section 4.5, the heat transfer coefficient h can be determined. The heat transfer between the surface and the fluid occurs in the cell at the salt layer-solution interface (SLSI) surface. The SLSI surface temperature, T_s can be determined from the following relation:

$$\dot{m}_e \frac{\mathrm{d}H}{\mathrm{d}x} = h\pi d(T_s - \overline{T}_e)\frac{\acute{R}}{R} \tag{7.15}$$

where $\overline{T}_e$ is the average fluid temperature of the cell at the SLSI surface, $\acute{R}$ is the actual number of fluid parcels in that cell, R is the average number of fluid parcels in each cell and $\dot{m}_e$ is the fluid mass fluid rate through the cell next to the salt deposit

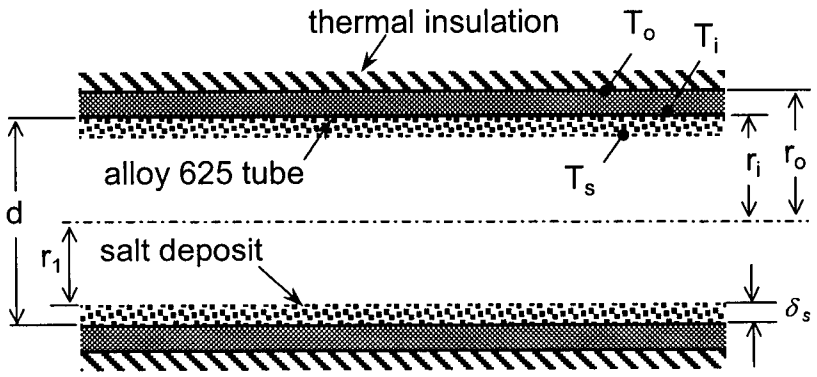

Figure 7.3: Temperature and radii schematic for the test section

surface. The actual number of parcels in each cell is not fixed. In Eq. 7.15, the mass flow rate is calculated from the actual mass of fluid parcels at the SLSI and a factor $\frac{\acute{R}}{R}$ is multiplied with the heat transfer rate to accommodate the fluctuations in the number of fluid parcels at SLSI.

If m_{salt} is the mass of salt present at the tube inner surface and assuming the density of deposit same as that of the salt, ρ_{salt}, the thickness of the deposit layer, $\delta_s = r_i - r_1$, can be calculated by determining r_1 as follows:

$$r_1 = \sqrt{r_i^2 - \frac{m_{salt}}{\pi \mathrm{d}x \rho_{salt}}} \tag{7.16}$$

For a known SLSI surface temperature, the tube surface temperatures are modeled using the radial heat conduction through the wall. Using the thermal conductivity of the salt deposit, k_d the tube inner surface temperature, T_i can be calculated from the following relation.

$$T_i = T_s + \frac{Q \ln(r_i/r_1)}{2\pi k_d L} \tag{7.17}$$

The differential equation for the heat conduction through the tube wall with internal heat generation $\dot{q}$ (W/m^3) is: [73]

$$\frac{1}{r}\frac{\mathrm{d}}{\mathrm{d}r}\left(r k_t \frac{\mathrm{d}T}{\mathrm{d}r}\right) + \dot{q} = 0 \tag{7.18}$$

Since the thermal conductivity of alloy 625 (tube material), k_t is a weak function of temperature, it can be assumed to be constant over the wall thickness. It is also assumed that the tube is perfectly insulated and the outer surface temperature is T_o. In order to solve the above second order differential equation, the two boundary conditions are; at the tube inner surface i.e., $r = r_i$, $T = T_i$ and at the tube outer surface i.e., $r = r_o$,

$dT/dr = 0$. Solving Eq. 7.18, the outer surface temperature, at a given T_i, can be determined from the following derived relation:

$$T_o = T_i + \frac{qr_i}{2k_t}\left[\frac{(r_i/r_o)^2 - \ln(r_i/r_o)^2 - 1}{1-(r_i/r_o)^2}\right] \tag{7.19}$$

7.5 Salt deposition

The salt has to transport from the bulk fluid before it can get deposited on the tube walls. The salt can reach the wall surface by deposition of *salt molecules* and/or by deposition of *salt particles*, which have nucleated in the bulk fluid.

7.5.1 Molecule deposition

The similarities of heat and mass transfer can be used to determine the mass transfer coefficient, h_m as discussed in Section 4.5. The molecular deposition rate is given by:

$$\dot{m}_m = h_m \pi d dx \rho_f \left(\overline{C} - C_s(sat)\right) \tag{7.20}$$

where $C_s(sat)$ is the saturated dissolved salt mass concentration at the fluid/deposit surface conditions, $\dot{m}_m$ (kg/sec) is the molecular deposition rate, $\overline{C}$ is the average dissolved salt mass fraction in the bulk fluid and is determined semi-implicitly as:

$$\overline{C} = \frac{C_{i+1} + C_i}{2} \tag{7.21}$$

7.5.2 Particle deposition

In order to calculate the deposition of particles that nucleated in the bulk fluid, the deposition velocity has to be determined. Papavergos and Hedley [84] studied the deposition of particles from a turbulent flow stream to adjacent surface. They did a comprehensive review of previous experiments mainly involving aerosol droplets entrained in duct air streams. Data for particle deposition in liquid streams would be more accurate but due to convenience and low cost, experiments are conducted for aerosol droplets. Furthermore, the data reviewed did not cover the variation in bulk and wall properties. Kostoglou and Karabelas [76] have reported using this deposition velocity for modeling deposition of lead sulfide particles in geothermal fluids. In the absence of data for deposition of particles in supercritical fluids, the results of the review were implemented in the current model. The proposed empirical relation to calculate the particle deposition velocity is: [84]

$$V_d = V_d^* U^* \tag{7.22}$$

V_d^* is the dimensionless salt deposition velocity determined as:

$$V_d^* = \begin{cases} 0.065Sc^{-0.667} & (\tau_p^+ < 0.2) \\ 3.5 \times 10^{-4}\tau_p^+ & (0.2 \leq \tau_p^+ \leq 20) \\ 0.18 & (\tau_p^+ > 20) \end{cases} \tag{7.23}$$

where τ_p^+ is the dimensionless particle relaxation time and is given by:

$$\tau_p^+ = \frac{\tau_p (U^*)^2}{\nu} \tag{7.24}$$

in which τ_p is the particle relaxation time which can be determined from the following relation using salt density ρ_{salt} and particle diameter d_p.

$$\tau_p = \frac{d_p^2 \rho_{salt}}{18\mu} \tag{7.25}$$

Also U^* is the wall friction velocity and is determined from the following relation:

$$U^* = \left(\frac{\tau_w}{\rho_w}\right)^{1/2} \tag{7.26}$$

where τ_w is the wall shear stress and is given by: $\tau_w = \rho_w V^2(\frac{f}{8})$.

For $\tau_p^+ < 0.2$, it is diffusion regime and the deposition velocity is considered as the mass transfer coefficient. For $0.2 \leq \tau_p^+ \leq 20$, it is inertia regime and the large particles have sufficient inertia to move through the viscous sub-layer. Finally for $\tau_p^+ > 20$, particle velocity toward the wall attains a similar magnitude to U^*. Stopping distance becomes the same order as the tube diameter. Effect of turbulent fluctuations on the particles is limited such that V_d^* becomes virtually constant. The particle deposition velocity, V_d can then be calculated using Eq. 7.22. Figure 7.4 shows the salt particle deposition velocity as a function of particle diameter for typical experimental conditions. The deposition velocity is determined for a fluid flow rate of 1.3 kg/min and salt deposition surface temperature of 400^oC at a system pressure of 24.5 MPa. The three regimes for calculating the deposition velocity are also shown. For the condition shown, the diffusion regime is for particle radius up to about 0.2 μm and the inertia regime extends to a particle radius of about 2 μm.

If C_{p_i} is the available mass concentration of particles in the bulk fluid for deposition and assuming the mass concentration of particles in fluid at the deposition surface is zero, the mass deposition rate of salt particles in a segment can be determined using the following relation:

$$\dot{m}_p = V_d \pi d \mathrm{d}x \rho_f \left(\frac{C_{p_{i+1}} + C_{p_i}}{2}\right) \tag{7.27}$$

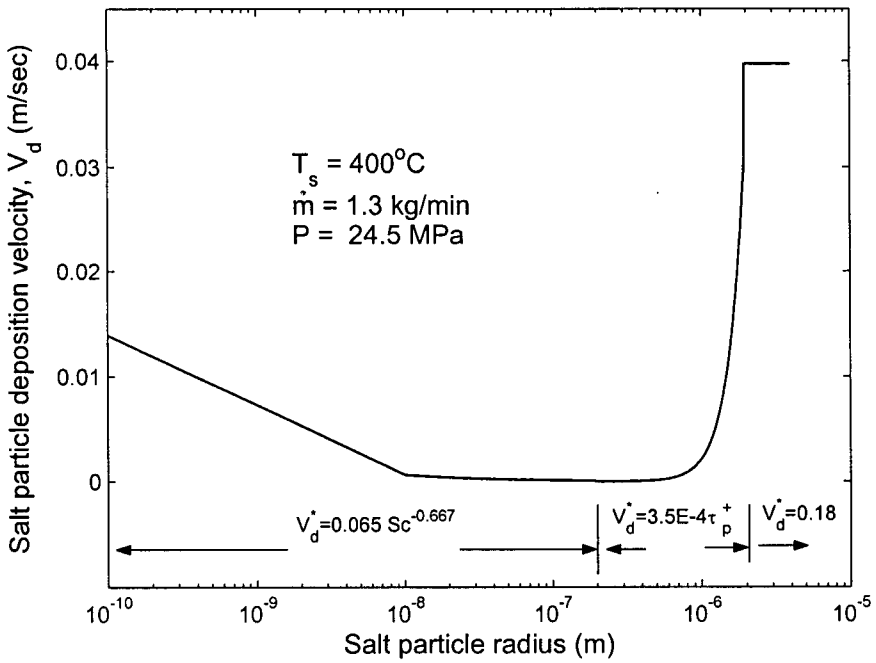

Figure 7.4: Salt particle deposition velocity vs particle radius

where $C_{p_{i+1}}$, the concentration of particles in the bulk after particle deposition can be determined as:

$$C_{p_{i+1}} = C_{p_i} - \frac{V_d \pi d \mathrm{d}x}{\dot{m}} \left(\frac{C_{p_{i+1}} + C_{p_i}}{2} \right) \tag{7.28}$$

7.6 Conservation equations

As mentioned earlier, heat transfer between the SLSI surface and the fluid occurs in the fluid cells at the surface. Equation 7.15 (mentioned again for completeness) was used to calculate the change in enthalpy.

$$\dot{m}_e \frac{\mathrm{d}H}{\mathrm{d}x} = h \pi d (T_s - \overline{T}_e) \frac{\acute{R}}{R} \tag{7.29}$$

After each mixing step, the mass of salt molecules and particulate salt deposited on the tube is removed from the cells at the fluid/salt deposit surface.

Conservation equations of salt mass fraction

For cells at the SLSI surface:

$$\dot{m}_e \frac{\mathrm{d}C_T}{\mathrm{d}x} = -h_m \pi d \rho_f (\overline{C_e} - C_s) \frac{\acute{R}}{R} - V_d \pi d \rho_f (\overline{C_{ep}} - C_{sp}) \frac{\acute{R}}{R} \tag{7.30}$$

The two terms on the right hand side of the above equation are for salt mass transfer due to molecule and particle deposition respectively. As mentioned earlier, the mass of salt deposited is removed from the cells next to the SLSI surface only in each integration step.

For bulk cells:

$$\dot{m}\frac{\mathrm{d}C_T}{\mathrm{d}x} = 0 \tag{7.31}$$

where h_m is the molecules mass transfer coefficient, V_d is the salt particle mass deposition coefficient, ρ_f is the cell fluid density, $\overline{C_e}$ & $\overline{C_{ep}}$ are the average dissolved salt and particulate salt mass fraction in the cell at the SLSI surface respectively. C_s and C_{sp} are the dissolved salt and particulate salt mass concentration at the salt deposit surface conditions. The particulate salt mass fraction at the salt deposition surface C_{sp}, is assumed to be zero. $\dot{m}_e$ and $\dot{m}$ are the fluid mass flow rate through the cells at the edge and the total fluid mass flow rate respectively.

Conservation equations of particulate salt mass fraction

For cells at the SLSI surface:

$$\dot{m}_e\frac{\mathrm{d}C_p}{\mathrm{d}x} = -V_d\pi d\rho_f(\overline{C_{ep}} - C_{sp})\frac{\acute{R}}{R} + Jm_{p^*}A_c + m_{p^1}N_p 2\pi\mathcal{D}_m(C - C_{sat})\frac{\rho_f}{\rho_{salt}} \tag{7.32}$$

For bulk cells:

$$\dot{m}\frac{\mathrm{d}C_p}{\mathrm{d}x} = Jm_{p^*}A_c + m_{p^1}N_p 2\pi\mathcal{D}_m(C - C_{sat})\frac{\rho_f}{\rho_{salt}} \tag{7.33}$$

where J is the rate of salt particles generated per unit volume and A_c is the cell cross sectional area. C and C_{sat} are the dissolved salt mass fraction and saturated salt mass fraction respectively. m_{p^*} and m_{p^1} are the mass of a nucleated particle and a grown particle respectively. The terms on the right hand side of the above equation are for the increase in particulate mass of salt due to salt particle nucleation and salt molecule condensation on salt particles respectively.

The number of particles nucleated and their size are determined as follows. Particle nucleation occurs in all cells with supersaturated conditions. The segment length $\mathrm{d}l$ is first determined as discussed in Section 7.3 and is divided into intermediate integration steps each $\mathrm{d}x$ long. Residence time $\mathrm{d}t$, for the integration step is then determined using the fluid velocity. Thus the number of particles nucleated per unit volume in each integration step is:

$$N_p = J\mathrm{d}t \tag{7.34}$$

The size of nucleated particles is determined using Eq. 7.2. In order to determine the increase in the size of the particle due to diffusion of salt molecules, the degree of

reaction α is first defined: [85]

$$\alpha = \frac{N_m - \acute{N}_m}{N_m - N_m\,(sat)} \tag{7.35}$$

α varies from 0→1, corresponding to time 0→∞. $\acute{N}_m$ is the dissolved salt molecule concentration in the cell and corresponds to α for an initial dissolved salt concentration of N_m. The growth of particle radius with time, r(t) is assumed to be: [85]

$$r(t) = r_f \alpha^{1/3} \tag{7.36}$$

This equation is valid for particles with morphologies close to spherical. r_f is the final particle radius and can be determined as: [85]

$$r_f = \left[\frac{(N_m - N_m\,(sat))\,V_m}{\frac{4}{3}\pi N_p}\right]^{1/3} \tag{7.37}$$

where N_p is the number of particles per unit volume. For bulk diffusion limited growth, the linear growth of the particle can be written as: [29] & [85]

$$\frac{\mathrm{d}r_p}{\mathrm{d}t} = \frac{V_m \mathcal{D}_m\,(N_m - N_m\,(sat))}{r_p} \tag{7.38}$$

Solving Eqs. 7.36-7.38:

$$\int_0^t \mathrm{d}t = K_D I_D \tag{7.39}$$

where

$$K_D = \left[48\pi^2 V_m N_p^2\,(N_m - N_m\,(sat))\right]^{-1/3} \mathcal{D}_m^{-1} \tag{7.40}$$

and

$$I_D = \int_0^\alpha \frac{\mathrm{d}\alpha}{\alpha^{1/3}(1-\alpha)} \tag{7.41}$$

Equation 7.39 can be solved, for a given residence time, to determine the extent of reaction, α. The growth of particle can then be calculated using Eqs. 7.36 & 7.37. Also the dissolved salt concentration after the growth of salt particles, $\acute{N}_m$ can be determined using Eq. 7.35 for known α. These particles grow with time and the particle size is determined using Eq. 7.36. Some of these particles deposit and the rest remain suspended in the fluid. The undeposited particles are considered to coagulate in the next segment length. The number of particles after coagulation is determined as discussed in Section 7.2.2. The diameter of the particles for deposition is determined to be the weighted average of the coagulated undeposited particles and the new particles nucleated & grown in the current segment. Assuming the concentration of particulate salt at SLSI is zero, the mass deposition of salt particles is determined as:

$$\dot{m}_p = V_d \pi d\mathrm{d}x \rho_f \left(\frac{C_{p_{i+1}} + C_{p_i}}{2}\right) \frac{\acute{R}}{R} \tag{7.42}$$

Conservation equations for the dissolved salt mass fraction

For the cells at the SLSI surface:

$$\dot{m}_e \frac{\mathrm{d}C}{\mathrm{d}x} = -h_m \pi d \rho_f (\overline{C_e} - C_s) \frac{\acute{R}}{R} - J m_{p^*} A_c - m_{p^1} N_p 2\pi \mathcal{D}_m (C - C_{sat}) \frac{\rho_f}{\rho_{salt}} \tag{7.43}$$

For the bulk cells:

$$\dot{m} \frac{\mathrm{d}C}{\mathrm{d}x} = -J m_{p^*} A_c - m_{p_1} N_p 2\pi \mathcal{D}_m (C - C_{sat}) \frac{\rho_f}{\rho_{salt}} \tag{7.44}$$

The molecule mass deposition rate is assumed to be based on salt concentration gradient at SLSI surface conditions and the cell next to this surface. For the known initial dissolved salt concentration, C_i, the dissolved salt mass fraction of the cell near the SLSI surface at the end of the step after molecule deposition is:

$$C_{i+1} = C_i - \frac{h_m \pi d \mathrm{d}x \left(\frac{C_{i+1} + C_i}{2} - C_s \right) \frac{\acute{R}}{R}}{\dot{m}_e} \tag{7.45}$$

where $\acute{R}$ is the actual number of fluid parcels in the cell next to the salt deposit surface, R is the average number of fluid parcels in each cell and $\dot{m}_e$ is the fluid mass flow rate through the cell next to the salt deposit surface.

The molecular mass deposition rate $\dot{m}_m$ is thus:

$$\dot{m}_m = h_m \pi d \mathrm{d}x \rho_f \left(\overline{C} - C_s \right) \frac{\acute{R}}{R} \tag{7.46}$$

Conservation equations for number of particles per unit volume

For the cells at the SLSI surface:

$$\dot{m}_e \frac{\mathrm{d}N_p}{\mathrm{d}x} = \frac{-V_d \pi d \rho_f^2 \left(\overline{C_{ep}} - C_{sp} \right)}{m_{p^o}} \frac{\acute{R}}{R} + J \rho_f A_c - \frac{1}{2} K_{12} {N_p}^2 \rho_f A_c \tag{7.47}$$

The first term on the right hand side of the above equation is for the deposition of particles on the SLSI surface. The second term is for the increase in the particle concentration due to nucleation of new particles and the last term is for the change in the number of particles due to coagulation.

For the cells in the bulk:

$$\dot{m} \frac{\mathrm{d}N_p}{\mathrm{d}x} = J \rho_f A_c - \frac{1}{2} K_{12} {N_p}^2 A_c \rho_f \tag{7.48}$$

where m_{p^o} is the mass of a salt particle.

This procedure is repeated for all integration steps and then the next mixing step occurs.

7.7 Results of model simulation

The model was run for conditions simulating the experimental conditions of Na_2CO_3 deposition experiments. The simulated model results have been compared to the experimental data and are discussed in this section.

7.7.1 Comparison of model simulation and experimental data

The mixing step length dl and the intermediate integration step length dx are determined first as discussed above. Figure 7.5 shows the fluid temperature at various radial locations (cell locations) for the conditions mentioned in the figure. For these conditions, ΔL was 0.1 m and dl was found to be about 0.003 m. The number of cells $(m+n)$ are 11 and the number of fluid parcels were taken to be 10000, i.e., $R = 909$. The fluid temperature profiles have been drawn at different axial locations as the two fluid streams are being mixed. At the beginning of the mixing process T_B is at 688.15 K and T_A is at 495.15 K. Mixing occurs along the length of the test section and at 500 mm location the fluid temperature attains an almost uniform temperature of about 670 K. A similar behavior can be observed for the salt mass fraction as shown in Fig. 7.6. At the beginning of the mixing process, salt mass fraction in stream A is 0.01, while stream B is pure water. The salt mass fraction profiles in various cells at different axial locations are shown in Fig. 7.6.

Figure 7.7 shows the results of model simulation of clean surface temperature profile. Data of three experiments performed at similar conditions are also shown for comparison. The details of these experiments are mentioned in Table A.1. For this particular case, the integration step is taken to be 0.036 mm and the surface tension is 88×10^{-3} N/m. The surface temperature at clean conditions at the inlet of the test section is almost the same as the temperature of stream B, i.e., pure water from the pre-heater 2. The surface temperature decreases along the test section as it mixes with the injected fluid which is at a lower temperature. Later, the surface temperature of the heated test section starts to increase along the test section.

When the fluid injected in the mixing tee is switched to salt solution, deposition of salt particles and salt molecules occurs. Figure 7.8 shows the number of particles nucleated at different location of the test section. For the conditions considered in this case, a high particle nucleation rate is seen at the inlet of test section which drops quickly along the test section length. The salt particle size increases due to diffusion limited growth and coagulation of particles. The size of the salt particle increases along the test section length and reaches a maximum diameter of about 0.16 μm at the test section outlet. Figure 7.9 shows the mass of salt molecules and particles deposited per unit length at different test section locations. The mass of salt deposited increases

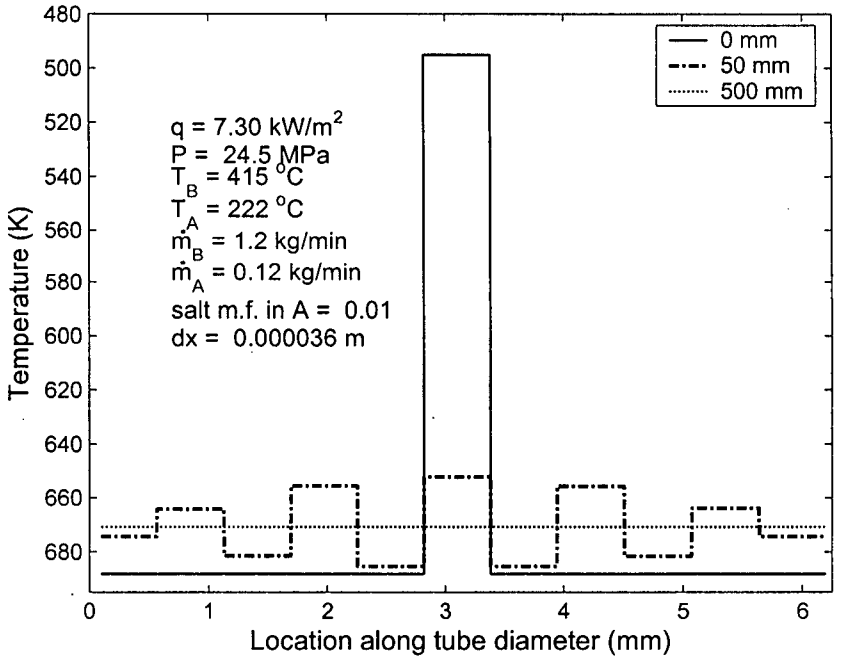

Figure 7.5: Temperature profiles at various axial locations

very quickly close to the test section inlet. After reaching its peak, it then decreases gradually along the length of the test section.

The surface temperature of the heated test section thus increases due to the fouling resistance. The thermal conductivity of the salt deposit layer is taken to be 0.48 W/mK based on the thermal conductivity values determined experimentally as discussed in Section 6.3. The increase in surface temperature after salt deposition is shown in Fig. 7.10. The results are plotted after 16 minutes of operation with salt deposition. As discussed in Chapter 5, the plug-like conditions were noticed after the thermocouple located at 0.15 m from the test section inlet. The model results show a maximum temperature rise slightly earlier than the 0.15 m location.

Figure 7.11 shows test section tube surface temperature simulation at clean conditions of experiments in which the test section was not heated. The data of two experiments performed and the experimental parameters are also shown in the figure. A bulk fluid temperature drop of about 1.5°C was observed across the unheated test section during this experiment. Due to the salt deposit layer a thermal resistance resulted in a drop of test section surface temperature and is shown in Fig. 7.12.

For these model runs, the predicted particle size and particle deposit mass were much lower than those observed. In the next section the model sensitivity to various param-

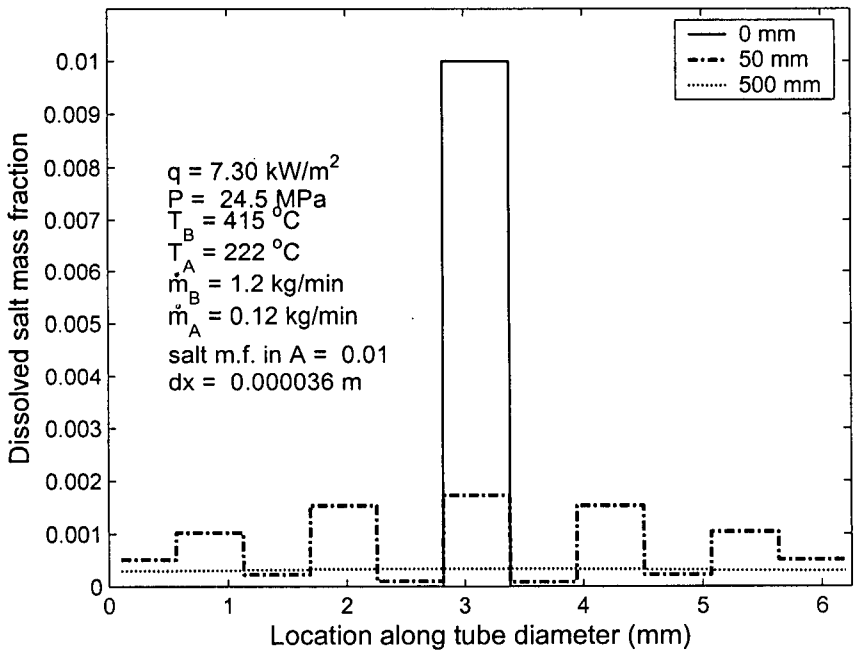

Figure 7.6: Salt mass fraction at various axial locations

eters is discussed in order to understand the cause of these errors.

7.8 Effect of parameters on the model results

Some parameter values were assumed in the model. The effect of these parameters are discussed in this section.

Surface tension: γ

The surface tension has a substantial effect on the number of nucleated salt particles and its exact value is not known for Na_2CO_3. The number of particles nucleated in an integration step was determined using Eq. 7.34, and thus the mass fraction of particles nucleated was used to update the mass fraction of dissolved salt after nucleation for a known initial dissolved salt mass fraction. For very low values of surface tension, the mass fraction of nucleated particles was found to be more than the dissolved salt mass fraction available for nucleation. The minimum value of surface tension was thus chosen such that the mass of salt nucleated was less than the available mass fraction of dissolved salt. The surface tension was varied from 88×10^{-3} to 100×10^{-3} N/m. The model showed a larger number of nucleated particle for lower values of surface tension. Figure 7.13 shows the effect of surface tension on the number of particles nucleated per unit volume at different locations of the test section. It can

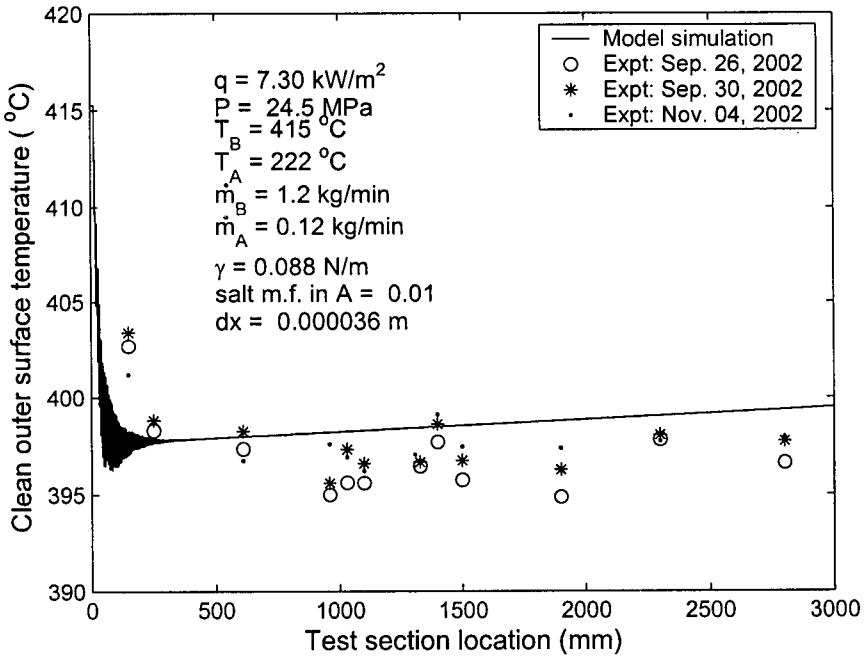

Figure 7.7: Comparison of clean surface temperature experiment data with the model results (heated test section case)

be observed that the number of particles nucleated decrease along the length of the test section and is maximum for lowest value of the surface tension. The particle radii at various test section locations for different surface tension values are shown in Fig. 7.14. Higher number of salt particles result in larger particle size due to coagulation of salt particles. The maximum particle diameter varied from 0.04 to 0.16 μm for the considered values of surface tension.

Figure 7.15 shows the mass of particles deposited per unit length for various surface tension values. The mass of particles deposited decreases with an increase in surface tension and is comparatively negligible for surface tension value of 100×10^{-3} N/m. However, more *molecule mass* is deposited for higher surface tension values as shown in Fig. 7.16. It should be noted that the actual salt particle size, from the SEM photographs, was more than 1 μm. Also based on the model results, lower values of surface tension resulted in larger particle size. Therefore the lower values of surface tension are more likely to determine the actual mass of particles deposited. Figure 7.17 shows the salt layer thickness after 16 minutes of operation for various values of surface tension.

Integration step length: dx

The test section was divided into a number of integration steps. The model was run for integration step lengths of 0.03 mm to 0.96 mm in order to determine the effect of

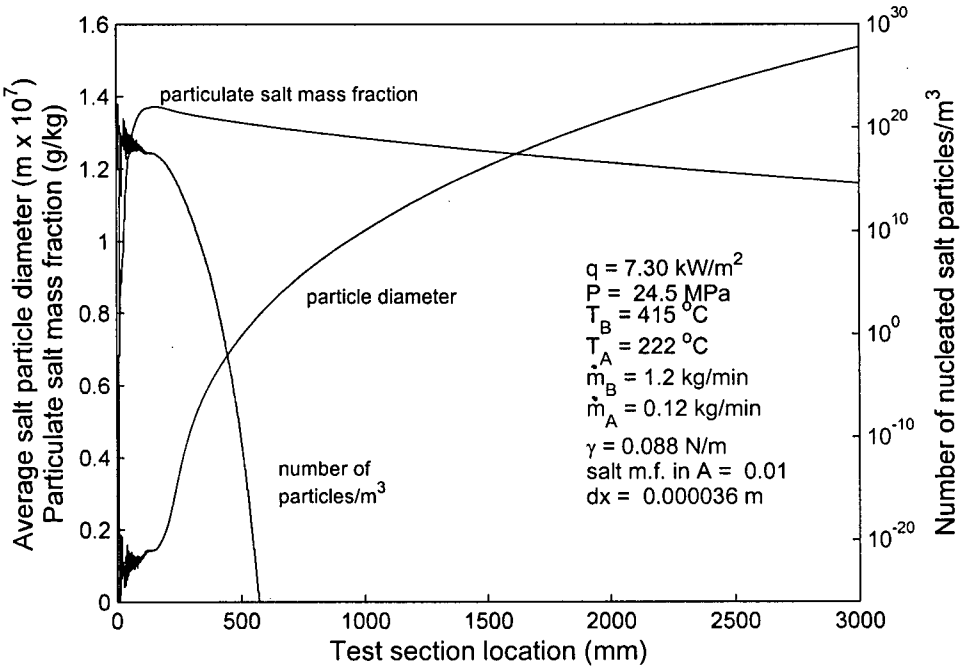

Figure 7.8: Number of nucleated particles and their average size at various test section locations (heated test section case)

step length on the mass of salt deposited and hence the change in surface temperature. Figures 7.18 shows the effect of segment length on the tube surface temperature after salt deposition. The surface temperature rise is almost the same for all step sizes.

Number of fluid parcels in each cell: R

Each cell comprised R number of fluid parcels. As mentioned earlier, during the simulated mixing process, the fluid parcels move in a vertical direction, either upwards or downwards and the number of fluid parcels in a cell was not fixed. The direction in which the fluid parcels move was determined by generating random signs (+ or −). Therefore, the higher the number of parcels, the higher the probability that exactly half of them move in either direction. The model was run for various number of fluid parcels and Fig. 7.19 shows the effect of number of fluid parcels on the mass of deposited salt. For the conditions shown in the figure there were 11 cells. The model was run considering 100, 1000 and 10000 fluid parcels and therefore fluid parcels per cell were 9, 91 and 909 respectively. The simulation with highest number of fluid parcels produced a relatively smooth curve for the deposited mass of salt. The mass of salt deposited, for the runs in which 100 and 1000 fluid parcels were considered, fluctuated about the mass deposition curve for the 10,000 fluid-parcel run.

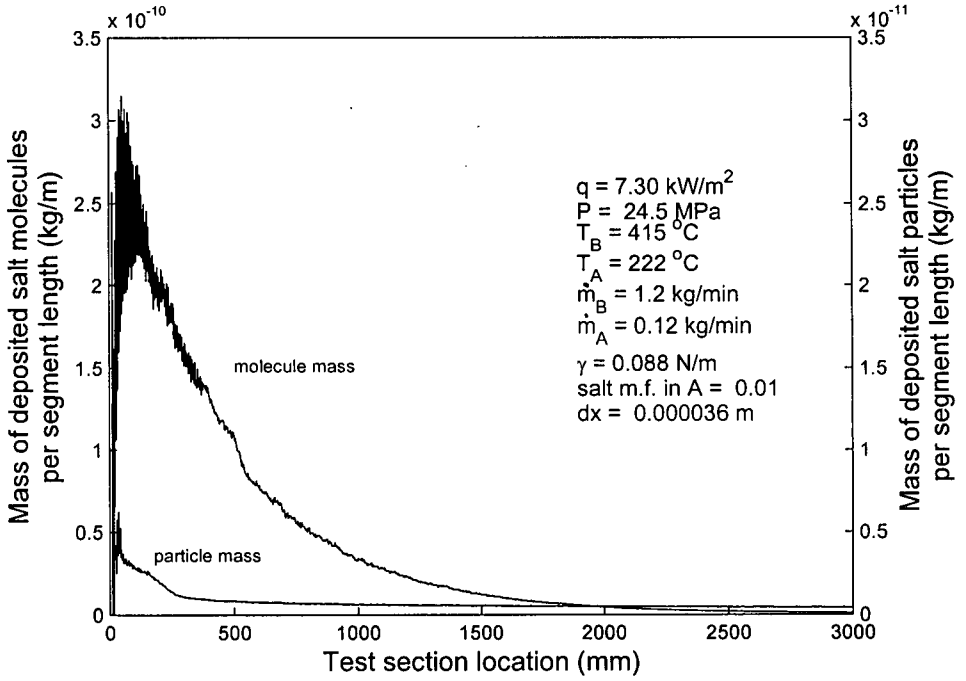

Figure 7.9: Mass of salt molecules and particles deposited per unit length at various test section locations (heated test section case)

7.9 Conclusion

Mixing of two fluid streams, heat transfer and salt deposition on the tube surface have been modeled. Salt particle nucleation, growth and coagulation have been considered to determine the mass of salt particles and molecules deposited on the tube surface. The change in tube outer surface temperature, due to the fouling resistance, has been calculated and compared with the experimental results. The model results have been compared with data from two types of experiments i.e., heated and unheated test section. The model estimates the tube surface temperature profile along the length of the quite well, during the mixing of the two fluid streams occurs at clean surface conditions. The location of the peak surface temperature change in the test section, calculated from the model, was in a good agreement with the experimental data. The model seems to estimate the peak surface temperature increase for the heated test section case quite well. It should be noted that the density of the deposit layer is assumed to be the same as that of the salt and effect of porosity has not been considered in the model. The modeled salt particle size was also found to be less than the size of the particles observed from the SEM analysis of the deposit structure. A possible reason could be the agglomeration of salt particles at the tube surface which has not been modeled.

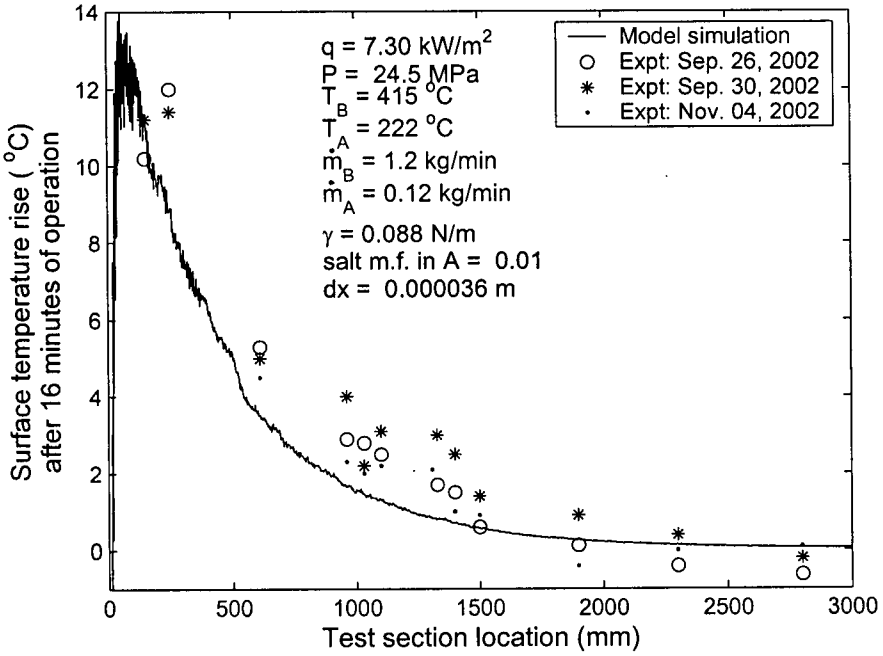

Figure 7.10: Surface temperature rise due to salt deposit: experiment data vs model results (heated test section case)

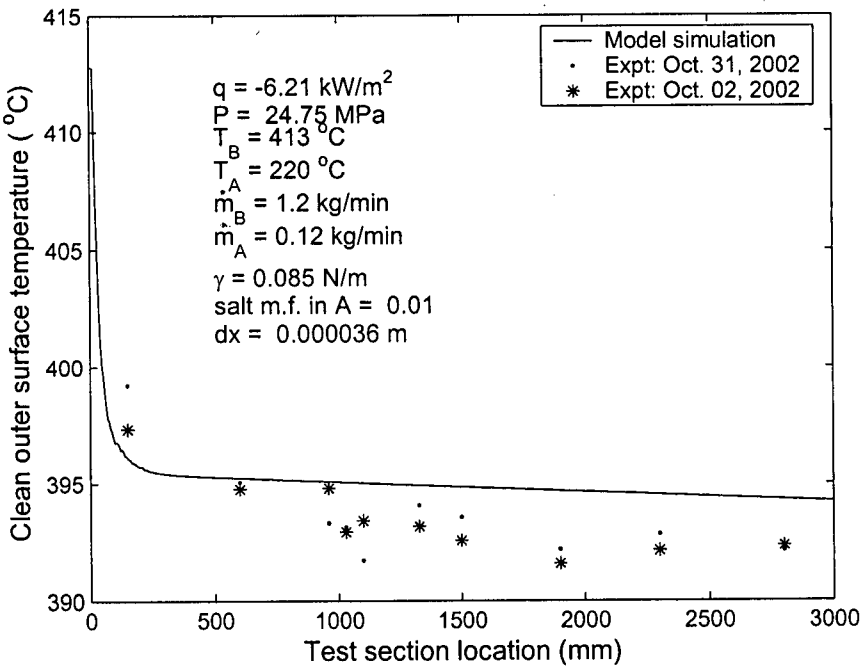

Figure 7.11: Comparison of clean surface temperature experiment data with the model results (unheated test section case)

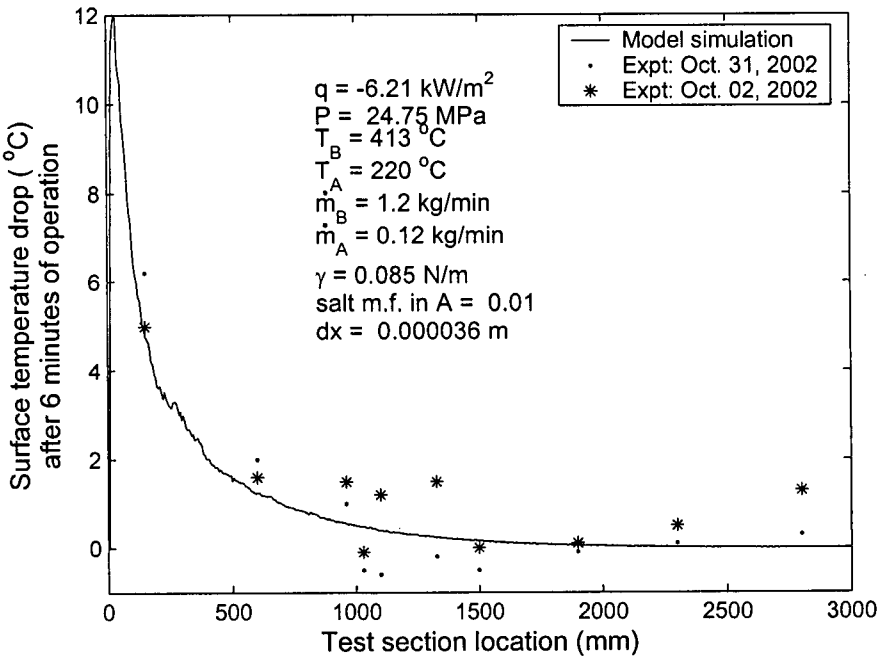

Figure 7.12: Surface temperature drop due to salt deposit: experiment data vs model results (unheated test section case)

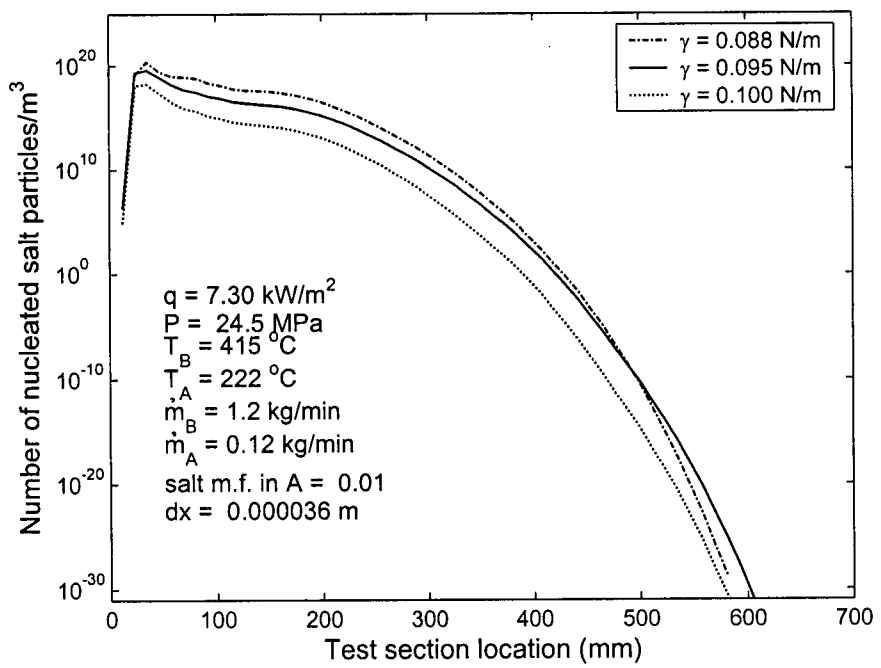

Figure 7.13: Effect of surface tension on the number of nucleated particles

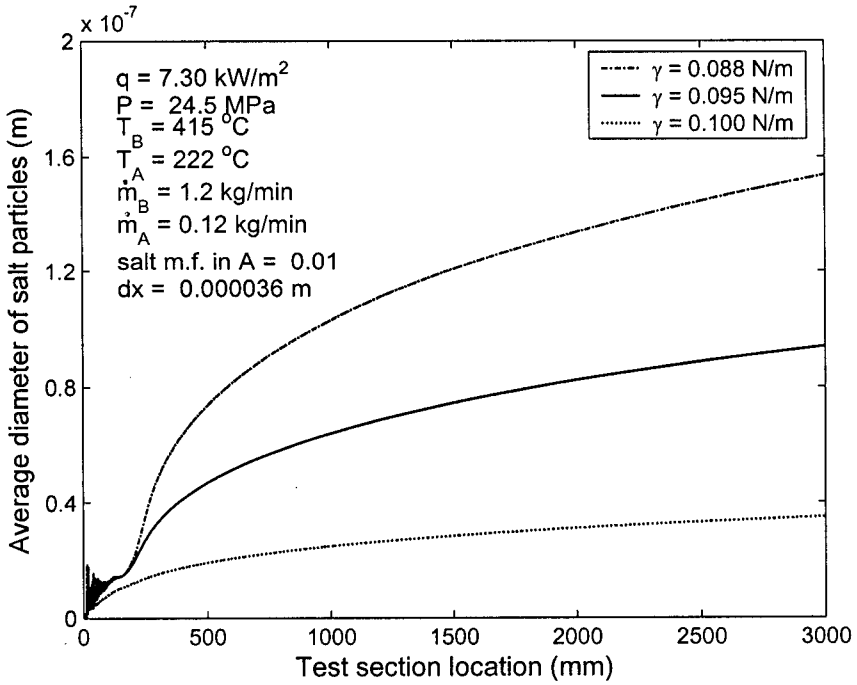

Figure 7.14: Effect of surface tension on particle size

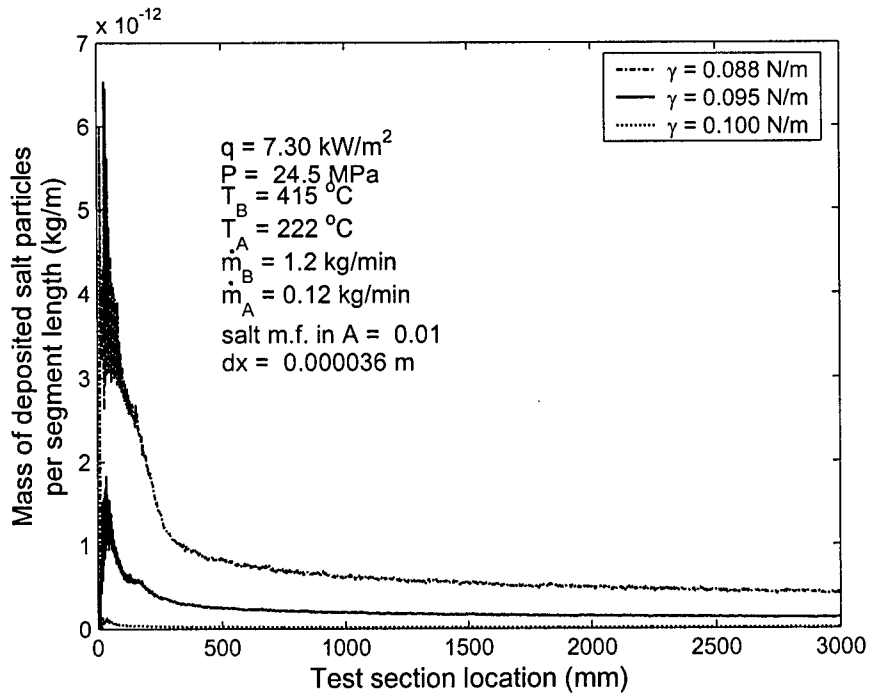

Figure 7.15: Effect of surface tension on particle deposition

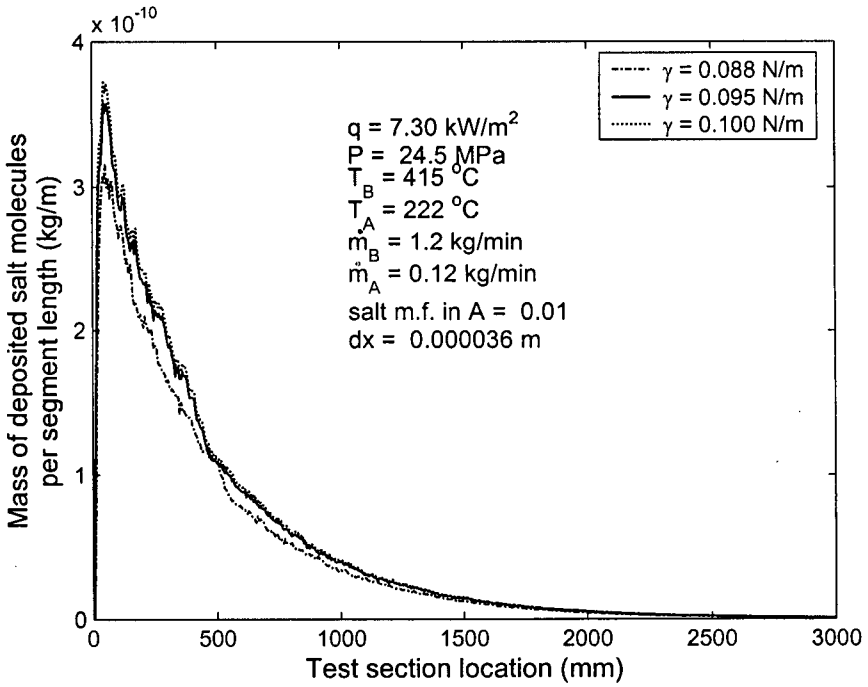

Figure 7.16: Effect of surface tension on molecule deposition

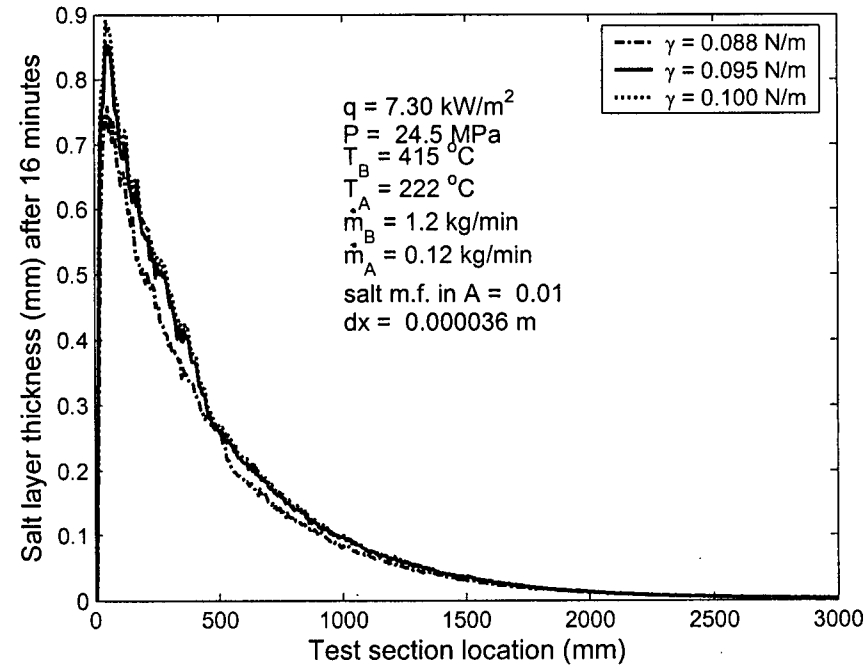

Figure 7.17: Effect of surface tension on salt layer thickness

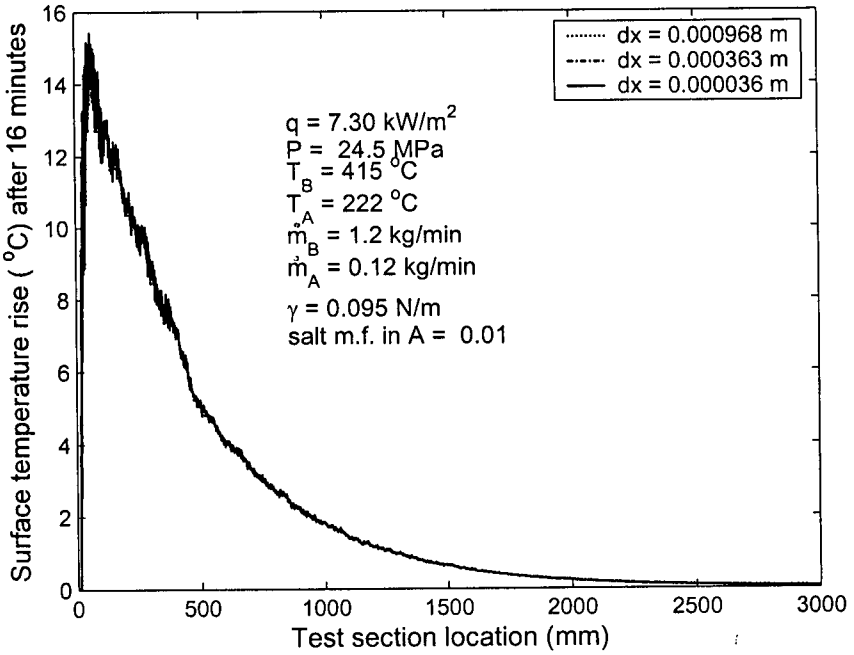

Figure 7.18: Effect of segment length on tube outer surface temperature

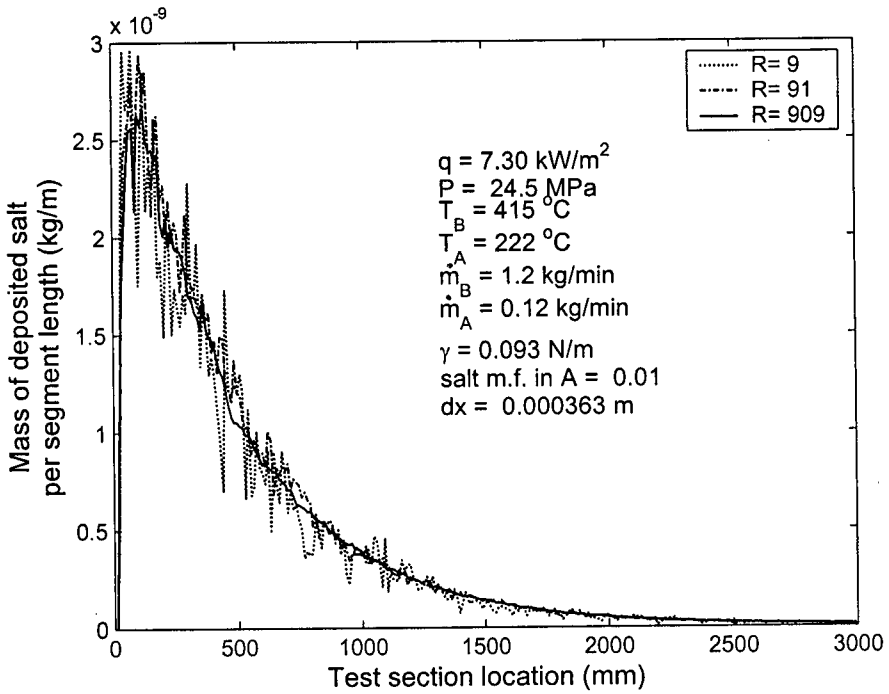

Figure 7.19: Effect of number of fluid parcels on salt deposition

Chapter 8

Summary of Conclusions and Future Work Recommendations

8.1 Thesis overview and conclusions

The supercritical water oxidation (SCWO) has the potential of being a viable technology for processing organic waste. However, its commercial application has not been successfully possible due to the problems of corrosion and salt precipitation on the heat transfer surfaces. Inorganic salts, which might be present in the waste feed or formed during the process have very low solubility at SCWO conditions. These salts are usually accumulate on the reactor surface. Due to the steady buildup of these salt deposits, the tubular reactors are ultimately plugged. The precipitation of salt on the reactor wall not only wastes energy, due to its thermal resistance, but also leads to even more cost associated system shutdowns. Several approaches have been suggested by companies trying to commercialize this technology to overcome this problem. In order to control the buildup of salt deposits, attempts have been made to develop specific reactor designs and to modify the operating techniques. All of these attempts have been successful to some extent but none of them has been able to eradicate the problem of fouling in the SCWO reactors. Some techniques are better suited for certain types of wastes only and none of them has proved to be superior than others. Due to this reason, importance of continued fundamental research in the phase behavior (particularly in ternary component systems), precipitation of salts, deposition dynamics and morphology of the deposits is evident.

The objective of this work was to study the deposition of Na_2CO_3 and Na_2SO_4 at high pressure and elevated pressure conditions associated with the SCWO process. These salts are encountered in wastes of mononitrobenzene plants, among several other organic wastes which are good candidates for SCWO treatment. Since the solubility of these salts (Na_2CO_3 in particular), at high pressure and a range of temperatures encountered in SCWO process was not known, an experimental study

was carried out to measure the solubility of these salts in binary (salt-water) and ternary (salt-salt-water) system. Experiments were performed in which heterogeneous nucleation of salt molecules (crystalline fouling) on the reactor surface occurred. Two heat and mass transfer correlation have been used to simulate the salt deposition process and a sophisticated model has been developed to verify the solubility reporting temperature. It was found that the solubility of these salts decreases rapidly after the pseudo-critical temperature. The solubility of these salts in the form of a mixture was quite close to that of pure salts. However, possibly due to the common ion effect, the solubility of Na_2SO_4 in the presence of Na_2CO_3 was found to be further reduced at near critical conditions. The solubility of these salts was presented in the form of correlations as a function of fluid density, which can be used to estimate the maximum amount of dissolved salt for a given fluid density. A heat and mass transfer model was also developed to confirm the solubility reporting temperature. During this experimental study, it was observed that the tubular reactor plugged due to the salt deposits in a very short time. The system had to be shut down, sometimes, within five minutes due to either high system pressure or excessive surface temperature of the heated sections.

Three types of experiments were performed in order to study the effect of type of fouling (crystalline and particulate) on the net salt deposition. Combined crystalline and particulate deposit runs were found to be longer than the pure crystalline deposit experiments. In order to make the salt particles nucleate in the bulk fluid, salt solution was injected in pure supercritical water such that supersaturation conditions were achieved. This was carried out at the inlet of the heated test section and resulted in combined crystalline and particulate deposition. In some experiments the test section was kept unheated to further reduce the crystalline deposition. The net salt deposition was found to be reduced for the combined crystalline and particulate runs compared to the pure crystalline deposition experiments. Four times more salt passed through the system when the salt particles nucleated in the bulk fluid. This resulted in longer runs before system shut down. The other observation for the pure crystalline type deposition experiments was that the surface temperature increased steadily with the steady growth of the deposits in the heated test section experiments. However, for the combined crystalline-particulate deposition experiments, the surface temperature initially increased gradually and then suddenly decreased, thus indicating unsteady buildup of the deposit layer. The location of the plug was found to be near the point where salt solution was injected and for the conditions studied, and all of the salt deposition occurred within the 3 m long test section. Similar unsteady growth of deposits was noticed in the experiments in which the test section was unheated. Thus for wastes with inorganic salt content, more salt is likely to flow through the system, if it is made to nucleate in the bulk fluid.

A novel procedure was developed to preserve the salt deposited, under turbulent

conditions, on the heat transfer surface for studying the structure of the deposits. The system was purged with nitrogen after enough salt deposition occurred on a tube inserted in the test section to collect deposit samples for SEM analysis. In this manner the salt deposit thickness profile along the test section was measured. Based on the measured surface temperature rise due to deposition, the thermal conductivity was calculated. Na_2CO_3 deposits were found to be stronger then the Na_2SO_4 deposits. The Na_2SO_4 deposits (combined crystalline-particulate in particular) were weaker and partially washed off during the purging process. The pure crystalline deposits were found to be different from the combined crystalline-particulate deposits. The SEM photographs revealed long salt crystals which nucleated at the tube inner surface and grew towards the center of the tube in case of pure crystalline deposition. These deposits were very dense. On the other hand for the combined crystalline-particulate deposition, salt particles were seen and the deposits were comparatively less dense and easy to remove. It is due to this reason a steady salt deposit layer buildup was observed for pure crystalline deposition experiments. For the combined crystalline-particulate deposition, the deposit layer was periodically removed (partially), because of the weaker deposit.

Finally, a computer code was written to model the deposition of combined crystalline-particulate deposition and heat transfer in the tubular reactor. In the model, simulation of mixing of two fluid streams was carried out. Homogeneous nucleation of salt particles, their growth, coagulation and deposition on the reactor tube was modeled in conjunction with the deposition of salt molecules nucleating on the tube. This model can thus be used to estimate the mass of salt deposited on the tube surface and hence the change in tube surface temperature due to the fouling resistance. The model results were compared to experimental data. It was noticed that the model predicts the heat transfer between the fluid and tube quite accurately and the surface temperature profile, as the two fluid streams were mixing along the test section length, was in good agreement with the experimentally measurements for clean surface conditions. The estimated increase in surface temperature due to fouling resistance agreed well with the experimental data. The location of the peak surface temperature change due to the fouling resistance was also estimated quite well. However, the calculated size of the particles was found to be smaller than the actual salt particle size observed in the SEM photographs.

8.2 Implications for SCWO system design

For wastes with inorganic salt content, more salt is likely to flow through the system, if it is made to nucleate in the bulk fluid. This can be achieved by heating pure water (and oxygen) only, to supercritical conditions in the pre-heaters and then injecting

the waste feed into it. In this manner, the SCWO system will be able to run for longer periods of time and also the problem of salt deposition will be restricted over a short length of the reactor. The salt deposits in this short length can be flushed/quenched by passing subcritical water through it. Or the deposits can be removed by mechanical means. During the salt removal process, the waste can be passed through a reactor parallel to the one being cleaned. Thus two short length reactors are needed such that while the feed is being treated in one, salt removal takes place in the alternate reactor. During the exothermal SCWO reaction, it may not be necessary to heat the surface of the reactors. Possible addition of fuel in the waste itself may ensure the process be self-sustaining.

As a possible fouling mitigation measure, use of additives to provide nucleation sites in the bulk fluid may be studied. Addition of solid, inert particles (e.g., silica) in the feed itself may provide the salt to adhere to a mobile surface instead of sticking to the reactor surface. If the particles are rough, they may scour the tube inner surface thereby removing the deposits on the wall. Since the combined crystalline-particulate deposits are easier to remove, even if the inert particles accumulate on the tube surface, they are more likely to result in a weaker deposit. In the UBC-NORAM pilot plant the injection of particles may be carried out at the inlet of the test section. However, consideration is required to design a system to collect these particles before the fluid pressure is reduced, in order to eliminate any erosion and choking problems at the back pressure regulator.

For some applications with high heating value wastes, it might be unnecessary to preheat past the critical temperature, in which cases, subcritical salty wastes can be injected into supercritical water, forming homogeneous particles. This in fact happens in the vessel and platelet reactors, and the results here show that only a modest force should be needed to remove deposits, at least initially. For other applications, salt solution could be injected prior to the cool down section. For example, in SCWO of chlorinated waste, HCl causes extreme corrosion at cool-down side unless neutralizers are added. Na_2CO_3 should be added to increase the pH without risking NaOH melt corrosion and apparently, with no risk of fouling.

8.3 Future work

It was concluded that combined crystalline-particulate fouling deposits are weaker than the crystalline deposits. For Na_2CO_3, a number of experiments were performed and it was observed that more salt was able to pass through the system, instead of depositing on the tube, when homogeneous nucleation occurred. This was because both *deposition* and *removal* processes occur simultaneously due to the weak deposit characteristics. For the experiments in which salt particles were made to nucleate

in the bulk fluid, the net salt deposit was less not necessarily because those salt particles did not deposit on the reactor surface at all and instead passed through the system. Thus flow conditions (preferably low turbulent) should be studied for which the particles are more likely to pass through the tubular reactor instead of depositing on the reactor wall. However, it might be tricky to have conditions where the fluid velocity is high, but still low turbulence, such that the particles remain suspended in the fluid.

During the process of preservation of the salt deposit layer for SEM analysis, it was noticed that the Na_2CO_3 deposits were easier to preserve by nitrogen purging technique. However, it was found that Na_2SO_4 deposits were weaker and were partially washed off during the purging process. In order to confirm this, combined crystalline-particulate deposition experimental study, similar to that performed with Na_2CO_3 salt should be carried out for Na_2SO_4 also. In case Na_2SO_4 deposit is found to be weak, the homogeneous nucleation may be more effective as a fouling mitigation technique for Na_2SO_4.

The SEM analysis of the salt deposits was carried out to study the structure of the deposit layer and its thickness along the test section length. The thermal conductivity of the salt deposit layer was then inferred from the measured increase in surface temperature. The deposits seemed to be quite dense, but further analysis may be carried out to determine the porosity of the deposited layer. This can be done if the size of the tube is larger then the one used as the insert in this study. In that case the system can be run for longer period of time and thus thicker deposit layer maybe preserved for analysis. The effect of aging of the deposit layer has not been studied. SEM analysis of deposits preserved at different time intervals may be carried out to determine of the change in deposit structure with time.

The simulation model developed for estimating combined crystalline-particulate deposition comprises salt particle nucleation, growth and coagulation of particles and their deposition on heat transfer surface, which occurs in parallel with deposition of salt molecules. It does not simulate the salt removal process of salt after a certain salt layer thickness is achieved as indicated from the experimental data. The model can thus be modified to simulate the actual fouling phenomenon during which both salt *deposition* and *removal* processes occur simultaneously. The model may thus be optimized to determine values of operating parameters in order to reduce net salt deposit rate on the heat transfer surface.

Appendix A

Discussion of the Na_2CO_3 Fouling Mitigation Experiments

Three types of salt deposition experiments have been performed. In the first type, the salt solution was heated in the pre-heaters before entering the test section. The objective of these experiments was to determine the solubility of Na_2CO_3 and Na_2SO_4 at different fluid temperatures. The bulk fluid temperature at the outlet of pre-heater 2 was set such that minimum salt deposition occurred in the pre-heaters. The test section heat input was kept low in order to have a near-isothermal condition in the test section. Heterogeneous nucleation of salt molecules resulted in crystalline scale on the test section in this type of experiment. The details of these experiments have already been discussed in Chapter 4 and the operating parameters are mentioned in Tables 4.1-4.3. These experiments will not be discussed in this chapter. However, two Na_2CO_3 heterogeneous nucleation experiments were later performed in which instead of heating the salt solution, pure water was passed through the pre-heaters. Salt solution was then injected into the supercritical water. The objective of these experiments was to compare the behavior of pure crystalline scale with combined crystalline-particulate deposits. These experiments will be discussed in Appendix A.3.

In the second type of experiments, Na_2CO_3 solution was injected in a stream of supercritical water just before the test section, for fouling mitigation purposes. The fluid temperature after mixing of the two streams was above the Na_2CO_3 saturation temperature and thus salt particles were expected to nucleate in the bulk fluid. In this type of experiments the test section was heated and thus combined crystalline-particulate fouling was expected. A sample experiment of this type has already been discussed in Chapter 5. Other experiments, of this type, are discussed in the next section. The third type of experiment was similar to the second type, but the test section was unheated, in order to further reduce crystalline scale. For the second and third type of experiments, the experimental procedures have been discussed in Section 5.2 and details of experimental parameters are mentioned in Table A.1.

Table A.1: Details of Na_2CO_3 deposition experiments

Experiment No.	Data file	Date performed	Pressure (MPa)	Fluid flow rate (kg/min)	Salt concentration at test section inlet (wt.%)	Salt concentration in collection tank (wt.%)	Time to terminate experiment	Comments
1	SEP13.xls	Sept. 13, 2002	24.61	(0.8+0.1)	0.055	not done	no plugging	Perhaps the salt concentration at test section inlet was quite low
2	SEP17.xls	Sept. 17, 2002	24.54	(0.84+0.1)	0.1	not done	60 minutes	Test section was not actually plugged, but the heating was reduced when PH2 outlet temperature was seen to be increasing
3	SEP17.xls	Sept. 17, 2002	24.54	(0.84+0.1)	0.1	not done	75 minutes	Experiment was stopped when relief valves opened slightly
4	SEP20.xls	Sept. 20, 2002		(1.2+0.12)		not done		Could not achieve a steady pressure, using the spring loaded BPR
5	SEP23.xls	Sept. 23, 2002		(1.2+0.12)	0.1	0.065	stopped after 40 minutes	Pressure was continuously increasing due to a leak in the BPR
6	SEP26.xls	Sept. 26, 2002	24.48	(1.2+0.12)	0.1	0.06	50 minutes	Experiment stopped when pressure relief valve opened slightly
7	SEP30.xls	Sept. 30, 2002	24.82	(1.2+0.12)	0.1	0.088	66 minutes	Experiment stopped when pressure relief valve opened fully
8	0CT02.xls	Oct. 02, 2002	24.65	(1.2+0.12)	0.1	0.08	55 minutes	Unheated test section, experiment stopped when pressure relief valve opened fully, plugged at the middle thermocouple
9	0CT31.xls	Oct. 31, 2002	24.72	(0.84+0.1)	0.1	0.018	50 minutes	Surface temperature rise of about 170°C, experiment terminated
10	0CT31.xls	Oct. 31, 2002	24.72	(1.2+0.12)	0.1	0.09	75 minutes	Unheated test section, parameters same as Experiment No. 8 but without middle thermocouple, no sign of plugging in 75 minutes
11	NOV04.xls	Nov. 04, 2002	24.75	(1.2+0.12)	0.1	0.075	90 minutes	Same as last run but with heated test section, plugged in 90 minutes
12	NOV8.txt	Nov. 08, 2002	24.46	(1.2+0.12)	0.1	not done	25 minutes	Due to the high heat input to the test section, a 10°C difference was observed between top and bottom thermocouples

A.1 Homogeneous & heterogeneous nucleation experiments

A.1.1 Experiment: 1

This was the first run of the second type of Na_2CO_3 deposition experiments. Salt solution was injected into the supercritical water at the inlet of the test section. The salt concentration, entering the test section was about 0.055 wt.%. The temperatures at 0.15 m (SB9, thermocouple at the top surface) and 0.25 m (S9, thermocouple at the bottom surface) were noted before and after the metering pump was started. The temperatures at these locations were very close to each other, before water was injected from the metering pump. However, when water was injected through the metering pump, the thermocouples at these locations showed temperatures different from each other. Thus around the 0.25 m location, the two fluids streams were not fully mixed. After the metering pump was started the SB9 (top surface thermocouple) showed about 4°C higher than S9 (bottom surface thermocouple). However at 1.03 m (SB3, thermocouple at the top surface) and 1.1 m (S3, thermocouple at the bottom surface) locations the thermocouples showed temperatures very close to each other, before and after water injection from the metering pump. The thermocouples S7 (at 0.61 m bottom) was also showing almost the same temperature as SB7 (at 0.52 m top surface). Thus the two streams were almost mixed around 0.6 m location.

Salt solution was injected at 13:02 with pre-heater 2 bulk fluid outlet temperature set at 403°C. The pre-heater 2 outlet temperature started increasing immediately after that and at 13:20 the power input to the pre-heater 2 was reduced to maintain the output at 416°C. Over the 50 minute salt deposition period, the temperature rise was as follows:

Location (m)	0.15	0.61	0.96	1.1	1.25	1.4	1.5	1.7	2.3	2.8
Temperature rise (°C)	4	7	7	8	7	6	4	4	2	2

A steady increase in surface temperature was noticed, but the system pressure remained constant during the 50 minute period. At 14:12 the flow from the metering pump was switched to pure water to redissolve the salt deposits. The time taken to reduce temperature back to clean surface conditions at 0.15 m location i.e., about 400°C was about 15 minutes. All thermocouples up to the 1.4 m location showed a reduction in temperature within 30 minutes of switching back to water. During this period, the temperature of thermocouples located at 1.5 to 2.8 m stayed almost the same, so either salt deposit was not being dissolved or there was no deposition at all in that area. The average clean surface temperature was about 399°C. Bulk fluid temperature at the test

section outlet was about 396°C. The solubility limit at 399°C is about 0.015 wt.%. However effluent conductivity fluctuated around 500 μS/cm corresponding to Na_2CO_3 solubility of 0.025 wt.% which actually corresponds to a fluid temperature of 390°C. Since the surface temperature and pressure rise during the 50-minute run were not high, it was decided that the next experiment would be carried out at double the salt concentration.

A.1.2 Experiments: 2 & 3

The salt concentration at the test section inlet for Experiment 2 was 0.1 wt.%. When the salt solution was injected, due to salt depostion in the test section, a sudden increase in pressure at the test section inlet was noticed. The bulk fluid temperature, at pre-heater 2 outlet, increased rapidly too, after salt solution was injected into the supercritical water stream. The experiment was thus terminated. It was then decided to do the experiment again and not to terminate the run until the pressure relief valve, located just after the main pump opened. In Experiment 3, salt solution was injected at 15:50 and the run was terminated when the pressure relief valve opened slightly at 17:08 i.e., after about 75 minutes of operation. The test section average-inner surface temperature was about 397-398°C under clean conditions. Fluid temperature at the exit of pre-heater 2 was maintained at 416°C. Due to the salt deposition, in ten minutes, a temperature rise of about 15°C was noticed at the 0.15 m location. The surface temperature then dropped to the clean surface condition suddenly. This 10 minute cycle was repeated seven times during the 75 minute run as shown in Fig. A.1. It seems that salt deposited in the test section, resulting in an increase of system pressure at the test section inlet. The bulk fluid temperature, at the exit of pre-heater 2, also increased with the increase in pressure at the test section inlet, thus indicating a *plug-like* condition. The pressure increased from 24.47 to 26.8 MPa, at the inlet of test section, which cleared the *plug* after the deposit layer reached a certain thickness. The system pressure at the outlet of the test section remained constant, thus the location of the *plug* was in the test section. At the 0.61 m location, three such cycles were observed but at the end of each cycle the temperature did not drop all the way to the clean surface condition thus the deposit layer was only partially removed. At the 0.96 m location, two deposition-removal cycles were observed. The thermocouple at 1.1 m location showed a steady temperature increase of about 14°C. After 75 minutes of operation, the temperature increase at various locations in the test section was as follows:

Location (m)	0.15	0.61	0.96	1.1	1.5	1.7	2.3	2.8
Temperature rise (°C)	15	14	13	14	10	7	3	3

During the experiment the effluent conductivity kept on fluctuating thus indicating

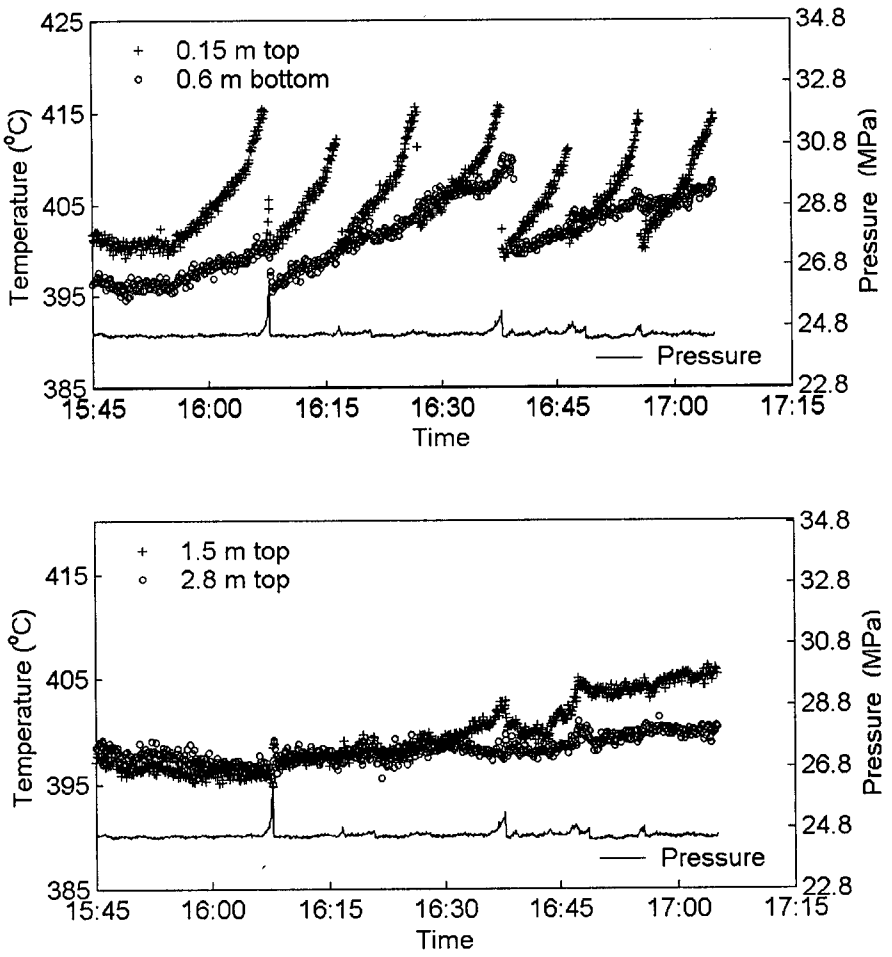

Figure A.1: Temperature and pressure behavior for the combined heterogeneous & homogeneous nucleation run (Experiment 3)

that salt deposition and removal were taking place in the system. Most of the time it was around 650 μS/cm, but increased to a maximum of 4 mS/cm. It was therefore decided that for the next run, the effluent would be collected, for salt concentration measurement.

The surface temperature behavior at the 0.15 m location was found to be different from the downstream surface temperatures. A deposition-removal cycle is shown in Fig. A.2. The pressure behavior shown in the figure is at the test section inlet. The pressure at the test section outlet remained constant. The surface temperature at that location increased with an increase in pressure and fluid temperature at pre-heaters 2 outlet. Thus indicating the location of the plug was just after this location. The temperature at other location did not increase with an increase in pre-heater 2 outlet temperature

and pressure. However, at other locations surface temperature increased for a short time, after the removal of the plug and then reduced back to initial condition. Thus the surface temperature increase was due to the fluid which started flowing again after the plug was removed. Another observation was that after the salt was removed from the 0.15 m location, no sudden temperature increase was noticed at the later locations. Thus the removed salt layer did not deposit at other locations in the test section.

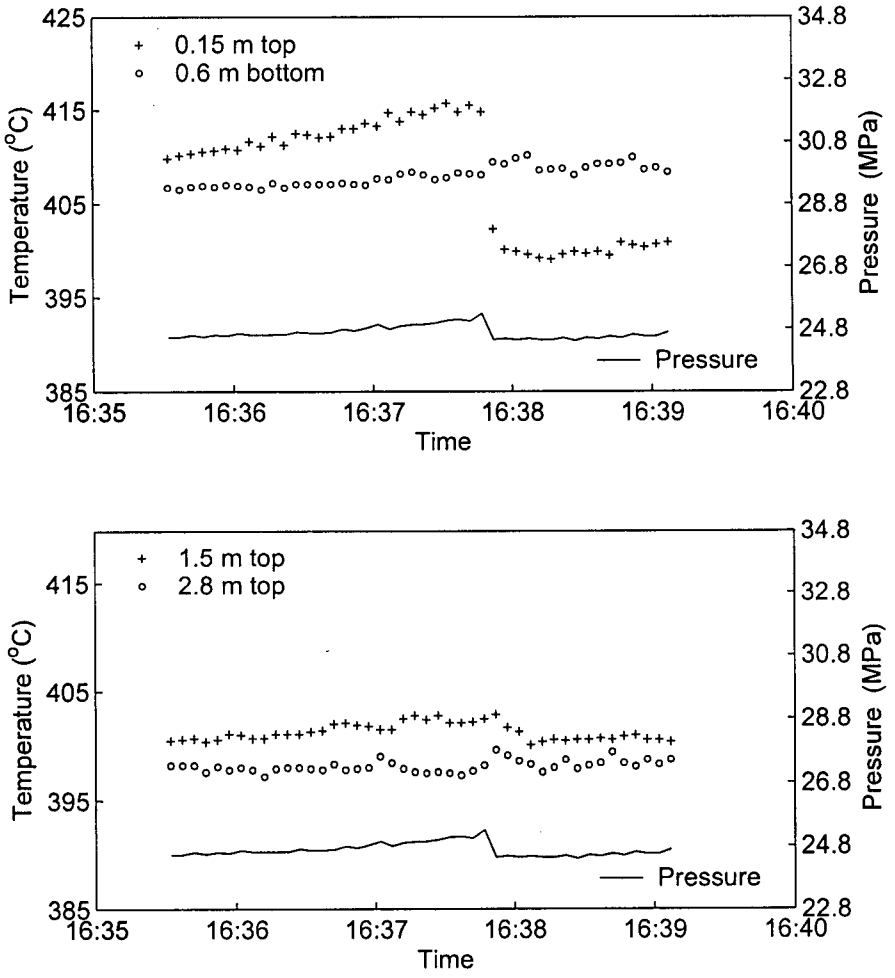

Figure A.2: Temperature and pressure behavior for the combined heterogeneous & homogeneous nucleation run (Experiment 3)

A.1.3 Experiment: 6

The effluent was collected in this run. Salt solution was injected at 10:54 and switched to pure water at 11:43. Five or six deposition-removal cycles were observed at the 0.15

m location during the 50 minute run as shown in Figure A.3. The surface temperature at this location increased gradually by more than 10°C and then dropped suddenly to almost the clean surface temperature. At the 0.61 m location, the surface temperature increase was about 30°C in 40 minutes and then the salt layer washed off. The experiment was terminated when the pressure increased to 26.8 MPa and the pressure relief valve, located just after the main pump, opened slightly. It was decided, for the next experiment, the run would be terminated only when the pressure relief valve remained open for some time.

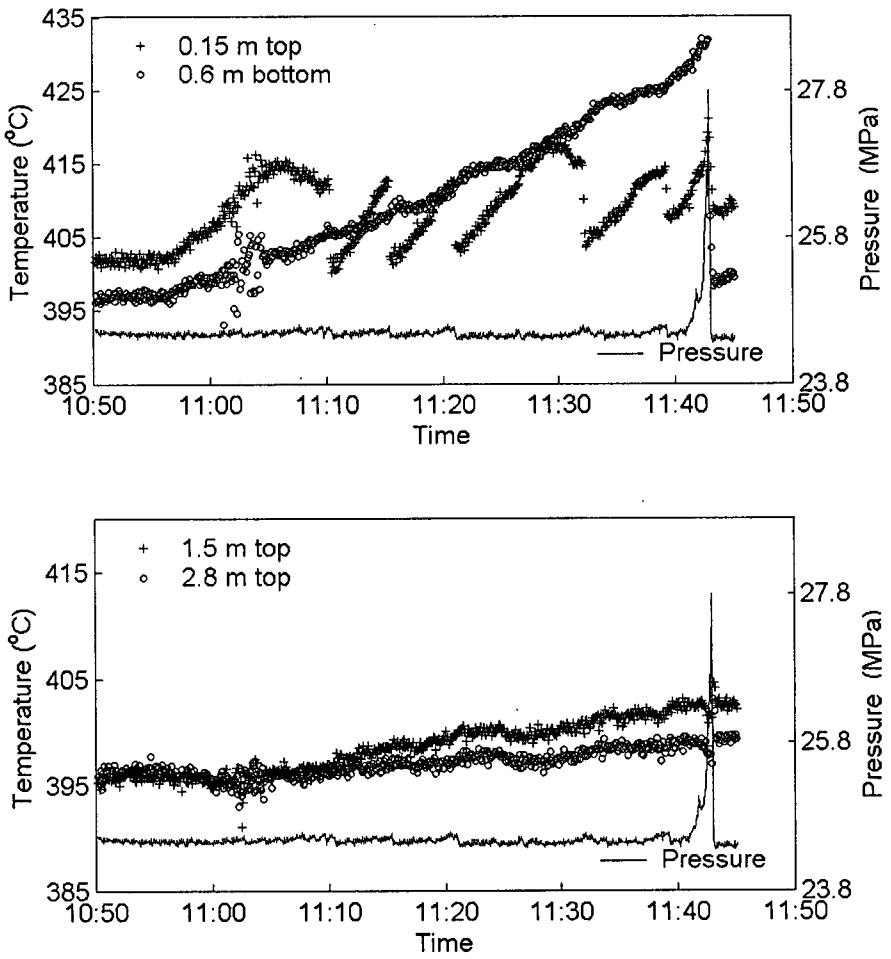

Figure A.3: Temperature and pressure behavior for the combined heterogeneous & homogeneous nucleation run (Experiment 6)

A.1.4 Experiment: 7

This run was terminated only when the pressure relief valve opened fully (the pressure at the inlet of the test section increased to 28.2 MPa). It lasted for 66 minutes. Again five or six deposition-removal cycles were noticed in this run at the 0.15 m location as shown in Fig. A.4. The temperature at this location increased gradually by about 12°C and then dropped suddenly to the clean surface condition. Three such cycles were noticed at the 0.61 m location and two at 0.96 m. A steady increase of surface temperature was noticed at later test section locations.

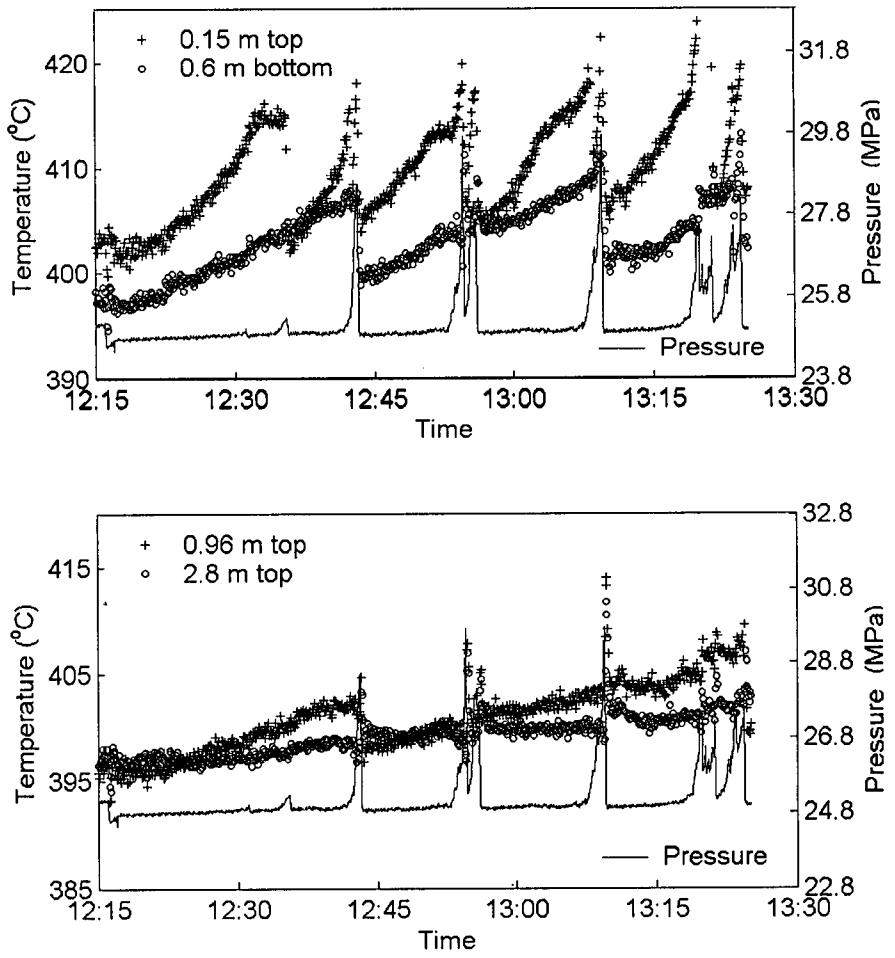

Figure A.4: Temperature and pressure behavior for the combined heterogeneous & homogeneous nucleation run (Experiment 7)

After 66 minutes of operation, the temperature increase at various locations in the test section was as follows:

Location (m)	0.15	0.61	0.96	1.1	1.25	1.4	1.5	1.7	2.3	2.8
Temperature rise (°C)	20	15	13	13	11	11	8	7	6	6

Pressure at the outlet of the test section remained constant. No sudden deposition occurred in the later parts of the test section when salt was washed away from the 0.15 m location. Again during the deposition-removal cycle, at 0.15 m the surface temperature behavior was different from the downstream locations. Two sample cycles are shown in Fig. A.5. When it was close to plugging the pressure and pre-heater 2 outlet temperature increased very quickly and only the thermocouple at 0.15 m behaved in the same manner. A sudden increase in temperature was noticed at later locations after the plug was removed. Thus the location of the plug was just after the 0.15 m location.

This run was slightly longer then Experiment 6, because it was terminated only after the pressure relief valve opened fully and constant fluid flow was observed through it for few seconds. The average clean inner-surface test section temperature was about 397°C. Na_2CO_3 solubility at this condition is 0.018 wt.%. The effluent salt concentration was 0.088 wt.%. The ratio of effluent salt concentration to saturation limit was thus 4.8 and it took around 66 minutes to plug the test section.

A.1.5 Experiment: 11

For this experiment, the ratio of effluent salt concentration to saturation limit was found to be 4.2. The test section got plugged after 90 minutes of operation. Figure A.6 shows the behavior of the thermocouple at the 0.15 m location compared to other downstream surface temperatures, during a deposition-removal cycle. As usual, the plug occurred after the 0.15 m location. This experiment has already been discussed in detail in Section 5.3.2.

A.2 Homogeneous & heterogeneous nucleation unheated test section experiments

A.2.1 Experiment: 8

The test section was not heated in this run. The clean test section inner-surface temperature was about 394°C. Four deposition-removal cycles were observed at the 0.15 m location as shown in Fig. A.7. While the salt was being deposited, the surface temperature *decreased* due to thermal resistance of the deposit layer. In the experiments with a heated test section, the test section surface temperature *increased*

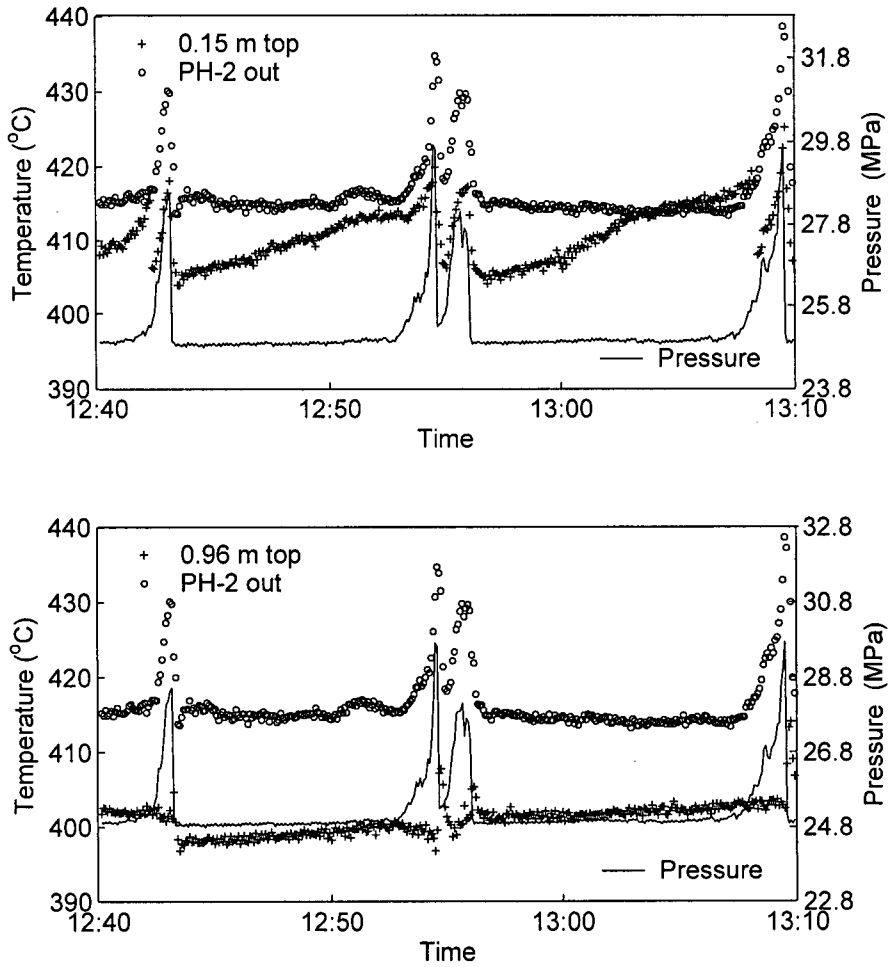

Figure A.5: Temperature and pressure behavior for the combined heterogeneous & homogeneous nucleation run (Experiment 7)

due to salt deposition. It was noticed that the surface thermocouples upstream of the bulk fluid thermocouple at the middle of the test section showed an increase in temperature with an increase in pressure and fluid temperature of pre-heater 2 outlet. This experiment was terminated when the pressure increased to 28.9 MPa after 55 minutes of operation with salt solution. Pressure at the end of the test section remained constant during the run. The salt deposition-removal cycle at 15:32 & 15:44 are shown in Fig. A.8. In both the cycles, the surface thermocouples upstream of the 1.4 m location showed an increase in temperature with an increase in pre-heater 2 outlet temperature and pressure. The thermocouples measuring the fluid temperature at the middle of the test section and the later portion of the test section showed either the same temperature or reduced a bit until the plug was washed away. Thus the plug could possibly be due to the thermocouple protruding in the fluid flow area, at

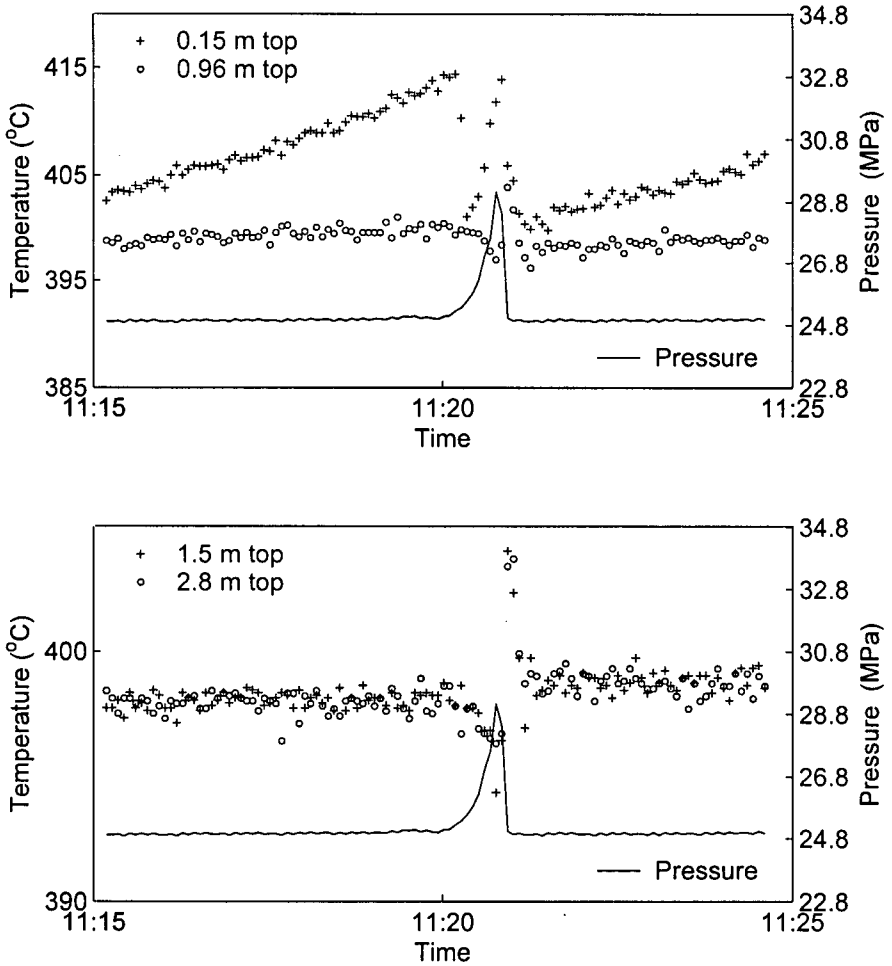

Figure A.6: Temperature and pressure behavior for the combined heterogeneous & homogeneous nucleation run (Experiment 11)

the middle of the test section, causing salt particle accumulation at this location. It was therefore decided to remove the bulk fluid thermocouple at the middle of the test section for the next experiment. The Na_2CO_3 solubility under test section conditions was 0.02 wt.% and the salt concentration the effluent tank was 0.0817 wt.%. The ratio of effluent salt concentration to saturation limit was thus 4.2. The experiment was terminated after 55 minutes due to plugging.

A.2.2 Experiment: 10

This experiment was carried out after removing the bulk fluid thermocouple at the middle of the test section. Other experimental conditions were kept the same as those

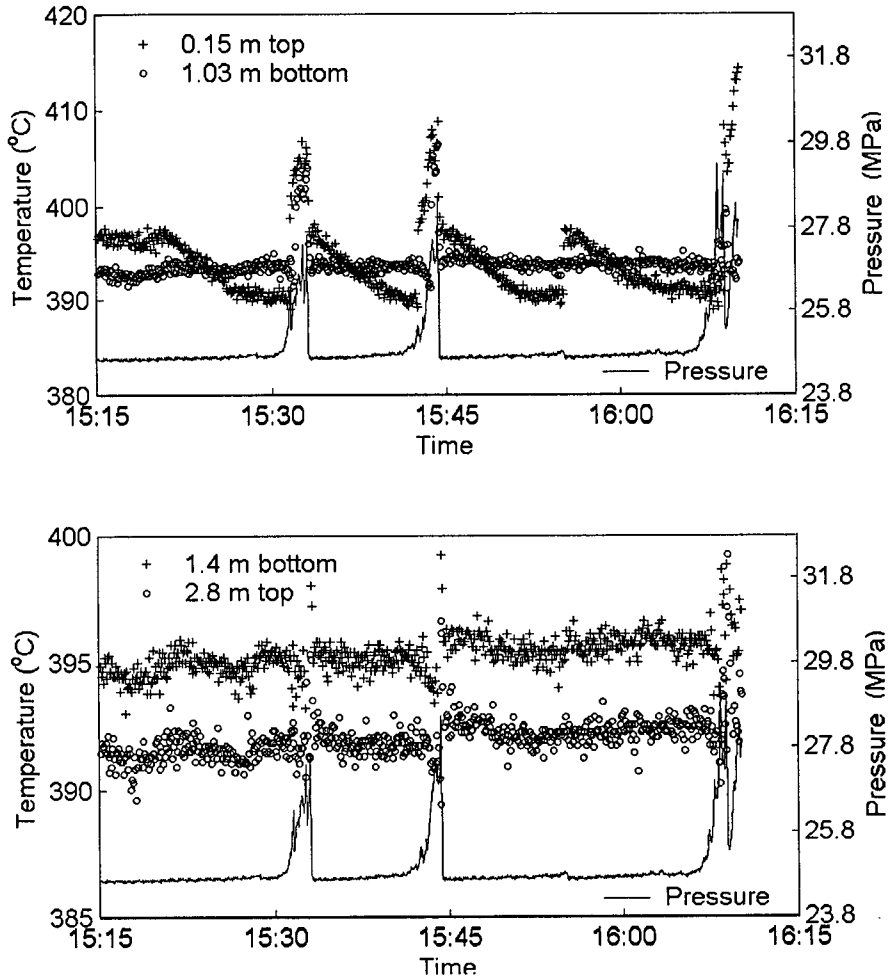

Figure A.7: Temperature and pressure behavior for the combined heterogeneous and homogeneous nucleation unheated test section run (Experiment 8)

of Experiment 11, for comparison purposes. It was noticed that the bulk fluid thermocouple had actually been plugging the test section earlier and no major sign of plugging was noticed in this experiment after running for 75 minutes. Salt concentration at the inlet of the test section was 0.1 wt.% and in the effluent tank the concentration was 0.09 wt.%. Therefore almost all of the salt was flowing through the system. The saturation limit for the test section temperature was 0.018 wt.%. For the run in which the test section is not heated the inner surface temperature was calculated as the average of the first few test section inner surface temperatures. The ratio of effluent salt concentration and saturation limit was 5 i.e., higher than Experiment 11. This experiment has been discussed in detail in Section 5.3.3. It is worth mentioning that a relatively small pressure increase, at the test section inlet, was enough to remove the salt deposit in this experiment as shown in Fig. 5.5. Therefore the bulk fluid temperature at pre-heater 2

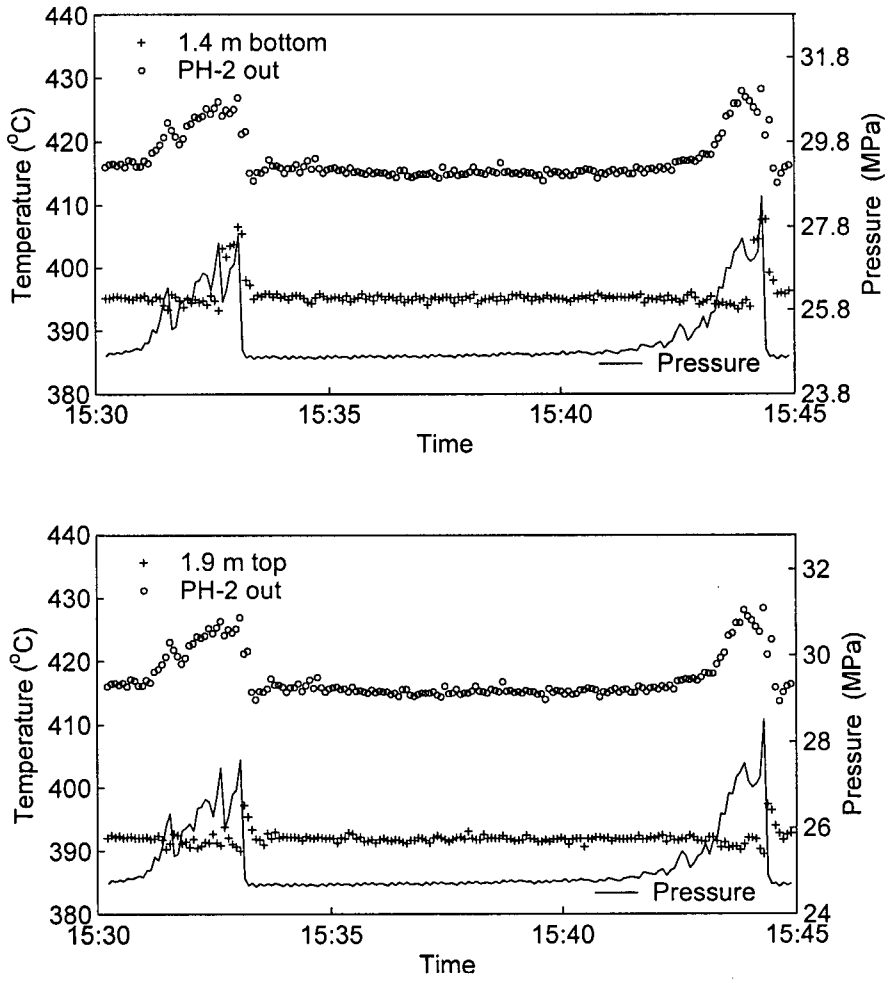

Figure A.8: Temperature and pressure behavior for the combined heterogeneous and homogeneous nucleation unheated test section run (Experiment 8)

outlet did not increase much during the deposition process as observed in Experiment 8 and the combined heterogeneous-homogeneous nucleation experiments. It can therefore be concluded that no major plug was occuring in the test section, therefore the data was not analyzed to determine its location.

A.3 Heterogeneous nucleation runs: Solubility type experiments

The heat input to the test section in these experiments was higher than the typical experiments carried out to determine the salt solubility. Also pure water was passed through the pre-heaters and salt solution was injected before the test section. How-

ever, the bulk fluid temperature after mixing was such that the salt solution remained subsaturated.

A.3.1 Experiment: 9

The hot fluid bulk temperature at pre-heater 2 outlet was set such that no salt homogeneous nucleation occurred when salt solution was injected at the test section inlet. High heat input (~7.5 kW) to the test section was thus required to achieve supersaturation conditions within the test section length. Salt solution was injected at 11:12. No cleaning cycles were observed (as seen in the homogeneous case) and the test section temperature (& pressure) increased steadily along the test section as shown in Fig. A.9. The pressure increased by about 172 kPa during the 40-minute run, which had to be terminated because of excessive surface temperature. At some test section locations the surface temperature increased in excess of 160°C, due to the salt deposit layer. The test section fluid outlet temperature did not increase much during this period. The conductivity was not constant and was around 380 μS/cm most of the time (Na_2CO_3 concentration of 0.018 wt.%) which is also the saturation limit corresponding to the clean test section inner-surface temperature i.e., 397°C. Thus this run was almost like the solubility experiment.

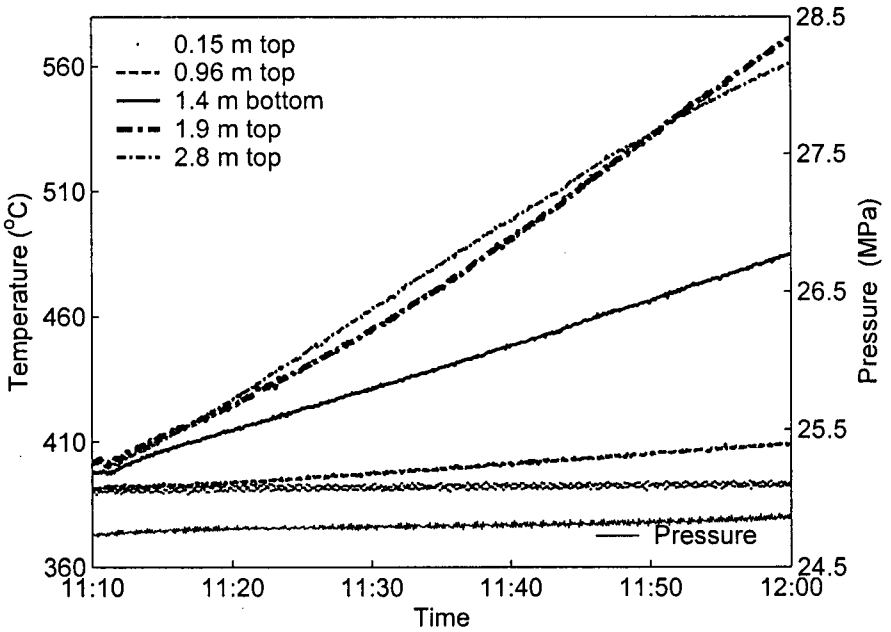

Figure A.9: Temperature and pressure behavior for the heterogeneous nucleation run (Experiment 9)

A.3.2 Experiment: 12

This experiment was performed under conditions similar to Experiment 10 but with a lower pre-heater 2 fluid exit temperature to ensure no homogeneous salt nucleation when salt solution was mixed in supercritical water. A high heat input (~15 kW) to the test section was thus required to achieve supersaturation in the test section and to have bulk fluid test section outlet temperature the same as that in Experiment 10. The high heating resulted in a temperature difference of about 10°C, between the adjacent top and bottom surface thermocouples. The experiment was therefore terminated and the data were not analyzed.

Appendix B

SEM photographs of Na_2CO_3 and Na_2SO_4 deposits

B.1 Na_2CO_3 deposits

Table B.1: Summary of Na_2CO_3 pure crystalline deposit characteristics (Experiment SEM-4)

SEM figure number	Deposit location (cm)	Deposit thickness (mm)	Crystal length (mm)	Comments
B.1-B.4	139	0.3	0.008-0.3	crystals of various lengths
B.5-B.11	109	0.3	0.03-0.3	long and irregularly shaped crystals
B.12-B.15	79	0.36	0.01-0.36	long and irregularly shaped crystals
B.16-B.22	64	0.4	0.01-0.4	crystals and needle shaped dendrites
B.13-B.24	49	0.36		dense crystalline deposit
B.25-B.27	19	0.1		dense deposits, non uniform thickness

Table B.2: Summary of Na_2CO_3 combined crystalline and particulate deposit characteristics (Experiment SEM-3)

SEM figure number	Deposit location (cm)	Deposit thickness (mm)	Particle size (mm)	Comments
B.28-B.37	154	0.7	0.005-0.01	irregularly shaped particles and crystals
B.38-B.44	139	0.59		irregularly shaped salt particles
B.45-B.50	109	0.7	0.004-0.01	crystals and particles
B.51-B.56	79	0.21	0.001-0.004	particles and long crystals
B.57-B.62	49	0.1	0.001-0.015	particles and long crystals

B.1.1 Na_2CO_3 crystalline scale

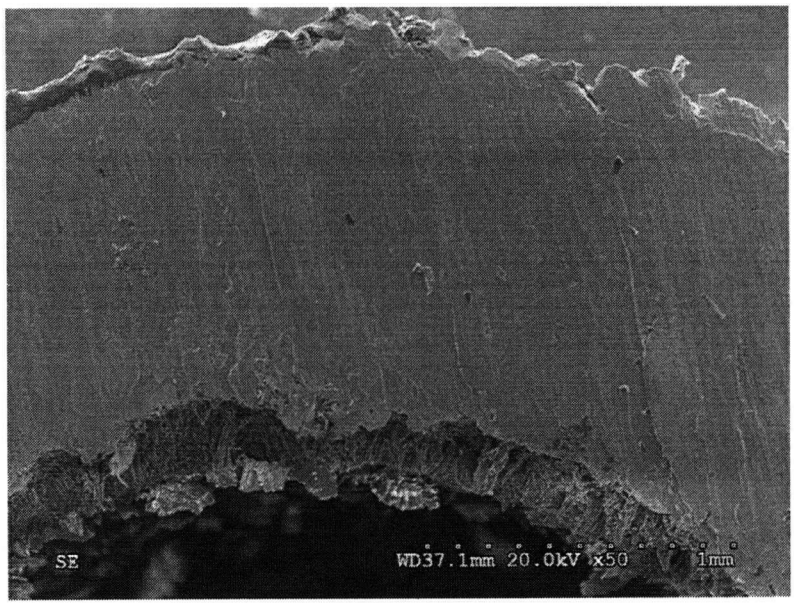

Figure B.1: SEM photograph of the Na_2CO_3 deposition due to heterogeneous nucleation at 139 cm location (Experiment SEM-4)

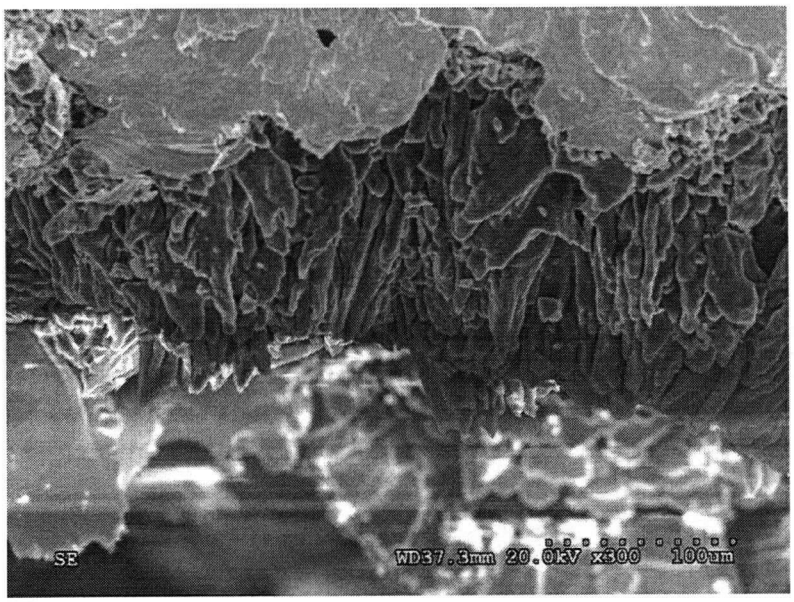

Figure B.2: SEM photograph of the Na_2CO_3 deposition due to heterogeneous nucleation at 139 cm location (Experiment SEM-4)

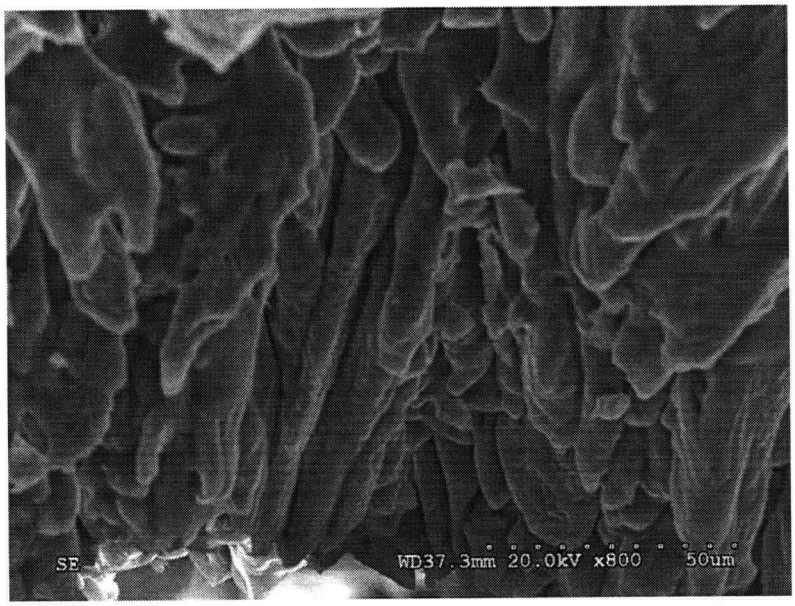

Figure B.3: SEM photograph of the Na_2CO_3 deposition due to heterogeneous nucleation at 139 cm location (Experiment SEM-4)

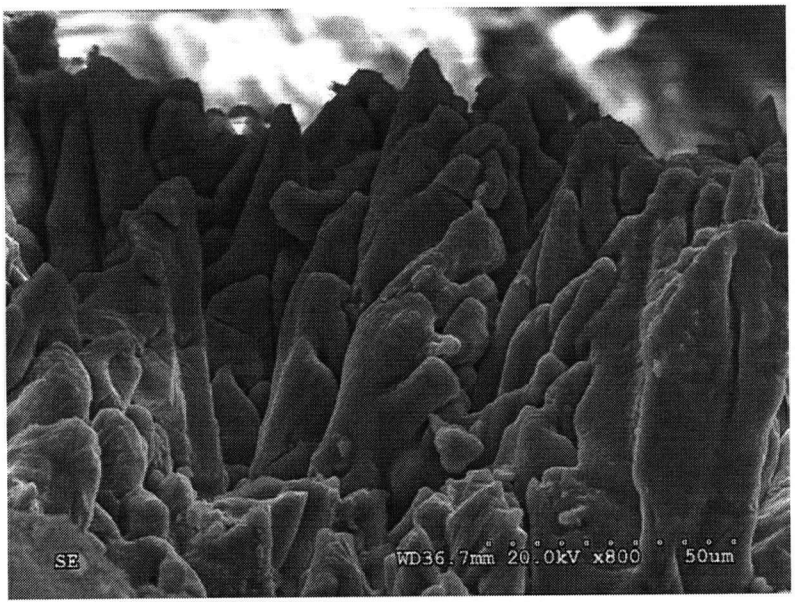

Figure B.4: SEM photograph of the Na_2CO_3 deposition due to heterogeneous nucleation at 139 cm location (Experiment SEM-4)

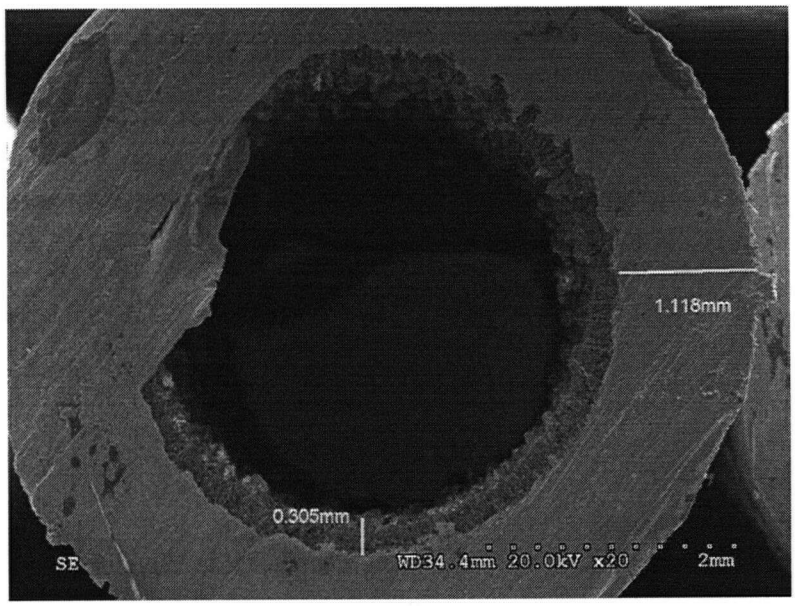

Figure B.5: SEM photograph of the Na_2CO_3 deposition due to heterogeneous nucleation at 109 cm location (Experiment SEM-4)

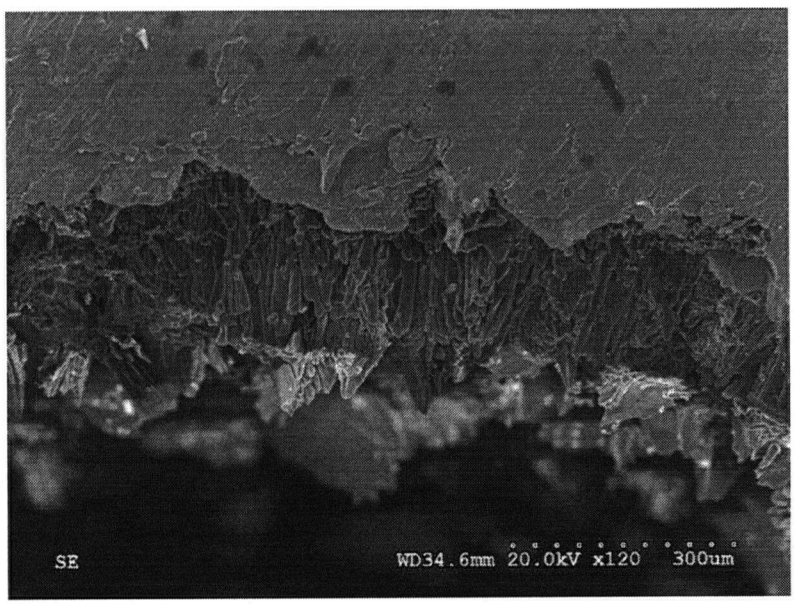

Figure B.6: SEM photograph of the Na_2CO_3 deposition due to heterogeneous nucleation at 109 cm location (Experiment SEM-4)

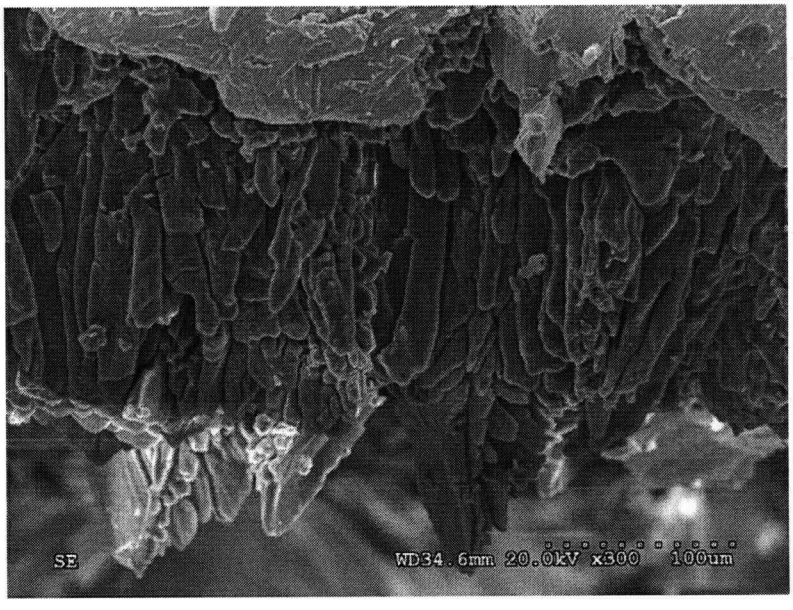

Figure B.7: SEM photograph of the Na_2CO_3 deposition due to heterogeneous nucleation at 109 cm location (Experiment SEM-4)

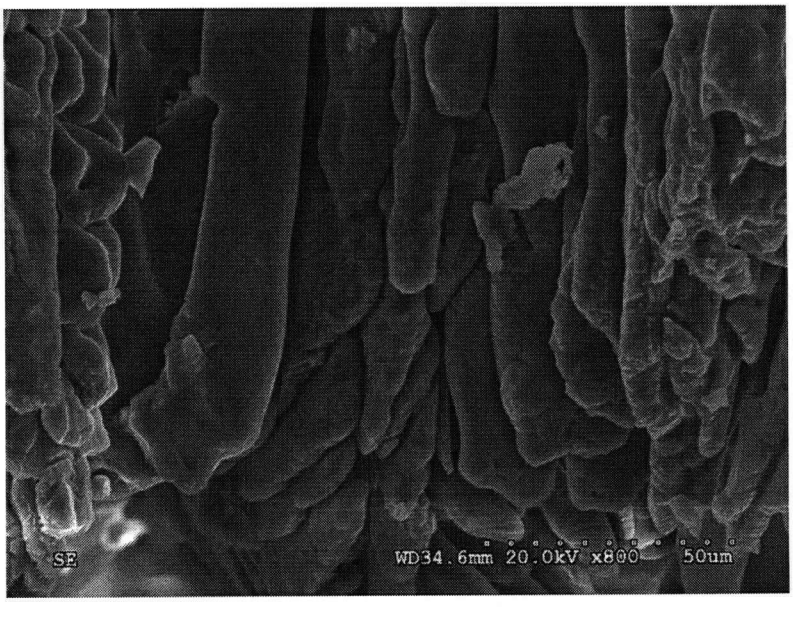

Figure B.8: SEM photograph of the Na_2CO_3 deposition due to heterogeneous nucleation at 109 cm location (Experiment SEM-4)

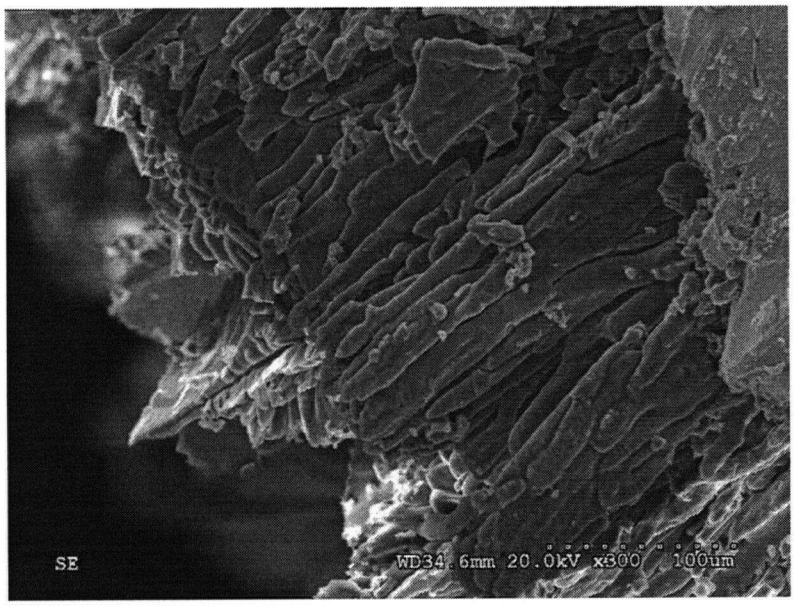

Figure B.9: SEM photograph of the Na_2CO_3 deposition due to heterogeneous nucleation at 109 cm location (Experiment SEM-4)

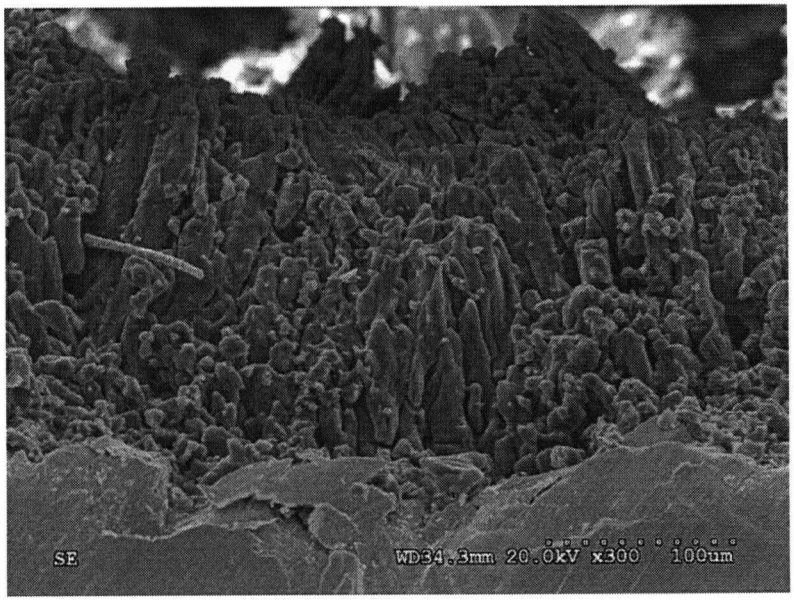

Figure B.10: SEM photograph of the Na_2CO_3 deposition due to heterogeneous nucleation at 109 cm location (Experiment SEM-4)

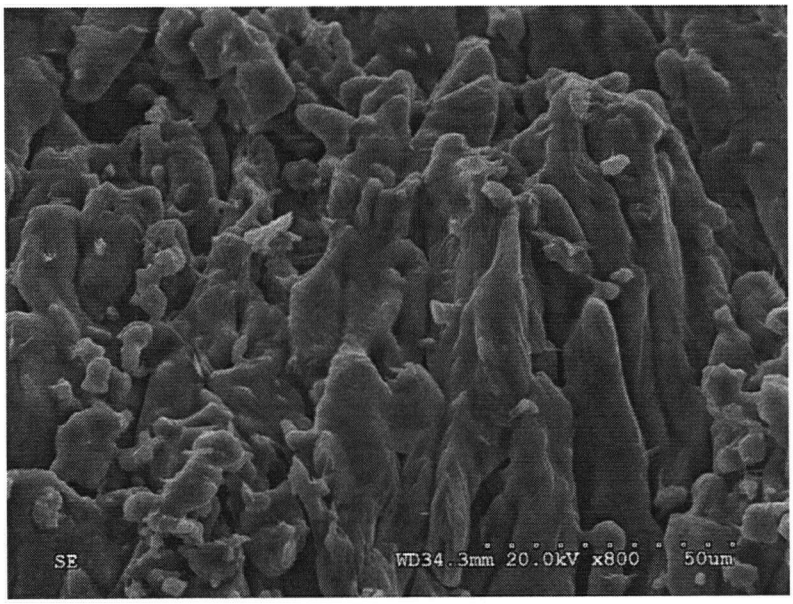

Figure B.11: SEM photograph of the Na_2CO_3 deposition due to heterogeneous nucleation at 109 cm location (Experiment SEM-4)

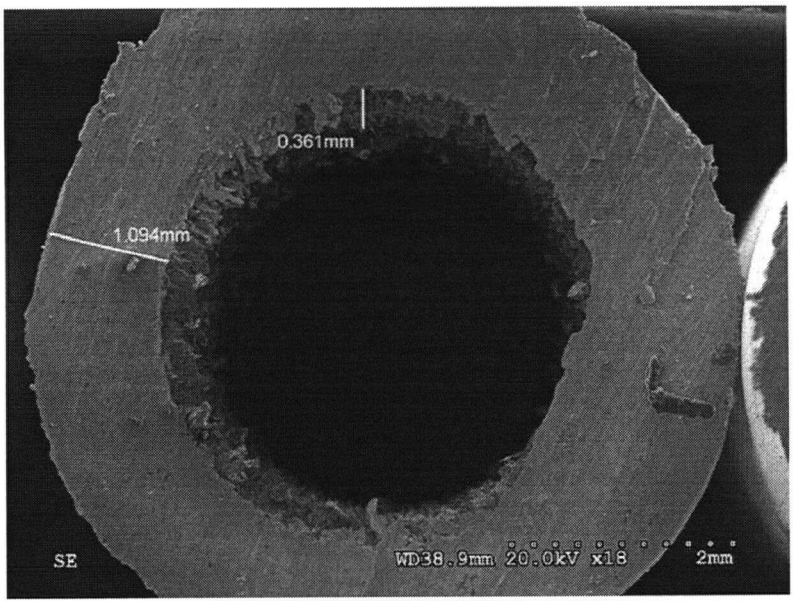

Figure B.12: SEM photograph of the Na_2CO_3 deposition due to heterogeneous nucleation at 79 cm location (Experiment SEM-4)

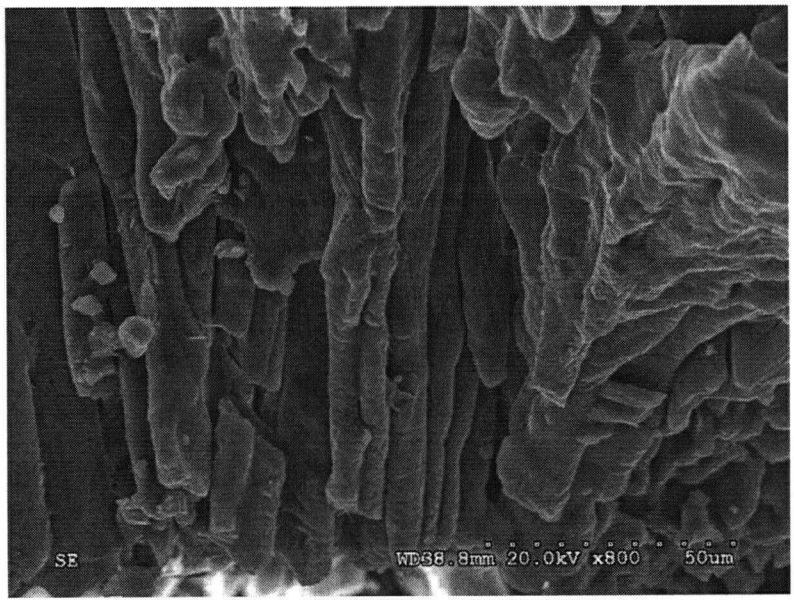

Figure B.13: SEM photograph of the Na_2CO_3 deposition due to heterogeneous nucleation at 79 cm location (Experiment SEM-4)

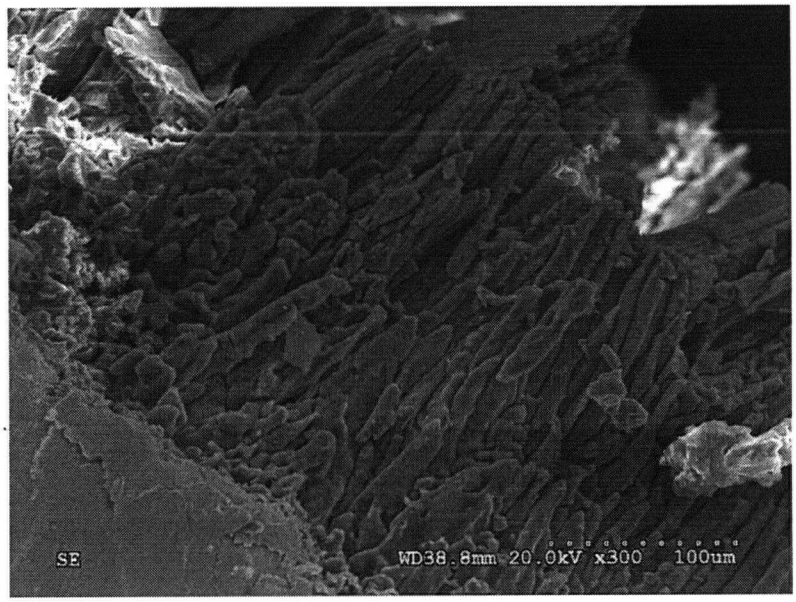

Figure B.14: SEM photograph of the Na_2CO_3 deposition due to heterogeneous nucleation at 79 cm location (Experiment SEM-4)

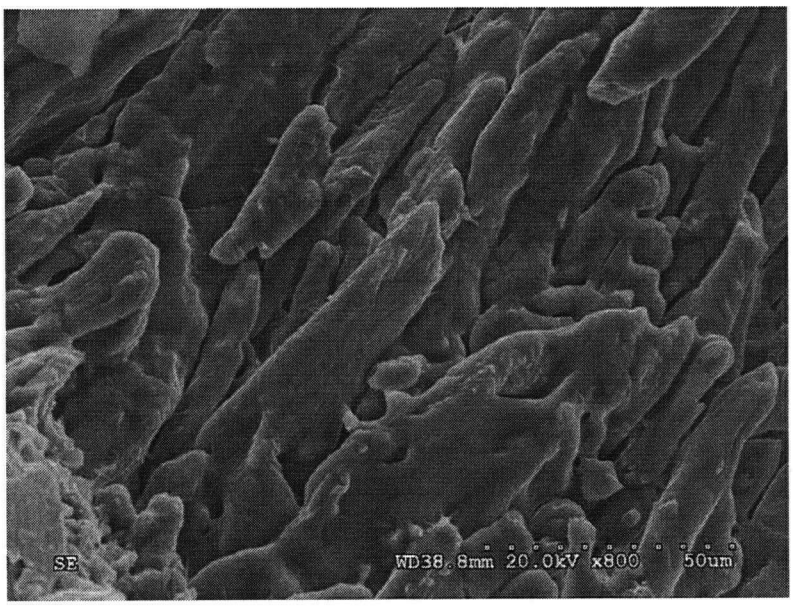

Figure B.15: SEM photograph of the Na_2CO_3 deposition due to heterogeneous nucleation at 79 cm location (Experiment SEM-4)

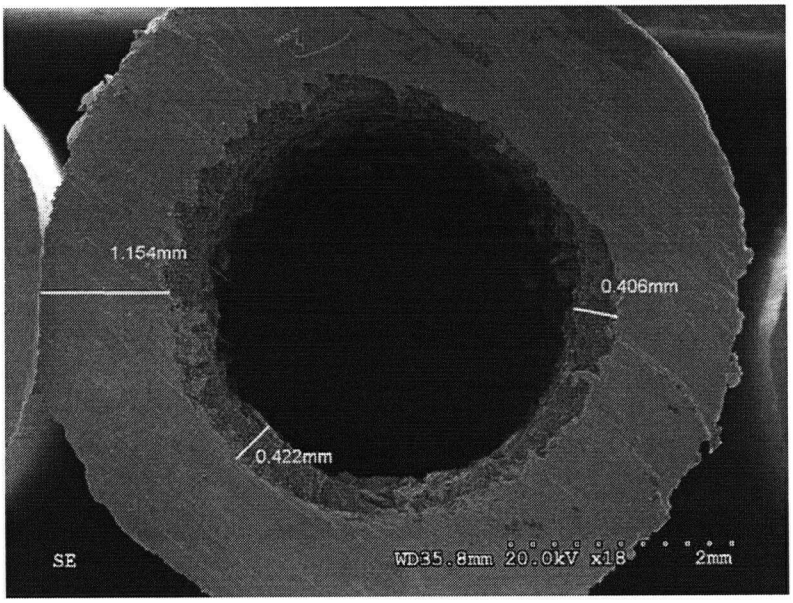

Figure B.16: SEM photograph of the Na_2CO_3 deposition due to heterogeneous nucleation at 64 cm location (Experiment SEM-4)

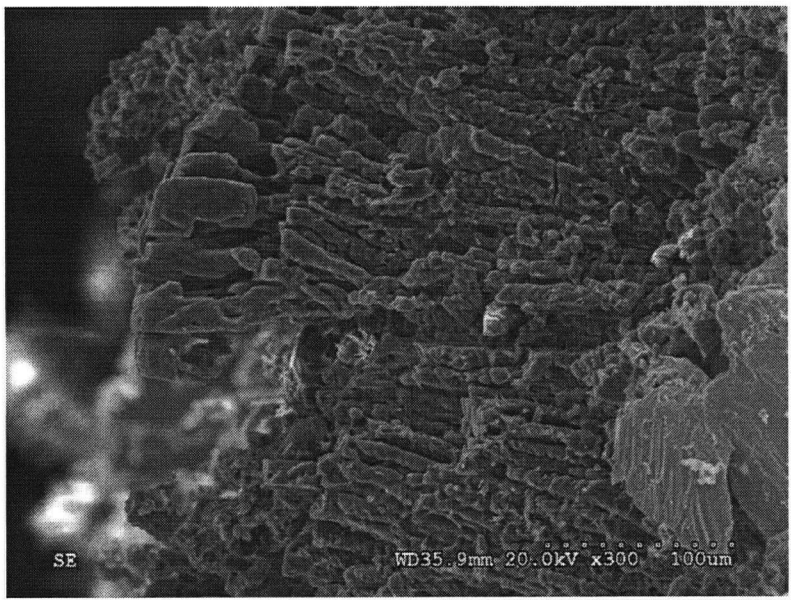

Figure B.17: SEM photograph of the Na_2CO_3 deposition due to heterogeneous nucleation at 64 cm location (Experiment SEM-4)

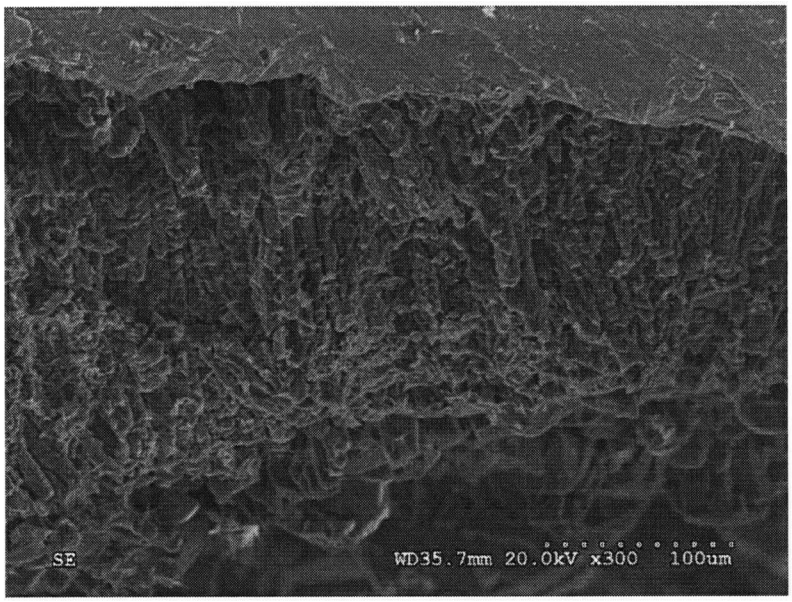

Figure B.18: SEM photograph of the Na_2CO_3 deposition due to heterogeneous nucleation at 64 cm location (Experiment SEM-4)

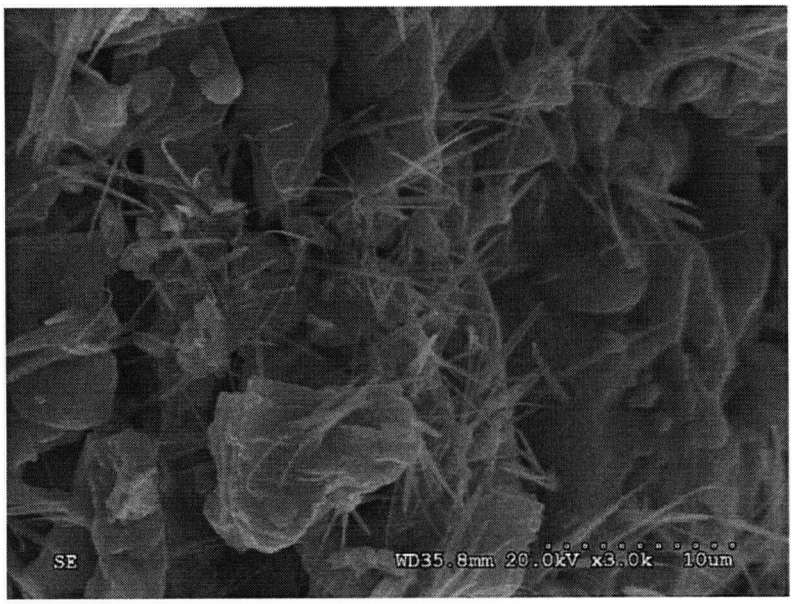

Figure B.19: SEM photograph of the Na_2CO_3 deposition due to heterogeneous nucleation at 64 cm location (Experiment SEM-4)

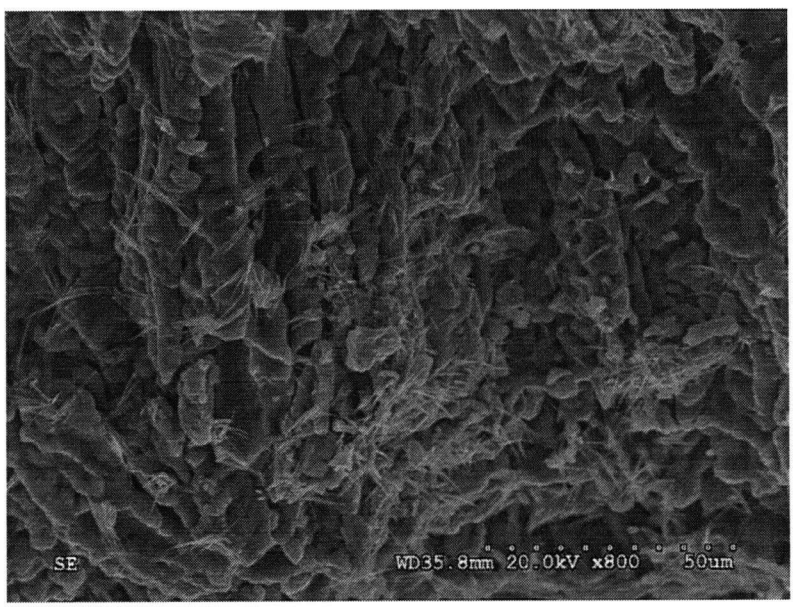

Figure B.20: SEM photograph of the Na_2CO_3 deposition due to heterogeneous nucleation at 64 cm location (Experiment SEM-4)

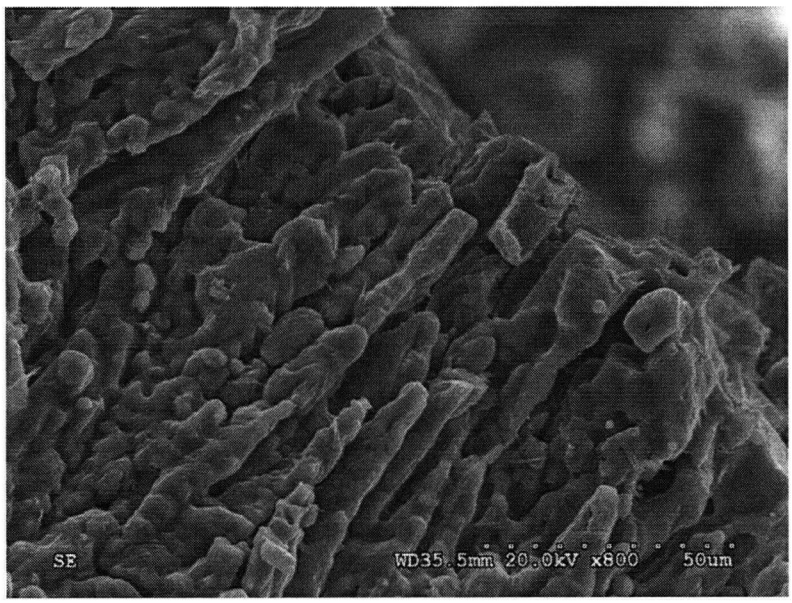

Figure B.21: SEM photograph of the Na_2CO_3 deposition due to heterogeneous nucleation at 64 cm location (Experiment SEM-4)

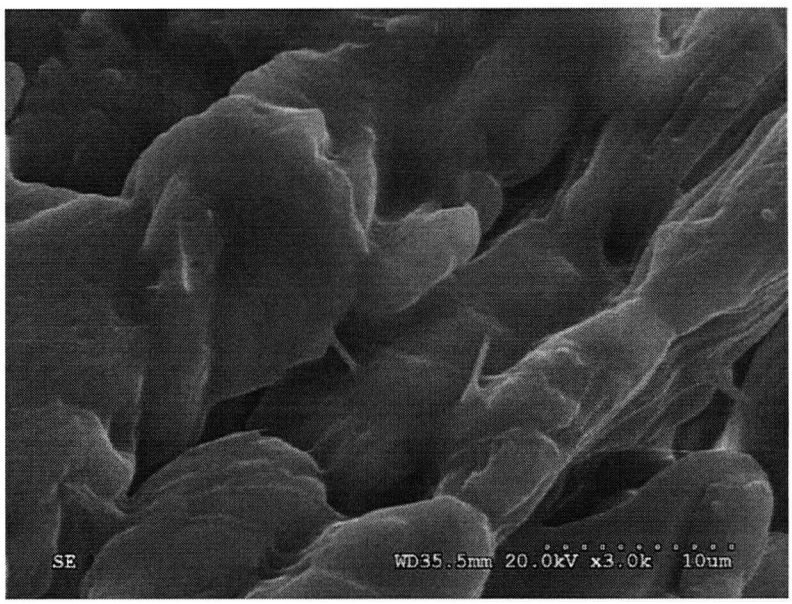

Figure B.22: SEM photograph of the Na_2CO_3 deposition due to heterogeneous nucleation at 64 cm location (Experiment SEM-4)

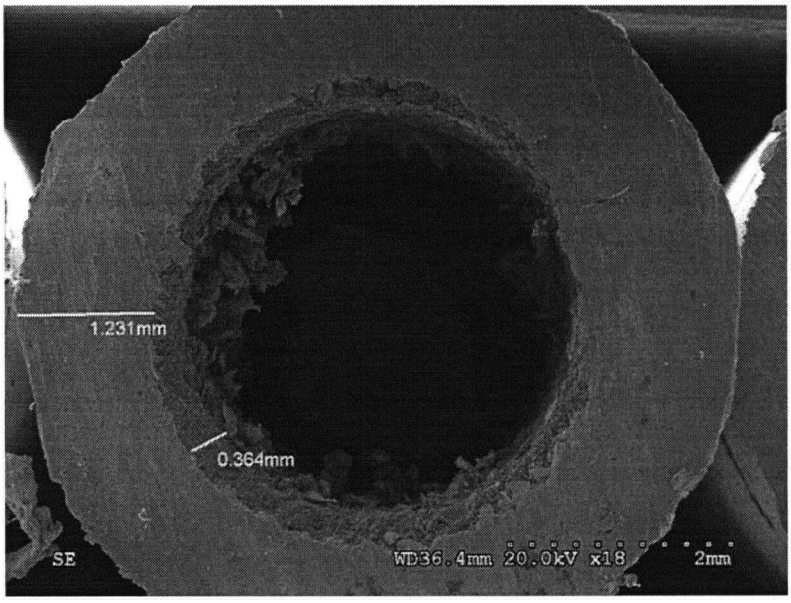

Figure B.23: SEM photograph of the Na_2CO_3 deposition due to heterogeneous nucleation at 49 cm location (Experiment SEM-4)

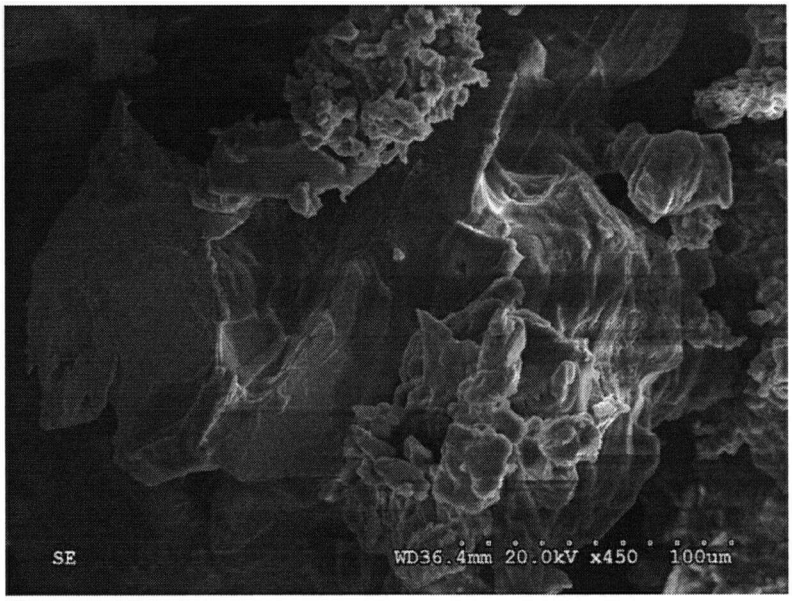

Figure B.24: SEM photograph of the Na_2CO_3 deposition due to heterogeneous nucleation at 49 cm location (Experiment SEM-4)

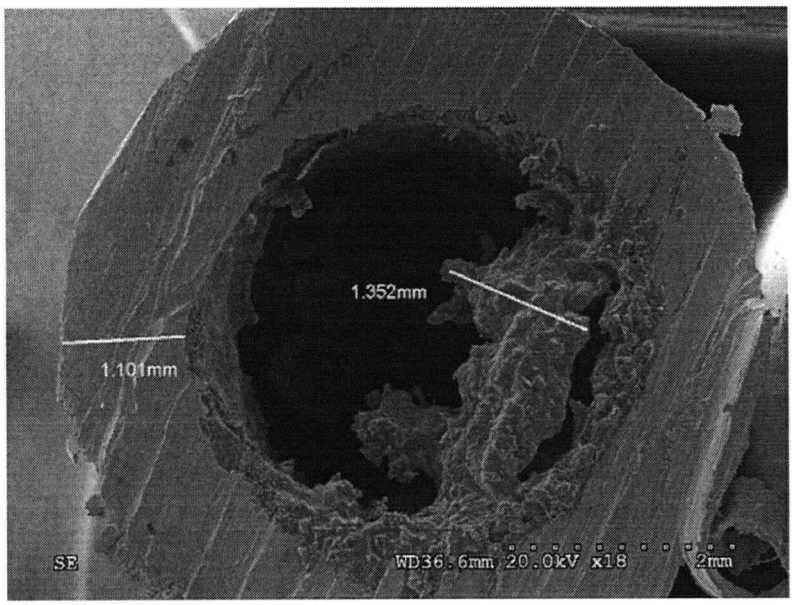

Figure B.25: SEM photograph of the Na_2CO_3 deposition due to heterogeneous nucleation at 19 cm location (Experiment SEM-4)

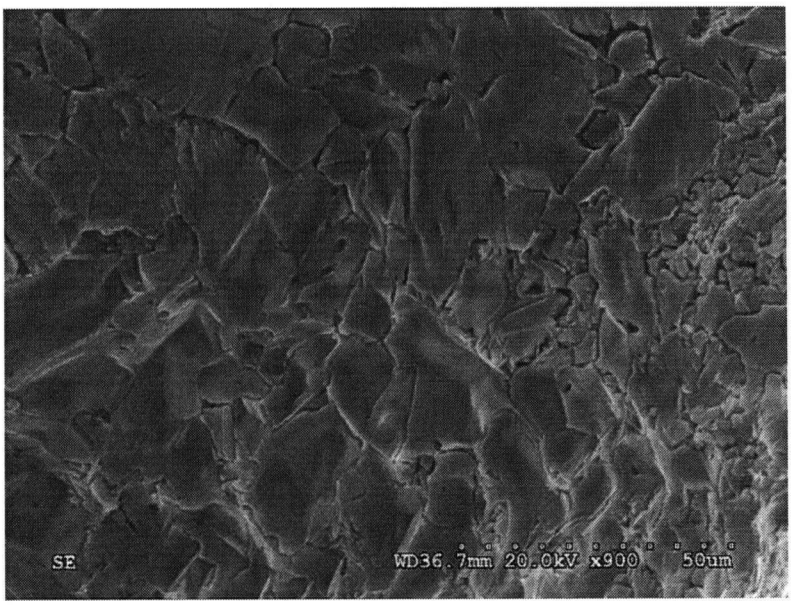

Figure B.26: SEM photograph of the Na_2CO_3 deposition due to heterogeneous nucleation at 19 cm location (Experiment SEM-4)

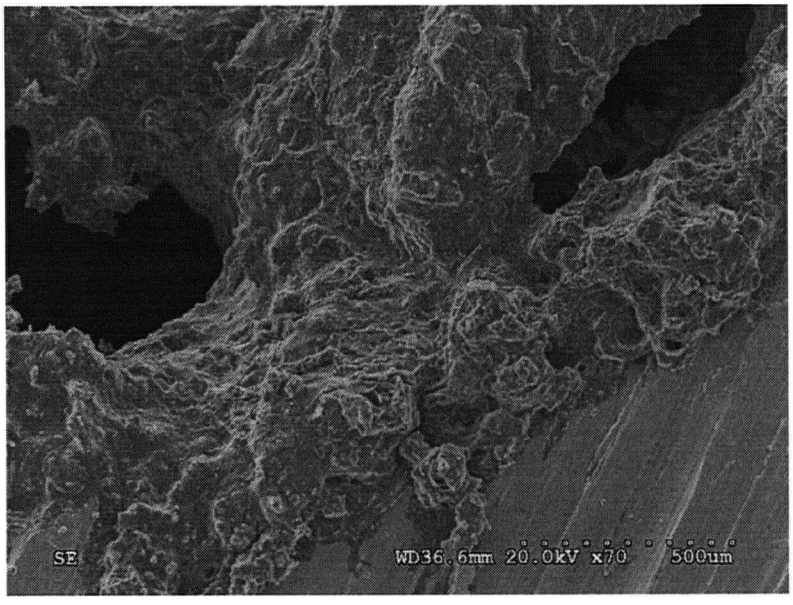

Figure B.27: SEM photograph of the Na_2CO_3 deposition due to heterogeneous nucleation at 19 cm location (Experiment SEM-4)

B.1.2 Na_2CO_3 combined crystalline and particulate deposits

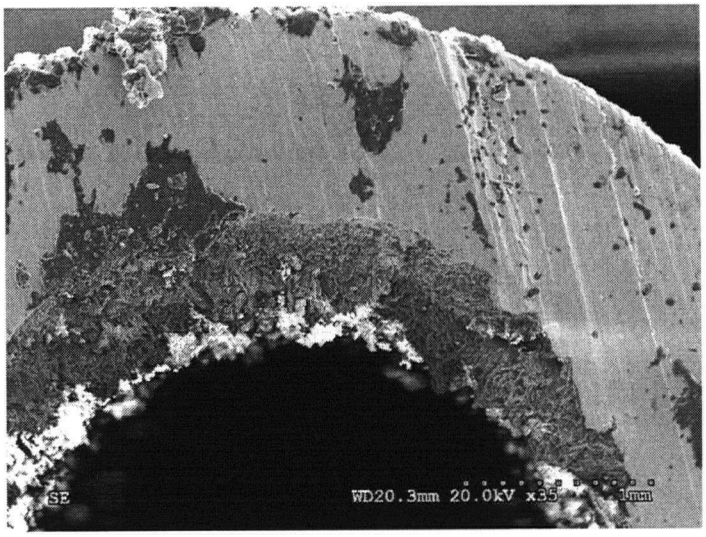

Figure B.28: SEM photograph of the Na_2CO_3 deposition due to combined homogeneous & heterogeneous nucleation at 154 cm location (Experiment SEM-3)

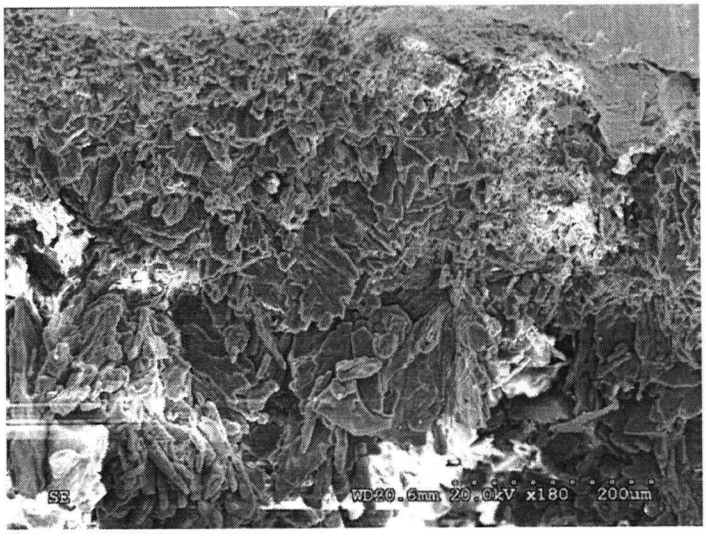

Figure B.29: SEM photograph of the Na_2CO_3 deposition due to combined homogeneous & heterogeneous nucleation at 154 cm location (Experiment SEM-3)

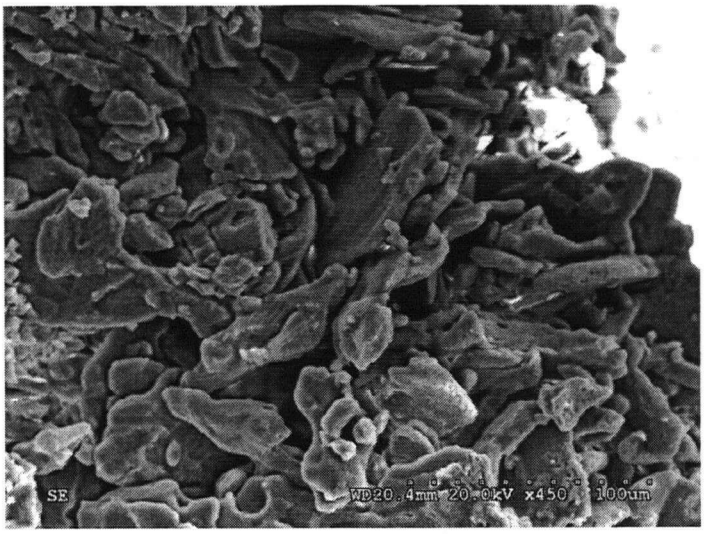

Figure B.30: SEM photograph of the Na_2CO_3 deposition due to combined homogeneous & heterogeneous nucleation at 154 cm location (Experiment SEM-3)

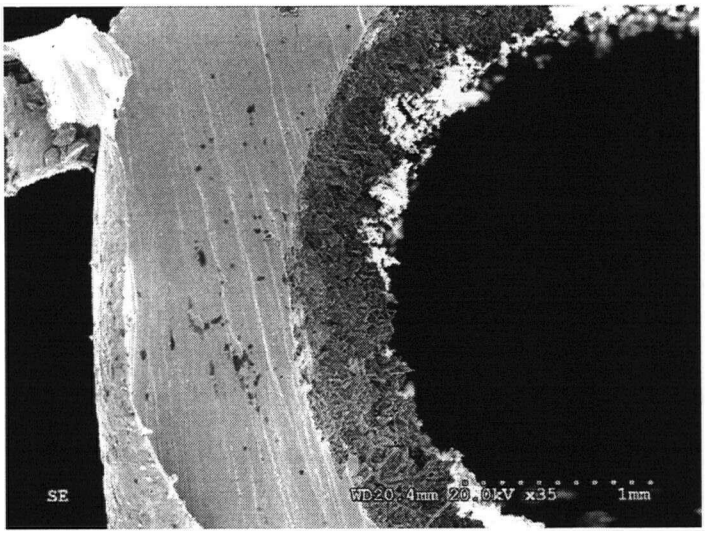

Figure B.31: SEM photograph of the Na_2CO_3 deposition due to combined homogeneous & heterogeneous nucleation at 154 cm location (Experiment SEM-3)

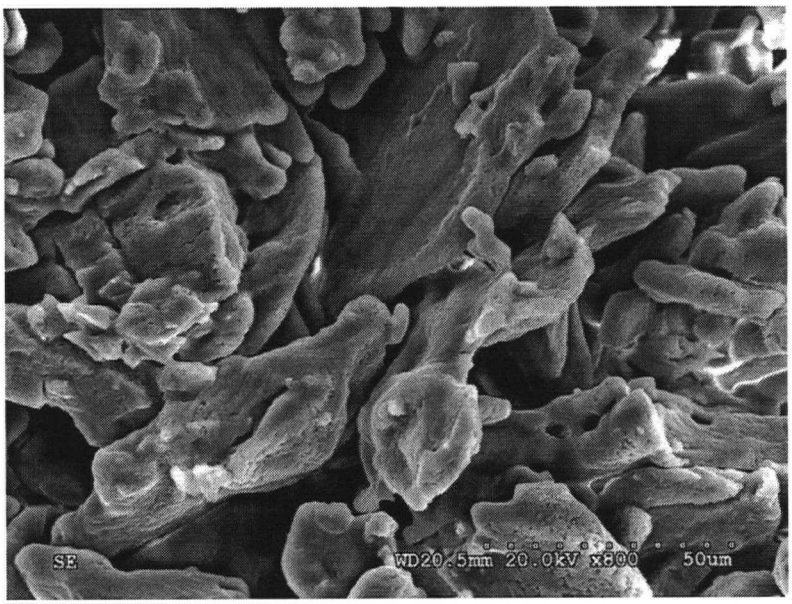

Figure B.32: SEM photograph of the Na_2CO_3 deposition due to combined homogeneous & heterogeneous nucleation at 154 cm location (Experiment SEM-3)

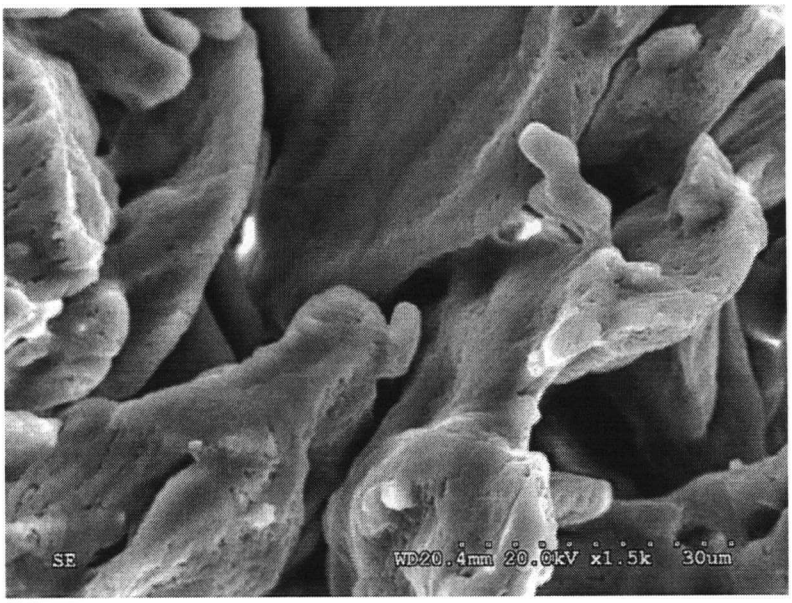

Figure B.33: SEM photograph of the Na_2CO_3 deposition due to combined homogeneous & heterogeneous nucleation at 154 cm location (Experiment SEM-3)

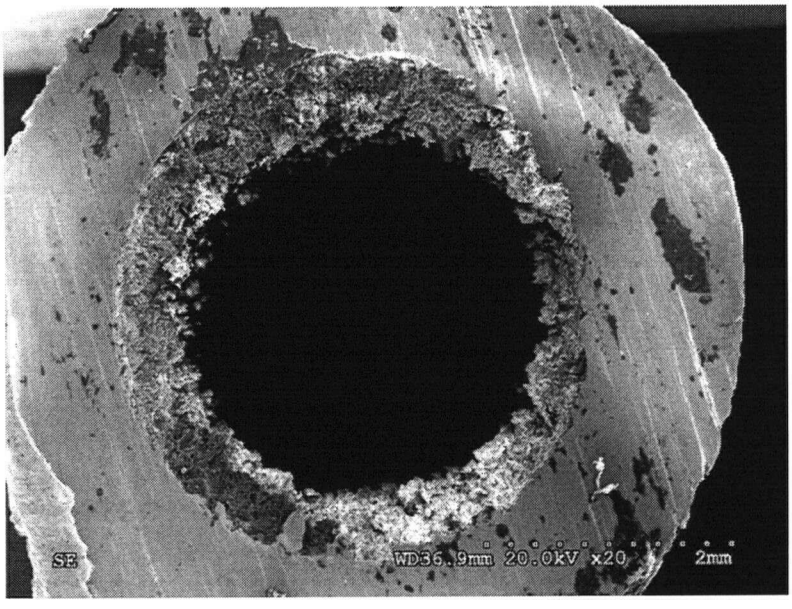

Figure B.34: SEM photograph of the Na_2CO_3 deposition due to combined homogeneous & heterogeneous nucleation at 154 cm location (Experiment SEM-3)

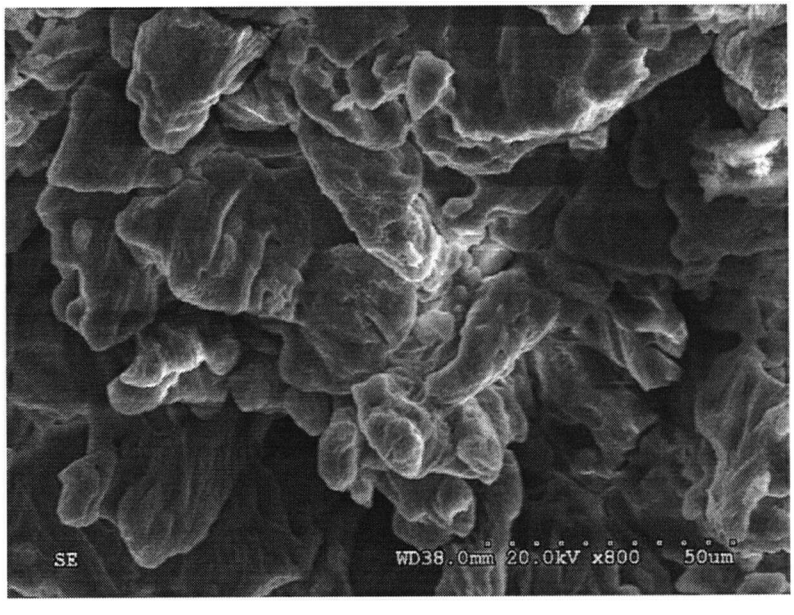

Figure B.35: SEM photograph of the Na_2CO_3 deposition due to combined homogeneous & heterogeneous nucleation at 154 cm location (Experiment SEM-3)

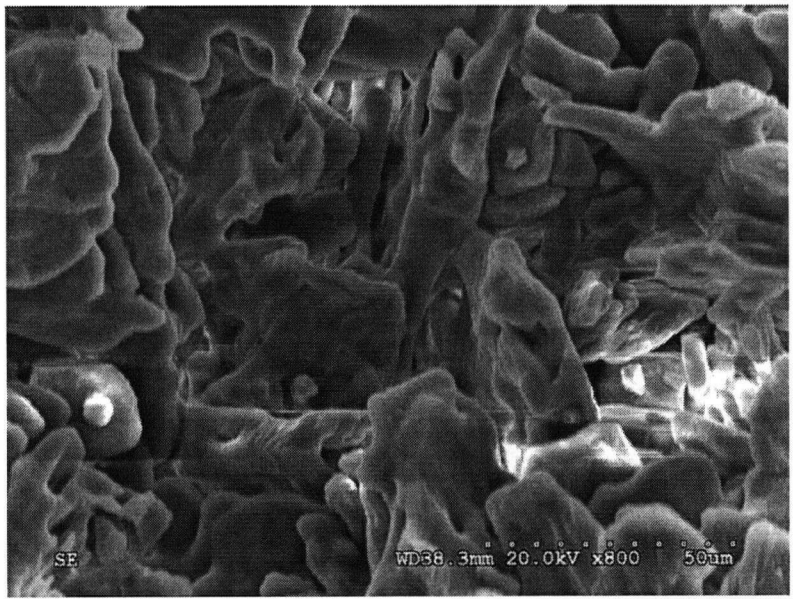

Figure B.36: SEM photograph of the Na_2CO_3 deposition due to combined homogeneous & heterogeneous nucleation at 154 cm location (Experiment SEM-3)

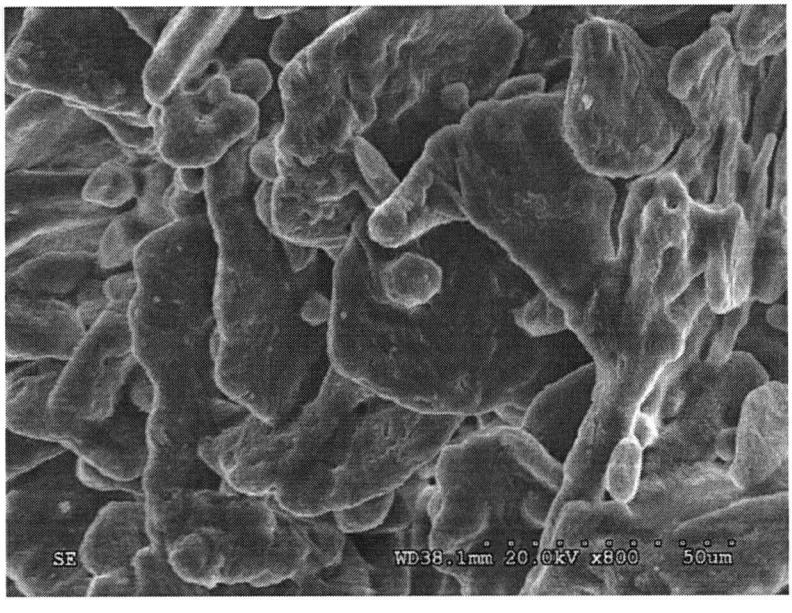

Figure B.37: SEM photograph of the Na_2CO_3 deposition due to combined homogeneous & heterogeneous nucleation at 154 cm location (Experiment SEM-3)

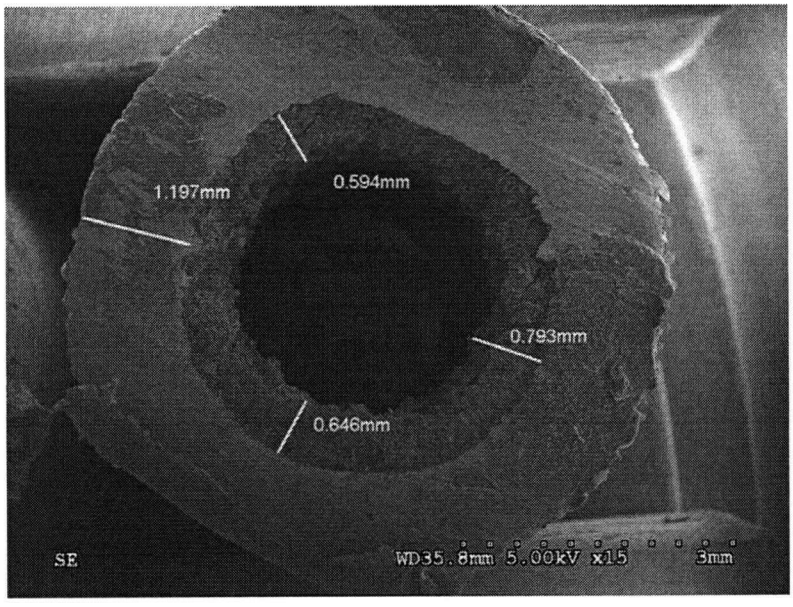

Figure B.38: SEM photograph of the Na_2CO_3 deposition due to combined homogeneous & heterogeneous nucleation at 139 cm location (Experiment SEM-3)

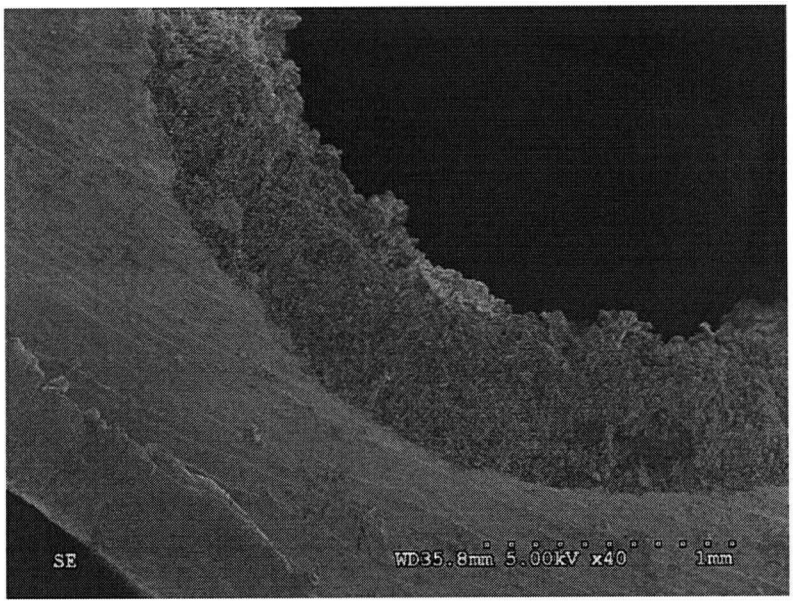

Figure B.39: SEM photograph of the Na_2CO_3 deposition due to combined homogeneous & heterogeneous nucleation at 139 cm location (Experiment SEM-3)

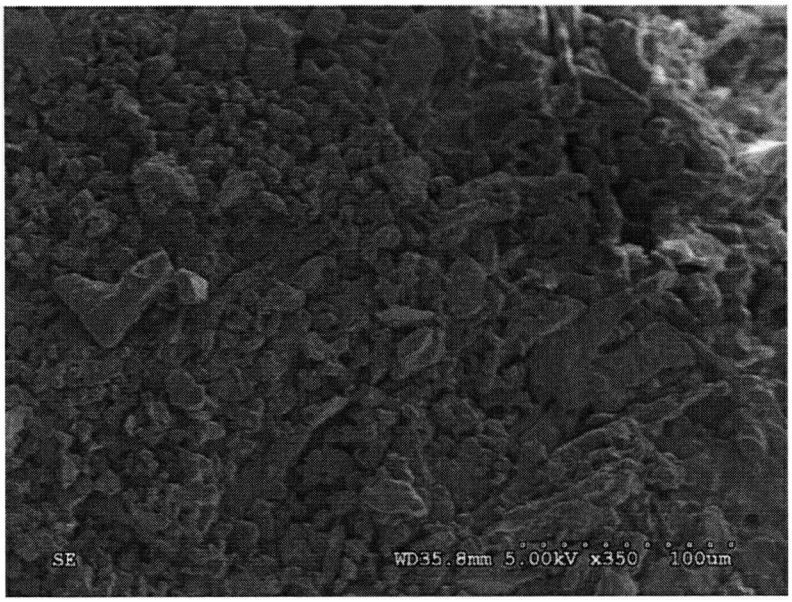

Figure B.40: SEM photograph of the Na_2CO_3 deposition due to combined homogeneous & heterogeneous nucleation at 139 cm location (Experiment SEM-3)

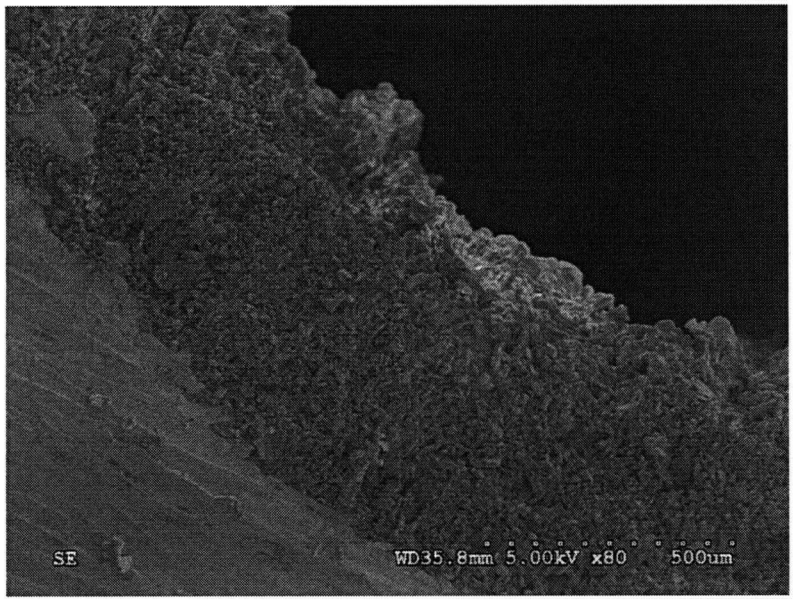

Figure B.41: SEM photograph of the Na_2CO_3 deposition due to combined homogeneous & heterogeneous nucleation at 139 cm location (Experiment SEM-3)

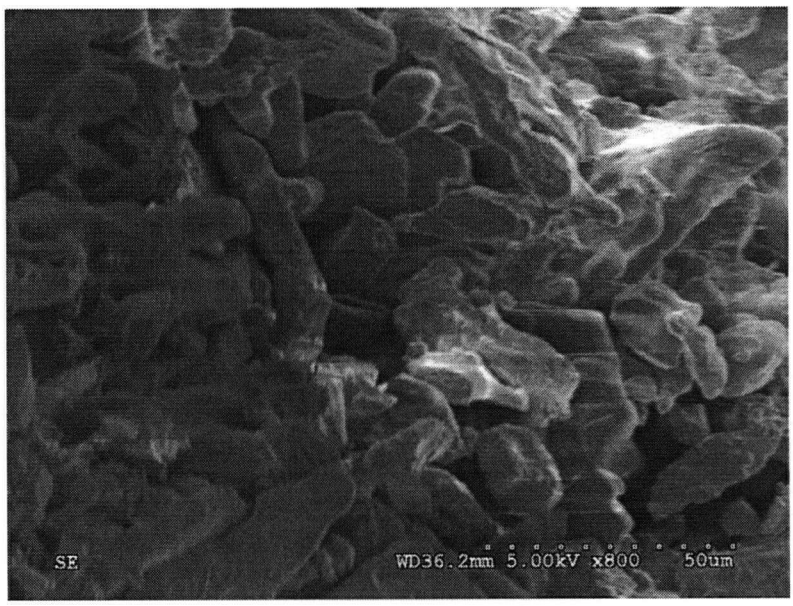

Figure B.42: SEM photograph of the Na_2CO_3 deposition due to combined homogeneous & heterogeneous nucleation at 139 cm location (Experiment SEM-3)

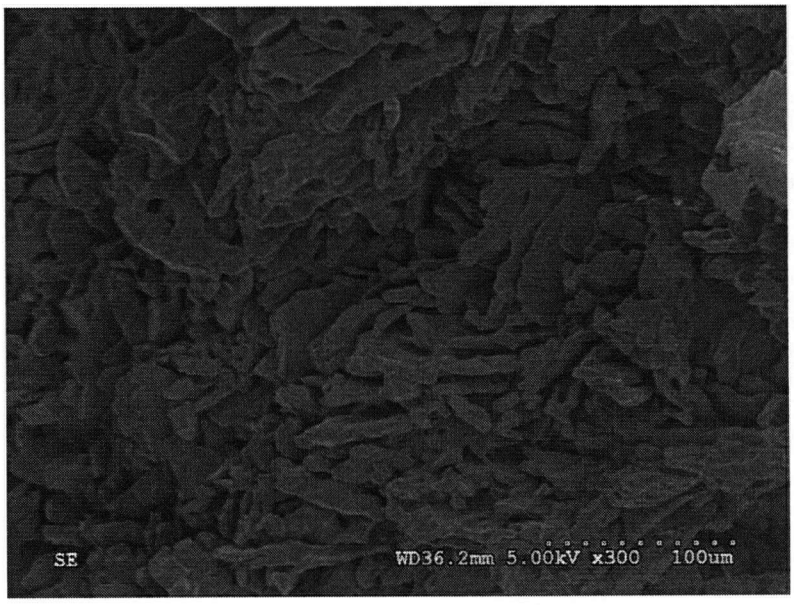

Figure B.43: SEM photograph of the Na_2CO_3 deposition due to combined homogeneous & heterogeneous nucleation at 139 cm location (Experiment SEM-3)

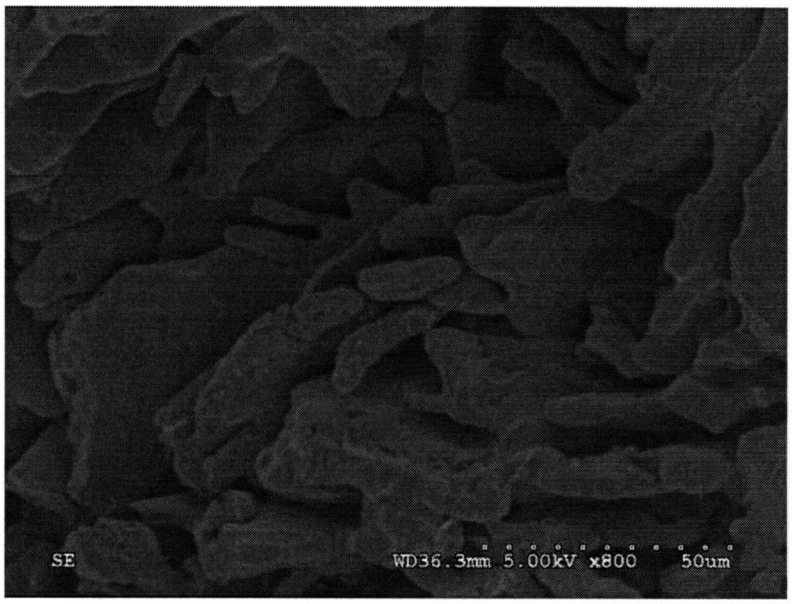

Figure B.44: SEM photograph of the Na_2CO_3 deposition due to combined homogeneous & heterogeneous nucleation at 139 cm location (Experiment SEM-3)

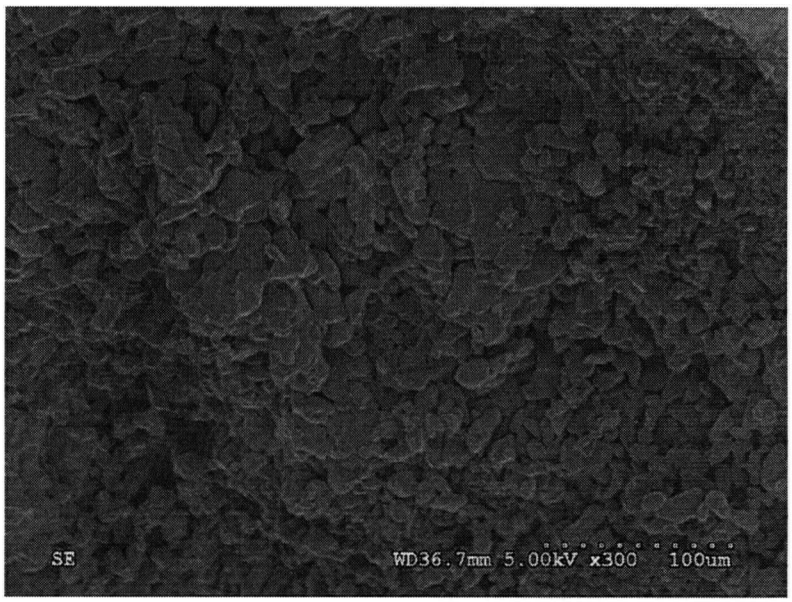

Figure B.45: SEM photograph of the Na_2CO_3 deposition due to combined homogeneous & heterogeneous nucleation at 109 cm location (Experiment SEM-3)

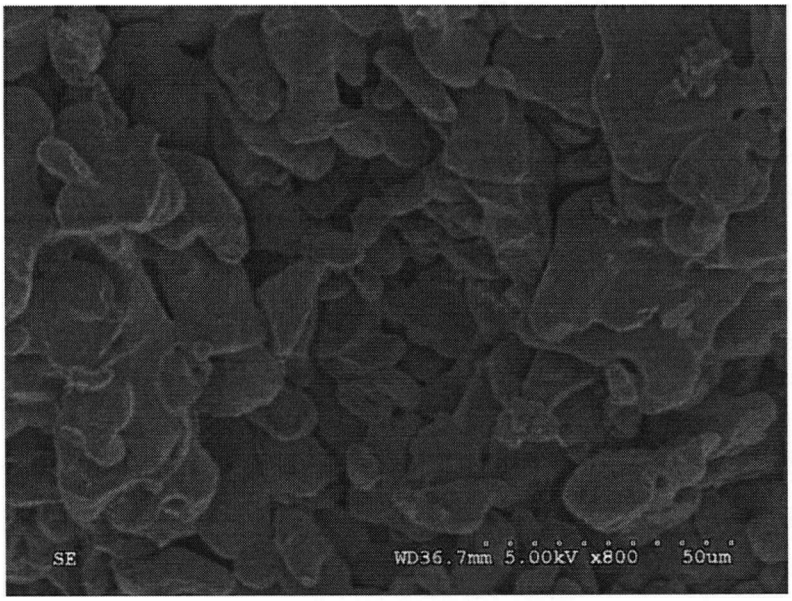

Figure B.46: SEM photograph of the Na_2CO_3 deposition due to combined homogeneous & heterogeneous nucleation at 109 cm location (Experiment SEM-3)

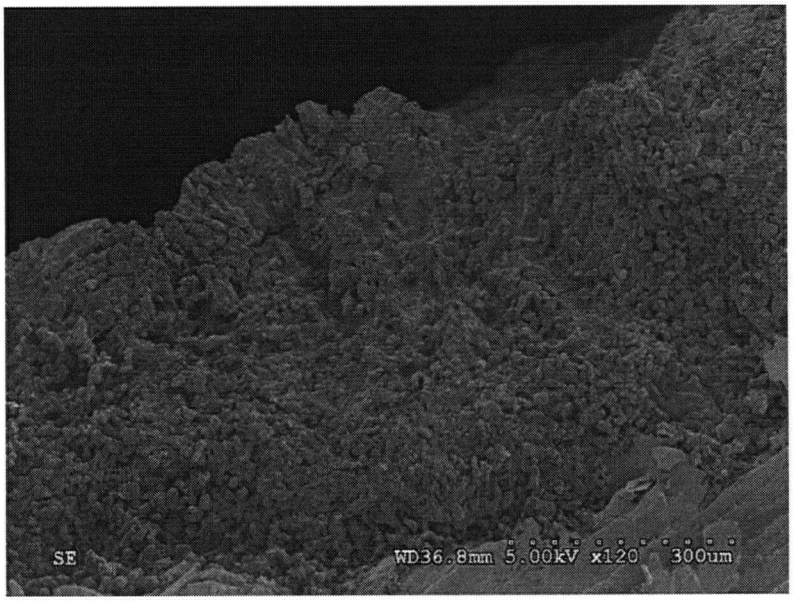

Figure B.47: SEM photograph of the Na_2CO_3 deposition due to combined homogeneous & heterogeneous nucleation at 109 cm location (Experiment SEM-3)

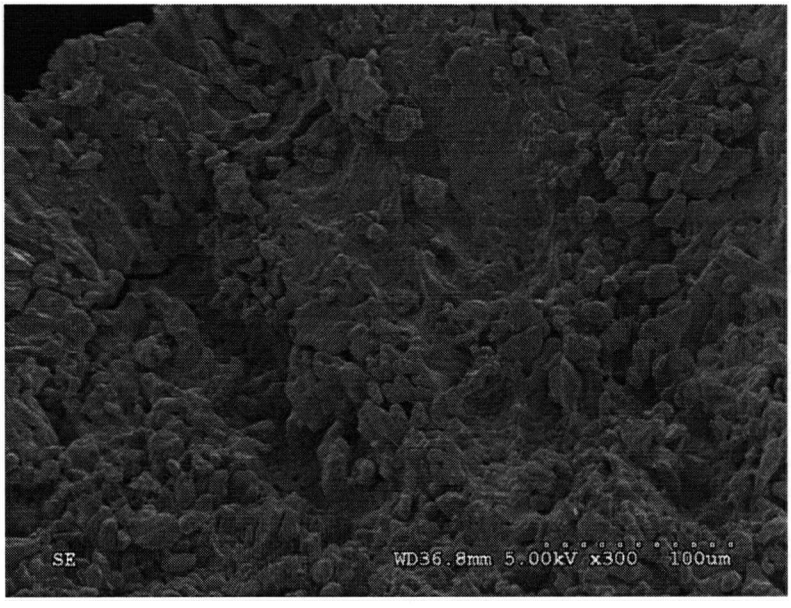

Figure B.48: SEM photograph of the Na_2CO_3 deposition due to combined homogeneous & heterogeneous nucleation at 109 cm location (Experiment SEM-3)

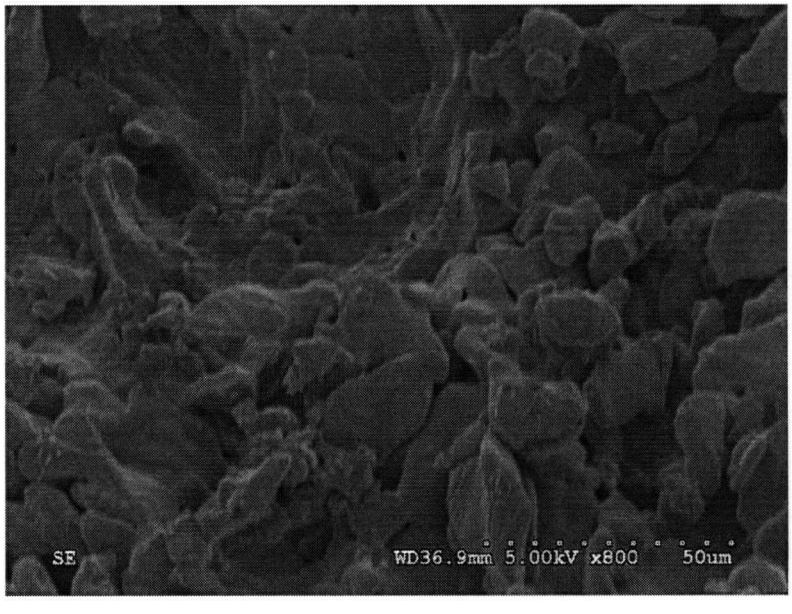

Figure B.49: SEM photograph of the Na_2CO_3 deposition due to combined homogeneous & heterogeneous nucleation at 109 cm location (Experiment SEM-3)

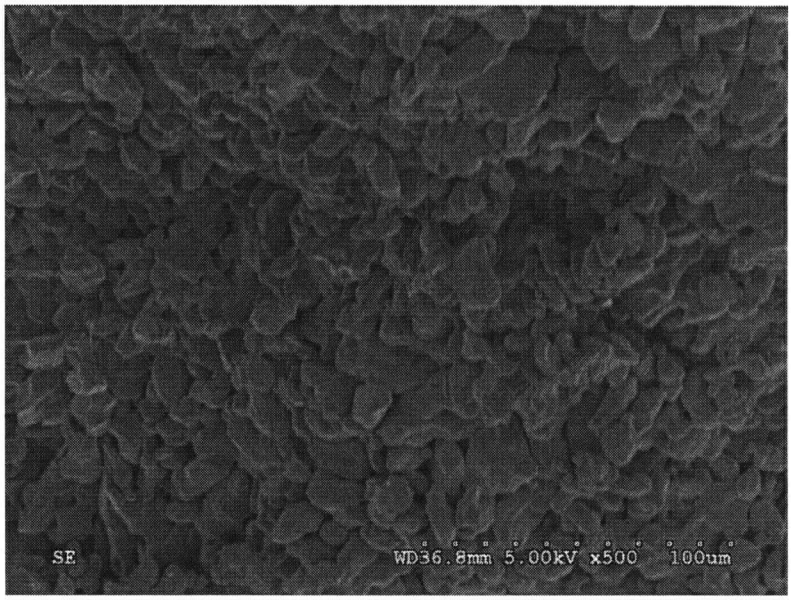

Figure B.50: SEM photograph of the Na_2CO_3 deposition due to combined homogeneous & heterogeneous nucleation at 109 cm location (Experiment SEM-3)

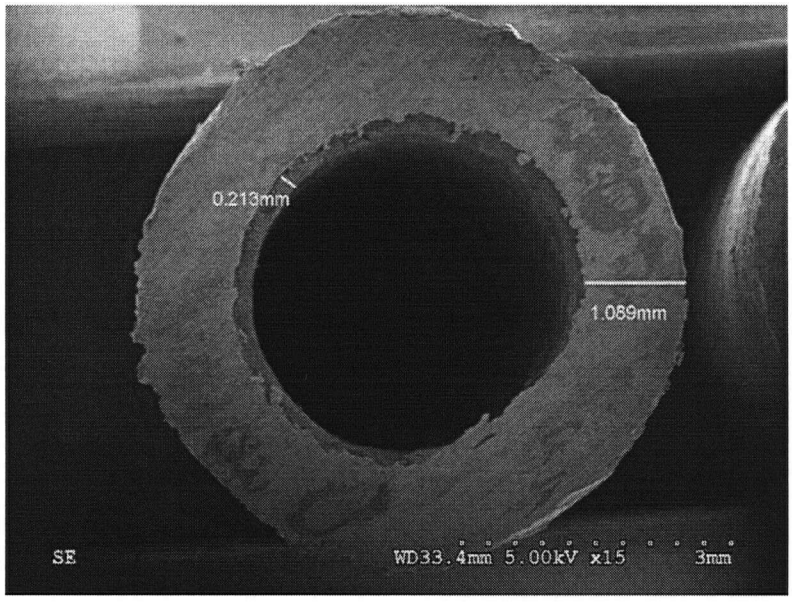

Figure B.51: SEM photograph of the Na_2CO_3 deposition due to combined homogeneous & heterogeneous nucleation at 79 cm location (Experiment SEM-3)

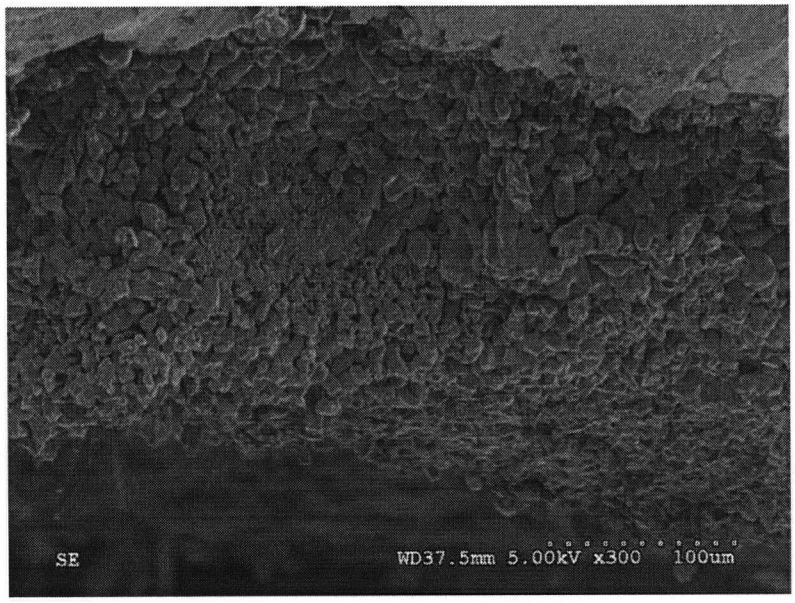

Figure B.52: SEM photograph of the Na_2CO_3 deposition due to combined homogeneous & heterogeneous nucleation at 79 cm location (Experiment SEM-3)

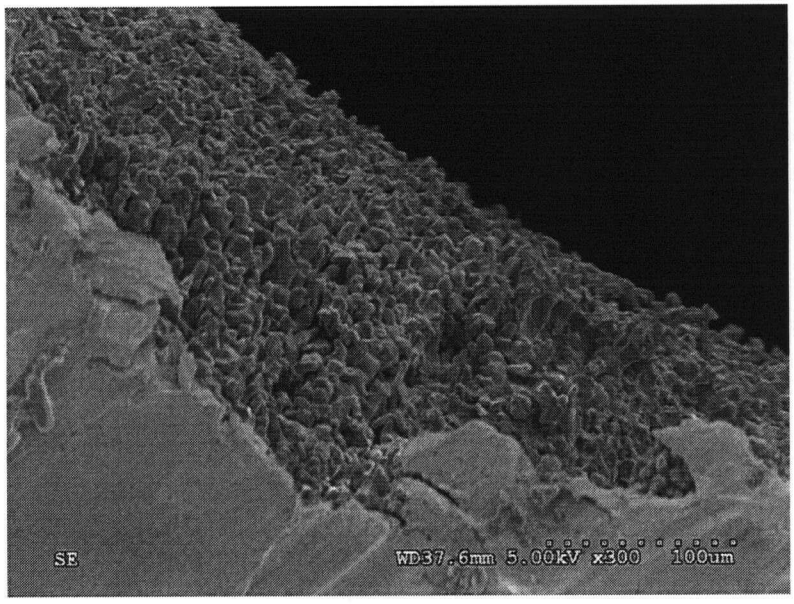

Figure B.53: SEM photograph of the Na_2CO_3 deposition due to combined homogeneous & heterogeneous nucleation at 79 cm location (Experiment SEM-3)

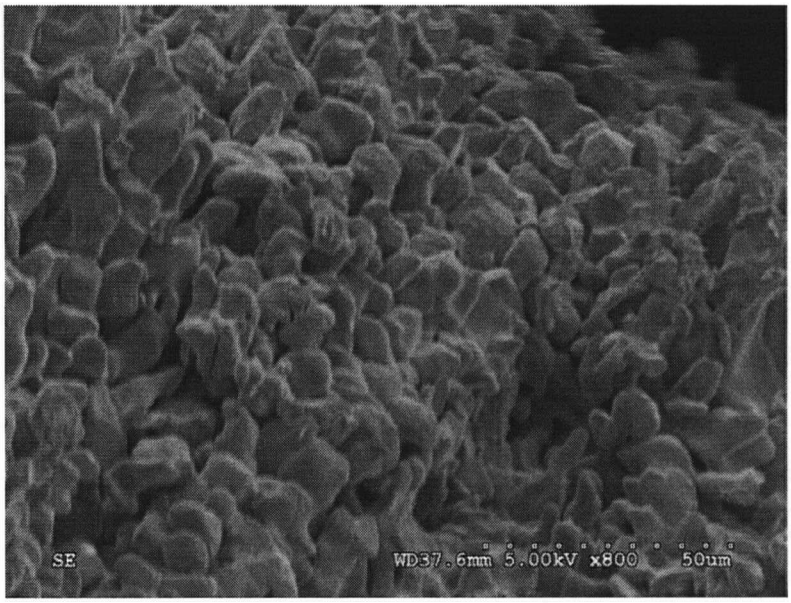

Figure B.54: SEM photograph of the Na_2CO_3 deposition due to combined homogeneous & heterogeneous nucleation at 79 cm location (Experiment SEM-3)

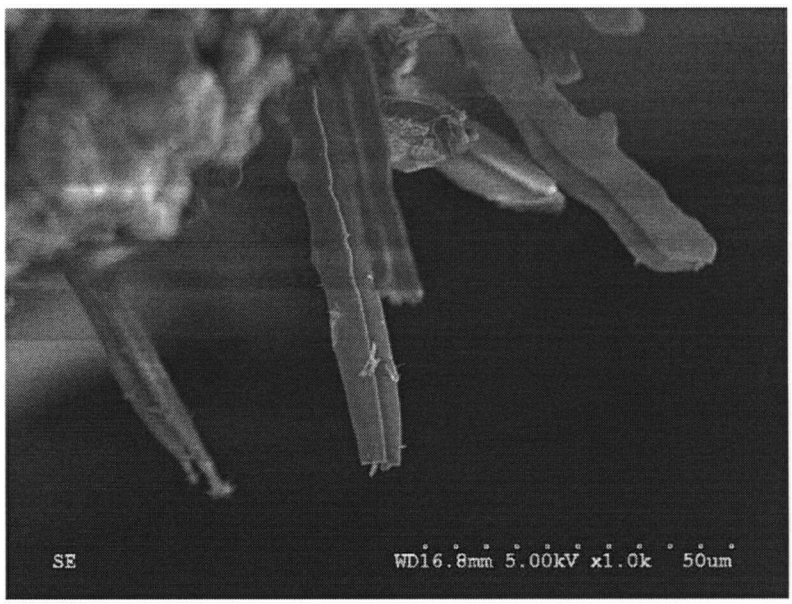

Figure B.55: SEM photograph of the Na_2CO_3 deposition due to combined homogeneous & heterogeneous nucleation at 79 cm location (Experiment SEM-3)

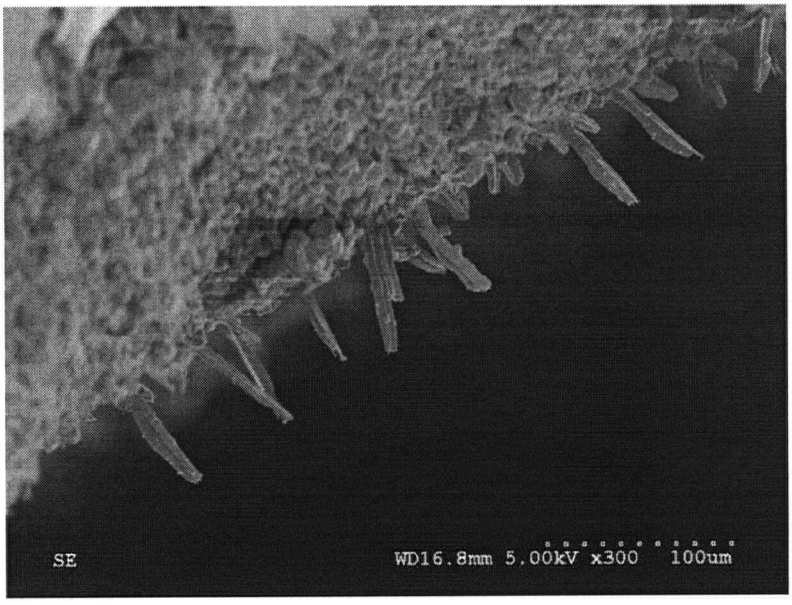

Figure B.56: SEM photograph of the Na_2CO_3 deposition due to combined homogeneous & heterogeneous nucleation at 79 cm location (Experiment SEM-3)

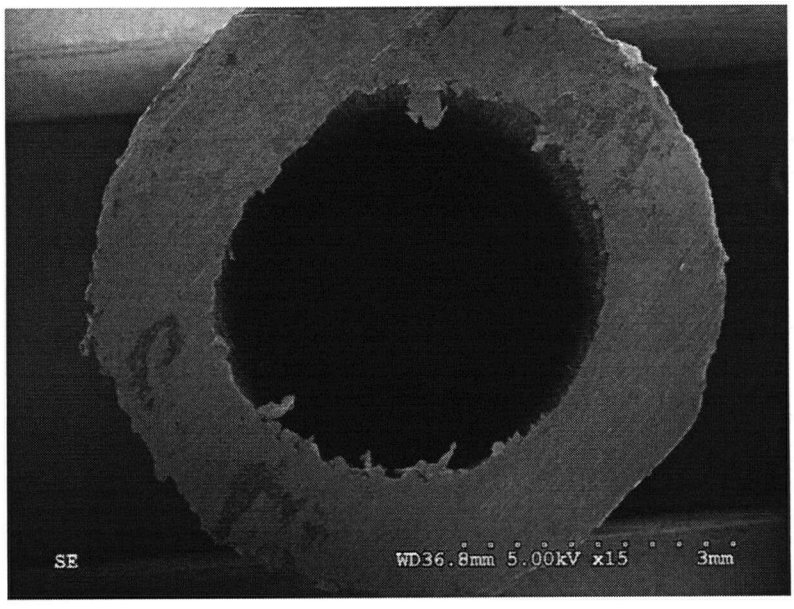

Figure B.57: SEM photograph of the Na_2CO_3 deposition due to combined homogeneous & heterogeneous nucleation at 49 cm location (Experiment SEM-3)

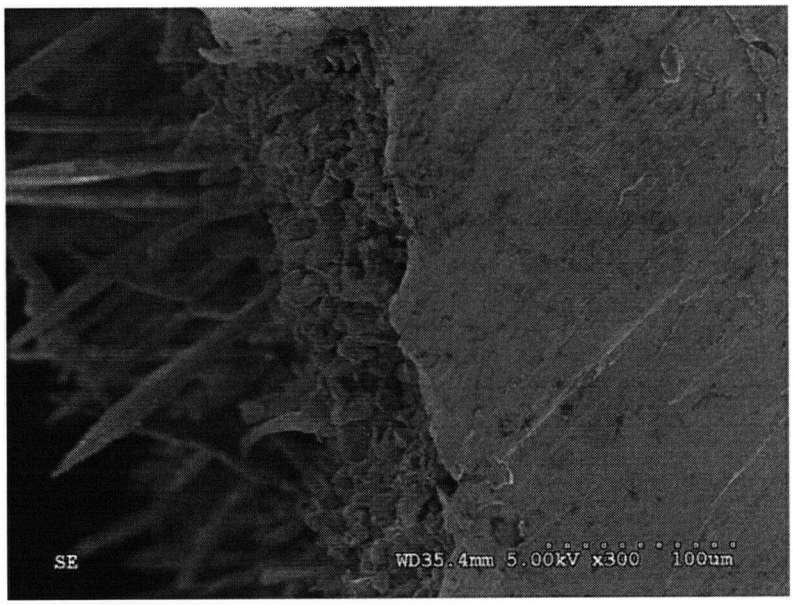

Figure B.58: SEM photograph of the Na_2CO_3 deposition due to combined homogeneous & heterogeneous nucleation at 49 cm location (Experiment SEM-3)

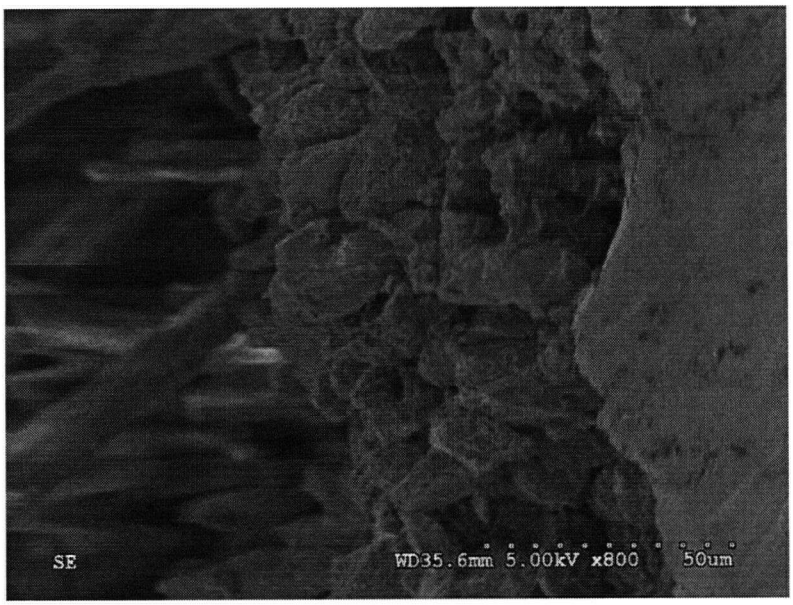

Figure B.59: SEM photograph of the Na_2CO_3 deposition due to combined homogeneous & heterogeneous nucleation at 49 cm location (Experiment SEM-3)

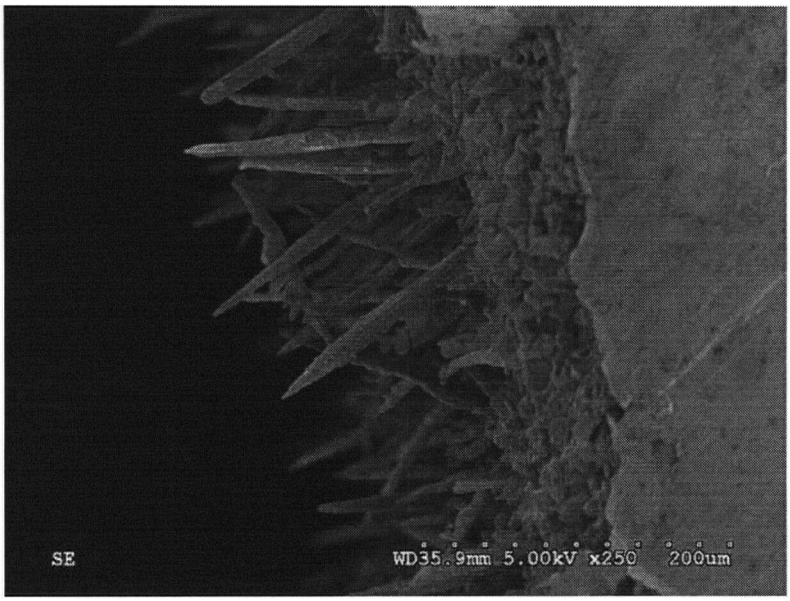

Figure B.60: SEM photograph of the Na_2CO_3 deposition due to combined homogeneous & heterogeneous nucleation at 49 cm location (Experiment SEM-3)

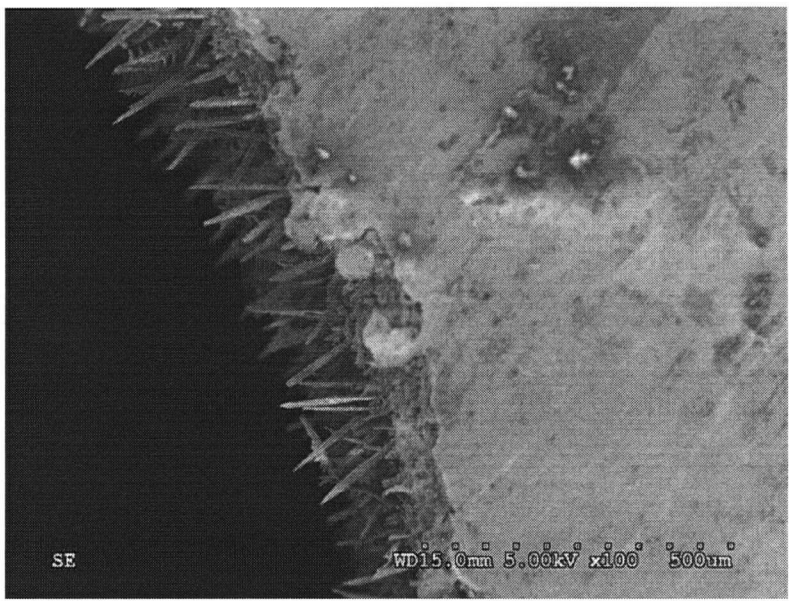

Figure B.61: SEM photograph of the Na_2CO_3 deposition due to combined homogeneous & heterogeneous nucleation at 49 cm location (Experiment SEM-3)

Figure B.62: SEM photograph of the Na_2CO_3 deposition due to combined homogeneous & heterogeneous nucleation at 49 cm location (Experiment SEM-3)

B.2 Na_2SO_4 deposits

Table B.3: Summary of Na_2SO_4 pure crystalline deposit characteristics (Experiment SEM-7)

SEM figure number	Deposit location (cm)	Deposit thickness (mm)	Crystal length (mm)	Comments
B.63-B.65	154	0.1	0.1	deposits of non uniform thickness and needle shaped dendrites
B.66-B.67	124	0.04	0.04	dense deposits of non uniform thickness
B.68-B.70	94	0.2		dense deposits of non uniform thickness
B.71-B.73	49	0.2		dense deposits of non uniform thickness
B.74-B.77	19	0.3		dense deposits of non uniform thickness
B.78-B.81	4	0.15		dense deposits of non uniform thickness

Table B.4: Summary of Na_2SO_4 combined crystalline and particulate deposit characteristics (Experiment SEM-6)

SEM figure number	Deposit location (cm)	Deposit thickness (mm)	Particle size (mm)	Comments
B.82	154	1		hollow particles and dense crystalline deposit
B.83-B.85	79			portions of deposits broken off from upstream location

B.2.1 Na_2SO_4 crystalline scale

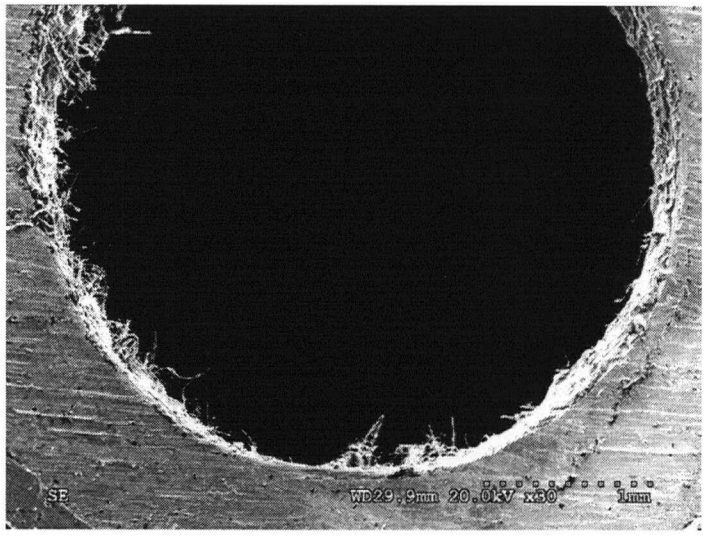

Figure B.63: SEM photograph of the Na_2SO_4 deposition due to heterogeneous nucleation at 154 cm location (Experiment SEM-7)

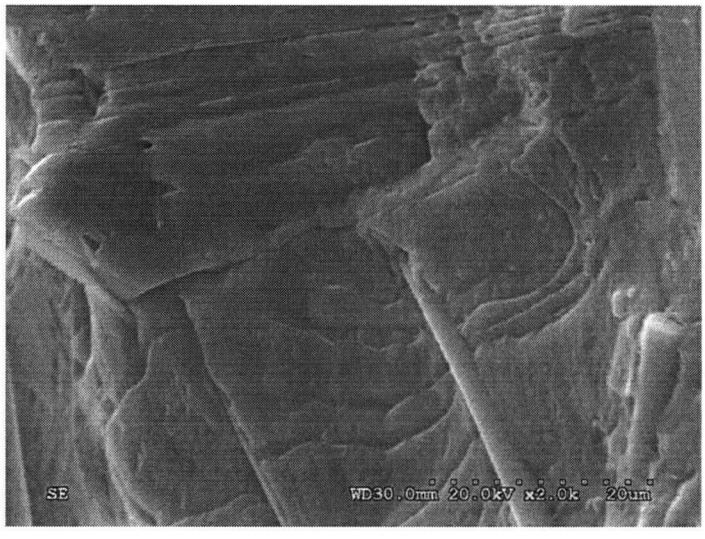

Figure B.64: SEM photograph of the Na_2SO_4 deposition due to heterogeneous nucleation at 154 cm location (Experiment SEM-7)

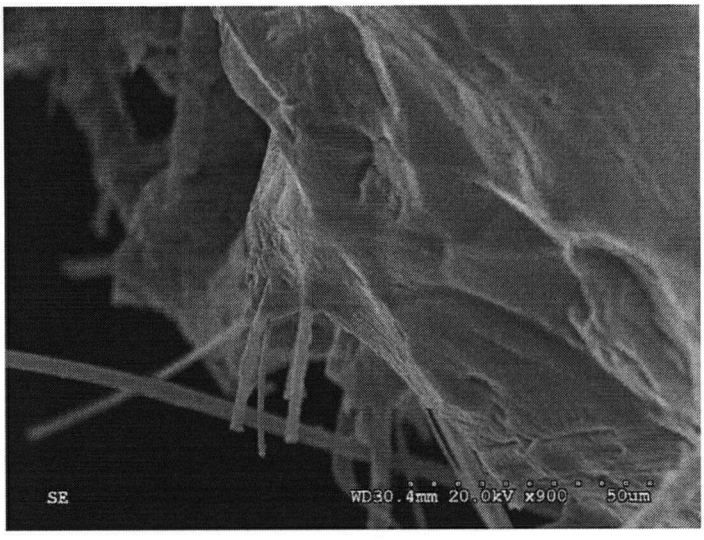

Figure B.65: SEM photograph of the Na_2SO_4 deposition due to heterogeneous nucleation at 154 cm location (Experiment SEM-7)

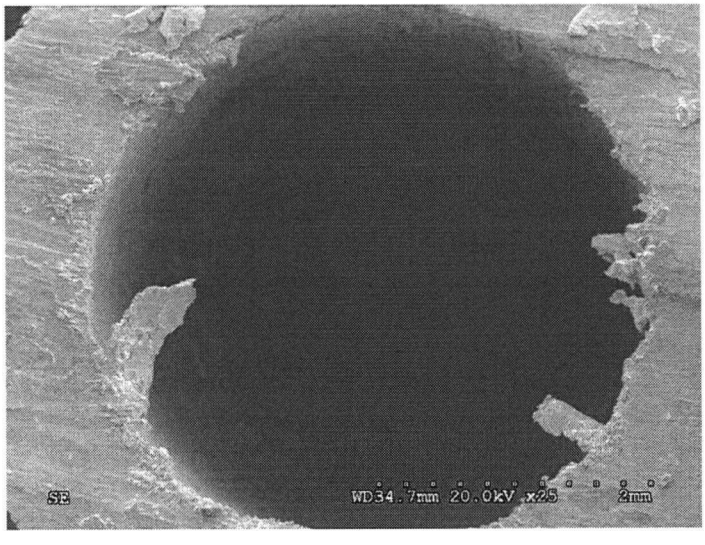

Figure B.66: SEM photograph of the Na_2SO_4 deposition due to heterogeneous nucleation at 124 cm location (Experiment SEM-7)

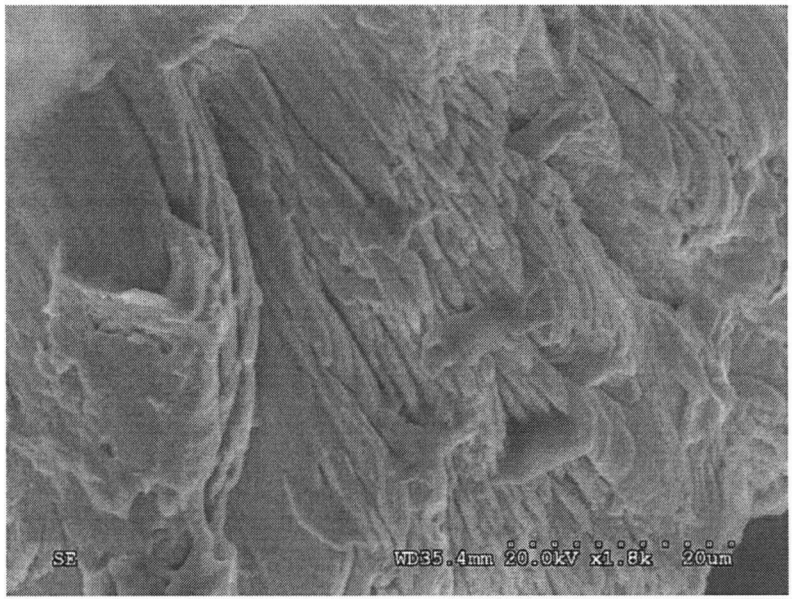

Figure B.67: SEM photograph of the Na_2SO_4 deposition due to heterogeneous nucleation at 124 cm location (Experiment SEM-7)

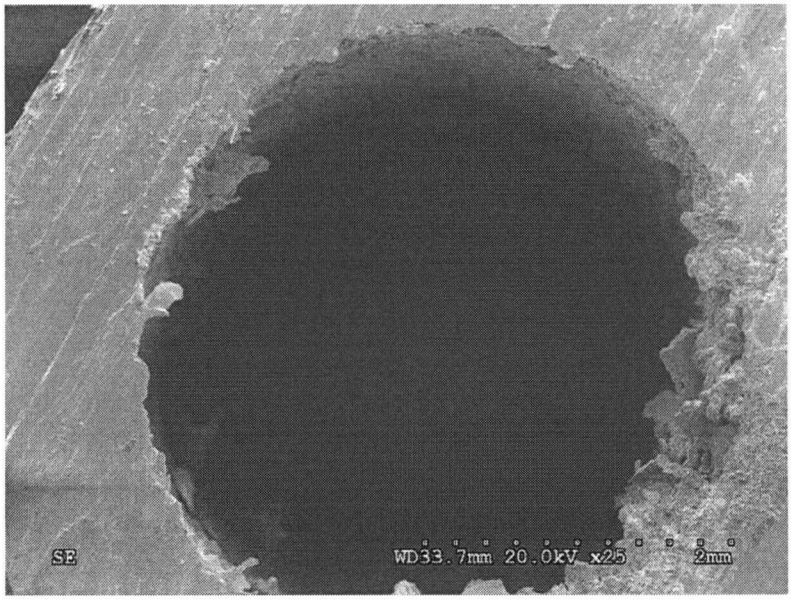

Figure B.68: SEM photograph of the Na_2SO_4 deposition due to heterogeneous nucleation at 94 cm location (Experiment SEM-7)

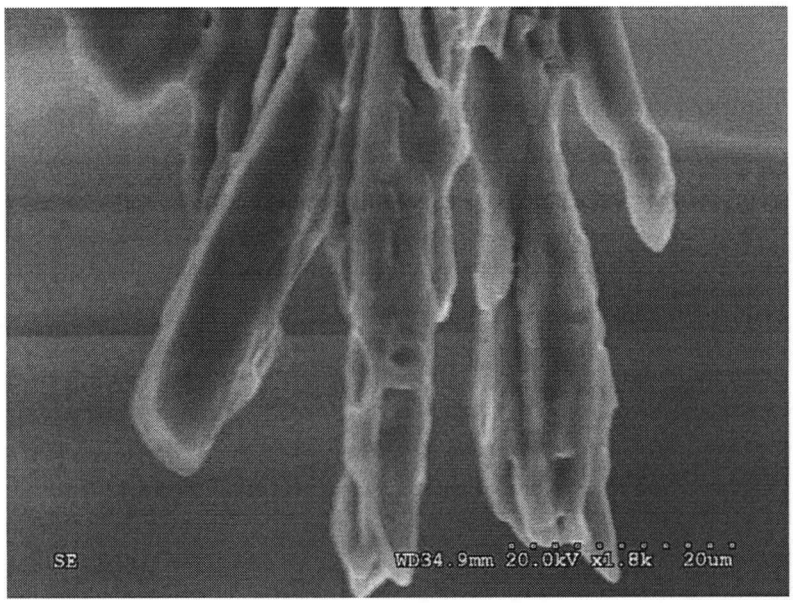

Figure B.69: SEM photograph of the Na_2SO_4 deposition due to heterogeneous nucleation at 94 cm location (Experiment SEM-7)

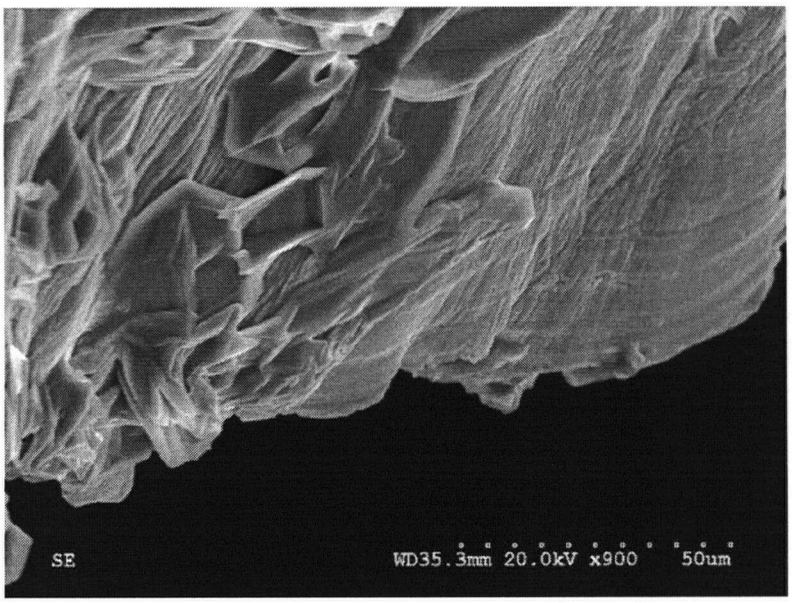

Figure B.70: SEM photograph of the Na_2SO_4 deposition due to heterogeneous nucleation at 94 cm location (Experiment SEM-7)

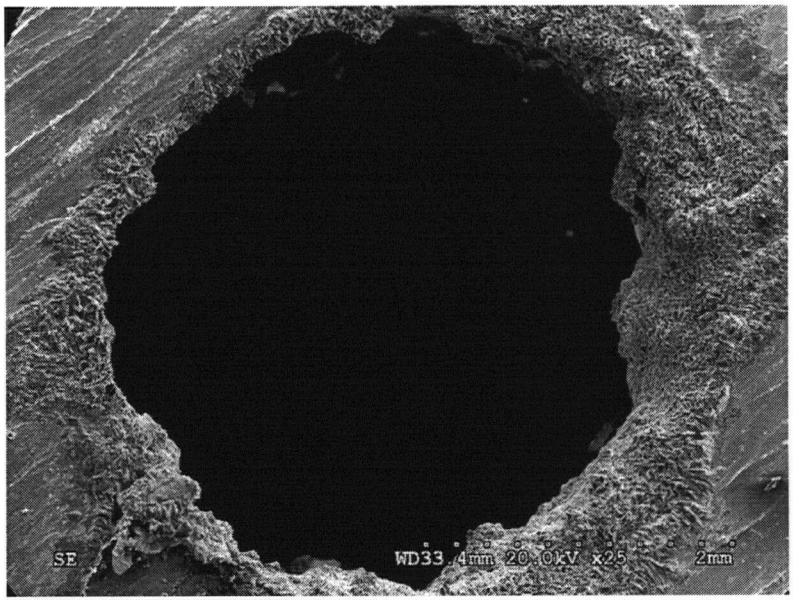

Figure B.71: SEM photograph of the Na_2SO_4 deposition due to heterogeneous nucleation at 49 cm location (Experiment SEM-7)

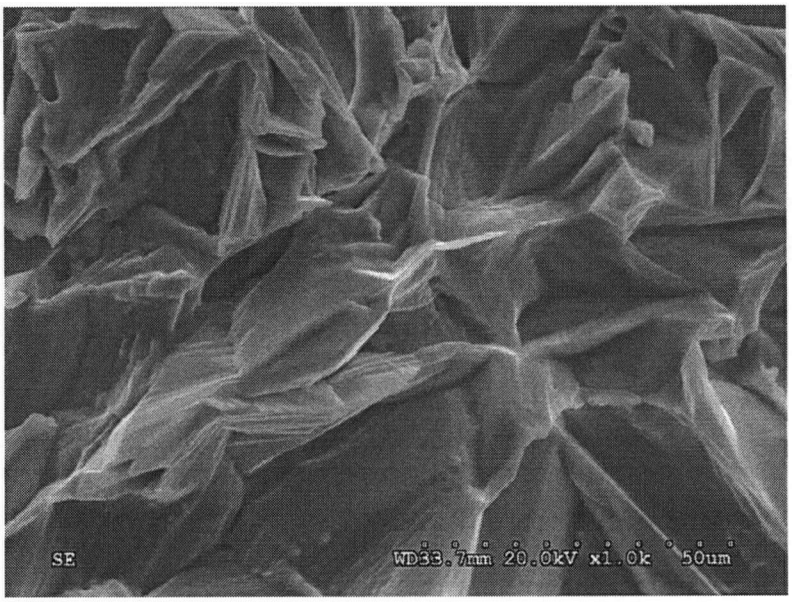

Figure B.72: SEM photograph of the Na_2SO_4 deposition due to heterogeneous nucleation at 49 cm location (Experiment SEM-7)

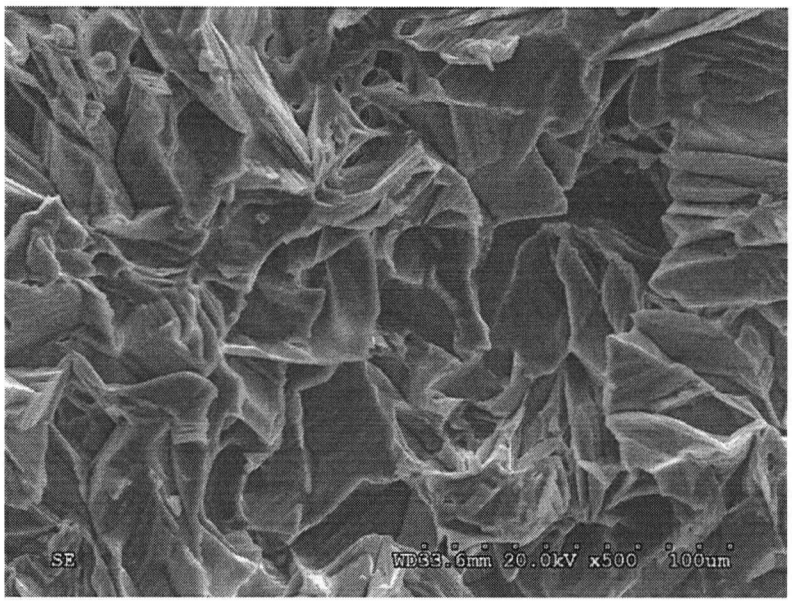

Figure B.73: SEM photograph of the Na_2SO_4 deposition due to heterogeneous nucleation at 49 cm location (Experiment SEM-7)

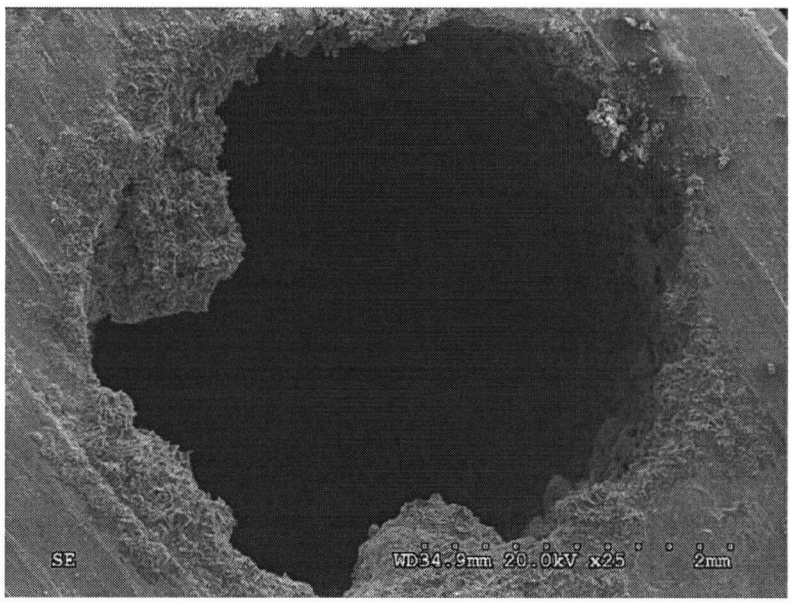

Figure B.74: SEM photograph of the Na_2SO_4 deposition due to heterogeneous nucleation at 19 cm location (Experiment SEM-7)

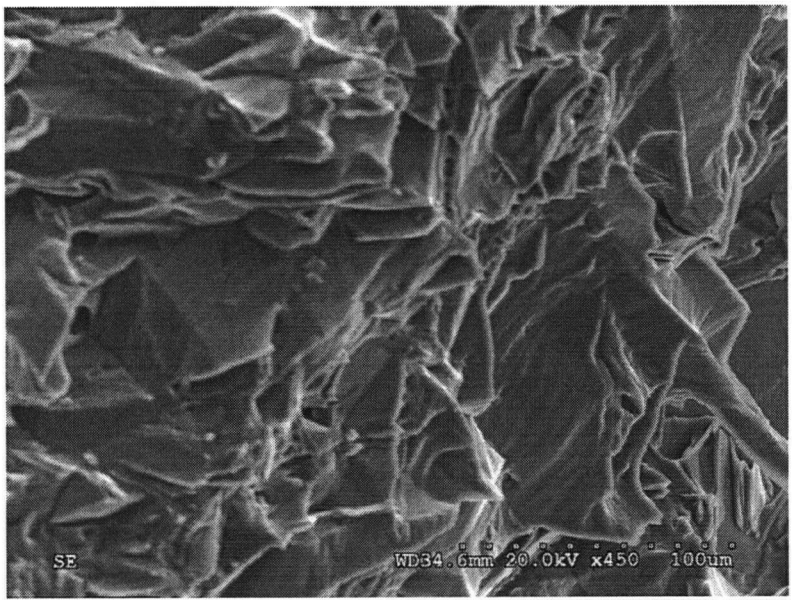

Figure B.75: SEM photograph of the Na_2SO_4 deposition due to heterogeneous nucleation at 19 cm location (Experiment SEM-7)

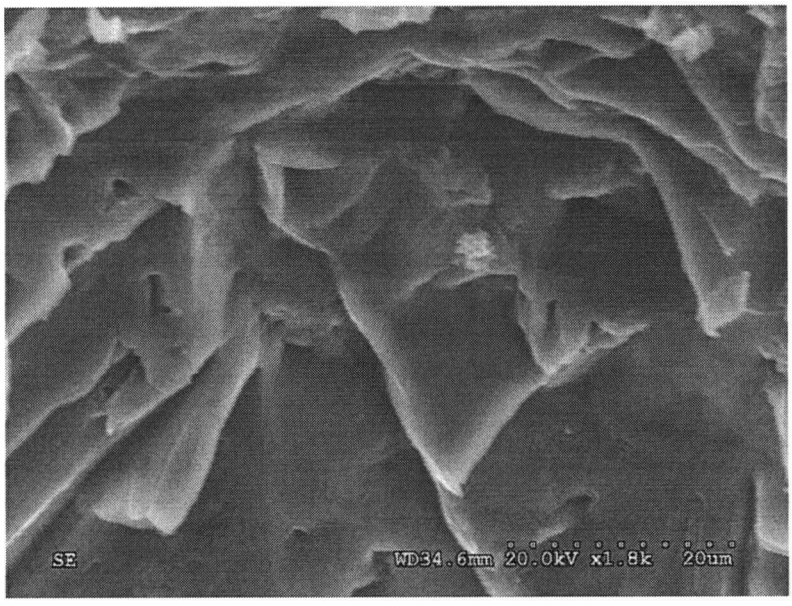

Figure B.76: SEM photograph of the Na_2SO_4 deposition due to heterogeneous nucleation at 19 cm location (Experiment SEM-7)

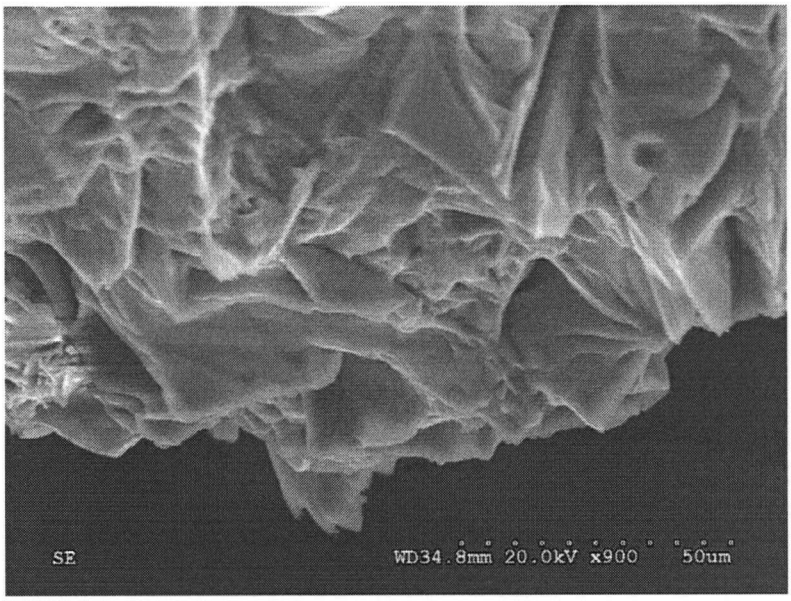

Figure B.77: SEM photograph of the Na_2SO_4 deposition due to heterogeneous nucleation at 19 cm location (Experiment SEM-7)

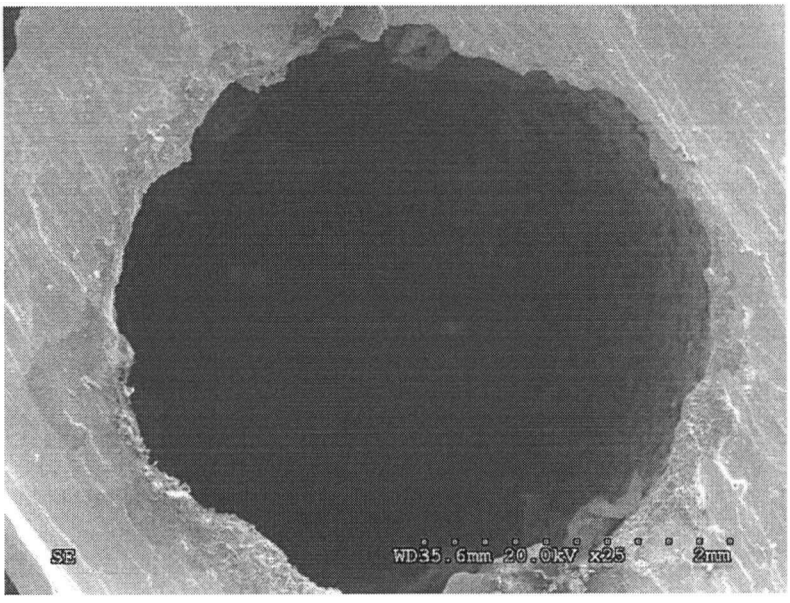

Figure B.78: SEM photograph of the Na_2SO_4 deposition due to heterogeneous nucleation at 4 cm location (Experiment SEM-7)

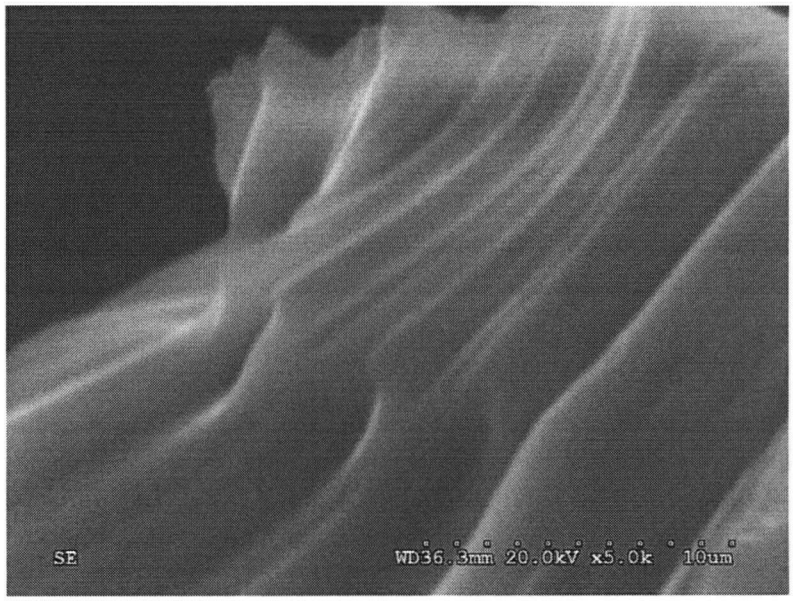

Figure B.79: SEM photograph of the Na_2SO_4 deposition due to heterogeneous nucleation at 4 cm location (Experiment SEM-7)

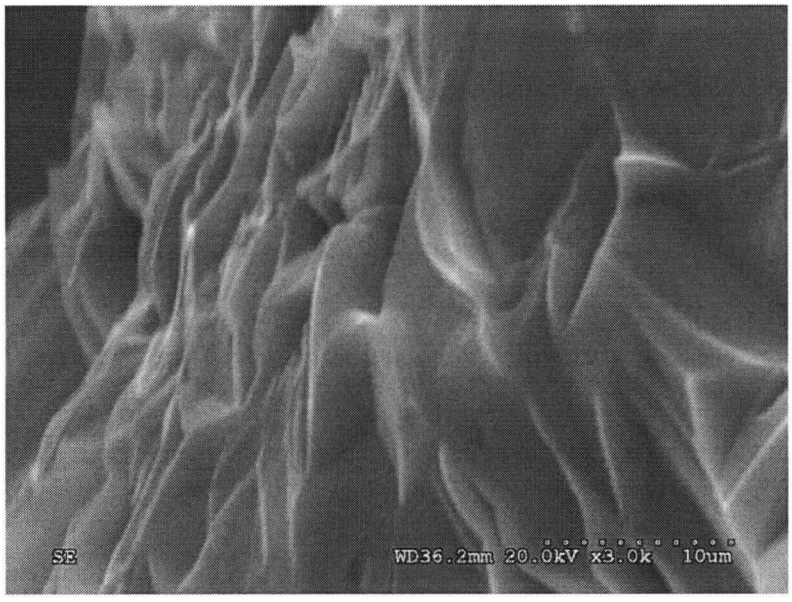

Figure B.80: SEM photograph of the Na_2SO_4 deposition due to heterogeneous nucleation at 4 cm location (Experiment SEM-7)

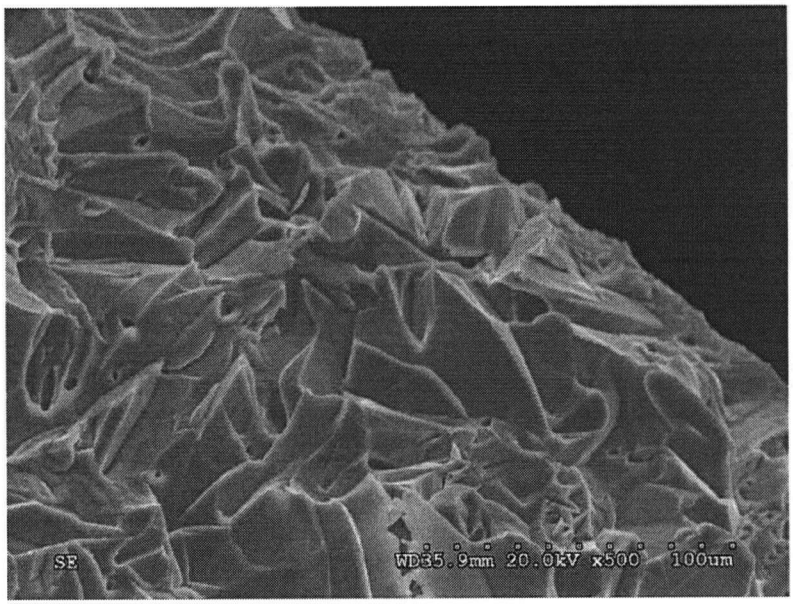

Figure B.81: SEM photograph of the Na_2SO_4 deposition due to heterogeneous nucleation at 4 cm location (Experiment SEM-7)

B.2.2 Na_2SO_4 combined crystalline and particulate deposits

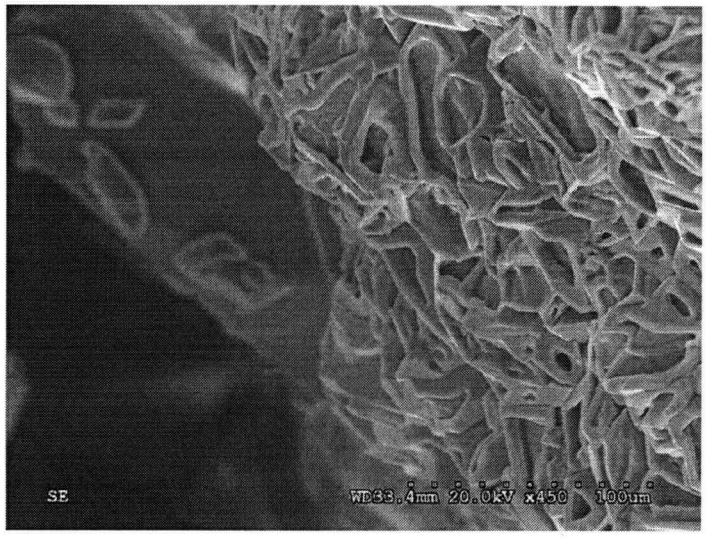

Figure B.82: SEM photograph of the Na_2SO_4 deposition due to combined homogeneous & heterogeneous nucleation at 154 cm location (Experiment SEM-6)

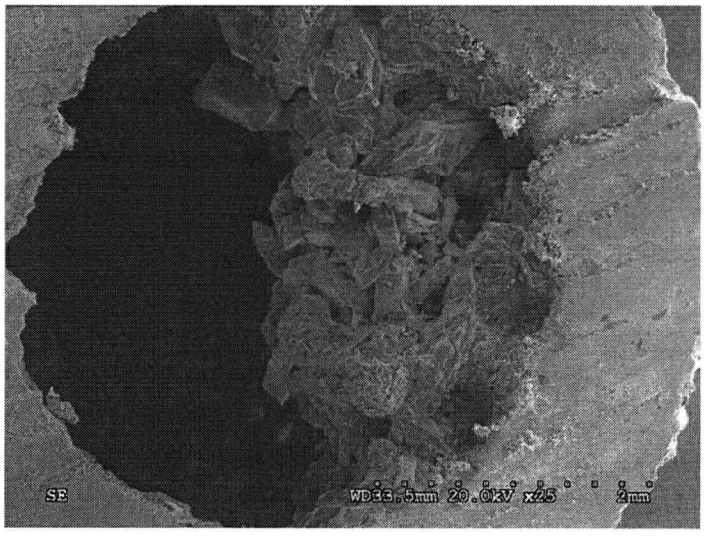

Figure B.83: SEM photograph of the Na_2SO_4 deposition due to combined homogeneous & heterogeneous nucleation at 79 cm location (Experiment SEM-6)

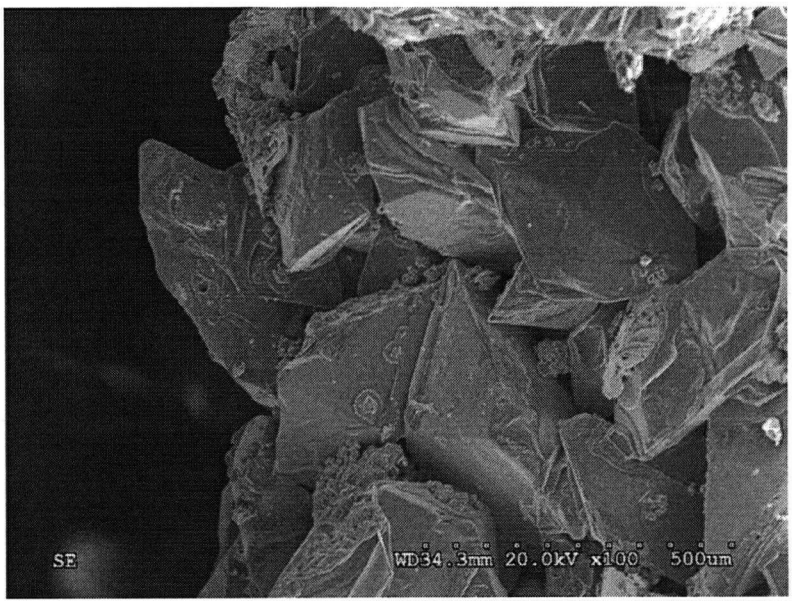

Figure B.84: SEM photograph of the Na_2SO_4 deposition due to combined homogeneous & heterogeneous nucleation at 79 cm location (Experiment SEM-6)

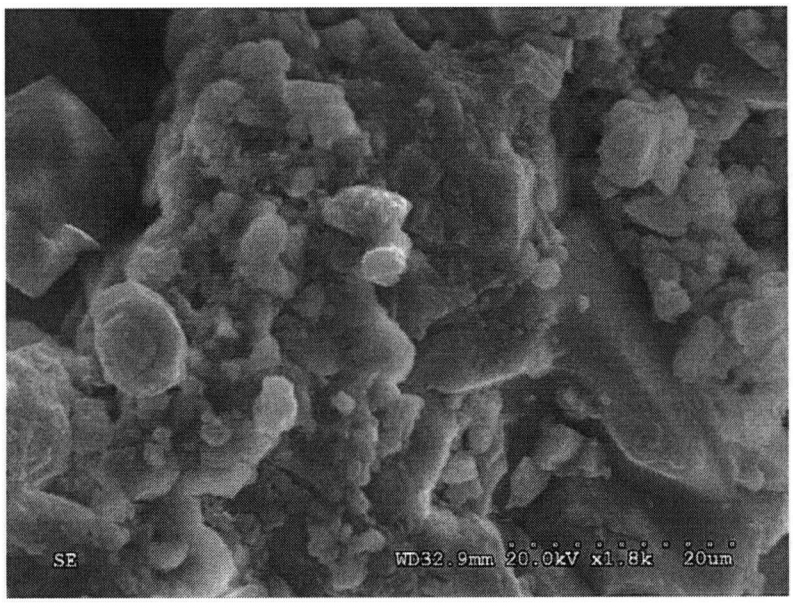

Figure B.85: SEM photograph of the Na_2SO_4 deposition due to combined homogeneous & heterogeneous nucleation at 79 cm location (Experiment SEM-6)

Appendix C

Computer Codes

C.1 Na_2CO_3 solubility codes

C.1.1 Main Code: mol.m

```
clear
%this program calculates the solubility for a calculated bulk fluid temperature..
%using the expt. solubility data at wall conditions. It uses the MOLCALC and ..
% LOOKUP files.
Pressure=25;%pressure in MPa
Tb=391.9+273;%Bulk Temperature at test section inletin K
Q=22.4;%Heat input in kW/m2
m=0.0116;%flow rate in kg/s
D=0.0062;%tube diameter in m
moldia=5.1E-10;%molecular dia in m, for sodium carbonate
rhos=2530;%salt density in kg/m3
Tw=Tb+.5;% guessed wall temperature
DZ=0.05;%segment length in m
[rhob,rhow,Hb,Hw,Cpb,Cpw,viscb,viscw,Kb,Kw,Prb,Prw,Reb,Rew]=...
  molcalc(Pressure,Tb,Tw,Q,m,D,moldia,rhos,DZ);
```

Subroutine: molcalc.m

```
function [rhob,rhow,Hb,Hw,Cpb,Cpw,viscb,viscw,Kb,Kw,Prb,Prw,Reb,Rew]...
  =molcalc(Pressure,Tb,Tw,Q,m,D,moldia,rhos,DZ);
length=0;
%load all the property tables
load dens.txt;
load K.txt;
load cp.txt;
load enth.txt;
load prand.txt;
load vis.txt;
% get file sizes from dens, but other files must have same size
[nT,nP]=size(dens);
% the first row contains the pressures in MPa
```

```
P=dens(1,2:nP);
% the first column contains the Temperatures in K
T=dens(2:nT,1);
A=cp(2:nT,2:nP);
Cp=interp2(P,T,A,Pressure,T);
[Tsort,i]=sort(T);
Cpsort=Cp(i);
[maxCp,imax]=max(Cp);
Tpc=T(imax)
A=prand(2:nT,2:nP);
Pr=interp2(P,T,A,Pressure,T);
Prpc=Pr(imax);
A=dens(2:nT,2:nP);
rhob=interp2(P,T,A,Pressure,Tb);
CB=.04;
CW=CB;
%number of segments
NZ=3/DZ;
for j=1:NZ
  % other than the first rows and columns, we have actual property values
  A=dens(2:nT,2:nP);
  rhob=interp2(P,T,A,Pressure,Tb);
  A=K(2:nT,2:nP);
  Kb=interp2(P,T,A,Pressure,Tb);
  A=enth(2:nT,2:nP);
  Hb=interp2(P,T,A,Pressure,Tb);
  A=cp(2:nT,2:nP);
  Cpb=interp2(P,T,A,Pressure,Tb);
  A=vis(2:nT,2:nP);
  viscb=interp2(P,T,A,Pressure,Tb);
  A=prand(2:nT,2:nP);
  Prb=interp2(P,T,A,Pressure,Tb);
  A=vis(2:nT,2:nP);
  viscb=interp2(P,T,A,Pressure,Tb);
  Reb=4*m/(pi*D*viscb);
  %Fluid properties at wall
  %Guess wall temperature
  for i=1:10
    A=dens(2:nT,2:nP);
    rhow=interp2(P,T,A,Pressure,Tw);
    A=K(2:nT,2:nP);
    Kw=interp2(P,T,A,Pressure,Tw);
    A=enth(2:nT,2:nP);
    Hw=interp2(P,T,A,Pressure,Tw);
    A=cp(2:nT,2:nP);
    Cpw=interp2(P,T,A,Pressure,Tw);
    A=vis(2:nT,2:nP);
    viscw=interp2(P,T,A,Pressure,Tw);
    A=prand(2:nT,2:nP);
    Prw=interp2(P,T,A,Pressure,Tw);
    Rew=4*m/(pi*D*viscw);
```

```
%Nusselt number from Swenson correlation
%Nu=0.00459*(Rew)^0.923*((Hw-Hb)*viscw/((Tw-Tb)*Kw))^0.613*(rhow/(rhob))^0.231;
% Calculation of Nusselt number from Yamagata correlation.
E=(Tpc-Tb)/(Tw-Tb);
if E>1
  Fc=1;
else
  if E<0
    n2=1.44*(1+1/Prpc)-0.53;
    Fc=((Hb-Hw)/(Tb-Tw)/Cpb)^n2;
  else
    n1=-.77*(1+1/Prpc)+1.49;
    Fc=0.67*Prpc^(-.05)*((Hb-Hw)/(Tb-Tw)/Cpb)^n1;
  end
end
Nu=0.0135*Reb^.85*Prb^.8*Fc;
Tw=Tb+Q*D/(Nu*Kw)*1000;
end
Tw;
Tb;
[CW]= lookup(rhow);
[C1]=lookup(rhob);
Rew;
Nu;
Prw;
Reb=4*m/(pi*D*viscb);
kviscw=viscw/rhow;
kviscb=viscb/rhob;
diff=1.38e-23*(Tw)*1/(3*pi*viscb*moldia);
Sc=kviscw/diff;
h=Nu*(Kb)/D;
Le=Sc/Prw;
% Le^0.387 for Swenson correlation and Le^0.2 for Yamagata correlation
%Hm=h/(rhow*Cpw*Le^0.387);
Hm=h/(rhow*Cpw*Le^0.2);
Flowmass=Hm*DZ*pi*D*rhow*(CB-CW)/100;
DIFF=Flowmass/m*100;
length=length+DZ;
results(j,1)=length;
results(j,2)=Tb-273;
results(j,3)=Tw-273;
results(j,4)=CB;
results(j,5)=CW;
results(j,6)=DIFF;
results(j,7)=C1;
save c:\matlabr11\work\results.txt results -ascii
figure(1)
hold on
plot(Tb-273,results(j,4),'k.',Tb-273,results(j,5),'k+',Tb-273,results(j,7),'k*')
title(['P= ',num2str(Pressure),' MPa',',  Q= ',num2str(Q),' kW/m^2',',  m= ', ...
    num2str(m),' kg/s'],'Fontsize',12)
```

```
  legend('CB, wt%','CW (SAT), wt%','CB(SAT), wt%')
  xlabel(['Bulk fluid temperature (C)'], 'FontSize', 16)
  %calculate the bulk fluid temperature and solubility for the next step
  Tb=Tb+Q*1000*pi*D*DZ/(m*Cpb);
  CB=CB-Flowmass/m*100;
  Tw;
end
load results.txt
aveTw=mean(results(1:NZ,3))
%figure(2)
%hold on
%plot(results(DZ:DZ:NZ,1),results(DZ:DZ:NZ,4),results(DZ:DZ:NZ,1),results(DZ:DZ:...
% NZ,5))
%legend('CB, wt%','CSATW, wt%')
%xlabel(['length along TS (m)'], 'FontSize', 12)
```

Subroutine: lookup.m

```
%this file can be used to calculate the solubility at a given density
function [C]= lookup(rho)
%load the solubility table
load solsort2.txt;
[nA,nB]=size(solsort2);
% the second column contains the wt%
Y=solsort2(1:nA,2);
% the first column contains the density in kg/m3
X=solsort2(1:nA,1);
C=interp1(X,Y,rho);
```

Figure Code: graphNa2CO3.m

```
clear
% This program graphs the Na2CO3 solubility vs density and temperature. ...
% It uses finddens.txt
% and solsortnew.txt files.
load solsort.txt;
load solsortnew.txt;
nT=20;
nP=20;
% the first column contains the Temperatures in C
T=solsortnew(1:nT,1);
% we measure gauge pressure from the transducer and the tables...
%are in absolute pressure i.e, a diff of 0.1 MPa
P=solsortnew(1:nT,3)+0.1;
[rho]=finddens(P,T+273.15);
% info for error bars
Pnew=solsortnew(5:18,3)+0.1;
Tlow=solsortnew(5:18,4);
Thigh=solsortnew(5:18,5);
wt=solsortnew(5:18,2);
```

```
[Dlow]=finddens(Pnew,Tlow+273.15);
[Dhigh]=finddens(Pnew,Thigh+273.15);
wt1=solsortnew(1:4,2);
wt2=solsortnew(5:7,2);
wt3=solsortnew(8:9,2);
wt4=solsortnew(10,2);
wt5=solsortnew(11:12,2);
wt6=solsortnew(13,2);
wt5new=solsort(14:18,2);
wt7=solsortnew(19:20,2);
density=rho;
figure(1)
semilogy(T(1:4),wt1,'k+', T(5:7),wt2,'k^', T(8:9), wt3, 'ko', T(10),wt4...
  ,'ks',T(11:12),wt5,'kp', T(13),wt6, 'k<',T(19:20),wt7, 'kx',T(14:18),...
  wt5new,'kp',Tlow(1:14),wt(1:14), 'k.',Thigh(1:14),wt(1:14),'k.')
hold on
semilogy(Tlow(1):.1:Thigh(1), wt(1),'k-',Tlow(2):.1:Thigh(2), wt(2),'k-',...
   Tlow(3):.1:Thigh(3), wt(3),'k-',Tlow(4):.1:Thigh(4), wt(4),'k-',...
   Tlow(5):.1:Thigh(5), wt(5),'k-',Tlow(6):.1:Thigh(6), wt(6),'k-',...
   'LineWidth', 1)
hold on
semilogy(Tlow(7):.1:Thigh(7), wt(7),'k-',Tlow(8):.1:Thigh(8), wt(8),'k-',...
   Tlow(9):.1:Thigh(9), wt(9),'k-',Tlow(10):.1:Thigh(10), wt(10),'k-',...
   Tlow(11):.1:Thigh(11), wt(11),'k-',Tlow(12):.1:Thigh(12), wt(12),'k-',...
   'LineWidth', 1)
hold on
semilogy(Tlow(13):.1:Thigh(13), wt(13),'k-',Tlow(14):.1:Thigh(14), ...
  wt(14),'k-','LineWidth', 1)
title(['Fig. 5: Sodium carbonate solubility vs temperature'],'Fontsize',16)
%axis([0.006 0.05 0.005 0.68])
legend('Ref. 7 (24.5 MPa)', 'C2-C4', 'C5-C6','C7',...
  'C8-C14', 'C1', 'Ref. 6 (24.1 MPa)')
xlabel(['temperature (^oC)'],'FontSize',14)
ylabel(['Solubility limit (wt %)'],'FontSize',14)
hold off
x=rho;
y=solsortnew(1:20,2);
wtnew=solsort(5:18,2);
xnew=x;
ynew=log(y);
p1=polyfit(xnew,ynew,3);
xnew=x(1):-10:100;
f1=polyval(p1,xnew);
f1=exp(f1);
%plot(x,y,'o',x,f,'-',xnew,f1,'-')
%set(gca,'XDir','reverse','YDir','normal');
figure(2)
%hold on
semilogy(rho(1:4),wt1,'k+', rho(5:7),wt2,'k^', rho(8:9),...
  wt3, 'ko', rho(10),wt4,'ks',rho(11:12),wt5,...
   'kp', rho(13),wt6, 'k<',rho(19:20),wt7, 'kx',xnew,f1,'k-',...
```

```
   rho(14:18),wt5new,'kp',Dlow(1:14),...
   wt(1:14),'k.',Dhigh(1:14),wt(1:14),'k.')
set(gca,'XDir','reverse','YDir','normal');
Dhigh(1)
Dlow(1)
wt(1)
hold on
semilogy(Dhigh(1):1:Dlow(1), wt(1),'k-',Dhigh(2):1:Dlow(2), wt(2),'k-',...
   Dhigh(3):1:Dlow(3), wt(3),'k-',Dhigh(4):1:Dlow(4), wt(4),'k-',...
   Dhigh(5):1:Dlow(5), wt(5),...
   'k-',Dhigh(6):1:Dlow(6), wt(6),'k-','LineWidth', 1)
hold on
semilogy(Dhigh(7):1:Dlow(7), wt(7),'k-',Dhigh(8):1:Dlow(8), wt(8),'k-',...
  Dhigh(9):1:Dlow(9), wt(9),'k-',Dhigh(10):1:Dlow(10), wt(10),'k-',...
 Dhigh(11):1:Dlow(11), wt(11),'k-',Dhigh(12):1:Dlow(12), wt(12),'k-',...
 'LineWidth', 1)
hold on
semilogy(Dhigh(13):1:Dlow(13), wt(13),'k-',Dhigh(14):1:Dlow(14), wt(14),...
  'k-','LineWidth', 1)
hold on
title(['Fig. 6: Sodium carbonate solubility vs density'],'Fontsize',16)
%axis([0.006 0.05 0.005 0.68])
legend('Ref. 7 (24.5 MPa)', 'C2-C4', 'C5-C6','C7', 'C8-C14', 'C1', ...
  'Ref. 6 (24.1 MPa)', 'Eq. 7 (curve fit)')
xlabel(['density (kg/m^3)'],'FontSize',14)
ylabel(['Solubility limit (wt %)'],'FontSize',14)
```

C.2 Na_2SO_4 solubility codes

C.2.1 Main Code: molNa2SO4.m

```
clear
%this program calculates the solubility for a calculated bulk fluid
%temperature using the expt. solubility data at wall conditions.
%It uses the MOLCALCSO4 and LOOKUPSO4 files.
Pressure=24.4;%pressure in MPa
Tb=379.6+273;Bulk Temperature at test section inletin K
Q=43.3;%Heat input in kW/m2
m=0.011;%flow rate in kg/s
D=0.0062;%tube diameter in m
%molecular dia in m, 5.1E-10 for sod. carb. and 5.27E-10 for sod. sulfate.
%moldia=5.1E-10;
moldia=5.27E-10;
rhos=2530;%salt density in kg/m3
Tw=Tb+.5;% guessed wall temperature
DZ=0.05;%segment length in m
[rhob,rhow,Hb,Hw,Cpb,Cpw,viscb,viscw,Kb,Kw,Prb,Prw,Reb,Rew]=molcalcSO4...
  (Pressure,Tb,Tw,Q,m,D,moldia,rhos,DZ);
```

Subroutine: molcalcSO4.m

```
function [rhob,rhow,Hb,Hw,Cpb,Cpw,viscb,viscw,Kb,Kw,Prb,Prw,Reb,Rew]...
  =molcalc(Pressure,Tb,Tw,Q,m,D,moldia,rhos,DZ);
length=0;
%load all the property tables
%all must have the same size and the same T,P spacing
load dens.txt;
load K.txt;
load cp.txt;
load enth.txt;
load prand.txt;
load vis.txt;
% get file sizes from dens, but other files must have same size
[nT,nP]=size(dens);
% the first row contains the pressures in MPa
P=dens(1,2:nP);
% the first column contains the Temperatures in K
T=dens(2:nT,1);
A=cp(2:nT,2:nP);
Cp=interp2(P,T,A,Pressure,T);
[Tsort,i]=sort(T);
Cpsort=Cp(i);
[maxCp,imax]=max(Cp);
Tpc=T(imax)
A=prand(2:nT,2:nP);
Pr=interp2(P,T,A,Pressure,T);
Prpc=Pr(imax);
A=dens(2:nT,2:nP);
rhob=interp2(P,T,A,Pressure,Tb);
CB=.27;
CW=CB;
%number of segments
NZ=3/DZ;
for j=1:NZ
  % other than the first rows and columns, we have actual property values
  A=dens(2:nT,2:nP);
  rhob=interp2(P,T,A,Pressure,Tb);
  A=K(2:nT,2:nP);
  Kb=interp2(P,T,A,Pressure,Tb);
  A=enth(2:nT,2:nP);
  Hb=interp2(P,T,A,Pressure,Tb);
  A=cp(2:nT,2:nP);
  Cpb=interp2(P,T,A,Pressure,Tb);
  A=vis(2:nT,2:nP);
  viscb=interp2(P,T,A,Pressure,Tb);
  A=prand(2:nT,2:nP);
  Prb=interp2(P,T,A,Pressure,Tb);
  A=vis(2:nT,2:nP);
  viscb=interp2(P,T,A,Pressure,Tb);
  Reb=4*m/(pi*D*viscb);
```

```
%Fluid properties at wall
%Guess wall temperature
for i=1:5
  A=dens(2:nT,2:nP);
  rhow=interp2(P,T,A,Pressure,Tw);
  A=K(2:nT,2:nP);
  Kw=interp2(P,T,A,Pressure,Tw);
  A=enth(2:nT,2:nP);
  Hw=interp2(P,T,A,Pressure,Tw);
  A=cp(2:nT,2:nP);
  Cpw=interp2(P,T,A,Pressure,Tw);
  A=vis(2:nT,2:nP);
  viscw=interp2(P,T,A,Pressure,Tw);
  A=prand(2:nT,2:nP);
  Prw=interp2(P,T,A,Pressure,Tw);
  Rew=4*m/(pi*D*viscw);
  %Nusselt number from Swenson correlation
  %Nu=0.00459*(Rew)^0.923*((Hw-Hb)*viscw/((Tw-Tb)*Kw))^0.613*(rhow/(rhob)...
  %)^0.231;
  % Calculation of Nusselt Number from Yamagata correlation.
  E=(Tpc-Tb)/(Tw-Tb);
  if E>1
    Fc=1;
  else
    if E<0
      n2=1.44*(1+1/Prpc)-0.53;
      Fc=((Hb-Hw)/(Tb-Tw)/Cpb)^n2;
    else
      n1=-.77*(1+1/Prpc)+1.49;
      Fc=0.67*Prpc^(-.05)*((Hb-Hw)/(Tb-Tw)/Cpb)^n1;
    end
  end
  Nu=0.0135*Reb^.85*Prb^.8*Fc;
  Tw=Tb+Q*D/(Nu*Kw)*1000;
end
Tw;
[CW]= lookupSO4(rhow);
[C1]=lookupSO4(rhob);
Rew;
Nu;
Prw;
Reb=4*m/(pi*D*viscb);
kviscw=viscw/rhow;
kviscb=viscb/rhob;
diff=1.38e-23*(Tw)*1/(3*pi*viscb*moldia);
Sc=kviscw/diff;
h=Nu*(Kb)/D;
Le=Sc/Prw;
% for Swenson Le^0.387
%Hm=h/(rhow*Cpw*Le^0.387);
% for Yamagata Le^0.2
```

```
  Hm=h/(rhow*Cpw*Le^0.2);
  Flowmass=Hm*DZ*pi*D*rhow*(CB-CW)/100;
  DIFF=Flowmass/m*100;
  length=length+DZ;
  resultsSO4(j,1)=length;
  resultsSO4(j,2)=Tb-273;
  resultsSO4(j,3)=Tw-273;
  resultsSO4(j,4)=CB;
  resultsSO4(j,5)=CW;
  resultsSO4(j,6)=DIFF;
  resultsSO4(j,7)=C1;
  save c:\matlabr11\work\resultsSO4.txt resultsSO4 -ascii
  figure(1)
  hold on
  plot(Tb-273,resultsSO4(j,4),'k.',Tb-273,resultsSO4(j,5),'k+',Tb-273,...
    resultsSO4(j,7),'k*')
  title(['P= ',num2str(Pressure),' MPa',',  Q= ',num2str(Q),' kW/m^2',',  m= ',...
      num2str(m),' kg/s'],'Fontsize',12)
  legend('C_B, (wt%)','C_{W(SAT)}, (wt%)','C_{B(SAT)}, (wt%)')
  %title(['Fig. 4: Modeled salt concentration along test section for run "S6"'],...
  %'Fontsize',14)
  xlabel(['bulk fluid temperature (^oC)'], 'FontSize', 14)
  ylabel(['salt concentration (wt. %)'], 'FontSize', 14)
  %calculate the bulk fluid temperature and solubility for the next step
  Tb=Tb+Q*1000*pi*D*DZ/(m*Cpb);
  CB=CB-Flowmass/m*100;
  Tw;
end
load resultsSO4.txt
aveTw=mean(resultsSO4(1:NZ,3))
%figure(2)
%hold on
%plot(resultsSO4(DZ:DZ:NZ,1),resultsSO4(DZ:DZ:NZ,4),resultsSO4(DZ:DZ:NZ,1),...
% resultsSO4(DZ:DZ:NZ,5))
%legend('CB, wt%','CSATW, wt%')
%xlabel(['length along TS (m)'], 'FontSize', 12)
```

Subroutine: lookupSO4.m

```
%this file can be used to calculate the solubility at a given density
function [C]= lookupSO4(rho)
%load the solubility table
load solsortSO4.txt;
[nA,nB]=size(solsortSO4);
% the second column contains the wt%
Y=solsortSO4(1:nA,2);
% the first column contains the density in kg/m3
X=solsortSO4(1:nA,1);
C=interp1(X,Y,rho);
```

Figure Code: graphNa2SO4

```
clear
%function [CSATW,rhow]= graph(CSATW,rhow)
%load all the property tables
%all must have the same size and the same T,P spacing
load paulsdata.txt;
load May242002.txt;
load May242002new.txt;
load Shvtre.txt;
% get file sizes from dens, but other files must have same size
[nT,nP]=size(paulsdata);
%the first row contains the pressures in MPa
PPaul=paulsdata(1:nT,2)+0.1;
TPaul=paulsdata(1:nT,1);
wtPaul=paulsdata(1:nT,3);
% we measure gauge pressure from the transducer and the tables
%are in absolute pressure i.e, a diff of 0.1 MPa
PMay=May242002(1:6,2)+0.1;
TMay=May242002(1:6,1);
wtMay=May242002(1:6,3);
Tlow=May242002(1:6,4);
Thigh=May242002(1:6,5);
[rholow]=finddens(PMay,Tlow+273.15);
[rhohigh]=finddens(PMay,Thigh+273.15);
%Shvedov and Tremaine model (1997)
rhomod=Shvtre(1:15,1);
Wtmod=Shvtre(1:15,2);
Tmod=Shvtre(1:15,3);
[rhoPaul]=finddens(PPaul,TPaul+273.15);
[rhoMay]=finddens(PMay,TMay+273.15);
PMay1=May242002new(1:12,2)+0.1;
TMay1=May242002new(1:12,1);
wtMay1=May242002new(1:12,3);
[rhoMay1]=finddens(PMay1,TMay1+273.15);
xnew=rhoMay1(1:12);
ynew=log(wtMay1);
p1=polyfit(xnew,ynew,2);
xnew=xnew(1):-10:80;
f1=polyval(p1,xnew);
f1=exp(f1);
figure(1)
%hold on
semilogy(TPaul(1:22),wtPaul(1:22),'k+', TMay(1:6),wtMay(1:6),'kx',Tmod(1:15),...
  Wtmod(1:15),'k-',500,1e-4,'k^',Tlow(1:6),wtMay(1:6),'k.',Thigh(1:6),...
  wtMay(1:6),'k.','MarkerSize',7)
hold on
semilogy(Tlow(1):0.1:Thigh(1), wtMay(1),'k-', Tlow(2):0.1:Thigh(2), wtMay(2)...
   ,'k-',Tlow(3):0.1:Thigh(3), wtMay(3),'k-', Tlow(4):0.1:Thigh(4), ...
   wtMay(4),'k-',Tlow(5):0.1:Thigh(5), wtMay(5),'k-', Tlow(6):0.1:Thigh(6),...
   wtMay(6),'k-','LineWidth',1)
```

```
%errorbar(T(1),wt1,0.005,0.019)
title(['Fig. 7: Sodium sulfate solubility vs temperature'],'Fontsize',16)
%axis([0.006 0.05 0.005 0.68])
%legend('Rogak and Teshima corrected data, 1999 (25 MPa)', 'May 24, 2002 ...
%(24.3-24.6 MPa)'
%,'Shvedov and Tremaine, 2000 (25 MPa)','Armellini and Tester, 1993 (25 MPa)')
legend('Ref. 4 corrected data (25 MPa)', 'S1-S6','Ref. 5 (25 MPa)','Ref. 3 ...
%(25 MPa)')
xlabel(['temperature (^oC)'],'FontSize',14)
ylabel(['Solubility limit (wt%)'],'FontSize',14)
figure(2)
%hold on
%set(gca,'XDir','reverse','YDir','reverse');
semilogy(rhoPaul(1:22),wtPaul(1:22),'k+', rhoMay(1:6),wtMay(1:6),'kx'...
   ,rhomod(1:15),Wtmod(1:15),'k-',89.74,1e-4,'k^',xnew,f1,'k-.',rholow(1:6)...
   ,wtMay(1:6),'k.',rhohigh(1:6),wtMay(1:6),'k.','MarkerSize',7)
set(gca,'XDir','reverse','YDir','normal');
%errorbar(rho(1),wt1,0.005,0.019)
hold on
semilogy(rhohigh(1):1:rholow(1), wtMay(1),'k-', rhohigh(2):1:rholow(2), ...
  wtMay(2),'k-',rhohigh(3):1:rholow(3), wtMay(3),'k-', rhohigh(4):1:rholow(4)...
  , wtMay(4),'k-',rhohigh(5):1:rholow(5), wtMay(5),'k-', rhohigh(6):1:rholow...
  (6), wtMay(6),'k-','LineWidth',1)
title(['Fig. 8: Sodium sulfate solubility vs density'],'Fontsize',16)
%axis([0.006 0.05 0.005 0.68])
legend('Ref. 4 corrected data (25 MPa)', 'S1-S6','Ref. 5 (25 MPa)','Ref....
3 (25 MPa)','Eq. 8 (curve fit)')
%legend('Rogak and Teshima corrected data, 1999 (25 MPa)', 'May 24, 2002
%(24.3-24.6 MPa)','Shvedov and Tremaine, 2000 (25 MPa)','Armellini and Tester,
%1993 (25 MPa)','2nd order fitted polynomial')
xlabel(['density (kg/m^3)'],'FontSize',14)
ylabel(['Solubility limit (wt%)'],'FontSize',14)
```

C.3 Figure Code: Na_2CO_3-Na_2SO_4 mixture (graphmixture.m)

```
clear
load mixturesol.txt;
load May242002new.txt;
load solsortnew.txt;
[nT,nP]=size(mixturesol);
% we measure gauge pressure from the transducer and ...
% the tables are in absolute pressure i.e, a difference  of 0.1 MPa
P=mixturesol(1:nT,2)+0.1;
T=mixturesol(1:nT,1);
wtna2co3=mixturesol(1:nT,3);
wtna2so4=mixturesol(1:nT,4);
Tlow=mixturesol(1:13,5);
```

```
Thigh=mixturesol(1:13,6);
[rholow]=finddens(P,Tlow+273.15);
[rhohigh]=finddens(P,Thigh+273.15);
[rho]=finddens(P,T+273.15);
PMay1=May242002new(2:12,2)+0.1;
TMay1=May242002new(2:12,1);
wtMay1=May242002new(2:12,3);
[rhoMay1]=finddens(PMay1,TMay1+273.15);
xnew=rhoMay1;
ynew=log(wtMay1);
p1=polyfit(xnew,ynew,2);
xnew=xnew(1):-10:80;
f1=polyval(p1,xnew);
f1=exp(f1);
PCO3=solsortnew(1:20,3)+0.1;
TCO3=solsortnew(1:20,1);
[DCO3]=finddens(PCO3,TCO3+273.15);
xc=DCO3;
%xc=solsort(1:20,3);
%yc=solsort(1:20,2);
yc=solsortnew(1:20,2);
xnewc=xc;
ynewc=log(yc);
p2=polyfit(xnewc,ynewc,3);
xnewc=xnew(1):-10:80;
f2=polyval(p2,xnewc);
f2=exp(f2);
%figure(1)
%hold on
%semilogy(T(1),wtna2co3(1),'k+', T(2:3),wtna2co3(2:3),'kx',T(4:6),...
% wtna2co3(4:6),'k*',T(7:8),wtna2co3(7:8),'kp',T(1),wtna2so4(1),'ko',...
% T(2:3),wtna2so4(2:3),'ks',T(4:6),wtna2so4(4:6),'k^',T(7:8),wtna2so4(7:8)...
% ,'kv',Tlow(1:8),wtna2so4(1:8),'k.',Thigh(1:8),wtna2so4(1:8),'k.',...
% Tlow(1:8),wtna2co3(1:8),'k.',Thigh(1:8),wtna2co3(1:8),'k.')
%errorbar(T(1),wt1,0.005,0.019)
%title(['Fig. 9: Solubility of mixture of sodium carbonate and sodium...
% sulfate'],'Fontsize',15)
%axis([0.006 0.05 0.005 0.68])
%legend('Na_2CO_3, Aug07, 2002', 'Na_2CO_3, Aug08, 2002','Na_2CO_3,...
% Aug14, 2002','Na_2CO_3, Aug16, 2002', 'Na_2SO_4, Aug07, 2002', ...
% 'Na_2SO_4, Aug08, 2002','Na_2SO_4, Aug14, 2002','Na_2SO_4, Aug16, 2002')
%xlabel(['temperature (^oC)'],'FontSize',14)
%ylabel(['Solubility limit (wt%)'],'FontSize',14)
figure(2)
%hold on
%set(gca,'XDir','reverse','YDir','reverse');
semilogy(rho(1),wtna2co3(1),'k+', rho(3),wtna2co3(3),'kx',rho(4:6)...
  ,wtna2co3(4:6),'k*',rho(7:8),wtna2co3(7:8),'kp',rho(9:13),wtna2co3(9:13)...
  ,'kh',xnewc,f2,'k-',rho(1),wtna2so4(1),'ko', rho(2:3),...
   wtna2so4(2:3),'ks',rho(4:6),wtna2so4(4:6),'k^',rho(7:8),wtna2so4(7:8),...
   'kv',rho(9:13),wtna2so4(9:13),'kd',xnew,f1,'k-.',rholow(1:13),...
```

```
   wtna2so4(1:13),'k.',rhohigh(1:13),wtna2so4(1:13),'k.',rholow(1)...
   ,wtna2co3(1),'k.',rholow(3:13),wtna2co3(3:13),'k.')
hold on
semilogy(rhohigh(1),wtna2co3(1),'k.',rhohigh(3:13),wtna2co3(3:13),'k.');
hold on
semilogy(rhohigh(1):1:rholow(1), wtna2so4(1),'k-',rhohigh(2):1:rholow(2)...
  , wtna2so4(2),'k-',rhohigh(3):1:rholow(3), wtna2so4(3),'k-',rhohigh(4)...
  :1:rholow(4), wtna2so4(4),'k-',rhohigh(5):1:rholow(5), wtna2so4(5),...
   'k-',rhohigh(6):1:rholow(6), wtna2so4(6),'k-','LineWidth', 1)
hold on
semilogy(rhohigh(7):1:rholow(7), wtna2so4(7),'k-',rhohigh(8):1:rholow(8)...
  , wtna2so4(8),'k-',rhohigh(9):1:rholow(9), wtna2so4(9),'k-',rhohigh...
  (10):1:rholow(10), wtna2so4(10),'k-',rhohigh(11):1:rholow(11), ...
  wtna2so4(11),'k-',rhohigh(12):1:rholow(12), wtna2so4(12),'k-',...
  rhohigh(13):1:rholow(13), wtna2so4(13),'k-','LineWidth', 1)
hold on
semilogy(rhohigh(1):1:rholow(1), wtna2co3(1),'k-',...
   rhohigh(3):1:rholow(3), wtna2co3(3),'k-',rhohigh(4):1:rholow(4), ...
   wtna2co3(4),'k-',rhohigh(5):1:rholow(5), wtna2co3(5),...
   'k-',rhohigh(6):1:rholow(6), wtna2co3(6),'k-','LineWidth', 1)
hold on
semilogy(rhohigh(7):1:rholow(7), wtna2co3(7),'k-',rhohigh(8):1:rholow(8)...
  , wtna2co3(8),'k-',rhohigh(9):1:rholow(9), wtna2co3(9),'k-',rhohigh(10)...
  :1:rholow(10), wtna2co3(10),'k-',rhohigh(11):1:rholow(11), wtna2co3(11),...
  'k-',rhohigh(12):1:rholow(12), wtna2co3(12),'k-',...
  rhohigh(13):1:rholow(13), wtna2co3(13),'k-','LineWidth', 1)
%semilogy(rho(1),wtna2co3(1),'k+', rho(3),wtna2co3(3),'kx',rho(4:6),...
% wtna2co3(4:6),'k*',rho(7:8),wtna2co3(7:8),'kp',xnewc,f2,'k-',rho(1),...
% wtna2so4(1),'ko', rho(2:3),wtna2so4(2:3),'ks',rho(4:6),wtna2so4(4:6),'k^',...
% rho(7:8),wtna2so4(7:8),'kv',xnew,f1,'k-.',rholow(1:11),wtna2so4(1:11),'k.'...
% ,rhohigh(1:11),wtna2so4(1:11),'k.',rholow(1),wtna2co3(1),'k.',rholow(3:11)...
% ,wtna2co3(3:11),'k.',rhohigh(1),wtna2co3(1),'k.',rhohigh(3:11),...
% wtna2co3(3:11),'k.')
set(gca,'XDir','reverse','YDir','normal');
%errorbar(rho(1),wt1,0.005,0.019)
title(['Fig. 9: Solubility of mixture of sodium carbonate and sodium sulfate'...
  ],'Fontsize',15)
%axis([0.006 0.05 0.005 0.68])
legend('Na_2CO_3, CS1', 'Na_2CO_3, CS2-CS3','Na_2CO_3, CS4-CS6',...
  'Na_2CO_3, CS7-CS8','Na_2CO_3, CS9-CS13', 'Eq. 7 for pure Na_2CO_3',...
  'Na_2SO_4, CS1', 'Na_2SO_4, CS2-CS3','Na_2SO_4, CS4-CS6',...
  'Na_2SO_4, CS7-CS8','Na_2SO_4, CS9-CS13',' Eq. 8 for pure Na_2SO_4')
xlabel(['density (kg/m^3)'],'FontSize',14)
ylabel(['Solubility limit (wt%)'],'FontSize',14)
```

C.4 Main Code: Mixing, heat and mass transfer (MixHtMassCode.m)

```
%~~~~~~~~~~~~~~~~~~~~~~~~~~~~~~~~~~~~~~~~~~~~~~~~~~~~~~~~~~~~~~~~~~~~~~~~~~~~
% THIS CODE CALCULATES: (1) salt molecule deposition, (2) particle nucleation...
% & (3) particle deposition rate. FILES REQUIRED TO RUN THE CODE: dens.txt ...
% cp.txt K.txt enth.txt prand.txt vis.txt finddens.m depositfigs.m DATA SAVED ..
% IN FILES: depositinput.dat, depositout1.dat and depositout2.dat
%~~~~~~~~~~~~~~~~~~~~~~~~~~~~~~~~~~~~~~~~~~~~~~~~~~~~~~~~~~~~~~~~~~~~~~~~~~~~
clear
XYZ=0;
rcoag=0;
partradius=0;
warning off MATLAB:divideByZero
Pressure=24.5;% pressure, MPa
MassA=0.12/60;% flow rate of salt solution stream, kg/sec
MassB=1.2/60;% flow rate of the hot water stream, kg/sec
MFA=0.01;% mass fraction of salt in stream A
MFB=0;% mass fraction of salt in stream B
TB=415+273.15;% temperature of stream B, K
TA=222+273.15;% temperature of stream A, K
Gam=88E-3;% surface tension, typically 60x10^-3 to 150x10^-3 N/m
RunTime=10;% time the experiment is run, minutes
dia=0.0062;% tube inner diameter, m
L=3;% length of the test section, m
molmass=0.106;% molar mass of sodium carbonate, kg/mole
moldia=5.1E-10;% sodium carbonate molecular diameter,  m
rhos=2530;% sodium carbonate density, kg/m^3
inter=80;
DZ=2.9037/(inter*1000);% segment length m (time step), this is denoted by ...
%  ..."X" in the thesis
Ktube=19;% thermal conductivity of the test section tube, W/mK
Ksalt=0.48;% thermal conductivity of salt layer, W/mK
Rin=dia/2;% tube inner radius, m
Rout=0.009/2;% tube outer radius, m
loca=[250,780,1000,1600,2900];% temp. vs time profiles drawn at these locations, mm
[ET,nloca]=size(loca);
numtime=1;% number of times a segment is exposed to flowing fluid
N=1;%number of cells in the salt solution i.e., stream A
%It is important to choose the correct cell height i.e., the number of cells
%The height should be such that the fluid parcel lands in a different cell every time
%it moves a distance (calculated from the energy dissipation rate)
NZ=round(round(1000*L/DZ)/1000);% number of segments
DZ=L/NZ;% calculated again after rounding of the NZ
jump(1:NZ)=0;
for kj=1:inter:NZ
 jump(kj)=1;
end
jump(1:NZ);
```

```
% ************************************************************************
% calculate heat transfer from the fluid enthalpy gain in the test section
%T1 and T2 are used to calculate the heat input from enthalpy gain. These
%temperatures are of fluid entering and leaving the test section without
%any fluid being injected at the mixing tee. These should not be confused by fluid
%stream temperatures TA and TB which are for the two fluid streams entering the
%mixing tee. However, the flow rate should be equal to MassA+MassB
T1=399+273.15;% bulk temperature at test section inlet, K
T2=401+273.15;% bulk temperature at the test section outlet, K
DelT=T2-T1;
load dens.txt;% fluid density, kg/m^3
[nT,nP]=size(dens);% get file sizes from dens
P=dens(1,2:nP);% the first row contains the pressures, MPa
T=dens(2:nT,1);% the first column contains the temperatures, K
A=dens(2:nT,2:nP);
rho1=interp2(P,T,A,Pressure,T1);
load cp.txt;% specific heat capacity, J/kgK
A=cp(2:nT,2:nP);
Cp1=interp2(P,T,A,Pressure,T1);
Cp2=interp2(P,T,A,Pressure,T2);
AvCp=(Cp1+Cp2)/2;
Q=(MassA+MassB)*AvCp*DelT;% heat supplied, Watts
q=Q/(pi*(dia+Rout*2)/2*L);% heat flux, W/m^2
qprime=Q/L;% heat supplied per unit length, W/m
%************************************************************************
A=dens(2:nT,2:nP);
rhoA=interp2(P,T,A,Pressure,TA);
rhoB=interp2(P,T,A,Pressure,TB);
M=N*MassB/MassA;% number of cells in the main flow i.e., stream B
M=round(M);
fid = fopen('depositinput.dat','w');
fs = [Pressure; MassA; MassB;MFA;MFB;TB;TA;Ksalt;Ktube;Gam;RunTime;Rin;Rout;...
  qprime;q;numtime;nloca;DZ;rhos;M;N;L];
fprintf(fid,'%2.2f %1.3f %1.3f %1.3f %1.3f %3.2f %3.2f %2.2f %2.1f %2.3f %3.1f ...
...%2.5f %2.5f %5.2f %5.2f %3.0f %1.0f %1.6f %4.2f %5.0f %2.0f %2.2f',fs);
ff = [loca(1:nloca)];
fprintf(fid,'%5.0f %5.0f %5.0f %5.0f %2.0f\n',ff);
fclose(fid);
daa = fopen('profile.dat','w');
MFN(1:M+N)=0;% mass fraction of nucleated salt
R=round(10000/(M+N));
NP=R*(M+N);% total number of fluid parcels
PMFN(1:NP)=0;% mass fraction of nucleated salt in a parcel
PMFP(1:NP)=0;% mass fraction of salt particles in a parcel
CMFP(1:M+N)=0;% mass fraction of salt partciles in a cell
CNP(1:M+N)=0;% number of salt particles in a cell
PNP(1:NP)=0;% number of salt particles in a parcel
PNPN(1:NP)=0;% number of nucleated particles in a parcel
CNPN(1:M+N)=0;% number of nucleated particles in a cell
Mass=MassA+MassB;% total mass flow rate, kg/sec
D(1:NZ)=dia;% initial/clean tube inside diameter
```

```
A=dens(2:nT,2:nP);
rhoA=interp2(P,T,A,Pressure,TA);
rhoB=interp2(P,T,A,Pressure,TB);
veloc=(MassA/rhoA+MassB/rhoB)/(pi*dia^2/4);% fluid velocity, m/sec
PM=(Mass/veloc)*DZ/NP;% mass of each parcel in a segment, kg
massstar=PM*NP;% total mass of fluid in a segment, kg
DD=dia/(M+N)*1000;% height of each cell, mm
CLoc(1:M+N)=(1:M+N)*DD;% location of the cells, mm
CNum(1:M+N)=1:M+N;% position of each cell starting from bottom surface
Ts(1:NZ)=TB;% Ts is required to find properties at wall
load K.txt;% fluid thermal conductivity, W/mK
load enth.txt;% enthalpy, J/kg
load prand.txt;% prandtl number
load vis.txt;% dynamic viscosity, N.s/m^2
massdeptotal(1:NZ)=0;
fid = fopen('depositout2.dat','w');% leave this for z>1 and append later even if z=1
% MAIN LOOP(i.e., calculation for each time fluid passes a segment DZ)
for z=1:numtime
 partradold=0;
 partgrowth=0;
 mpart=0;
 segment=0;
 mmol=0;
 BalMFN=0;
 moldep=0;
 partdep=0;
 TotMFN(1:NZ)=0;
 MFNB(1:NZ)=0;
 BalMFN(1:NZ)=0;
 j=0;
 % Initialize cell temperatures
 CT(1:M/2)=TB;
 CT(M/2+N+1:M+N)=TB;
 CT(M/2+1:M/2+N)=TA;
 TMC=mean(CT);% mixed cup temperature, K
 % ************************************************************************
 % This calculation is for the Yamagata correlation
 A=cp(2:nT,2:nP);
 Cplist=interp2(P,T,A,Pressure,T);
 [Tsort,i]=sort(T);
 Cpsort=Cplist(i);
 [maxCp,imax]=max(Cplist);
 Tpc=T(imax);
 A=prand(2:nT,2:nP);
 Pr=interp2(P,T,A,Pressure,TMC);
 Prlist=interp2(P,T,A,Pressure,T);
 Prpc=Prlist(imax);
 %************************************************************************
 CMF(1:M/2)=MFB;% initializing for the cell salt mass fraction
 CMF(M/2+N+1:M+N)=MFB;
 CMF(M/2+1:M/2+N)=MFA;
```

```
das = fopen('profile1.dat','w');
dad = [CLoc;CMF;CT];
fprintf(das,'%2.4f %1.5f %3.4f\n',dad);
fclose(das);
Saltkg=sum(CMF)*massstar;% mass of salt present in a segment, kg
for i=0:1:M+N-1% initializing for the fluid parcel temperature and salt content
 PLoc(i*R+1:(i+1)*R)=CLoc(i+1);% fluid parcel location from the bottom surface, mm
 PCNum(i*R+1:(i+1)*R)=CNum(i+1);% fluid parcel location (in terms of cell number)
 %  from the bottom surface
 PT(i*R+1:(i+1)*R)=CT(i+1);% fluid parcel temperature
 PMF(i*R+1:(i+1)*R)=CMF(i+1);% salt mass fraction in each fluid parcel
end
figure (1)
subplot(4,1,1)
massfrac=plot(CMF,CLoc);% plots the cell salt mass fraction
axis([0 .011 -0.5 6.5]);
set(massfrac,'EraseMode','xor');
xlabel(['dissolved salt mass fraction'])
ylabel(['tube dia (mm)'])
subplot(4,1,2)
temp=plot(CT-273.15,CLoc);% plots cell temperatures
axis([325 425 -0.5 6.5]);
set(temp,'EraseMode','xor');
xlabel(['temperature (^oC)'])
ylabel(['tube dia (mm)'])
subplot(4,1,3)
Nucl=plot(MFN,CLoc);% plots nucleated salt mass fraction at cell locations
axis([0 1 -0.5 6.5]);
set(Nucl,'EraseMode','xor');
xlabel(['mass fraction of nucleated salt'])
ylabel(['tube dia (mm)'])
%subplot(3,2,4)
%pplot=plot(segment,partdep,'.');% plots salt particle deposition, kg
%axis([0 3000 0 0.002E-11]);
%set(pplot,'EraseMode','xor');
%ylabel(['salt particle deposition (kg)'])
%xlabel(['distance (mm)'])
%subplot(3,2,5)
%mplot=plot(segment,moldep,'.');% plots molecule deposition, kg
%axis([0 3000 0 0.006E-9]);
%set(mplot,'EraseMode','xor', 'MarkerSize',12);
%ylabel(['molecule deposition (kg)'])
%xlabel(['distance (mm)'])
record=hist(PLoc,CLoc);
subplot(4,1,4)
histogram=plot(record,CLoc);% plots histogram of the number of fluid parcels
axis([0 1860 -0.5 6.5]);
set(histogram,'EraseMode','xor');
ylabel(['tube dia (mm)'])
xlabel(['# of fluid parcels'])
for j=1:NZ
```

```
drawnow
segment=segment+DZ*1000;% length, mm
%pro=round(segment*10000000000);
if j==30
 daa = fopen('profile.dat','a');
 da = [CLoc;CMF;CT];
 fprintf(daa,'%2.4f %1.5f %3.4f\n',da);
 fclose(daa);
 ttt=-1;
end
if j==130
 daa = fopen('profile.dat','a');
 da = [CLoc;CMF;CT];
 fprintf(daa,'%2.4f %1.5f %3.4f\n',da);
 fclose(daa);
 qqq=-1;
end
if j==1400
 daa = fopen('profile.dat','a');
 da = [CLoc;CMF;CT];
 fprintf(daa,'%2.4f %1.5f %3.4f\n',da);
 fclose(daa);
 fff=-1;
end
if j==14000
 ggg=3;
 daa = fopen('profile.dat','a');
 da = [CLoc;CMF;CT];
 fprintf(daa,'%2.4f %1.5f %3.4f\n',da);
 fclose(daa);
end
A=dens(2:nT,2:nP);
rhob=interp2(P,T,A,Pressure,TMC);% fluid density at bulk conditions
A=K(2:nT,2:nP);
Kb=interp2(P,T,A,Pressure,TMC);% fluid thermal conductivity at bulk conditions
A=enth(2:nT,2:nP);
Hb=interp2(P,T,A,Pressure,TMC);% fluid enthalpy at bulk conditions
A=cp(2:nT,2:nP);
Cpb=interp2(P,T,A,Pressure,TMC);% specific heat at bulk conditions
A=prand(2:nT,2:nP);
Prb=interp2(P,T,A,Pressure,TMC);% Prandtl number at bulk conditions
A=vis(2:nT,2:nP);
viscb=interp2(P,T,A,Pressure,TMC);% dynamic viscosity at bulk conditions
A=dens(2:nT,2:nP);
rhow=interp2(P,T,A,Pressure,Ts(j));% fluid density at wall conditions
A=K(2:nT,2:nP);
Kw=interp2(P,T,A,Pressure,Ts(j));% fluid thermal conductivity at wall conditions
A=enth(2:nT,2:nP);
Hw=interp2(P,T,A,Pressure,Ts(j));% fluid enthalpy at wall conditions
A=cp(2:nT,2:nP);
Cpw=interp2(P,T,A,Pressure,Ts(j));% specific heat at wall conditions
```

```
A=vis(2:nT,2:nP);
viscw=interp2(P,T,A,Pressure,Ts(j));% dynamic viscosity at wall conditions
A=prand(2:nT,2:nP);
Prw=interp2(P,T,A,Pressure,Ts(j));% Prandtl number at wall conditions
Reb=4*Mass/(pi*D(j).*viscb);% Reynolds number at bulk conditions
Rew=4*Mass/(pi*D(j).*viscw);% Reynolds number at wall conditions
kviscw=viscw/rhow;% kinematic viscosity at wall conditions
kviscb=viscb/rhob;% kinematic viscosity at bulk conditions
% Calculate Nusselt number from Swenson correlation or Yamagata correlation
% Also change expression for Hm (molecular diffusivity) accordingly
% Calculation of Nusselt number from Swenson correlation
%Nu=0.00459*(Rew)^0.923*((Hw-Hb)*viscw/((Ts(j)-TMC)*Kw))^0.613*(rhow/(rhob))...
%^0.231;
% Calculation of Nusselt number from Yamagata correlation.
E=(Tpc-TMC)/(Ts(j)-TMC);
if E>1;  Fc=1;
else
 if E<0;  n2=1.44*(1+1/Prpc)-0.53;
  Fc=((Hb-Hw)/(TMC-Ts(j))/Cpb)^n2;
 else n1=-.77*(1+1/Prpc)+1.49;
  Fc=0.67*Prpc^(-.05)*((Hb-Hw)/(TMC-Ts(j))/Cpb)^n1;
 end
end
Nu=0.0135*Reb^.85*Prb^.8*Fc;% Nusselt number correlation
V=Mass/(rhob*pi*D(j)^2/4);% fluid velocity, m/s
% Calculation for salt particle deposition rate (kg/sec)
dt=DZ/V;% fluid residence time in each segment DZ, sec
F=(1.8*log10(6.9/Rew+(0.002/(3.7*D(j)*1000))^1.11))^(-2);% friction factor
Epsln=2*F*V^3/D(j);% dissipation rate
uprime=(Epsln*D(j)/2)^(1/3);
KE=(D(j)/2*Epsln)^(2/3);
turbvisc=0.09*KE^2/Epsln;% turbulent viscosity
Xvel=(turbvisc/0.9)/(D(j)/2);% charateristic fluid parcel velocity
Deltime=(D(j)/2)/Xvel;% time taken by fluid parcel to move a distance of D/2 i.e.,
% characteristic length
Ldash=Deltime*V;% the fluid parcel moves one X-tic length while fluid move this
% length along test section, m
DZRad=(((turbvisc/0.71)*Deltime)^0.5)*1000;% mm distance
CH=6.02/11;
DZRad=CH;
TotCel=6.02/CH;% total number of cells, M+N
DX=(6.02/(1000*(M+N)))^2*V/turbvisc*0.71*1000;
Vmol=4/3*(pi)*(moldia/2)^3;% volume of salt molecules, m^3
if jump(j)==1
 %Calculate the distance a fluid parcel would move using turbulent characteristic
 %velocity.
 DIST=(DZRad).*sign(-1+2.*rand(1,NP));% random +/- signs are multiplied by maximum
 % distance a fluid parcel can move
 Move=DIST./DD;% the distance moved in terms of # of cell locations
 numbers=hist(PLoc,CLoc);
 nuu=numbers(1);
```

```
PCNum=round(PCNum+Move);% update fluid parcel position after moving
nuulast=numbers (M+N);
for r=1:NP
 if  PCNum(r)<1;  PCNum(r)=1;
 elseif PCNum(r)>M+N; PCNum(r)=M+N;
 else PCNum(r)=PCNum(r);
 end
end
PLoc=PCNum.*DD;
histo=hist(PLoc,CLoc);
[rho(1:M+N)]=finddens(Pressure,CT(1:M+N));% fluid density in each cell
for b=1:M+N
 CT(b)=mean(PT(find(PCNum==b)));% update cell temperature
 PT(:,find(PCNum==b))=CT(b);% update fluid parcel temperature
 CMF(b)=mean(PMF(find(PCNum==b)));% mass fraction of dissolved salt in each cell
 CM(b)=(histo(b)).*PM;% mass of fluid in each cell, kg
 if j>1
  CMFP(b)=mean (PMFP(find(PCNum==b)));% m. f. of particulate salt in a cell
  PMFP(:,find(PCNum==b))=CMFP(b);% m. f. of particulate salt in a parcel
  CNP(b)=CMFP(b).*rho(b)./(4/3*pi*rhos.*partradius^3);% # of ...
  %  particles per m^3 in a cell
  PNP(:,find(PCNum==b))=CNP(b)./histo(b);% number of particles in a parcel
 end
end
gg=hist(PLoc,CLoc);
rrt=gg(1);%number of parcels in bottom cell per unit segment length
rrf=gg(M+N);%number of parcels in top cell
medge=Mass*(rrt+rrf)/NP;
[rho(1:M+N)]=finddens(Pressure,CT(1:M+N));% fluid density in each cell
end
CSat(1:M+N)=0.01*(exp(6.24E-8.*(rho(1:M+N)).^3-8.48E-5.*(rho(1:M+N)).^2+...
 0.046.*rho(1:M+N)-9.74));% cell salt saturation limit (mass fraction)
DEGSAT(1:M+N)=CMF(1:M+N)./CSat(1:M+N);% degree of saturation in each cell
for u=1:M+N;
 if DEGSAT(u)< 2;
  %JJ are the number of salt particles nucleated per unit time per cm^3
  JJ(u)=0;
  rstar(u)=0;
 else JJ(u)=10E30*exp(-16*pi*Gam^3*Vmol^2/(3.*1.38E-23^3.*CT(u).^3*...
   (log(DEGSAT(u))).^2));
  rstar(u)=2*Gam*Vmol/(1.38E-23.*CT(u).*log(DEGSAT(u)));% critical radius..
  % of nucleated salt particles, m
 end
 mperpart(u)=rstar(u)^3/(moldia/2)^3;% # of salt molecules per salt particle
 NPN(u)=JJ(u).*dt*(100)^3;% # of salt particles nucleated per m^3
 mpstar(u)=4/3*pi*rstar(u).^3*rhos;%kg salt per particle
 MFN(u)=mpstar(u).*NPN(u)./rho(u);% mass...
 % fraction of nucleated salt (kg salt/kg soln)
 CMFOLD(u)=CMF(u);
 CMF(u)=(CMF(u)-MFN(u));% update mass fraction of dissolved salt in each cell
 if JJ(u)>1
```

```
 if CMF(u)<0;
  line=344
 end
end
PMF(:,find(PCNum==u))=CMF(u);% update dissolved salt m. f. of fluid parcels
PMFN(:,find(PCNum==u))=MFN(u);% mass fraction of nucleated salt in the parcel
PNPN(:,find(PCNum==u))=NPN(u)*2/(rrt+rrf);%number of nucleated particles...
% in a fluid parcel
end
NPNtotal(j)=sum(NPN);% total number of salt particles nucleated/m^3 at segment j
if NPNtotal (j)>0
 XYZ=2;
end
NPNtot=sum(NPN);
if rstar(rstar~=0)>0;
 averstar=mean(rstar(rstar~=0));% mean radius of nucleated particles, m
else averstar=0;
end
diffmol=1.38e-23*(Ts(j))*1/(3*pi*viscb*moldia);% molecular diffusivity ...
% coefficient (m^2/sec) from Stokes Einstein relation
rhoave=mean(rho);% average fluid density at the segment, kg/m^3
if XYZ>1
 for hf=1:M+N;
  if NPN(hf) >1
   if CMF(hf)>CSat(hf)
    rf(hf)=((CMF(hf)-CSat(hf)).*rho(hf).*6.023E23/molmass*...
     Vmol/(4*pi*NPN(hf)./3))^(1/3);
    KD=(48*pi^2*Vmol.*NPN(hf).^2.*(CMF(hf)-CSat(hf)).*rho(hf...
     ).*6.023E23/molmass)^...
     (-1/3)*(diffmol)^(-1);% factor, sec
    syms g;
    TIMEtot=KD*int(1/(g^(1/3)*(1-g)),g,0,0.99);% time to reach final particle size
    TIMEtot=double(TIMEtot);
    alph=dt/TIMEtot;% extent of reaction
    if alph>1;  alph=1;
    end
    partgrowth(hf)=rf(hf).*alph^3;% grown salt particle radius after time dt, m
   end
  end
 end
 if rcoag>0;
  if sum(NPN)>1
   partradius=(sum(NPN).*mean(partgrowth(partgrowth~=0))+...
    sum(CNP).*rcoag)/(sum(NPN)+sum(CNP));
  else
   partradius=rcoag;
  end
else partradius=averstar;% i.e., only for the first segment with nucleation
 end
end
if NPNtotal (j)>0
```

```
 partradius;
end
rbalance=partradius;
partradreco(j)=partradius;% salt particle radius at each segment, m
CMFBottom=CMF(1);% dissolved salt mass fraction of cell at bottom
CMFTop=CMF(M+N); % dissolved salt mass fraction of cell at top
CMFWall=(CMFBottom+CMFTop);% dissolved salt mass fraction of cells near the wall
CMFB=mean(CMF);% mean mass fraction of dissolved salt
diffpart=1.38e-23*(Ts(j))*1/(3*pi*viscb*2*partradius);% salt particle diffusivity
% coefficient (m^2/sec) from Stokes Einstein relation
ScPart=kviscw/diffpart;% salt particle Schmidt number
taup=rhos*(2*partradius)^2/(18*viscb);% salt particle relaxation time, sec
tauw=rhow*V^2*F/8;% wall shear stress, N/m^2
Ustar=(tauw/rhow)^0.5;% wall friction velocity, m/sec
taupplus=taup*(Ustar^2)/kviscb;
if taupplus>20; Vdstar=0.18;
elseif taupplus<0.2; Vdstar=0.065*ScPart^-.667;
else Vdstar=3.5E-4*taupplus^2;
end
Vd=Vdstar*Ustar;% salt particle deposition velocity, m/sec
if taup==0; Vd=0;
end
radius=partradreco(j);
for hf=1:M+N;
 CMFP(hf)=CMFP(hf)+MFN(hf);
 PMFP(:,find(PCNum==hf))=CMFP(hf);
 if radius >0
  CNP(hf)=CMFP(hf)*rho(hf)/(4/3*pi*rhos.*radius^3);
  PNP(:,find(PCNum==hf))=CNP(hf)./gg(hf);
 else CNP(hf)=0;
 end
end
PMASS(j)=sum(CMFP);
for bg=1:M+N;
 if CNP(bg)>1
  K12=8*1.38e-23*CT(bg)/(3*viscb);
  critcoagtime=2./(K12.*CNP(bg));
  CNPco(bg)=CNP(bg)./(1+dt/critcoagtime);
  newpartradi=radius*(CNP(bg)./CNPco(bg))^(1/3);
 else
  newpartradi=radius;
 end
end
if newpartradi>0
 rcoag=mean(newpartradi(newpartradi~=0));
end
rbalance;
partradreco(j)=rbalance;
if CMFP(1)>0
 P1=(Vd*DZ*pi*D(j)*rho(1)*(rrt+rrf)/(2*R*2*medge));
 CMFPold=CMFP(1) ;
```

```
 CMFP(1)=(1-P1)/(1+P1)*CMFPold;
 CMFP(M+N)=CMFP(1);
 mpart(j)=Vd.*pi.*D(j).*DZ.*rho(1).*(CMFP(1)+CMFPold)*(rrt+rrf)/(2*2*R);% salt ...
 % particle deposition rate, kg/sec
 CMFP(1)=CMFP(1)-mpart(j)/medge;
 CMFP(M+N)=CMFP(1);
 PMFP(:,find(PCNum==1))=CMFP(1);
 PMFP(:,find(PCNum==M+N))=CMFP(M+N);
 CNP(1)=CMFP(1).*rho(1)/(4/3*pi*rhos.*radius^3);
 PNP(:,find(PCNum==1))=CNP(1);
 PNP(:,find(PCNum==M+N))=CNP(M+N);
else mpart(j)=0;
end
partdep(j)=mpart(j).*dt;% mass of salt particles deposited in the segment kg
% Calculation of molecular deposition rate from heat & mass transfer analogy
CB=CMFB*100;% Balance dissolved salt conc. after the particle nucleation, wt%
Sc=kviscw/diffmol;% Schmidt number of salt molecules
h=Nu*(Kb)/D(j);% heat transfer coefficient from the correlation, W/m^2K
Le=Sc/Prw;% Lewis number
% NOTE: Choose Hm for the Nu# relation, Le^0.387 for Swenson and Le^0.2 for
%Yamagata correlation
%Hm=h/(rhow*Cpw*Le^0.387);
Hm=h/(rhow*Cpw*Le^0.2);
CW=CMFWall*100;% dissolved salt concentration at wall,  wt%
CWmax=exp(6.24E-8*(rhow)^3-8.48E-5*(rhow)^2+0.046*rhow-9.74);% maximum possible
% dissolved salt at wall, wt%
if  CW>CWmax;
 A1=Hm*pi*D(j)*rhow*DZ/medge*(rrt+rrf)/(2*R);
 CMFnew= ((1-A1/2)/(1+A1/2)*CW+A1/(1+A1/2)*(CWmax))/100;%updated ...
 % mass fraction of the edge cell
 www=2;
 mmol(j)=Hm*DZ*pi*D(j)*rhow*((CMFnew*100+CW)/2-CWmax)/100*(rrt+rrf)/(2*R);% mol-...
 %ecule deposition rate, kg/sec
 CMF(1)=CMF(1)-mmol(j)/medge;
 dsd=mmol(j);
 CMF(M+N)=CMF(1);
 PMF(:,find(PCNum==1))=CMF(1);
 PMF(:,find(PCNum==M+N))=CMF(M+N);
else mmol(j)=0;
end
moldep(j)=mmol(j)*dt;% mass of salt molecules deposited in the segment, kg
massdep(j)=moldep(j)+partdep(j);% total salt mass deposited in the segment, kg
set(massfrac,'XData',CMF,'YData',CLoc)
set(temp,'XData',CT-273.15,'YData',CLoc)
set(Nucl,'XData',MFN,'YData',CLoc)
%set(pplot,'XData',segment,'YData',partdep)
%set(mplot,'XData',segment,'YData',moldep)
set(histogram,'XData',histo,'YData',CLoc)
title(['                                                    ',num2str(j)...
 ],'Color','b','Fontsize',12)
% Updating conditions for the next segment length
```

```
A=cp(2:nT,2:nP);
Cpe=interp2(P,T,A,Pressure,CT(1));% specific heat at wall conditions
CTold=CT(1);
CT(1)=CT(1)+qprime*DZ/(medge*Cpe);
PT(:,find(PCNum==1))=CT(1);
CT(M+N)=CT(1);
PT(:,find(PCNum==M+N))=CT(1);
PW=h*pi*D(j)*(rrt+rrf)/(2*R);
Tif(j)=qprime*DZ/PW+(CT(1)+CTold)/2;% fluid-salt/tube interface temp. after heating
Ts(j+1)=Tif(j);% calculate interface properties for the next segment
TMC=mean(CT);% updating mixed cup temperature after heating
devo(j)=(moldep(j)+partdep(j))./rhos; % volume of deposited salt layer, m^3
deth(j)=(Rin-(((Rin*2)^2-4*devo(j)./(pi*DZ)).^(0.5))/2);% salt layer thickness, m
if D(j)>deth(j);
 D(j)=D(j)-deth(j);
else    disp(['plugging']);
end
R1(j)=D(j)/2;
if Rin==R1(j); Tw(j)=Tif(j);
else Tw(j)=Tif(j)+Q*log(Rin./R1(j))/(2*pi*Ksalt*L);% tube inner surface temp.
end
To(j)=Tw(j)+q*Rin/(2*Ktube)*((Rin/Rout)^2-log((Rin/Rout)^2)-1)/(1-(Rin/Rout)^2);
saved1(j)=segment;
saved2(j)=TMC-273.15;
saved3(j)=dt;
BalSaltkg=Saltkg-massdep;
Saltkg=BalSaltkg;
kg(j)=Saltkg(j);
Saltkg=Saltkg(j);
RecoSaltkg(j)=kg(j);% salt mass present for the next segment, kg
end
Ts(j)=Tif(j);% this is done to update interface temp for the next z
if z==1; Tclean(1:NZ)=Ts(1:NZ)-273.15;% clean tube inner surface temp
end
massdepnew(1:NZ)=massdep(1:NZ)+massdeptotal(1:NZ);
massdeptotal=massdepnew;% total mass of salt deposited (kg) after z # of cycles
% this is used to find deposit thickness
yy = [saved1; saved2; moldep;partdep;massdep;partradreco;NPNtotal;saved3;PMASS];
fid = fopen('depositout1.dat','w');
fprintf(fid,'%4.0f %5.2f %12.8e %12.8e %12.8e %12.8e %12.8e %5.4E %8.7E\n',yy);
fclose(fid);
y = [saved1; RecoSaltkg; Tif-273.15;Tw-273.15;To-273.15;Tclean;mmol+mpart];
fid = fopen('depositout2.dat','a');
fprintf(fid,'%4.0f %1.3E %5.2f %5.2f %5.2f %5.2f %4.5E\n',y);
%Variables are: segment number, undeposited mass (kg) of salt after every segment,
%fluid-tube/salt layer interface temperature,inside wall temp,
%outside wall temp, salt mass deposition rate
fclose(fid);
end
[j]=depositfigs(j);
```

C.4.1 Figures Code: Mixing, heat and mass transfer (Deposit-figs.m)

```
%clear
%This code runs with deposit.m and is used to draw figure # 2 to 6
function [j]=depositfigs(j)
load depositout1.dat
load depositout2.dat
load depositinput.dat
[NZ,vn]=size(depositout1);
length=depositout1(1:NZ,1);
%length=0:0.2:NZ*3/0.2
moldep=depositout1(1:NZ,3);
partdep=depositout1(1:NZ,4);
massdeptotal=depositout1(1:NZ,5);%kg of salt deposited
partradreco=depositout1(1:NZ,6);
NPNtotal=depositout1(1:NZ,7);
dt=depositout1(1:NZ,8)';
PMass=depositout1(1:NZ,9);
Pressure=depositinput(1,1);
MassA=depositinput(1,2);
MassB=depositinput(1,3);
MFA=depositinput(1,4);
TB=depositinput(1,6);
TA=depositinput(1,7);
Ksalt=depositinput(1,8);
Ktube=depositinput(1,9);
Gam=depositinput(1,10);
RunTime=depositinput(1,11);
Rin=depositinput(1,12);
Rout=depositinput(1,13);
qprime=depositinput(1,14);
q=depositinput(1,15);
numtime=depositinput(1,16);
nloca=depositinput(1,17);
DZ=depositinput(1,18);
rhos=depositinput(1,19);
M=depositinput(1,20);
N=depositinput(1,21);
L=depositinput(1,22);
loca(1:nloca)=depositinput(1,23:nloca+22);
DZloca(1:nloca)=round(round(loca(1:nloca)/DZ)/1000);
Tclean=depositout2(1:NZ,6)';% clean surface temperature, oC
GG=depositout2(1:NZ,7);%kg/sec of salt deposition
WW=depositout2(1:NZ,3);% fluid/salt ir tube interface temperature, oC
str1(1) = {['q = ',num2str(q/1000,'%3.2f'),' kW/m^2']};%heat flux, kW/m^2
str1(3) = {['T_{B} = ',num2str(TB-273.15),' ^oC']};% temp. of hot water stream, oC
str1(4) = {['T_{A} = ',num2str(TA-273.15),' ^oC']};% temp. of salt solution, oC
str1(5) = {['m_{B} = ',num2str(MassB*60),' kg/min']};% flow of hot water, kg/min
str1(6) = {['m_{A} = ', num2str(MassA*60),' kg/min']};% m.f. of salt solution, kg/min
```

```
str1(7) = {['\gamma = ', num2str(Gam,'%5.3f'),' N/m']};% surface tension, N/m
str1(8) = {['salt m.f. in A =  ', num2str(MFA)]};% salt m. f. of salt solution stream
str1(9) = {['dx =  ', num2str(DZ,'%1.6f'),' m']};% segment length
str1(2) = {['P =  ', num2str(Pressure),' MPa']};% system pressure
str1(10) = {['\Deltad =  ', num2str(6.2/1000/(M+N),'%1.5f'),' m']};%
% CHECK if the tube is plugged before RunTime
dtnew=dt';
DThickFinal(1:NZ)=GG(1:NZ).*dtnew;%this is kg of salt deposit
depvolume=DThickFinal./rhos;
depthickness=(Rin-(Rin.^2-depvolume./(pi*DZ)).^(0.5));% deposit thickness in m
DThickFinal(1:NZ)=1000*depthickness;% mm of deposit thickness in one residence time
slopfinal(1:NZ)=DThickFinal(1:NZ)./dt(1:NZ);% slope mm/sec
slopsort=slopfinal(1:NZ);
[maxslop,maxd]=max(slopfinal);
plugtime=(2/maxslop)/60;%time to plug, minutes
%####################################################################
figure (2)
%####################################################################
%this figure plots the molecule and particle deposition at various TS ...
% ..locations after one residence time at each segment
text(500,moldep(500)/DZ, 'molecule mass','Color','r',  'VerticalAlignment',...
 'bottom', 'HorizontalAlignment','left','FontSize',8)
text(2100,moldep(2)/DZ,str1,'HorizontalAlignment','left','VerticalAlignment'...
 ,'top','Fontsize',10)
hl1 = line(length(1:80:NZ),moldep(1:80:NZ)/DZ,'Color','r');
ax1 = gca;
ylabel(['Mass of deposited salt molecules per segment length (kg/m)'],'FontSize',12)
set(ax1,'XColor','r','YColor','r','FontSize',9)
ax2 = axes('Position',get(ax1,'Position'),'YAxisLocation','right','Color','none',...
 'XColor' ,'k','YColor','b','FontSize',9);
hl2 = line(length(1:80:NZ),partdep(1:80:NZ)/DZ,'Color','b');
xlabel (['Test section location (mm)'],'FontSize',12)
ylabel(['Mass of deposited salt particles per segment length (kg/m)'],'FontSize',12)
text(500,partdep(500)/DZ,[' particle mass',],'Color','b', 'VerticalAlignment'...
 ,'bottom','HorizontalAlignment','left','FontSize',8)
%axis([0 NZ 0 1.4001E-8]);
%####################################################################
figure (3)
%####################################################################
%plots the particle radius and # of salt particles at various TS locations...
%after one residence time at each segment
text(600,partradreco(600), ['particle diameter'],'Color','k', ...
 'VerticalAlignment','bottom','HorizontalAlignment','right','FontSize',9)
text(600,partradreco(500), ['particulate salt mass fraction'],'Color'...
 ,'k',  'VerticalAlignment','bottom','HorizontalAlignment','right','FontSize',9)
text(600,partradreco(1000),['number of particles/m^3',],'Color','k', ...
 'VerticalAlignment','bottom','HorizontalAlignment','left','FontSize',9)
text(600,partradreco(500),str1,'HorizontalAlignment','left',...
 'VerticalAlignment','top','Fontsize',10)
hl1 = line(length,partradreco*2E7,'Color','k');
hl4 = line(length,PMass*1000,'Color','k');
```

```
ax1 = gca;
ylabel(['Average salt particle diameter (m x 10^7) Particulate salt m. f. (g/kg)'....
 ],'FontSize',12)
set(ax1,'XColor','r','YColor','k')
ax2 = axes('Position',get(ax1,'Position'),'YAxisLocation','right','Color','none'...
 ,'XColor', 'k','YColor','k');
hl3 = line(length,NPNtotal,'Color','k','Parent',ax2);
xlabel (['Test section location (mm)'],'FontSize',12)
ylabel(['Number of nucleated salt particles/m^3'],'FontSize',12)
%####################################################################
figure (4)
%####################################################################
%this figure plots the deposit thickness after "RunTime" minutes of running
depthick=depthickness*RunTime*60./dt;% salt thickness m
plot(length,depthick*1000,'k-');% plots the mass fraction of salt at cell locations
xlabel (['Test section location (mm)'],'Fontsize',12)
ylabel(['Salt deposit thickness (mm) after ' num2str(RunTime),' min'],'Fontsize',12)
text(1500,depthick(5),str1,'HorizontalAlignment','left','VerticalAlignment'...
 ,'top','Fontsize',10)
%####################################################################
%figure(5)
%####################################################################
%plots the increase in temperature with time at "loca" locations of test section
for locax=1:nloca;% this loop is for each location where temp is to be plotted
  for runtime=1:1:RunTime% this loop is for variation of time at each location
  DThick(locax)=DThickFinal(DZloca(locax));
  slop(locax)=DThick(locax)./dt(DZloca(locax));
  TotalThick(runtime,locax)=(slop(locax).*runtime*60);
  Rfoul(runtime,locax)=Rin-TotalThick(runtime,locax)./1000;
  Tintface(locax)=WW(DZloca(locax));
  Twallin(runtime,locax)=Tintface(locax)+qprime*log(Rin./Rfoul...
   (runtime,locax))/(2*pi*Ksalt);
  Twallout(runtime,locax)=Twallin(runtime,locax)+q*Rin/(2*Ktube...
   )*((Rin/Rout)^2-log((Rin/Rout)^2)-1)/(1-(Rin/Rout)^2);
 end
end
time = 1:1:RunTime;

%####################################################################
figure(6)
%####################################################################
%plots outer surface temp of clean tube and after "RunTime" minutes of exposure
depthick=depthickness*RunTime*60./dt;% salt thickness m
RfoulFinal(1:NZ)=Rin-depthick(1:NZ);
TintfaceFinal(1:NZ)=WW(1:NZ);
TwallinFinal(1:NZ)=TintfaceFinal(1:NZ)+qprime*...
 log(Rin./RfoulFinal(1:NZ))/(2*(pi)*Ksalt);
TwalloutFinal(1:NZ)=TwallinFinal(1:NZ)+q*Rin/(2*Ktube)*...
 ((Rin/Rout)^2-log((Rin/Rout)^2)-1)/(1-(Rin/Rout)^2);
TCwallout(1:NZ)=Tclean(1:NZ)+q*Rin/(2*Ktube)*((Rin/Rout)^2-...
 log((Rin/Rout)^2)-1)/(1-(Rin/Rout)^2);%clean surface outer temp.
```

```
plot(length,TwalloutFinal,'k-',length,TCwallout,'k-.')
xlabel(['Test section location (mm) '],'FontSize',12)
ylabel(['Outer surface temperature ( ^oC) '],'FontSize',12)
text(1500,TwalloutFinal(5),str1,'HorizontalAlignment','left',...
 'VerticalAlignment','top','Fontsize',10)
text(500,TCwallout(500), 'clean surface','Color','k',  'VerticalAlignment',...
 'bottom','HorizontalAlignment','left','FontSize',8)
text(500,TwalloutFinal(500),['after ',num2str(RunTime),' minutes'],'Color','k',...
 'VerticalAlignment','bottom','HorizontalAlignment','left','FontSize',8)
%#####################################################################
% the following figure is plotted to confirm the linear growth ...
% of deposit with repeatetive
% exposure of test section to the scaling fluid
if numtime>1
 figure (7)
 %###################################################################
 [nI,nK]=size(depositout2);
 GG=depositout2(1:nI,7);
 sect=10;%enter section location (mm) where deposit ...
 % ...profile is to be drawn for numtime>1
 inc=dt(sect);
 depprof(1:numtime,1)=GG(sect:NZ:NZ*(numtime-1)+sect);
 times(1:numtime)=inc:inc:inc*numtime;
 plot(times(1:numtime),depprof(1:numtime),'-r^');
 xlabel([num2str(sect),' mm location exposure time  (sec)'])
 ylabel(['deposit thickness (mm) '])
end
```

Bibliography

[1] R. E. Sonntag, Borgnakke C., and G. J. Van Wylen. *Fundamentals of Thermodynamics.* John Wiley and Sons, New York, 6^{th} edition, 2003.

[2] P. Kritzer and E. Dinjus. An assessment of supercritical water oxidation (SCWO) existing problems, possible solutions and new reactor concepts. *Chemical Engineering Journal*, 83:207–214, 2001.

[3] R. W. Shaw and N. Dahmen. Destruction of toxic organic materials using supercritical water oxidation: Current state of technology. In E. Kiran, P. G. Debenedetti, and C. J. Peters, editors, *Supercritical Fluids - Fundamentals and Applications*, volume 366 of *NATO Science Series E*, pages 425–438. Kluwer Academic Publishers, Dordrechht, 2000.

[4] O. I. Martynova. Solubility of inorganic compounds in subcritical and supercritical water. In deG Jones, D, J. E. Slater, and R. W. Staehle, editors, *High Temperature and High Pressure Electrochemistry in Aqueous Solutions*, pages 131–138, Texas, 1973. Nat. Assoc. of Corrosion Engrs, NACE 4.

[5] F. J. Armellini and J. W. Tester. Solubility of sodium chloride and sodium sulfate in sub- and supercritical water vapor from 450-550°C and 100-250 bar. *Fluid Phase Equilibria*, 84:123–142, 1993.

[6] F. J. Armellini and J. W. Tester. Experimental methods for studying salt nucleation and growth from supercritical water. *Journal of Supercritical Fluids*, 4:254–264, 1991.

[7] S. N. Rogak and P. Teshima. Deposition of sodium sulfate in a heated flow of supercritical water. *AIChE Journal*, 45:240–247, 1999.

[8] M. Hodes, P. A. Marrone, G. T. Hong, K. A. Smith, and J. W. Tester. Salt precipitation and scale control in supercritical water oxidation - part A; fundamentals and research. *Journal of Supercritical Fluids*, 29:265–288, 2004.

[9] M. Perrut. Supercritical fluid applications: Industrial developments and economic issues. *Industrial and Engineering Chemistry Research*, 39:4531–4535, 2000.

[10] J. F. Connelly. Solubilities of hydrocarbons in water near critical solution temperature. *J. Chem. Eng. Data*, 11:13–16, 1966.

[11] G. M. Schneider. Phase equilibria in fluid mixtures at high pressures. In I. Prigogine and S. A. Rice, editors, *Advances in Chemical Physics*, volume XVII, page 39. John Wiley, New York, 1970.

[12] H. Schmieder and J. Abeln. Supercritical water oxidation: State of the art. *Chemical Engineering and Technology*, 22(11):903–908, 1999.

[13] J. W. Tester, H. R. Holgate, F. J. Armellini, P. A. Webley, W. R. Killilea, G. T. Hong, and H. E. Barner. Supercritical water oxidation technology: Process development and fundamental reserach. In D. W. Tedder and F. G. Pohland, editors, *Emerging technologies in hazardous waste management III*, ACS symposium series 518, chapter 3, pages 35–76. ACS, Washington DC, 1993.

[14] J. W. Tester and G. T. Hong. Salt precipitation and plugging session. In *Supercritical water oxidation - Achievements and challenges in commercial applications strategic analysis, Inc. Workshop*, Washington DC, August 14-15, 2001.

[15] *Supercritical water oxidation - Achievements and challenges in commercial applications strategic analysis, Inc. Workshop*, Washington DC, August 14-15, 2001.

[16] P. A. Marrone, M. Hodes, K. A. Smith, and J. W. Tester. Salt precipitation and scale control in supercritical water oxidation - part B; commercial/full-scale applications. *Journal of Supercritical Fluids*, 29:289–312, 2004.

[17] R. N. McBrayer and J. W. Griffith. Turn off the heat. *Industrial Wastewater*, July/August:1–3, 1996.

[18] E. F. Gloyna and L. Li. Supercritical water oxidation: An engineering update. *Waste Management*, 13:379–394, 1993.

[19] S. A. Gairns and J. Joustra. Apparatus for self cleaning of process tubes. US Patent 5,890,531, 1998.

[20] M. S. Khan and S. N. Rogak. Solubility of Na_2SO_4 and Na_2CO_3 and their mixture in supercritical water. *Journal of Supercritical Fluids*, 30:359–373, 2004.

[21] M. S. Khan and S. N. Rogak. Phase equilibrium of Na_2SO_4 and Na_2CO_3 at elevated temperature and pressure. In *52nd Canadian Chemical Engineering Conference*, Vancouver, Canada, October 2002.

[22] M. S. Khan and S. N. Rogak. Deposition of Na_2CO_3 in supercritical water oxidation systems and its mitigation. In A. P. Watkinson, H. Muller-Steinhagen, and M. R. Malayeri, editors, *2003 ECI Conference Heat Exchanger Fouling and*

Cleaning Fundamentals and Applications NM. USA, pages 53–59. The Berkeley Electronic Press, 2004.

[23] I. Vera-Perez, S. N. Rogak, and R. Branion. Supercritical water oxidation of phenol and 2,4 Dinitrophenol. *Journal of Supercritical Fluids*, 30:71–88, 2003.

[24] E. Asselin, A. Alfantazi, S. N. Rogak, I. Vera-Perez, D. Faraji, and R. Branion. Case study of the failure of supercritical water oxidation reactor tubing during the treatment of 2,4 DNP with ammonium sulfate. In *International Symposium on the Environmental Degradation of Materials and Corrosion Control in Metals*, Vancouver, Canada, August 2003.

[25] J. Abeln. Cost effective destruction of toxic organic wastes by supercritical hydrothermal oxidation. In *European Workshop on Environmental Technologies*, Darmstadt, 16-19 June 1998.

[26] C. Casal and H. Schmidt. SUWOX - a facility for the destruction of chlorinated hydrocarbons. *Journal of Supercritical Fluids*, 13:269–276, 1998.

[27] A. Gidner, L. Stenmark, J. Abrahamsson, and K. Carlsson. The Chematur Engineering SCWO pilot plant. Treatability studies. In *Sixth Meeting on Supercritical Fluids*, page 427, Nottingham, UK, 1999.

[28] T. R. Bott. *Fouling of Heat Exchangers.* Elsevier, Netherlands, 1995.

[29] F. J. Armellini. *Phase equilibria and precipitation phenomena of sodium chloride and sodium sulfate in sub- and supercritical water.* PhD thesis, Department of Chemical Engineering, Mass. Inst. of Technology, 1991.

[30] C. A. LaJeunesse, S. F. Rice, R. G. Hanush, and J. D. Aiken. Salt deposition studies in a supercritical water oxidation reactor. Interim report, Engineering and Combustion Technology Departments, Sandia National Laboratories, 1993.

[31] J. P. C. Chan, C. A. LaJeunesse, and S. F. Rice. Experimental techniques to determine salt formation and deposition in supercritical water oxidation reactors. In S. Acharya, K. Annamalai, C. Presser, and R. D. Skocypec, editors, *Fire, Combustion and Hazardous Waste Processing*, volume 296, pages 171–176. ASME Heat Transfer Division (HTD), 1994.

[32] M. S. Hodes, K. A. Smith, W. S. Hurst, W. J. Bowers, and P. Griffith. Measurements and modeling of deposition rates from a near supercritical aqueous sodium sulfate solution to a heated cylinder. In *National Heat Transfer Conference*, volume 350, pages 107–119. ASME Heat Transfer Division (HTD), 1997.

[33] P. Teshima. Fouling rates from a sodium sulfate-water solution in supercritical water oxidation reactors. Master's thesis, Department of Mechanical Engineering, The University of British Columbia, 1997.

[34] D. Filipovic. Deposition of sodium chloride from supercritical water. Master's thesis, Department of Mechanical Engineering, The University of British Columbia, 1999.

[35] L. F. Melo, T. R. Bott, and C. A. Bernardo. Cleaning of fouled surfaces; a discussion. In E. F. C. Somerscales and J. G. Knudsen, editors, *Fouling Science and Technology*, volume 145 of *NATO ASI*, pages 721–726, Boston, 1988. Kluwer Academic.

[36] M. Modell, Kuharich E.F., F. Evan, and M. R. Rooney. Supercritical water oxidation process of organics with inorganics. US Patent 5,252,224, 1993.

[37] E. A. Duffy. *Investigation of magnetic water treatment devices.* PhD thesis, Clemson University, 1977.

[38] J. D. Donaldson. Scale prevention and descaling. *Tube International*, pages 39–42, 1988.

[39] E. Nordell. *Water treatment for industrial and other uses.* Reinhold Publication Corp., New York, 2^{nd} edition, 1961.

[40] J. D. Donaldson and S. M. Grimes. Scale prevention in steel pretreatment by magnetic treatment. *Steel Times Int.*, pages 44–45, 1987.

[41] J. D. Donaldson and S. M. Grimes. Lifting the scales from our pipes. *New Scientist*, pages 43–46, 1988.

[42] G. F. Hewitt, G. Shires, and T. R. Bott. *Process Heat Transfer.* CRC Press Inc., 1994.

[43] M. J. Gough and J. V. Rogers. Reduced fouling by enhanced heat transfer using wire matrix radial mixing elements. *AIChE Symposium series 257*, 83:16–21, 1987.

[44] M. J. Gough. Tubeside inserts solve refinery wax crystallization fouling problem. *Chem. Tech. Europe*, 1(1):21, 1994.

[45] G. Gardner. No fouling. *Chem. Engr.*, August(541):Supplement S9, 1994.

[46] B. D. Crittenden, S. T. Kolaczkowski, and T. Takemoto. Use of tube inserts to reduce fouling from crude oils. *AIChE Symp. Series*, 295(89):300–307, 1993.

[47] M. Forster, W. Augustin, and M. Bohnet. Influence of the adhesion force crystal/heat exchanger surface on fouling mitigation. *Chemical Engineering and Processing*, 38:449–461, 1999.

[48] H. M. Muller-Steinhagen and Q. Zhao. Investigation of low surface alloys made by ion implantation technology. *Chemical Engineering Science*, 52(19):3321–3332, 1997.

[49] J. W. Mayer, L. Eriksson, and J. A. Davies. *Ion Implantation of Semiconductors.* Academic Press, New York, 1970.

[50] H. E. Barner, C. Y. Huang, J. Johnson, G. Jacobs, M. A. Martch, and W. R. Killilea. Supercritical water oxidation: an emerging technology. *Journal of Hazardous materials*, 31(1):1–17, 1992.

[51] P. J. Crooker, K. S. Ahluwalia, Z. Fan., and J. Prince. Operating results from supercritical water oxidation plants. *Ind. Eng. Chem. Res*, 39(12):4865–4870, 2000.

[52] T. G. McGuiness. Developments in transpiring-wall SCWO reactor technology. In *First International Workshop on Supercritical Water Oxidation*, Jacksonville, Florida, February 6-9, 1995.

[53] J . W. Griffith W. T. Wofford, R. W. Humphries, and J. W. Lawrence. Apparatus and method for applying an oxidant in a hydrothermal oxidation process. US Patent 6,475,396, 2002.

[54] M. Modell, E. F. Kuharich, and M. R. Rooney. Supercritical water oxidation process and apparatus of organics with inorganics. US Patent 6,264,844, 2001.

[55] C. Aymonier, M. Bottreau, B. Berdeu, and F. Cansell. Ultrasound for hydrothermal treatments of aqueous wastes: Solution for overcoming salt precipitation and corrosion. *Ind. Eng. Chem. Res.*, 39(12):4734–4740, 2000.

[56] P. Muthukumaran and R. B. Gupta. Sodium carbonate assisted supercritical water oxidation of chlorinated waste. *Ind. Eng. Chem. Res.*, 39(12):4555–4563, 2000.

[57] M. I. Ravich. Phase equilibria in aqueous salt systems at elevated temperatures and pressures. *Russian Journal of Inorganic Chemistry*, 15(8):1041–1048, 1970.

[58] W. J. Frederick and T. M. Grace. Scaling in alkaline spent pulping liquor evaporators. In E. F. C. Somerscales and J. G. Knudsen, editors, *Fouling of Heat Transfer Equipment*, Washington, 1981. Hemisphere publication corporation.

[59] M. L. Ravich and F. E. Borovaya. Phase equilibria in the sodium-sulfate-water system at high temperatures and pressures. *Russian Journal of Inorganic Chemistry*, 9:520, 1964.

[60] P. C. Dell'Orco, E. F. Gloyna, and S. J. Buelow. The separation of solids from supercritical water. In *ACS Symposium Series*, ACS Symp. Ser. 514, chapter 25. American Chemical Society, Washington, D.C., 1993.

[61] L. Lixiong and E. F. Gloyna. Separation of ionic species under supercritical water conditions. *Separation Science and Technology*, 34:1463–1477, 1999.

[62] V. M. Valyashko, I. M. Abdulagatov, and M. H. L. Sengers. Vapor-liquid-solid phase transitions in aqueous sodium sulfate and sodium carbonate from heat capacity measurements near the first critical end point. 2. phase boundaries. *Chem. Eng. Data*, 45:1139–1149, 2000.

[63] D. Shvedov and P. R. Tremaine. The solubility of sodium sulfate and the reduction of aqueous sulfate by magnetite under near-critical conditions. *Journal of Solution Chemistry*, 29(10):889–904, 2000.

[64] L. Lia and E. F. Gloyna. Separation of ionic species under supercritical water conditions. *Separation Science and Technology*, 34:1463–1477, 1999.

[65] V. M. Valyashko. Phase equilibria in water-salt systems: Some problems of solubility at elevated temperature and pressure. In deG Jones, D, J. E. Slater, and R. W. Staehle, editors, *High Temperature and High Pressure Electrochemistry in Aqueous Solutions*, pages 153–157, Texas, 1973. Nat. Assoc. of Corrosion Engrs, NACE 4.

[66] A. D. Eaton, L. S. Clesceri, and A. E. Greenberg. *Standard Methods for the Examination of Water and Wastewater.* APHA, Washington, D.C., 19^{th} edition, 1995.

[67] H. S. Swenson, J. R. Carver, and C. R. Kakarala. Heat transfer to supercritical water in smooth-bore tubes. *ASME Journal of Heat Transfer*, pages 477–484, November 1965.

[68] K. Yamagata, K. Nishikawa, S. Hasegawa, T. Fujii, and S. Yoshida. Forced convection heat transfer to supercritical water flowing in tubes. *International Journal of Heat and Mass Transfer*, 15(12):2575–2593, 1975.

[69] M. Bazargan. *Forced convection heat transfer to turbulent flow of supercritical water in a round horizontal tube.* PhD thesis, Department of Mechanical Engineering, University of British Columbia, 2001.

[70] P. G. Debenedetti and R. C. Reid. Diffusion and mass transfer in supercritical fluids. *AIChE*, 32(12):2034–2046, 1986.

[71] M. S. Hodes. *Measurements and modeling of deposition rates from a near-critical, aqueous, sodium sulfate and potassium sulfate solutions to a heated cylinder.* PhD thesis, Department of Chemical Engineering, Mass. Inst. of Technology, 1998.

[72] K. A. Smith, M. S. Hodes, and P. Griffith. On the potential for homogeneous nucleation of salt from aqueous solution in a natural convection boundary layer. *ASME Journal of Heat transfer*, 124:930–937, 2002.

[73] F. P. Incropera and D. P. DeWitt. *Fundamentals of Heat and Mass Transfer.* John Wiley & Sons, New York, 4^{th} edition, 1996.

[74] W. Wagner and A. Pruss. The IAPWS formulation 1995 for the thermodynamic properties of ordinary water substance for general and scientific use. *Journal of Physical and Chemical Reference Data*, 31(2):387–535, 2002.

[75] P. Chiang and M. D. Donohue. A kinetic approach to crystallization from ionic solution I. Crystal nucleation. *Journal of Colloid Interface Science*, 122(1):230–250, 1988.

[76] M. Kostoglou and A. J. Karabelas. Comprehensive modeling of precipitation and fouling in turbulent pipe flow. *Ind. Eng. Chem. Res*, 37(4):1536–1550, 1998.

[77] R. Sheikholeslami. Nucleation and kinetics of mixed salts in scaling. *AIChE Journal*, 49(1):194–202, 2003.

[78] J. W. Mullin. *Crystallization.* Butterworth Heinemann, Boston, 4^{th} edition, 2001.

[79] J. H. Seinfeld. *Atmospheric chemistry and physics of air pollution.* John Wiley & Sons, New York, 1997.

[80] M. Roelands, J. Derksen, J. ter. Horst, H. Kramerm, and P. Jansens. An analysis of mixing in a typical experimental setup to measure nucleation rates of precipitation processes. *Chemical Engineering Technology*, 26(3):296–302, 2003.

[81] S. E. Halland. Simple and explicit formulas for the friction factor in turbulent pipe flow. *Journal of Fluid Engineering, Transactions of ASME*, 105(1):89–90, 1983.

[82] B. Y. Shekunov, J. Baldyga, and P. York. Particle formation by mixing with supercritical antisolvent at high Reynolds numbers. *Chemical Engineering Science*, 56:2421–2433, 2001.

[83] J. O. Hinze. *Turbulence.* McGraw-Hill, New York, 2^{nd} edition, 1975.

[84] P. G. Papavergo and A. B. Hedley. Particle deposition behavior from turbulent flows. *Chemical Engineering Research and Design*, 62:275–295, 1984.

[85] J. W. Nielson. *Kinetics of precipitation.* Pergamon Press, New York, 1964.